RHODES UNIVERSITY

Where leaders learn

High-resolution geological, petrological and geochemical investigation of the mid-lower c. 3.3 Ga Kromberg type-section, Barberton greenstone belt, South Africa.

By: Sibusisiwe Ndlela

ORCHID: 0000-0002-1258-9970

Supervisor: Dr. Eugene G. Grosch

Rhodes University

Department of Geology

2020

Thesis submitted in partial fulfilment of the requirements of Master of Science degree in the Department of Geology, Rhodes University.

Acknowledgements

I would like to acknowledge and thank the Rhodes University Research Committee, Rhodes Research Office and the National Research Foundation for providing me with funds to continue my study as a postgraduate student in the geoscience field. I thank Rhodes University for giving me access to analytical facilities, namely with the electron microprobe (EPMA – purchase of which was partially funded by the NRF National Equipment Program grant UID 74464) in the Geology Department, X-Ray Diffraction instrument (Chemistry Department) and Scanning Electron Microscope SEM (Physics Department). I also thank Dr. Deon Van Niekerk for providing me with technical support on the electron microprobe, Martin Randall for training me during use of the SEM and Dr. Jonathan Britton for assistance during XRD analyses. I would like to thank Riana Rossouw and Mareli Grobbelaar (CAF Stellenbosch University) for conducting XRF and ICPMS analyses of rock powders. I also thank Dr. Jiri Slama and the Geological Institute of the Czech Academy of Sciences for carrying out whole-rock Lu-Hf radiogenic isotope analyses.

I thank my supervisor, Dr. Eugene Grosch, for his support throughout the duration of this thesis. He is acknowledged for training me on the petrographic microscope, geochemistry methods and for training me in the field to conduct high-resolution geological mapping in the Barberton greenstone belt. I thank him for awarding me with the NRF Thuthuka Grant; if it was not for his patience and academic wisdom, I would have not been able to complete my thesis. My local geology chapter forms part of an international publication (Precambrian Research, 2020) and I would like to thank my supervisor for giving me the opportunity to co-author a paper and engage with other co-authors. I thank all geology lecturers and staff members at Rhodes University Department of Geology. Prof. Jock Harmer is acknowledged for assisting me with INCA software for my SEM chapter and Dr Nicola McLoughlin for assisting me with the petrography of volcano-sedimentary rocks (cherts).

I thank my family for their continuous support; my parents Nobukhulu Nomzi Ndlela and Sipelele Grant Ndlela, my son Hlokomela Buchule Ndlela, Pheloletu Ndlela, Masixole Ndlela and all my siblings, my nieces and nephews. I also thank the Rhodes University ZCCSF for their support academically and spiritually, Mnoneleli Dingiswayo, Xolelwa Ngantweni, Manezi Mbeju, Awethu Putumani and all my friends in Makanda/Grahamstown.

Lastly, I thank the God of Mount Zion for his blessings over my life. Thank You for giving me strength to complete my thesis.

Declaration

I, Sibusisiwe Ndlela, declare this thesis to be my own work except where due acknowledgement has been made. It is submitted in partial fulfillment of the Degree of Master of Science at Rhodes University. It has not been submitted before for any degree or examination in any other University or tertiary institution.

Signature of the candidate: S.Ndlela

Date: 15 June 2020

Abstract

The geology of the SE limb of the Kromberg type-section, its origin and its evolution has remained controversial for more than five decades since its discovery by Viljoen and Viljoen (1969). Different lithostratigraphy and geodynamic models have been proposed that were centred around two end-member models, a continuous layer-cake stratigraphy model (Viljoen and Viljoen, 1969c, Lowe et al., 1999) or a tectono-stratigraphic model (de Wit et al., 2011, Furnes et al., 2012). Additionally, the Kromberg type-section mafic-ultramafic sequence represents a relatively thin, dismembered sequence compared to other formations or 'complexes' in the Onverwacht Group. Previous geology workers relied on the field interpretations for the construction of the geological architecture of the Kromberg type-section; but no petrographic analyses were conducted for accurate, integrated geological characterization of different rock compositions. To address controversies centred around the Kromberg type-section geology and geodynamic setting, this study is aimed at testing previously proposed stratigraphic and geodynamic models by integrating high-resolution geological mapping, petrography, mineral chemistry and whole-rock geochemistry to verify rock characterization. The aim is to accurately reconstruct the volcano-sedimentary architecture of the Kromberg type-section and to compare this to the results of previous fieldwork. Moreover, the manner in which the Kromberg sequence may relate to current Archean geodynamic models is evaluated, and a new model explaining the origin and evolution of the Kromberg type sequence is proposed.

The integration of high-resolution field mapping, petrography and geochemistry has allowed for a high precision study and that has resulted in the construction of a new geological architecture for the SE limb of the Kromberg type-section. The stratigraphic thickness of the SE limb of the Kromberg sequence comprises dominant c. 80% volcanic rocks and minor c. 15% intrusive rocks, intercalated by 7 volcano-sedimentary chert horizons (c. 5%). Four main rock types (groups) are present in the Kromberg type-section with two sub-types of komatiitic basalts (the Badplaas-type and Geluk-types), Fe-rich tholeiitic basalt, cumulate peridotite, and a metadunite. Although the Kromberg type-section records sub-greenschist to lower greenschist facies, more than 50% of the rock samples classify as altered with parts of the stratigraphy recording extensive chloritization and severe ocean-floor silicification. Geochemical data revealed an enrichment in SiO_2, K_2O, Ba, Rb and variation in HREE for

highly silicified samples whereas, chloritized samples are enriched in FeO and have concave upward LREE patterns. Partially chloritized tholeiites and komatiitic basalts have overlapping SiO_2 signatures, relatively flat REE patterns and a small negative Nb anomaly in the primitive mantle-normalized spider diagrams.

This thesis provides the first Lu-Hf isotope data on whole rock samples from the Kromberg type-section. The ε_{Hf} values at t=3.33 Ga range between -0.62 to +4.18 and Hf model ages range between 3.43 - 4.27 Ga. The rock compositions are compared to the geochemistry of other greenstone belt rocks, which are considered to provide insight onto the geodynamic setting under which the Kromberg mafic-ultramafic sequence formed. The rock compositions reveal plume-related processes where a primitive mantle melt interacts with recycled mafic crust or mafic lower crust of older units of the Onverwacht Group. Only a small Nb anomaly is found in some samples and the data plots outside the subduction zone (forearc and back-arc) field. Rare-Earth element profiles are flat and not consistent with a subduction zone signature, as proposed in previous studies. Rifting of an oceanic floor in a juvenile basin is proposed for the formation of the Kromberg type-section rocks, prior to being tectonically accreted during regional transpressional deformation at c. 3.23 Ga.

Table of Contents

List of figures

List of Tables

Tables in Appendix:

Abbreviations

AGC – Ancient Gneiss Complex

BGB – Barberton greenstone belt

ESZ – Ekulindini Shear Zone

FeO^T – FeO total

GM-1 – Grid map 1

HFSE – High Field Strength Elements

HREE – Heavy Rare Earth Elements

IPH – inter-pillow hyaloclastite

KSM – Kromberg Section Mylonites

KSZ – Komati Schist Zone

L.O.I. – Loss on ignition

LREE – Light Rare Earth Elements

MM – Middle Marker

OAF – Onverwacht Anticlinal Fold

OctTriv – Trivalent cations in octahedral site

O site – octahedral site

T site – tetrahedral site

TTG – tonalite-trondhjemite-gneiss

XFe or XMg – Bulk Fe composition or bulk Mg composition

[R3+]OctTriv = sum of trivalent cations in octahedral sites

1 Introduction

A photograph showing the location of the mid-lower part of the Kromberg type-section shown in the background with (from left to right) my colleague and a geology honours student at Rhodes University, Siyolise Phunguphungu, my supervisor Dr Eugene Grosch and myself, Sibusisiwe Ndlela. This photograph was taken during the fieldwork at Songimvelo Nature Reserve in July 2018.

The location of this study is in the oldest part of the Barberton greenstone belt (BGB) in the 3.334 Ga Kromberg type-section of the Onverwacht Group, in the south-eastern (SE) limb of the Onverwacht Anticline (**Figure 1.1**). The Kromberg type-section is exposed along the Komati River and has generally been reported to consist of a section of pillow lavas, intrusions, massive basaltic sheet flows with interlayered volcano-sedimentary cherts (Viljoen and Viljoen, 1969c). More, recently mafic-ultramafic shear zones have been

described from this locality (Grosch et al., 2009a; de Wit et al., 2011; Grosch et al., 2012) and been referred to as the 'Kromberg Complex' by de Wit et al., (2011). On the north-western (NW) limb of the Onverwacht Anticline no shear zones have been reported in the so-called Kromberg Formation, and it has been described as consisting of 3 continuous lithofacies: a lower chert unit, mafic lapilli unit and volcano-clastic deposits, and an upper dominantly basaltic flow unit (Lowe and Byerly, 1999, 2020). The Kromberg type-section, on the SE limb of the Onverwacht Anticline preserves a rock record of mafic-ultramafic and volcano-sedimentary rocks that provides a unique window into early Earth igneous activity, geodynamics, water-rock interaction and oceanic lithosphere formation. There are various interpretations for the geological stratigraphy and architecture, magmatic/volcanic petrogenetic origin and geodynamic setting of the Kromberg sequence of volcaniclastic-mafic-ultramafic rocks, prompting the need for high-resolution geological and petrological investigations. This current MSc thesis studies the mid-lower part of the Kromberg type-section to investigate the geology/stratigraphy at high-resolution, igneous petrogenesis and volcano-sedimentary history and early crust-mantle geodynamic setting of the mafic-ultramafic rocks. A paper of Grosch et al. (2020), in which I am a co-author, (having contributed river pavement grid maps), is entitled *Geological record of Paleoarchean oceanic flake tectonics preserved the ca. 3.3 Ga Kromberg volcanic type-section, Barberton greenstone belt, South Africa* and investigates the subsequent tectonic accretion of the Kromberg type-section rocks (**Appendix A4**).

1.1 Archean tectonics and the geodynamic settings of Archean greenstone belts

There is an ongoing debate on the timing for the onset of modern-style plate tectonics; some authors argue for uniformitarian views (where Archean tectonics is similar to the Phanerozoic Earth), whereas others argue for non-uniformitarian views. The operation of plate tectonics during the Archean can account for the geochemical, structural and lithological characteristics of the Archean greenstone belts (Condie, 1981). However, it is also argued that the Archean greenstone belts have lower preservation, with much of their rocks recycled into the mantle (Herzberg and Rudnick, 2012). The topic of geodynamics in the Archean is thus important as it provides insight into earliest Earth crust-mantle processes and the formation and development of the crust.

Different dates have been proposed for the onset of plate tectonics, i.e. 4.2 Ga (Cavosie et al., 2007), 4.0 Ga (de Wit, 1998), 3.8 Ga (Furnes et al., 2007), 3.6 Ga (Nutman et al., 2007) and 3.0 Ga (Shirey and Richardson, 2011; Dhuime et al., 2012). According to Turner et al. (2013), the onset of modern-day subduction is marked by the eruption of boninites depleted in compatible elements like Ti and Nb. However, the authors argue that geochemical stratigraphy (Stern et al., 2012) and trace element data, for example the negative Nb anomalies, can be used to detect the initiation of subduction. For instance, similarities between the 4.4 to 3.8 Ga Nuvvuagittuq mafic rocks to the Izu-Bonini-Mariana forearc (Reagan et al., 2010) has been suggested to relate to subduction processes at 3.8 Ga and 4.4 Ga (Turner et al., 2013). Furthermore, eclogite inclusions in diamonds is envisioned to reveal the onset of the Wilson cycle related to subduction at 3.0 Ga (Shirey and Richardson, 2011). According to Moyen and van Hunen (2012), a small and short-lived subduction is suggested for the hot Archean mantle where short-term episodicity is envisioned to have been superimposed onto longer-term mantle-overturns, supercontinent formation, plate locking and breakup. According to this model, the Archean subduction is dissimilar to modern-day steep subduction processes, but continuously matured over time. Moreover, van Hunen and van Berg (2008) suggested that the hotter Archean mantle provides low-density lower crust (up to 20 km) causing inefficient subduction. Other forms of tectonic modes/processes have thus been proposed for the Archean, for example crustal delamination or vertical 'drip tectonics (Zegers and van Keken, 2001; Johnson et al., 2014). Additionally, oceanic 'flake tectonics' is suggested for the 3.3 Ga Archean Kromberg type section, in the Barberton greenstone belt of South Africa (Grosch et al., 2020). In the oceanic flake tectonic model, silicified upper oceanic crustal fragments are delaminated from a thick and denser lower oceanic crust that is recycled into the Paleaoarchean mantle.

Archean greenstone belts are characterized by supracrustal sequences comprised mainly of mafic-ultramafic volcanic rocks, surrounded and intruded by granitic and gneissic rocks (Condie, 1981). Some examples of Archean greenstone belts (compared to the Barberton greenstone belt in this thesis) include the Abitibi greenstone belt formed at ca. 2.7 Ga (Canada, Laflèche et al., 1992), the Isua greenstone belt at ca. 3.7 Ga (Greenland, Polat et al., 2002), the Sumozero greenstone belt at ca. 2.9 Ga (Baltica; Puchtel et al., 1999), the Holenarsipur greenstone belt at ca. 3.3 Ga (India; Khanna et al., 2018), Koolyanobbing greenstone belt at ca. 3.0 Ga (Australia; Angerer et al., 2013) and 3.1-2.7 Ga Wawa greenstone belts (Superior Province, USA; Polat et al., 1999). These greenstone belts have

either an oceanic arc setting or an oceanic plateau setting geochemical characteristics. The Wawa sub-province of the Superior Province is located Minnesota and comprises basalts and both Al-depleted and Al-undepleted komatiites (Polat et al., 1999). Their volcanic rocks are similar to the basalts of the Phanerozoic, having anomalies for Th and Nb that are interpreted as representing crustal recycling (Polat et al., 1999). The basalts and komatiites of the Wawa greenstone belt are thereby interpreted to have been derived from an oceanic plateau setting. This interpretation is similar to that of the lower unit of the ca. 2.9 Ga Sumozero greenstone belt (Puchtel et al., 1999). The ca. 3.3 Ga Holenarsipur greenstone belt is located in India and comprise Si- and Mg-rich metavolcanic boninite (Khanna et al., 2018). The negative Nb and Ti anomalies of these rocks are interpreted to represent intra-oceanic subduction processes and the onset of modern-style plate tectonic settings (Khanna et al., 2018). The ca. 2.7 Ga Abitibi greenstone belt is located in Canada. The southern Abitibi belt comprises volcanic, sedimentary and plutonic rocks. Tholeiitic metabasalts of the southern Abitibi belt are derived by both subduction and rifting processes (Lafléche et al., 1992). Subduction processes are related to the central Abitibi, whereas the low CaO/Al_2O_3 and FeO/TiO_2 of the upper Mg-rich basalts suggest rising mantle diapirs along a rifting plate (Lafléche et al., 1992). The ca. 3.0 Ga Koolyanobbing greenstone belt is in Western Australia (Yilgarn craton) and comprises Al-depleted and Al-undepleted komatiites, tholeiitic basalts, boninites with U-shaped REE patterns and banded iron formations (BIF; Angerer et al., 2013). The Koolyanobbing greenstone belt komatiites are proposed to have erupted proximal to the spreading ridge, whereas the boninite-series is envisioned to have formed in an intra-oceanic arc setting.

1.2 Stratigraphy models and project rationale

Since the work of Viljoen and Viljoen (1969c), the geology of the Kromberg type-section in the south-eastern limb of the Onverwacht Anticline has received less attention compared to the north-western limb (see Lowe and Byerly, 1999, 2020). Various stratigraphy models have been proposed for the Kromberg type-section on the SE Onverwacht Anticline limb where some workers have proposed major structural discontinuities in the form of shear zones (e.g. Grosch et al 2012, de Wit et al., 2011) whereas others proposed a continuous volcano-sedimentary sequence (e.g. Lowe et al., 1999). Recent preliminary field studies on the

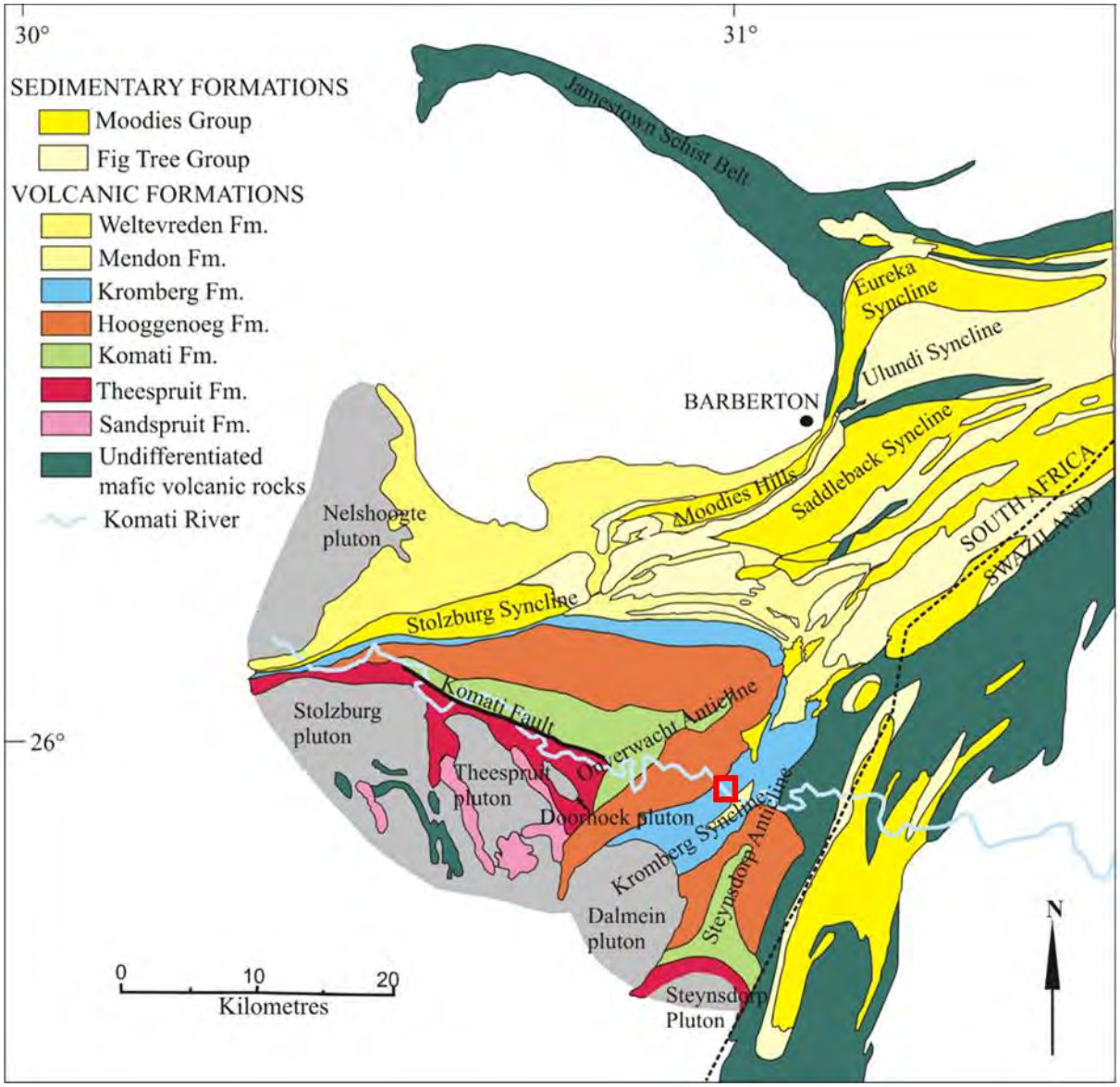

Figure 1.1*: A simplified geological map of Barberton Supergroup, BGB (modified after Lowe et al., 1999). In this map different formations of the Onverwacht Group are shown, with each formation assigned to a different colour. The Kromberg mafic-ultramafic sequence is given a blue colour and it is found partly exposed in the north-western and south-eastern limb of the Onverwacht Anticline. The location of the study area in its type section is shown by the red box inset.*

Kromberg type-section (SE limb of the Onverwacht Anticline) has been conducted by Furnes et al. (2012) and de Wit et al., (2011) although much attention in these studies are given the older formations in the Onverwacht Group, such as the c. 3.472 Ga Hooggenoeg Formation. Contrary to previous continuous stratigraphy models, these workers have proposed that the Kromberg type-section consists mainly of shear-zone bounded mafic-ultramafic intrusions

and basalts that record tectonic stacking and imbrication (see de Wit et al., 2011; Furnes et al., 2012; Furnes et al., 2013). De Wit et al. (2011) propose in a tectono-stratigraphy model, referring to the Kromberg Formation as the 'Kromberg Complex' and indicate modern-style plate tectonics on the Mesoarchean Earth. This differs from the continuous stratigraphy model proposed by Viljoen and Viljoen (1969c) and the geology of the Kromberg sequence in the northern limb proposed by Lowe and Byerly (1999). Furthermore, other stratigraphy and eruption models have been proposed involving eruption of the Kromberg sequence on early felsic crust in a partial convective overturn model (van Kranendonk et al, 2009). Recent detailed geological, petrological and U-Pb zircon geochronological studies has presented a new, high-resolution and multi-disciplinary approach to studying supra-crustal, volcano-sedimentary sequences in the early-mid Archean BGB (e.g. Grosch et al., 2012; Grosch and Slama, 2017). Furthermore, the Kromberg sequence has recently been proposed to represent a tectonically accreted remnant of a juvenile ca. 3.3 billion-year-old oceanic crust (Grosch and Slama, 2017), arguing strongly against eruption of lavas through and on felsic Archean crust.

Poor outcrop exposure, diachronism recorded in lithological differences across the Onverwacht anticline, and varied interpretation of field observations have resulted in large uncertainty for stratigraphic correlations, stratigraphy models and geodynamic models for the Kromberg type-section. This uncertainty is true also for the Onverwacht Group (or Onverwacht Suite, see de Wit et al., 2011) and the BGB in general. In light of all the uncertainties in the stratigraphy and tectonic interpretation, the geology of the Kromberg type-section requires further detailed high-resolution geological mapping to further our understanding of the geological processes, attempt to resolve the stratigraphy models, characterize the various protoliths rock types and their petrogenetic origin, and evaluate the geodynamic setting. Detailed geological mapping and petrological studies of the Kromberg type-section can have potential to further our understanding of mid-Archean geodynamic processes and oceanic lithosphere formation. There are currently no detailed studies for the Kromberg type-section that combines high-resolution field observations with petrography and geochemical protolith ratification. It is thus timely to revisit the Kromberg Formation in more detail than before, using a multi-disciplinary approach. The mid- to lower part of the Kromberg type-section (SE Onverwacht limb) is the focus of this research study, as the upper part has been shown to have been affected by deformation and metamorphic processes near a major shear zone, referred to as the Kromberg Section Mylonites (KSM see Grosch et al., 2012). To avoid later fluid-related tectonic processes and to identify the best, most well-

preserved protolith to the variably altered oceanic Kromberg rocks, the current study aims to focus on the best preserved mid-to-lower part of the Kromberg type-section, where some of the lowest sub-greenschist facies metamorphic conditions of T = 240 – 140ºC in the Barberton greenstone belt have been reported (Grosch et al. 2012). Recent work on the Kromberg type-section includes field mapping from this study (see Grosch et al., 2020). The abstract of the paper is included in **Appendix A4**.

1.3 Competing geodynamic models

There is an on-going debate and controversy regarding the petrogenetic origin and geodynamic setting of the mafic-ultramafic rock types in the Kromberg type-section and the nature of the type of tectonic processes operating at the time the Kromberg was forming on the Mesoarchean Earth. The debate has been centred on two end-member arguments: vertical crustal tectonics (Anhaeusser, 1984, Hamilton, 1998, van Kranendonk, 2009, Kroner et al., 2013) or horizontal modern-style tectonics (de Wit, 1998, de Wit et al., 2011, Furnes et al., 2012; 2014). A diapiric model was first proposed after Viljoen and Viljoen (1969) where the Barberton greenstone belt (BGB) is interpreted as a deformed greenstone succession intruded by granitoid magmas and folded by the vertical movement of tonalitic diapirs (Viljoen and Viljoen, 1969; Anhaeusser, 1984). Further studies by Van Kranendonk et al. (2009) in the lower Onverwacht Group, the Tjakastad subgroup, on the geodynamic setting supported vertical tectonics by proposing partial convective overturn for the BGB. The vertical tectonics model for the BGB was contested after the discovery of repetitions in the stratigraphy, tectonic nappes, high strain zones and reverse faults (de Wit, 1982, 1983, 1991, 2011, 2018) and horizontal thrust subduction-accretion processes proposed for BGB (de Wit et al., 1992; Lowe 1994; Stevens et al., 2002; Moyen et al., 2006; Grosch et al., 2012). Based also on geochemical and structural evidence of the Onverwacht Group of the BGB, a subduction and island arc setting were further proposed for the construction of the Onverwacht Group (de Wit et al., 2011). The dominant basaltic rocks of the Onverwacht Group were thus reported to form in connection to subduction (Furnes et al., 2012). Recently, the Kromberg type-section was proposed to represent relatively thin slivers of dismembered Paleoarchean oceanic crust tectonically emplaced on top of coarse-grained conglomerates of the ca. 3.432 Ga Noisy Formation (Grosch and Slama, 2017; Grosch, 2019).

1.4 Motivation and hypothesis

Historically, the Kromberg-type section has been at the centre of a number of controversial debates and to date a number of important geological questions remain outstanding. These include:

(a) Is there any evidence for sheeted dykes or sill intrusions (c.f. de Wit, 1987; de Wit et al., 2011) in the Kromberg type-section recording ocean floor spreading?

(b) Is the Kromberg type-section dominated by mafic-ultramafic intrusive rocks or volcanic rocks marking eruptive cycles (c.f. Furnes et al., 2012 versus Viljoen and Viljoen, 1969)?

(c) Are previous field observations reporting on the geology of the Kromberg correct and can the rock-types and field relationships throughout the entire type-section be confirmed by petrographic/petrological imaging at high-resolution? For example, are komatiites *senso-stricto* present in the sequence (c.f. Vennemann and Smith, 1999)?

(d) Why is there so much controversy centred around the presence of fuchsite-chlorite-carbonate-quartz horizons in the mafic-ultramafic sequence and possible tectonic repetition of mafic-ultramafic units? Do they possibly represent atmospheric weathering horizons (Lowe et al., 1984); altered felsic volcanic ash horizons (Vennemann and Smith, 1999; Anhaeusser, 1973?) or important flaser-banded tectonites in extensional glide planes (see de Wit et al., 1982, 2011) or mylonitic/listvenitic shear zones (Grosch et al., 2012).

(e) What is the most likely tectonic setting (subduction zone, back-arc, oceanic island arc, oceanic plateau, continental eruption) recorded by the petrology and geology of various rocks throughout the Kromberg type-section (e.g. see Furnes et al., 2012)?

(f) What does the geochemistry of the Kromberg mafic-ultramafic rocks record about the Archean mantle source regions and mantle conditions at ca. 3.3 Ga?

(g) To what extent does the Kromberg type-section represent a sliver of obducted Archean ophiolite, similar to Phanerozoic ophiolites (see discussion in de Wit, 2004; de Wit et al., 2018; Grosch and Slama, 2017)?

(h) Why does the Kromberg type-section represent such a relatively thin (ca. 1.65km) mafic-ultramafic sequence of rocks in comparison to other formations or 'complexes' of the Onverwacht Group (ca. 3 km)?

(i) Despite the controversy of the number of seafloor chert horizons present, how come no evidence for extensive subseafloor silicification has been reported in the Kromberg, unlike in other Onverwacht Formations such as the Hooggenoeg Formation (Hanor and Duchac, 1990)?

This MSc project aims to contribute constructively to these debates and also in helping to potentially resolving some of these controversies. It is clear from the above outstanding questions that high-resolution field studies are required to confirm or reject previous field observations and interpretations. Field observations needs to be corroborated carefully with petrographic and petrological observations. In addition, mineral compositional data is required to understand igneous and metamorphic processes and protolith rock type. Previous geochemical work on these rocks also points to a wide range of geochemical approaches each with their own assumptions and uncertainties, for example: the normalization approach in primitive mantle spider-diagrams, using tectonic discrimination diagrams based on modern-day basalt compositions, using modern terminologies to describe Archean rocks, (e.g. see Furnes et al. 2012, 2013, 2014, versus Viljoen and Viljoen, 1969c and Vennemann and Smith, 1999; Chavagnac, 1999; Parman and Grove, 2004) and geochemical interpretations using geochemical methods that assumes a uniformitarian concept that plate-tectonics was operating locally and globally in the Archean (e.g. de Wit et al., 2011, 2017; Furnes et al., 2012).

The MSc project also aims at testing these various stratigraphy, geodynamic and geochemical models for the Kromberg type-section. It is hypothesized herein, that the controversies that have emerged over the past ca. 60 years are due to potential bias and possible error in field observations and widely varying and inconsistent uniformitarian treatment of geochemical and field data. It is further hypothesized that geodynamic processes unique to the Archean are recorded by the Kromberg type-section and that modern-style Phanerozoic plate-tectonics was most likely not in operation in the Archean due to an Archean mantle that was significantly hotter (200 – 300 K, e.g. Herzberg, 1992; Nisbet et al., 1993 and Abbott et al., 1994a; Johnson et al., 2014) than the modern Phanerozoic Earth.

Based on new observations and results current Archean geodynamic models will be tested, and a new geodynamic model will be proposed for the origin and evolution of the Kromberg mafic-ultramafic sequence.

1.5 Project objectives

The objectives of this project are closely related to the questions outlined in Section 1.4 above. They have been designed to address some of the controversial issues regarding the Kromberg type-section and regionally in the BGB.

The objectives of this study are:

1) Identify and conduct high-resolution geological mapping of exposed rock outcrop along river pavements on both the eastern and western sides of the Komati river, representing exposed parts of the mid-lower Kromberg type-section, to characterize in detail the volcanic architecture of exceptionally well-preserved 3.33 Ga Mesoarchean oceanic crust. Integrate, compare and cross-check field results and observations with the more regional geological work of supervisor E. Grosch on the Kromberg type-section. Contribute towards reconstructing a high-resolution geological-section of the 3.3 Ga Kromberg type-section and compare final geological mapping results to that published in the literature.

2) Perform detailed petrographic description of each representative rock-type encountered to characterize relic igneous and low-grade metamorphic assemblages observed in each rock unit of the sequence. Conduct petrography to identify magmatic/volcanic assemblages for protolith classification.

3) Assess the degree and extent of seawater or tectonic related metamorphic alteration. Identify and characterize evidence for silicification, chloritization and serpentinization in the sequence and their impact on altering protolith geochemistry. Evaluate syn- to post-magmatic low-temperature alteration trends preserved in the sequence.

4) Geochemical/petrological characterization of least-altered rock types using major, trace and rare-earth element whole-rock geochemistry to identify likely rock protolith (e.g. tholeiitic basalt, massive basaltic komatiite, massive komatiite). Compare geochemical protolith identification to field mapping results in the study and other local/regional geological field observations of supervisor E. Grosch.

5) Determine whole-rock Lu-Hf isotope composition of selected mafic-ultramafic samples (with assistance from Dr. Jiri Slama, Czech Academy of Science, E. Grosch collaboration). Calculate a Lu-Hf isochron. Calculate epsilon-Hafnium values and initial Hf-isotope ratios for each representative rock type. Determine for the first time Mesoarchean mantle source characteristics from which the mafic-ultramafic rocks were derived. Test for Archean mantle heterogeneity currently in the Archean eon.

6) Combine field, petrographic and geochemical data at high-resolution to reconstruct the geological stratigraphy and structure of the mid-lower 3.3 Ga Kromberg type-section preserved in the BGB to better constrain the geology and to compare to previous, relatively limited geological work on the section locally and aim to resolve some of the field-based controversies.

7) Compare the reconstructed geology of the mid-lower Kromberg type-section on the SE Onverwacht limb of the Onverwacht Anticline to the mid-lower Kromberg Formation on the north-western limb of the Onverwacht Anticline (e.g. Lowe et al., 1999), to assess if geological units are similar or diachronous and to develop a foundation to determine regional geologic/stratigraphic correlation.

8) Combine field, petrographic and geochemical data to test current Archean geodynamic models for the Kromberg Formation and to propose a new geodynamic model for the Kromberg type-section sequence of rocks.

The above objectives are satisfied scientifically using different analytical methods which are discussed in each chapter. In this study, my supervisor (Dr. E. Grosch) and I visited the Barberton greenstone belt in Mpumalanga at Songimvelo nature reserve, where the Kromberg

type-section outcrops along the Komati river. In prior field work, the area was studied by Dr. E. Grosch where he collected different rock samples and availed them for use in the laboratory. In preparation for thin sections and powder analyses, the Rhodes University geology department was used to cut rock samples in thin slabs for thin section preparations. Offsets were crushed to produce sample powders, which were further sent to Stellenbosch University for XRF and ICP-MS analysis. Another batch of powder samples were sent to the Chemistry department at Rhodes University where Dr. Britton provided the analytical setup for XRD. Thin section preparation was conducted at Rhodes University and at Stellenbosch University. Twenty thin sections were prepared in the Geology department, at Rhodes University, by Mr. Thulani Royi and Andile Pikoli. Another batch comprising sixteen rock slabs was sent to Stellenbosch University for thin section preparations. Furthermore, selected thin sections were carbon-coated at Rhodes University in preparation for Scanning Electron Microprobe (SEM) and electron microprobe (EPMA). SEM analysis was conducted at the Physics Department, Rhodes University with technical assistance provided by Mr. Marvin Randall. Electron microprobe analysis for mineral composition was conducted at the Department of Geology, Rhodes University, with the assistance of Dr. Deon van Niekerk.

1.6 Terminology used

One of the controversies in the BGB concerns the divisions of the Onverwacht Group, where it was traditionally divided into different 'formations' (Viljoen and Viljoen, 1969). Owing to the tectonic discontinuities and multiple intrusions, the formations in the Onverwacht Group were re-defined as 'complexes' (e.g. 'Kromberg Complex') and Onverwacht Group as 'Onverwacht Suite' (de Wit et al., 2011), implying an ophiolite origin and tectono-stratigraphy. 'Suite' refers to a continuous volcanic sequence, whereas 'complexes' in their model refer to accreted allochthonous, tectonic slivers of mafic-ultramafic rocks. The ophiolite model for the Onverwacht Group is one possible model for the Barberton greenstone belt. To prevent confusing nomenclature, in this study the historical term 'formations' and 'groups' are retained and assessed to some extent. The term Kromberg Formation is used to refer regionally to the Kromberg Formation, particularly for the NW limb of the Onverwacht Anticline (e.g. Lowe et al., 1999), whereas the Kromberg type-section is represented on the SE limb of the Onverwacht Anticline, in the southern part of the BGB (this study, see map in **Figure 3.1**).

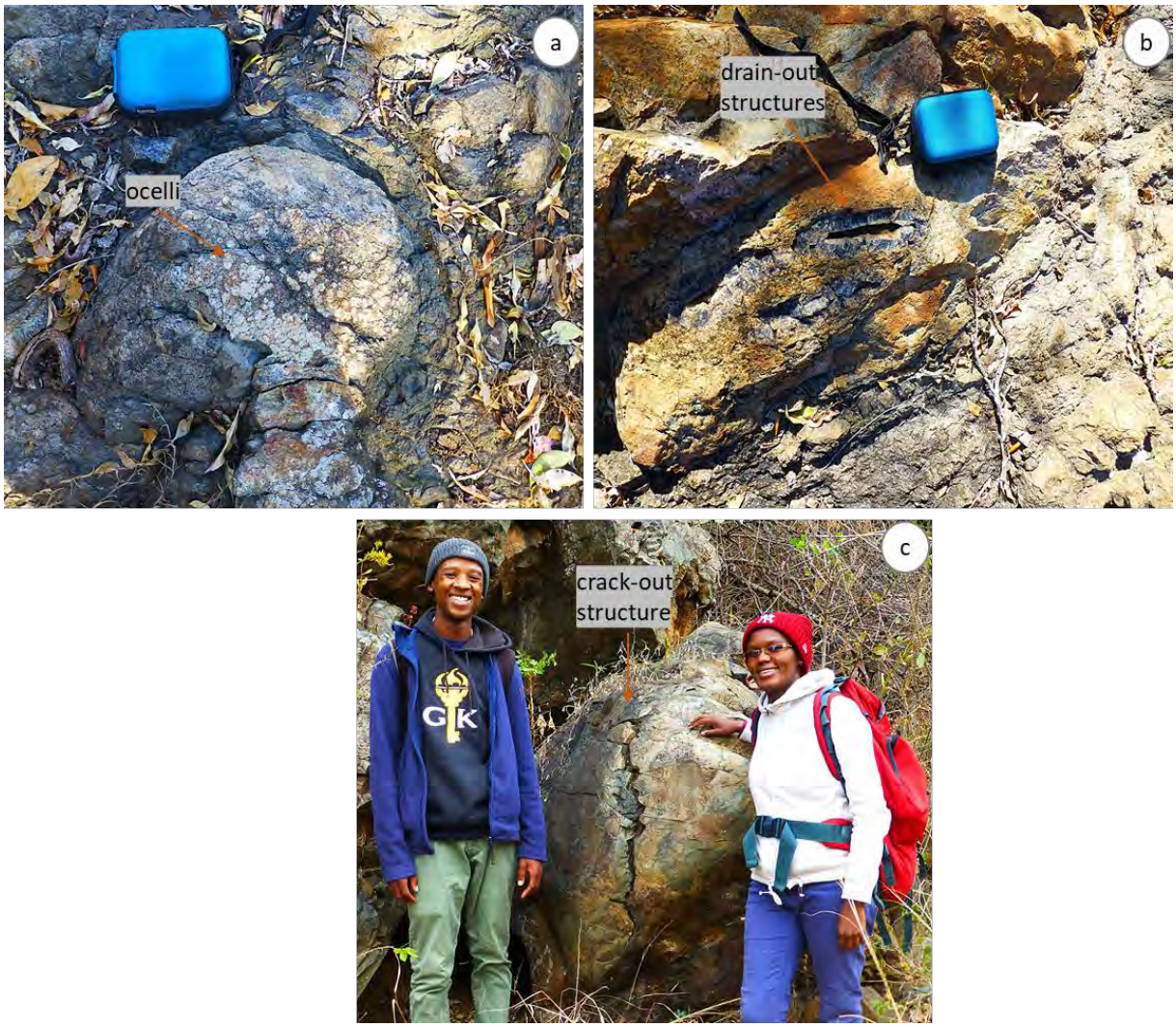

Figure 1.2: *Photographs showing (a)ocelli structures which are rounded leucocratic bodies contained in the pillow core, (b) drain-out structures which represent pouring of hot lava on pre-existing lava, (c) crack-out structures which represents a crack opening resulting from the solidification of a pillow lobe from a pre-existing frozen pillow.*

After fieldwork was conducted, it was discovered that tholeiitic rocks in the Kromberg type-section have varying features. While other tholeiitic pillow lavas are massive, some are ocelli-bearing while others have drain-out structures. The term 'ocelli' is used to describe the rounded and leucocratic (Ferguson and Currie, 1972) internal structures in the basaltic pillows. They are formed through liquid-immiscibility, with one liquid more felsic than the other. The felsic liquid forms immiscible globules which solidifies within the less felsic liquid, resulting in ocelli structures observed in the Kromberg type-section (**Figure 1.2a**). Drain-out structures result from the pouring of hot lava into pre-existing pillows. These

structures are infilled by secondary quartz and carbonate (**Figure 1.2b**). Consequently, the term crack-out structure is used to denote a spreading crack within the pillow lobe that forms as a result of the formation of a pillow lobe on a pre-existing pillow (**Figure 1.2c**). For the different rock compositions encountered in the Kromberg type-section, a classification scheme by Viljoen and Viljoen (1969c), Williams and Furnell, (1979), Smith and Erlank, (1982), and Viljoen et al., (1983) was applied. According to this classification scheme, komatiitic basalts have MgO content between 11 – 24 wt.%. In the Kromberg type-section, komatiitic basalts have MgO contents between 14 and 21 wt.%. They have overall interlocking pyroxene crystals with quartz in the matrix between pyroxene crystals. Cumulate peridotite on the other hand have MgO content between 21 and 30 wt.%. They are cumulate with a poikilitic texture where ca. 50% olivine crystals forms chadacrysts and less than ca. 60% clinopyroxene, oikocrysts. In this thesis, cumulate peridotite or peridotitic cumulate is also referred to as the poikilitic wehrlite. Based on their modal proportions, this group plots in the wehrlite field. Furthermore, the absence of plagioclase in the mineralogical compositions rules out the rock being termed picrite. Some sections in the volcano-sedimentary architecture of the Kromberg type-section (SE limb of OAF) are silicified whereas others are chloritized. Both these terms are used to describe secondary alteration processes in the Kromberg type-section. Chloritization is closed system metamorphism and silicification is open system metasomatism. Silicification results in extensive increase (>50 wt.%) in SiO_2 content in rocks whereas partial chloritization does not significantly change the geochemistry of rock. In chloritized rocks, the rock minerals are partially pseudomorphed by secondary chlorite (amesite and/or clinochlore). The term magma mingling is also used in this study. Magma mingling is the interaction of magma resulting in heterogeneous compositions and physically distinct magma (Johnson and Barnes, 2006). This is different from magma mixing wherein magma interaction results in a homogeneous melt.

2 Regional geology

A photograph showing the Komati river, the river along which the Kromberg type-section is exposed. This photograph shows a NE view with an outcrop of pillow lavas along the Komati river.

2.1 Geology and stratigraphy of the Onverwacht Group

The ca. 3.5-3.1 Ga Barberton Greenstone Belt (BGB) is located south and southeast of Nelspruit, on the border between Swaziland and South Africa (Brandl et al., 2006). It is one of five major greenstone belts (namely: Rhenosterkoppies, Pietersburg, Giyani and Murchison) of the Kaapvaal Craton (Brandl et al., 2006) and is structurally in contact with the Ancient Gneiss Complex (AGC) in the north-western parts of Swaziland, forming the oldest crustal nucleus in the Kaapvaal Craton (Compston and Kroner, 1988). The BGB covers an area of 120 x 50 km (Brandl et al., 2006) and comprises supracrustal sequences of mafic-ultramafic rocks interlayered with volcano-sedimentary cherts and banded-iron

formations (Anhaeusser et al., 1981; Anhaeusser, 1978a). It is regionally characterised by nearly vertical and tight, isoclinal folds trending in an E-W and NE-SW direction (Heubeck and Lowe, 1999; Brandl et al., 2006) bounded by numerous transpressional strike slip faults. It has been divided into four blocks or fault bounded terranes that record early diachronous magmatic activity and sedimentation at 3550-3440 and 3223-3228 Ma (Lowe, 1994). These are: the Steynsdorp Block, Songimvelo Block and the Umaduha Block in the north central BGB; and the Kaap Valley Block, north of Saddleback-Inyoka Fault System (Lowe, 1999c). The Steynsdorp Block is the oldest block and includes the ca. 3530 Ma Theespruit tonalite-trondhjemite-gneiss (TTG) complex and the ca. 3509 ± 8 Ma Steynsdorp trondhjemitic gneiss whereas the Songimvelo Block includes the ca. 3460-3437 Ma Stolzberg TTG complex and the Onverwacht supracrustal greenstone sequence (Lowe, 1999c; **Figure 1.1**).

The BGB is divided stratigraphically into the Swaziland Supergroup (Anhaeusser et al., 1981), the Barberton Sequence (SACS, 1980), or the Barberton Supergroup (Brandl et al., 2006). Traditionally, a continuous stratigraphy model was proposed by Viljoen and Viljoen (1969) and adopted by Lowe and Byerly (1999). In the continuous stratigraphy model, the Barberton Supergroup is subdivided into the oldest Onverwacht Group (ca. 3550-3334 Ma), Fig Tree Group (ca. 325-3226 Ma) and Moodies Group (ca. 3230-3110 Ma; Viljoen and Viljoen, 1969a; Brandl et al., 2006; Lowe and Byerly, 1999, 2007; **Figure 1.1**). The Onverwacht Group is situated in the central and southern regions of the BGB (Brandl et al., 2006) and comprises mainly ultramafic to mafic volcanic rocks. The Fig Tree group comprises chert, shale, greywackes and dacitic volcanic rocks and the Moodies Group comprises mainly sedimentary sequences including conglomerates, shale, siltstone and sandstone (Lowe and Byerly, 1999, 2020). In the continuous stratigraphy model, a layer-cake stratigraphy was proposed in the south of the Onverwacht Group where the group was initially divided into six formations (Viljoen and Viljoen, 1969a, b; **Figure 2.1**).

Further scientific drilling and fieldwork in the south have reported a clastic sedimentary succession known as the Noisy Formation (Grosch et al., 2011; **Figure 2.2**). The Onverwacht Group thus comprises seven formations, namely: Sandspruit, Theespruit, Komati, Hooggenoeg, Noisy, Kromberg, and Mendon Formations (see Grosch et al., 2011). Viljoen and Viljoen (1969) reported the Onverwacht Group to young from the Sandspruit Formation to the Mendon Formation. Further studies on the structure of the Onverwacht Group reported the top four formations (Komati, Hooggenoeg, Kromberg and Mendon Formations) to represent an intact sequence (Lowe et al., 1985). This was further disproved

by the age data obtained from precise zircon age dating which reported the Komati Formation as older and structurally overlying the younger Theespruit Formation (Armstrong et al., 1990). This suggests that there is a structural discontinuity along the Komati Fault (or Komati Shear Zone; KSZ see map in **Figure 2.1**) and therefore suggest the top four formations as not intact. In the BGB, the low-grade volcano-sedimentary sequence and high-grade TTG gneiss complex is separated by the KSZ (de Wit, 1991).

The ***Sandspruit Formation*** (**Figure 2.1**) is stratigraphically the lowest formation and structurally the oldest formation in the Onverwacht Group (Viljoen and Viljoen, 1969). It is ca. 2135 m thick (Viljoen and Viljoen, 1969c) and comprise predominantly of metamorphosed basaltic and peridotitic komatiites and minor units of chert, calc-silicate rocks, banded iron formation and arkoses. The formation is represented in part by xenoliths, stringers and isolated remnants of mafic to ultramafic amphibolite which are enclosed by intrusive trondhjemitic gneisses of the Theespruit, Stolzberg and other south-western plutons of the BGB (**Figure 1.1**). The arkoses that form part of the metasedimentary unit of the Sandspruit Formation contains detrital zircons dated between ca. 3540 and 3521 Ma (Dziggel *et al.*, 2002). The trondhjemitic gneisses intruding the greenstone remnants of the Sandspruit Formation gives the minimum age of 3411 ± 11 Ma (Brandl *et al.*, 2006).

The 3.55-3.45 Ga ***Theespruit Formation*** (**Figure 2.1**) is a ca. 1890 m thick formation that comprise metamorphosed lavas, tuffs and cherts, and infrequently pillow- and ocelli-rich basalt (Brandl et al., 2006). It also consists of relatively uncommon metamorphosed komatiite rocks that occur mainly as conformable layers of serpentinite and schists, but also as lenses. The distinguishing feature of the Theespruit Formation are the volcanoclastic, pyroclastic and autoclastic units which form protruding aluminous, sericitic and siliceous schistose beds with minor chert (Viljoen and Viljoen, 1969). Van Kranendonk (2009) supported the continuous stratigraphy model for the Onverwacht Group and interpreted the Theespruit Formation as older than the Komati and Noisy Formation. Van Kranendonk (2009) reported U-Pb zircon ages of 3453 ± 6 Ma from felsic volcaniclastic units, giving a depositional age for the Theespruit Formation. The Theespruit Formation rocks has been intruded by the Theespruit and Doornhoek Plutons (Figure 1.1) and is traversed by several mylonitic shear zones, one of which is the regionally referred to as the Theespruit shear zone (de Wit at al., 1983, 2011).

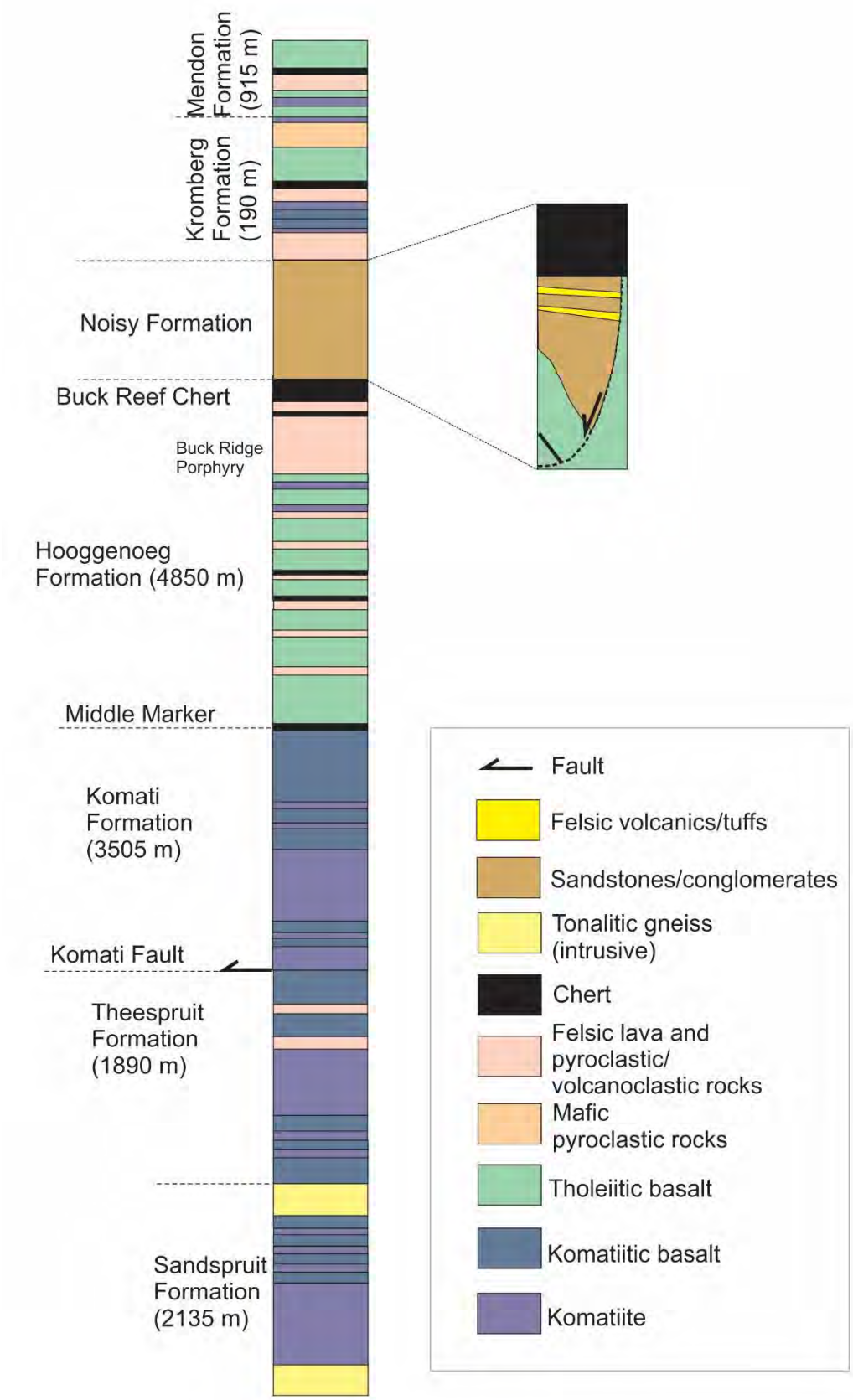

Figure 2.1: *A simplified geological lithostratigraphy model of the Onverwacht Group (modified after Viljoen and Viljoen, 1969) that shows the layer-cake stratigraphy model. Noisy Formation insert after de Vries et al. (2008), Grosch et al. (2011) and de Wit et al. (2011).*

The (ca. 3.48 Ga) ***Komati Formation*** (**Figure 2.1**) is a ca. 3500 m thick formation, located on the western limb of the Onverwacht Anticlinal Fold (OAF; Brandl et al., 2006). The formation consists mainly of low-grade metamorphosed komatiites, komatiitic basalts and, to a lesser extent tholeiitic metabasalts (Viljoen and Viljoen, 1969). It is the best-preserved formation of interlayered komatiites and basalts in the world and is also well-known for its spinifex textures restricted by chilled margins (Dann, 2000). A single tuff zone in the Komati Formation yielded a U-Pb age of c. 3481 ± 2 Ma (Parman and Grove, 2004). Also, cross cutting the Komati Formation are ca. 3467 Ma felsic dykes (Kamo and Davis, 1994), which yields the minimum age for the Komati Formation (de Wit et al., 2011). In the upper part of the formation, Armstrong et al. (1990) conducted a U-Pb SHRIMP analysis of the zircons found in the metagabbro which yielded an age of 3482 ± 5 Ma. The same metagabbro yielded a U-Pb baddeleyite date of 3351 ± 6 Ma, and this was interpreted to be the age of the intrusion (Kamo and Davis, 1994). The Komati Formation comprises a shear zone (Dann, 2000) known as the Mbjega shear zone with uppermost shear zone comprising talc-phyllite layers with extensional quartz-carbonate veins (Dann, 2000; Dann and Grove, 2007). It is bounded by shear zones in its upper and lower contacts, where below or within the first 100 m of chert horizon, similar shear zones to the Mbjega shear zone occur (de Wit et al., 2011). The Komati Formation is thus bounded by shear zones, the lower KSZ and upper Mbjega Shear Zone.

The (<3472 ± 5 Ma) ***Middle Marker*** (MM) chert (**Figure 2.1**) is a 1-5 km thick layer divided in the northern limb into three to five noticeable horizons (Armstrong et al., 1990; Brandl et al., 2006). It divides the Onverwacht Group into a lower dominantly ultramafic Tjakastad Subgroup and the upper mostly tholeiitic Geluk Subgroup. It consists of silicified ash, volcanoclastic sediments and black chert. It is a pyroclastic layer consisting of graded beds of lapilli which are overlain by fine-grained cross beds (Lowe, 1999a). Between the MM and the Mbjega shear zone are komatiitic breccias and silicified pillow lavas which host flaser-banded quartz-carbonate-serpentine rocks interpreted as subseafloor weathering zones (Lowe and Byerly, 1986) or as extensional shear zones (de Wit, 1982, 1983). A depositional age of c. 3472 ± 5 Ma has been proposed by Armstrong et al., (1990) based on U-Pb zircon dating.

The ***Hooggenoeg Formation*** (**Figure 2.1**) is stratigraphically situated directly above the Middle Marker, forming the base of the upper Onverwacht Group. It is c. 4850 m thick and is characterised with at least five volcanic cycles of metabasaltic rocks (Brandl et al.,

2006). The thickness of these rocks progressively decreases with each cycle where thick zones of pillowed and massive basalts are followed by thinner dacite and rhyodacite lavas overlain by a chert zone. The Hooggenoeg Formation is further subdivided into the Upper and the Lower Hooggenoeg. The lower Hooggenoeg Formation is a 1800 m thick unit with pillowed and massive basalts (Dann, 2000). The base of the formation, marked by the Middle Marker chert horizon records the maximum age of 3472 ± 5 (Armstrong et al., 1990). At the bottom of the Upper Hooggenoeg Formation are 700 m thick pillowed and sheet flows of komatiitic basalts with pyroxene spinifex zones. The 1 km thick unit of komatiitic basalts extends to the entire western limb of the Onverwacht Anticline. This makes the Hooggenoeg formation a bimodal extrusive sequence (Brandl et al., 2006). Olivine-spinifex komatiites with bladed spinifex textures occur towards the Upper Hooggenoeg Formation. The northern limb of Hooggenoeg Formation is therefore characterised by vesicular basalts divided by chert horizons and bounded by an upward tectonic contact with dacitic intrusions (de Wit et al., 2011).

The south-eastern limb of the Hooggenoeg Formation comprises two steeply dipping brittle faults with opposing offsets with the top of the formation truncated by an angular unconformity overlain by the ca. 3432 Ma (Grosch et al., 2011) Noisy Formation, eroding more than 1.5 km of the Hooggenoeg Formation volcanic rocks, intrusive rocks and the five chert horizons, (de Wit et al., 2011). It has a regional shear zone at its lower contact traversed by undeformed mafic-ultramafic intrusions, whereas at the top it is truncated by the unconformably overlying Noisy Formation polymictic conglomerate (Grosch et al., 2009a,b, 2011; Furnes et al., 2011; de Wit et al., 2011). The south-eastern limb of the Hooggenoeg comprises various mafic-ultramafic sills and mafic intrusions. The sills and dykes comprise coarse-grained metapyroxenite to metawehrlite and metadunite while mafic intrusions comprise metadolerite with coarse-metagabbro.

The (ca. 3432 Ma) ***Noisy Formation*** (Grosch et al., 2011; **Figure 2.2**) is exposed on the SE limb of the OAF along the Komati River (Grosch et al., 2011). It comprises ca. 120 m thick lower upward-fining unit of polymictic diamictites (rhyodacitic to granitic clasts) and ca. 80 m thick upper monomictic zone consisting of cross-bedded, angular sandstones and a yellow felsic tuff layer overlain by an upper laminated, black and grey chert (Grosch et al., 2011). The base of the Noisy Formation forms an angular unconformity with the underlying uppermost Hooggenoeg Formation. Along the Mtsoli river, the conglomerates directly above the unconformity contain a range of clast compositions, namely fuchsite-rich metabasalts,

dacites, rhyolites and tonalites (Grosch et al., 2011; de Wit et al., 2011). De Wit et al., (2011) stratigraphically correlated the Buck Ridge volcano-sedimentary complex on the north-western limb to the Noisy Formation on the south-eastern limb.

The (ca. 3334 Ma) ***Kromberg Formation*** (**Figure 2.1**) comprises mafic to ultramafic sequences on the north-western and south-eastern limb of the Onverwacht Anticline, also known as the Onverwacht Anticlinal Fold (OAF;). Lowe and Byerly (1999, 2020) informally divided the north-western limb of the OAF of the Kromberg Formation into three members: (1) K1, the Buck Reef; (2) K2, mafic lapilli tuff and lapillistone; and (3) K3, tholeiitic basalt. The Buck Reef Chert (K1) was named by Hall (1918). It forms the base of the Kromberg Formation, is located on the north-western limb of the OAF. On the north-western limb, K1 Buck Reef Chert has a number of subdivisions namely: silicified evaporate forming the basal unit, banded black-and-white chert, ferruginous chert and the upper black-and-white chert (Lowe and Byerly, 1999, 2020). K2, the mafic lapilli tuff and lapillistone is predominantly massive, coarse-grained and heavily altered. It is situated in the middle part of the Kromberg Formation. It has a 10-100 m fine-grained base of tuff and fissile, tuffaceous, non-silicified, carbonaceous shale with thin local mafic flows. The carbonaceous sediments are overlain by a 300-1000 m thick coarse-grained mafic lapillistone with discontinuous mafic flows. The lower third to half of the mafic lapillistone contains 0.5-4 cm massive and unstratified lapilli with Buck Reef Chert clasts, fine-grained mafic flow and coarse-grained rare pyroxenite chunks (Lowe and Byerly, 1999, 2020). The upper K2v comprises of stratified and cross-stratified finer-grained lapilli and thin layers of altered silicified ash, while the topmost lapilli which are less than 1 cm show current structures including cross-stratification. K2v, on the hinge region, is associated with polymictic conglomerates, quartzose sandstone and breccia with banded ferruginous chert in a quartzose matrix (Lowe and Byerly, 1999, 2020). K3 overlies K2 and comprises 500-600 m thick silicified pillowed basalts (K3v; Ransom, 1987) with thick upper units of pillow breccia. Capping the formation is a Footbridge Chert (K3c) that consist of, on the western limb, 15-25 m black and black-and-white banded chert (Lowe and Byerly, 1999, 2020).

The $^{207}Pb/^{206}Pb$ zircon evaporation ages of the Footbridge Chert yield dates of 3334 ± 3 Ma (Byerly et al., 1996). The Footbridge Chert zircons on the south-eastern limb, from a study by Grosch and Slama (2017) revealed a relatively homogeneous Pb-Pb age distribution with the majority of zircons yielding similar ages to that of a c. 3353 Ma gabbro and related mafic volcanic rocks from the Komati Formation (Kamo and Davis, 1994). A recent detrital

zircon U-Pb study using the SIMS technique provides a maximum depositional age of c. 3.31 Ga for the Footbridge Chert, based on the youngest group of zircon grains (Grosch et al., 2020). The lower parts of the south-eastern limb of the Kromberg type-section, the focus of this study, comprise pillow vesicular lavas that become non-vesicular and variolitic further up, as well as massive flows. The massive lava flows in the upper 40 m of the section have vesicular tops and are up to 20 m thick (Furnes et al., 2011). The occurrence of vesicles in the lower stratigraphy and varioles in the upper stratigraphy suggests deep waters and basin eruption that diminished by more than 3 km (Furnes et al., 2011). Vennemann and Smith (1999) reported varying sizes of basaltic pillows in the Kromberg type-section with sizes from 0.6 x 0.5 m to 2 x 1 m and for some massive lavas to grade to thinner pillows. The authors further report tholeiitic intrusive sills with a coarser-grained texture in their central part and a mineralogy and bulk chemical composition similar to extrusive tholeiitic compositions of the type-section. Grosch et al., (2020) has recently provided a revised volcano-sedimentary stratigraphy model for the Kromberg type-section, indicating that most of the rocks are extrusive in nature and that at least three shear zones are present.

The ***Mendon Formation*** (**Figure 2.1**) is the uppermost formation of the Onverwacht Group. It is 15-20 km and comprises komatiitic to basaltic volcanic lavas and intrusions and interlayered with thick chert horizons (Byerly, 1999). The rocks in the Mendon Formation were previously divided into at least five cycles of komatiitic volcanism (M1v-M5v) separated by thin chert layers (M1c-M5c; Lowe and Byerly, 1999). The dacitic intrusions yielded U-Pb zircon ages of 3232 and 3229 Ga (de Ronde et al., 1991; de Ronde and de Wit, 1994; Kamo and Davis, 1994), and the volcaniclastic and volcanic rhyodacites in the upper part, youngest part of the Mendon Formation yielded an age of c. 3230 Ma (Lowe and Byerly, 1999). The Mendon Formation also comprises tectonic slices along thrust faults and are emplaced as nappes across the sediments of the Fig Tree (Lowe and Byerly, 1999; de Wit, 1982). The uppermost Mendon Formation comprises laminated and massive black chert, black and white banded chert, ferruginous chert and silicified ash beds (Trower and Lowe, 2016).

Since the work of Viljoen and Viljoen (1969a), the continuous layer-cake stratigraphy model was contested by de Wit, (1982a) and de Wit et al. (1982b; 1987a,b; 2011) suggesting an ophiolite origin for the BGB in the proposed Jamestown Ophiolite Complex (de Wit et al., 1987a) for the Onverwacht Group. Subsequently, de Wit et al., (2011; 2018) proposed Onverwacht ‘Suite’ in a tectono-stratigraphy model in which formations bounded by

extensional glides planes and/or shear zones are referred to as ‘complexes’ (see **Figure 2.2)**. These authors argue for a discontinuous and dismembered stratigraphy for the BGB Archean supracrustal rocks and base their model on the identification of proposed tectonic repetitions in the Archean BGB (de Wit, 1982). In the discontinuous tectono-stratigraphy model (**Figure 2.2**) the southern part of the BGB comprises folds and thrust nappes that have been horizontally translated along the glide planes (de Wit, 1982). In this model the Onverwacht ‘Suite’ comprises a major unconformity and at least seven shear zones separating it into seven complexes (namely: Sandspruit, Theespruit, Komati, Hooggenoeg, Noisy, Kromberg and Mendon Formation; de Wit et al., 2011; **Figure 2.2**).

The Kromberg type-section on the south-eastern limb of the OAF (**Figure 2.2**) is shown in the tectono-stratigraphy model of de Wit et al. (2011) and compared to the continuous stratigraphy model of Lowe et al. (1999). In this stratigraphic model the Kromberg type-section comprises minor gabbroic intrusions, silicified chert, tholeiitic massive and pillowed lava flows, coarse-grained ultramafic intrusive rocks, silicified lapilli tuff and minor komatiitic basalts bounded my structural discontinuities namely shear zones and extensional ‘glide planes’. In the de Wit et al. (2011) and Furnes et al. (2012, 2013) geological interpretation of the Kromberg type-section, a large volume (about 85%) of the exposed lithological section is interpreted to represent of undifferentiated intrusions (in the middle part of the section) and about 15% is made up of volcanic rocks (**Figure 2.2**). These intrusions are mostly gabbroic intrusions with poorly developed contacts (de Wit et al., 2011; Furnes et al., 2012). A shear zone termed the Kromberg Section Mylonites or Kromberg Shear Zone (KSM; Grosch et al., 2012; Grosch and Slama, 2017) occurs in the upper Kromberg type-section. The lowermost unit of the Kromberg consist of serpentinized metadunite bounded by a shear zone (de Wit et al., 2011). A 10m thick shear zone occurs directly above the metadunite (**Figure 2.2**). The shear zone is in turn overlain by a thinly banded and carbonaceous chert with millimetre to centimetre thick ferruginous carbonate layers (de Wit et al., 2011). A metagabbro and diabase encloses the carbonaceous chert and is overlain by 150 m thick basaltic lavas with KV1 in the lower sequence (**Figure 2.2**). KV1 consists of a ca. 25 m thick massive basaltic unit that overlies a chert. It has vesicles near the top suggesting a single lava flow or a series of thinner massive flows (Furnes et al., 2011). The massive basalt is overlain by 70 m thick vesicular pillow lava that becomes more massive in the upper 20 m. The sequence of massive layers

has two volcaniclastic thin layers and the uppermost part of KV1 comprise ca. 5 m thick pillow fragments embedded in a hyaloclastite matrix (Furnes et al., 2011).

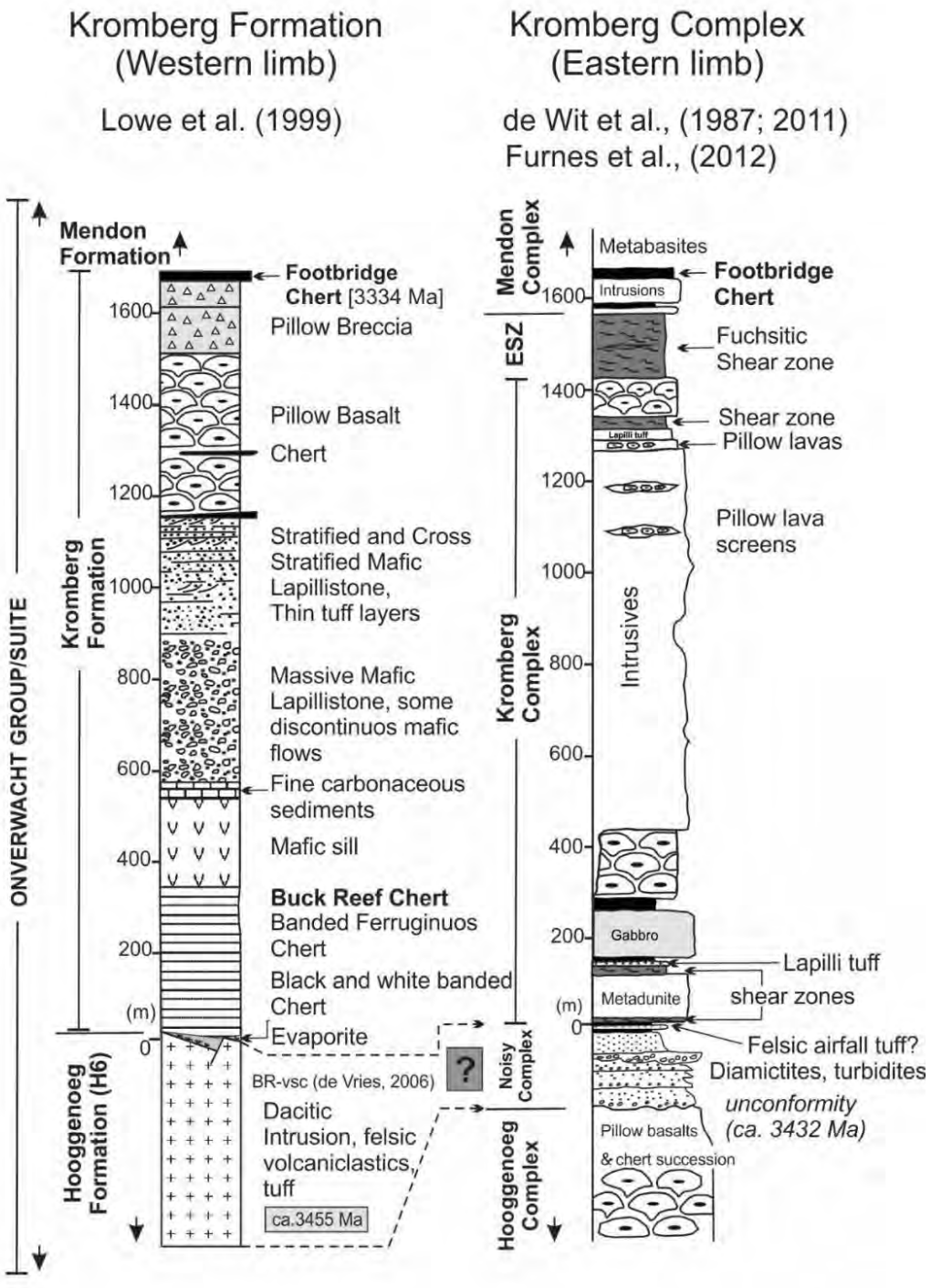

Figure 2.2: *Lithostratigraphy models of the Kromberg Formation or Kromberg 'complex' exposed on the north-western limb of the Onverwacht Anticlinal Fold (continuous stratigraphy, Lowe et al., 1999) and on the south-eastern limb of the Onverwacht Anticlinal Fold (tectono-stratigraphy, de Wit et al., 2011; Furnes et al., 2012). The type-section for the Kromberg is on the south-eastern limb. This figure is modified after Grosch et al., (2011).*

The uppermost unit of the Kromberg type-section is a Footbridge Chert, a 15-25 m thick black carbonaceous sedimentary chert (Lowe and Byerly, 1999, 2020; Grosch et al., 2012). In this area is a 600 m thick lapilli tuff traced around the Kromberg Fold hinge with large-scale cross beds. The lapilli tuff is tectonically separated from the pillowed and massive basaltic units (KV2; de Wit et al., 2011). Section KV2 is a poorly exposed and discontinuous section that is bounded by a ca. 5 m thick shear zone and the upper ca. 150 m thick KSM (de Wit et al., 2011; Grosch et al., 2012). It is overlain by a coarse-grained serpentinized pyroxenite boudins and brecciated screens of pillow lavas flaser-banded gneiss with quartz veins and carbonate separated by mafic-ultramafic mylonite (de Wit et al., 2011).

In the south eastern limb of the OAF, de Wit et al. (2011) and Furnes et al. (2011) names the lower part of the Mendon Formation, the Ncakini section. The Ncakini section is ca. 50 m thick and comprise 3-9 m thick variolitic and massive basaltic flows separated by thin and discontinuous chert layers (Furnes et al., 2013). The Ncakini section (Mendon complex) is separated from the Kromberg type-section by the KSM shear zone (Furnes et al., 2011; de Wit et al., 2011; Grosch et al., 2012) In the de Wit et al., (2011) and Furnes et al., (2012) stratigraphy model, the Footbridge chert occurs in the Ncakini section. The gabbros and massive tholeiitic basaltic flows occur above the KSM in this model.

2.2 Structural geology

Three major deformation events are distinguished in the BGB (D_1 to D_3; de Ronde and de Wit, 1994; Brandl et al., 2006). These are pre-Moodies deformation events that are manifested differently in both the northern and the southern parts of the belt. In the southern parts, D_1 structures are those associated with the emplacement of allochthon of the Komati, Hooggenoeg, Kromberg and Mendon Formation along the Komati Fault thrust in the model of de Ronde and de Wit (1994) and de Wit et al. (2011). The D_2 structures of the south and the central parts affect the E-W or NE-SW trending tight to isoclinal folds with sheared limbs along oblique-slip faults (Tomkinson and King, 1991). D_3 structures in the south subdivide the region into several structural domains that reveal sinistral-reverse faults (Brandl et al., 2006). The D_1 structures of the northern parts are associated with ribbon-like zones of black and white chert, fuschite-carbonate-quartz and green and grey talc-carbonate schist. The

fuchsite-chlorite-carbonate-quartz were suggested to represent shear zones or overthrust glide planes (Fripp et al., 1980; de Wit, 1982a; Grosch et al., 2012; Grosch, 2019). The D_1 structures affects rocks of the Ulundi Syncline associated with gold deposits, the E-W and NE-SW trending isoclinal folds of the Moodies Group are affected by D_2 structures (see Heubeck and Lowe, 1999). However, there is some controversy regarding the evidence of the early D_1 event around ca. 3455 Ma in the BGB.

The D_2 has been characterized to represent the major deformation event recording the thrusting and folding at around 3223-3229 Ga during subduction and major felsic magmatism (Lowe and Byerly, 1999a,b; Heubeck and Lowe, 1999c; de Ronde and Kamo, 2000; Moyen et al., 2006; Schoene et al., 2008). A precise U-Pb single-zircon dating of a suite of deformed and undeformed intrusive porphyries into D_2 thrusts, coeval with Kaap Valley Pluton emplacement, has yielded ages of ca. 3227 Ma (de Ronde and de Wit, 1994). This suggest that the D_2 event continued after the emplacement of the Kaap Valley Pluton (Visser, 1956). The D_2 event resulted in isoclinal folds, thrust faults oriented in the NE-SW and the amalgamation of the southern and northern parts of the BGB along the Saddleback-Inyoka fault system (Ronde and Kamo, 2000; Schoene et al., 2008). The major D_3 shows, as evidence of late reactivation, sub-horizontal to horizontal slickensides (Tomkinson and King, 1991). It affects the NE-SW pattern of the BGB. Its early stages include some D_2 folds and its late stages are associated with gold mineralization in the BGB (de Ronde and de Wit, 1994). It reflects the final assembly of the both the arc and trench blocks. The late stages associated with gold mineralization shear zones are argued to represent transtensional and extensional processes. D_3 is associated with deformation of ca. 3126 Ma porphyry dykes and formation of rutile (de Ronde et al., 1991). D_3 shear zones and gold mineralization coincide with deformational fabrics of the intrusions of sheet-like potassic granite at 3100 Ma which include batholiths of Nelspruit, Mpuluzi and Heerenveen (Robb et al., 1983). Schoene et al. (2008) therefore suggested little disturbance of the BGB tectonically and thermally after emplacement of these batholiths.

2.3 Metamorphic constraints

The TTG terrane of the BGB records high-grade metamorphic conditions in the south-eastern and metamorphic evidence for subduction and tectonic exhumation (Diener et al., 2005;

Dziggel et al., 2006; Moyen et al., 2006, Kato et al., 2018). In the south, SW of the Komati Fault in the Stolzberg TTG granitoid-gneiss terrain, high-grade metamorphic conditions of T = 550 -700ºC and P = 6 - 15 kbar were reported (Dziggel et al., 2002). Moreover, temperatures of 600 - 650ºC and pressures of 12-15 kbar were obtained for the garnet-albite-epidote-amphibole-bearing boudins from the Inyoka shear zone (Moyen et al., 2006). High-grade metamorphic conditions were used as evidence for subduction type metamorphism and horizontal plate tectonic processes for the mid-Archean, occurring during D2 deformation at 3227 Ma (Moyen et al., 2006; Nédélec et al., 2012; Kato et al., 2018). The tectonically juxtaposed greenstone supracrustal sequence records low-grade to medium-grade metamorphic conditions (see Grosch et al., 2019).

According to Schneider et al. (2019) the Theespruit and Sandspruit Formation record amphibolite facies metamorphism with an overprint of greenschist facies metamorphism. In the northern part of the BGB, at least four types of metamorphism are proposed, namely: contact metamorphism (Anhaeusser, 1969), regional metamorphism (Xie et al., 1997), sea-floor hydrothermal alteration (de Wit et al., 1983) and burial metamorphism (Cloete, 1991). It was estimated, by chlorite thermometry, that the metamorphic temperature of the basalts, dacites and ultramafic rocks of the upper Onverwacht Group to be ca. 320 ºC (Cloete, 1991; Xie et al., 1997). Based on Raman spectroscopy of organics in different chert horizons, regional temperatures of ca. 315 ºC have been estimated (Tice et al., 2004). Seafloor metamorphism at 150 ºC was reported for the entire Onverwacht Group, based on oxygen isotope thermometry of silicified basalts (Hofmann and Harris, 2008) beneath cherts. Furthermore, in the Hooggenoeg Formation, U-Pb dating of titanite together with microscale metamorphic condition mapping of metabasalt revealed thermal contact metamorphism around the ca. 2913 Ma due to late Archean diabase intrusions (Grosch and McLoughlin, 2014).

Seafloor hydrothermal alteration evidence in the Komati Formation is indicated by actinolitic amphibole in komatiites yielding $^{40}Ar/^{39}Ar$ ages of 3486 ± 8 Ma (Lopez-Martinez et al., 1992) which shows an overlap with the gabbroic intrusion SHRIMP U-Pb zircon ages of 3482 ± 5 Ma (Armstrong et al., 1990). This was recently confirmed by Grosch (2019), where in the Komati Formation komatiites and related rocks were reported to preserve subseafloor alteration. The author of this study estimated that the Komati Formation to preserves metamorphic conditions of 250 to 445ºC. In the Middle Marker Chert, metamorphic temperatures of between 281 and 301 ºC was reported (Grosch, 2019) using

Raman thermometry, which is lower than the constraints reported by Tice et al. (2004) of 320 ^{o}C. Raman thermometry on the chert unit HC5 and the $\delta^{18}O$ oxygen isotope values of the metabasalt in the Hooggenoeg Formation were used to estimate the metamorphic conditions of the Hooggenoeg Formation. The metamorphic conditions reported in the formation are less than 340 ^{o}C (Grosch, 2019).

The mafic-ultramafic rocks of the Kromberg type-section preserves metamorphic conditions ranging from the lower greenschist to the upper greenschist facies (Grosch et al., 2012; Grosch, 2019). An inverted metamorphic field gradient was discovered beneath a major fuschite-chlorite-quartz shear zone, known as the Kromberg Section Mylonites (KSM). Retrograde metamorphism in the Kromberg shear zone was further discovered to occur along the kyanite-type geothermal gradient, thereby supporting thrusting or transpressional tectonics at ca. 3227-3223 Ma (Grosch et al., 2012; Grosch, 2019). Seawater alteration in the Mendon Formation occurred at T = 150 ^{o}C with log $aCO_{2\ (aq)}$ of -2.74 (Grosch, 2019). Metamorphic conditions in the mid-lower Kromberg is estimated to be sub-greenschist facies conditions with exceptional preservation of mafic – ultramafic rocks (Grosch, 2012).

2.4 Geodynamic setting of the Paleaoarchean Onverwacht Group

The geodynamic setting of the Onverwacht Group are centred around two end-member arguments: vertical crustal tectonics (Anhausser, 1984; Hamilton, 1998; Van Kranendonk, 2009; Kroner et al., 2013) or horizontal modern-style tectonics (de Wit, 1998; de Wit et al., 2011; Furnes et al., 2012, 2014). Horizontal tectonics implies modern plate-style tectonics, whereas vertical tectonics implies a different style to what exists today. These have major implications for the thermal regime in the early Earth and the time at which modern-style tectonics began. A diapiric model was proposed where the BGB is interpreted as a deformed greenstone succession intruded by granitoid magmas and folded by the vertical movement of tonalitic diapirs (Viljoen and Viljoen, 1969; Anhaeusser, 1984). Furthermore, an intracratonic setting was proposed, which was based on the idea that the Onverwacht Group youngs upwards from the Komati Formation and based on the thick greenstone stratigraphy (van Kranendonk et al., 2009). These authors suggested the BGB to have formed by convective overturn and that igneous processes in the middle to upper part of felsic crust triggered the vertical movement (Van Kranendonk et al., 2009). This model explains the dome-and-keel

structure of the BGB where 3.45 Ga dome-like TTG surrounds steeply dipping greenstone keels (Kisters and Anhaeusser, 1995). The lower Onverwacht Group (Sandspruit, Theespruit and Komati Formation) was proposed to have erupted in an oceanic plateau setting (Anhaeusser, 1984; Chavagnac, 2004; van Kranendonk et al., 2009, 2014). Geochemical evidence was based on the similarities between primitive-mantle normalized trace element patterns of the lower Onverwacht with the Phanerozoic large igneous provinces (Kerr et al., 1996; Chavagnac, 2004). However, the model was questioned by Schneider et al. (2019) due to the presence of interlayered felsic volcanic rocks in the Sandspruit and Theespruit Formation. In this model, felsic volcanic rocks of the Sandspruit and Theespruit Formation are proposed to have formed by rifting initiated after a mantle plume stalled beneath the lithospheric mantle. The Komati Formation volcanic rocks is proposed to have erupted rapidly onto the surface (Schneider et al., 2019) involving no crustal contamination (Robin-Popieul et al., 2012; Puchtel et al., 2013; Shneider et al., 2019).

Contrary to the vertical tectonics model for the lower Onverwacht Group, a horizontal subduction setting was proposed based on geochemical evidence that suggested a subduction-related metasomatized mantle source for the lower Onverwacht Group (Parman et al., 1997; Furnes et al., 2012). This model was based on the concept that the Onverwacht Group rocks are tectonically stacked (de Wit et al., 2011, 2018). According to this model and based on geochemical evidence and structural interpretations, the Onverwacht Group was envisioned to have been constructed as obducted oceanic slices formed in volcanic arcs and back-arc basins (Furnes et al., 2013). The tholeiitic basaltic rocks of the Onverwacht Group revealed positive Cs and Pb anomalies and small negative Ta and Nb anomalies in N-MORB and primitive mantle normalized plots which differ from plume related magmas (Furnes et al., 2012). The igneous rocks of the Theespruit Formation were proposed to have formed along the margins of the continental crust, during the island arc growth. An oceanic plateau setting has been proposed for the Komati Formation based on the trace element geochemistry and εNd-values averaging +1.75 (Chavagnac, 2004). After the Hooggenoeg Formation eruption, a period of tectonic uplift of eroded oceanic crust resulted in the deposition of the Noisy Formation conglomerates (Grosch et al., 2011). The Ncakini section of the Mendon Formation is suggested to have formed in a subduction-related setting (Furnes et al. 2012, 2013).

3 Local geology

Geological mapping on the eastern bank of the Komati river, Kromberg type-section, in Songimvelo Nature Reserve.

3.1 Introduction

The simplified geological map in **Figure 3.1** shows the Onverwacht Anticline in the southern part of Barberton greenstone belt. The Kromberg Formation is highlighted in blue, and the Kromberg type-section on the south-eastern limb of the OAF has been marked by the profile marked A-A' (**Figure 3.1**). The Kromberg type-section is exposed along the Komati river in Songimvelo Nature Reserve, in Kromdraai. The high-resolution geological profile in **Figure 3.2** indicates the different volcano-sedimentary, volcanic and intrusive rock types of the Kromberg type-section as observed in the field (Grosch et al., 2020). Sample numbers have

been included in the geological profile to show the location and stratigraphic height from which they were collected.

Rock compositions reported in this chapter have been confirmed by petrography (Chapter 6) and bulk-rock geochemistry (Chapter 8) where geochemical classification was conducted using the Viljoen and Viljoen (1983) classification scheme. Furthermore, field photographs of the different rock compositions encountered in the Kromberg type-section have been provided and their localities in the geological log marked (e.g. p1, p5, etc.). A major 150 m shear zone has been documented in the upper Kromberg type-section (see **Figure 3.2** and **3.3b**), with smaller (10 m) shear zones part of the lower sequence (Grosch et al., 2012). The shear zone has been argued to have formed at 3.23 Ga during regional transpressional deformation during horizontal crustal accretion in an oceanic flake tectonic process (Grosch and Slama, 2017; Grosch et al., 2020). The uppermost chert of the Kromberg type-section (Footbridge Chert) has been dated at c. 3.3 Ga (Grosch and Slama, 2017; Grosch et al., 2020; **Figure 3.2** and **3.3a**). The uppermost part of the Kromberg volcanic stratigraphy has experienced tectonic deformation and later retrograde fluid alteration (Grosch et al., 2012; Grosch, 2019). The Kromberg sequence has been argued to have been thrusted over polymictic conglomerates of the 3.43 Ga Noisy Formation (Grosch et al., 2011; **Figure 3.2** and **3.5h**). To understand the early igneous and seafloor alteration processes, this local geology chapter focuses on field observations and high-resolution geological grid-mapping of all exposed river pavement sections identified in the mid-lower Kromberg type-section, about 600 m away from the major shear zone in the upper Kromberg type-section.

3.2 New geological profile for the south-eastern limb of the Kromberg type-section

The Kromberg type-section consists of silicified chert, tholeiitic massive and pillowed basaltic lava flows, subordinate coarse-grained ultramafic intrusive rocks, silicified lapilli tuff and minor komatiitic basalts (see Grosch et al., 2020; **Figure 3.2** and **3.3**). It is dominated by tholeiitic basaltic flows and minor massive and pillowy basaltic komatiites. It is characterised by at least six volcanic cycles, but with some uncertainty due to dismemberment, tectonic thrusting, stratigraphic repetition and limited outcrop in parts. The end of each cycle is marked by a chert unit which represents a quiet, volcano-sedimentary subseafloor

depositional environment. The pillow lavas directly beneath the chert units have been heavily silicified (**Figure 3.2**) and are thus characterised by higher silica contents

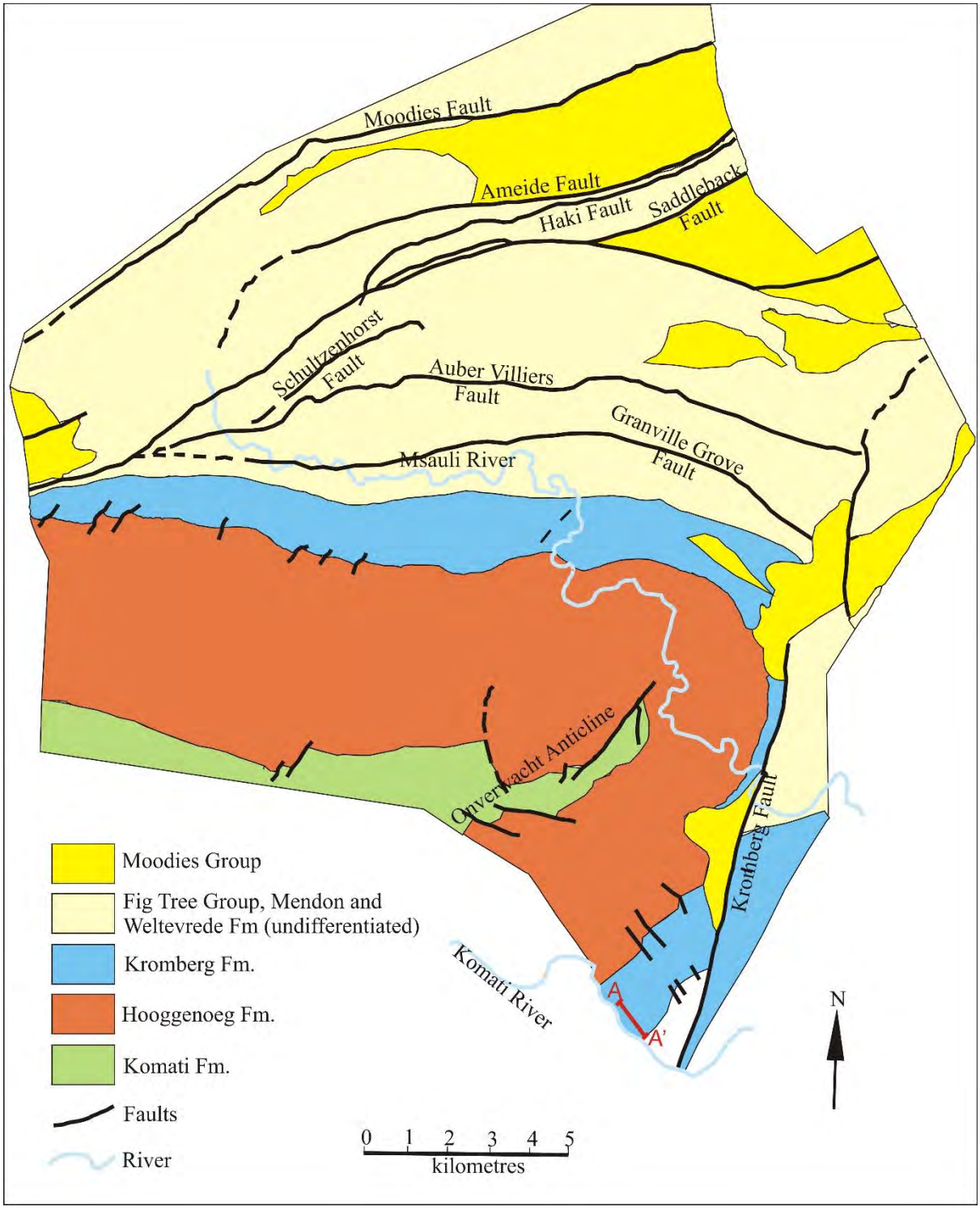

Figure 3.1: *A simplified geological map that shows the upper Onverwacht Group formations, the Fig Tree Group and the Moodies Group. An A-A' profile along the Komati river, on the south-eastern limb of the Onverwacht Anticlinal Fold (OAF) represents the location of the current MSc study.*

(see **Geochemistry Chapter 7**). In between these chert units are mafic tholeiitic extrusive rocks, with minor basaltic komatiite, cumulate peridotite, and intrusions in places. Cumulate peridotites are sill intrusions with a fining upwards sequence.

The first and lowermost volcanic cycle comprises a ca. 35 m thick metadunite with serpentine veins (**Figure 3.5g**), overlain by a ca. 5 m thick komatiitic basalt. Above the komatiitic basalt is ca. 150 m poor outcrop exposure. A fuchsite-carbonate-quartz shear zone outcrops above this poor outcrop section. A lapilli ash unit occurs directly above this lower Kromberg shear zone. A ca. 10 m sedimentary chert (KrC_1) marks the end of the first cycle. Above the first volcanic cycle is a ca. 120 m thick massive and vesicular komatiitic basaltic flow overlain by a ca. 25 m thick unit of black chert with a banded upper ferruginous layer (KrC_2). Overlying the chert is a ca. 20 m thick massive and vesicular tholeiitic basalt. It is in turn overlain by a ca. 120 m pillow lava flow with pillow structures up to 6 m in height (**Figure 3.5e,f**). Within this unit is a pillow lava crack-out structure preserving evidence for pillow lava eruption processes. The pillow lava flow is overlain by ca. 10 m thick pillow breccias which are overlain by a peridotitic intrusion with a fining upward texture (**Figure 3.5b**). Another zone of peridotite with a coarse- to medium-grained cumulate texture, consisting of olivine and pyroxene can also be observed within the same volcanic cycle overlying lobate tholeiitic pillow lavas (**Figure 3.5a**). The peridotitic cumulate units are overlain by ca. 73 m thick pillow lava flow which are in turn overlain by 33 m silicified pillow lavas (**Figure 3.6**). Silicified pillow lavas have higher silica content (>57 wt.%) than typical tholeiitic lavas (45 ≤ 57 wt.%; see Table 1). A ca. 30 m banded ferruginous chert (KrC_3) marks the end of the third volcanic cycle (**Figure 3.6**).

The fourth volcanic cycle consist of a ca. 35 m massive and/or ocelli-bearing komatiitic basalts overlain by a thin pillowy layer that is in turn overlain by a ca. 75 m thick massive and vesicular tholeiitic basalt. A thin chert layer (KrC_4) marks the end of the fourth volcanic cycle. The fifth volcanic cycle a ca. 120 m thick massive tholeiitic basalt overlain by a ca. 20 m tholeiitic flow with high silica tholeiitic N-S oriented feeder dyke and E-W oriented sheet intrusions (**Figure 3.4h,i**), which is in turn overlain by a ca. 5 m thick massive tholeiitic flow. The intrusive tholeiitic sheets with chilled margins have been previously reported by de Wit (1987), but the N-S larger dike is a new observation. A ca.

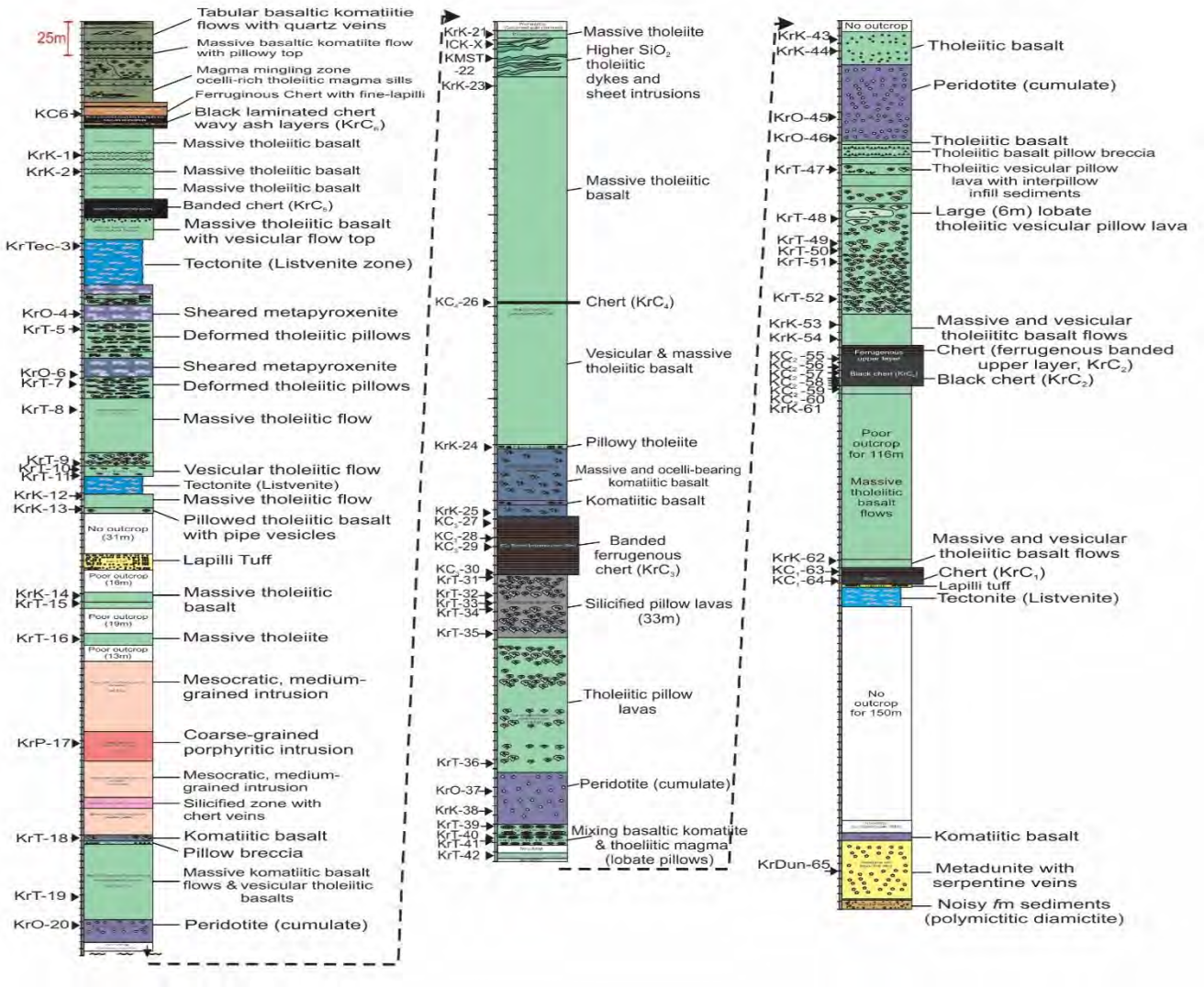

Figure 3.2: *A new geological profile for the Kromberg type-section on the south-eastern limb of the OAF modified after Grosch et al. (2020). The sample numbers have been included in the diagram to show the location from which different samples were taken.*

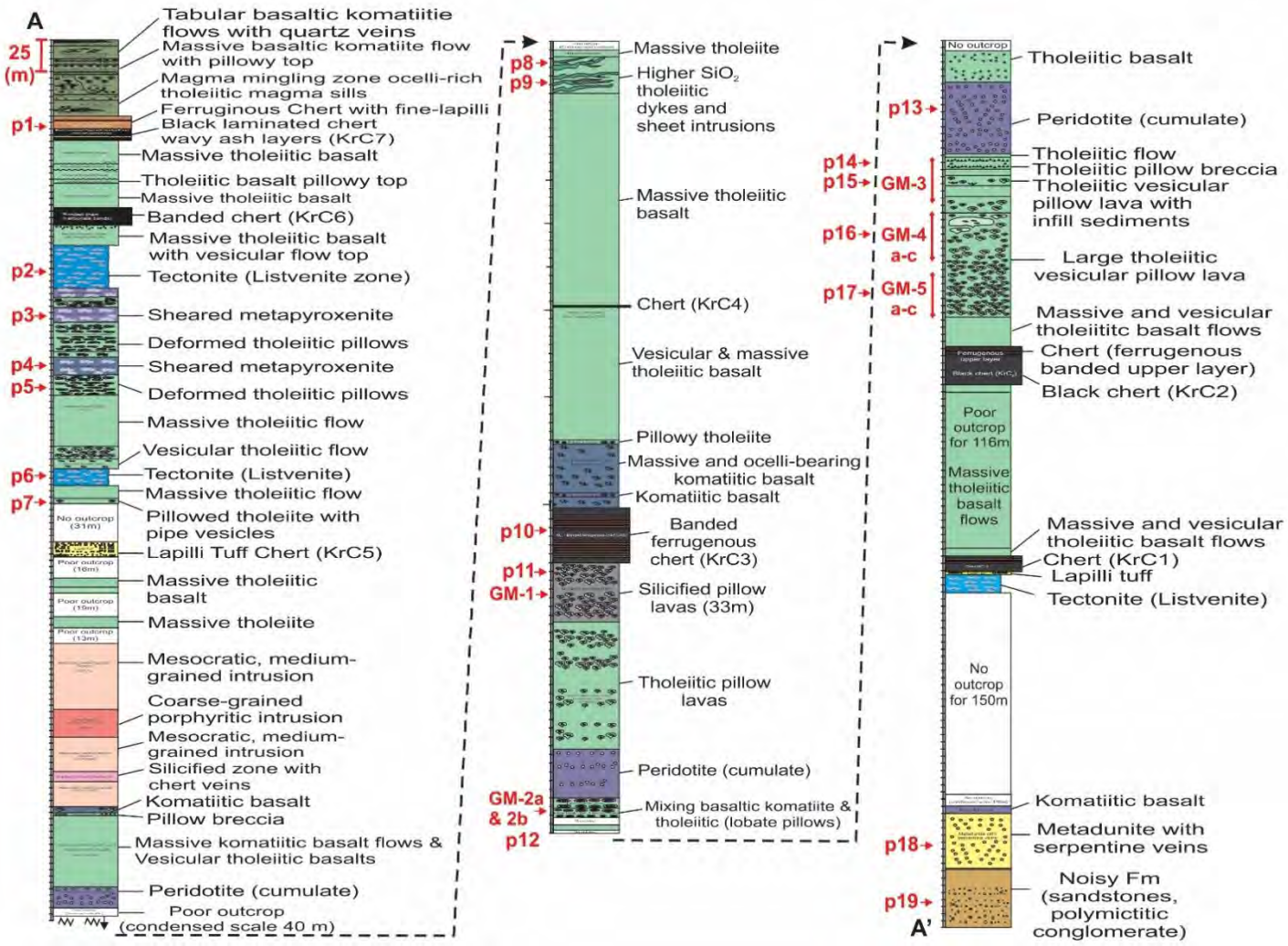

Figure 3.3*: A new geological profile for the Kromberg type-section on the south-eastern limb of the OAF modified after Grosch et al. (2020). p1 to p19 represents the location of field photographs taken and shown in* ***Figure 3.4-3.6****. GM-1 to GM-5 represent the location from which grid mapping was conducted. A-A' represents the SE limb of the Kromberg Formation and its associated rock composition.*

15 m thick peridotite cumulate overlies of 40 m poorly outcropping rocks. This is overlain by a ca. 55 m thick massive komatiitic basaltic flow and vesicular tholeiites above which lies a thin layer of tholeiitic breccia and komatiitic basalts. Above this zone is a ca. 130 m thick mesocratic and porphyric diabase intrusions overlain by massive tholeiitic basalts and a ca. 10 m lapilli tuff chert (KrC_5). The lapilli tuff chert, marking the end of the fifth volcanic cycle, records volcanic subaerial activity and deposition in a sub-aqueous setting.

The sixth volcanic cycle comprises an intensely foliated rock representing a small shear zone overlain by a vesicular and massive tholeiitic flow. This volcanic cycle comprises a major (ca. 150 m thick) shear zone. The lower part of the shear zone comprises less competent foliated metapyroxenite deformed around more competent boudins and the upper part of the shear zone comprises a listvenitic zone, a banded and strongly deformed fuchsite-chlorite-carbonate-quartz rock, underlain by deformed metapyroxenite. The base of the shear zone comprises deformed and thermally altered pillow metabasalts. Marking the end of the sixth cycle is the ca. 13 m banded chert unit (thin KrC_6). The seventh and last volcanic cycle is the shortest cycle comprising ca. 15 m massive tholeiitic basalt with a ca. 18 m tholeiitic basalt pillowy top, which is in turn overlain by a ca. 16 m thick massive tholeiitic flow. Marking the end of the Kromberg type-section is the Footbridge chert; a ca. 20 m black ferruginous chert (KrC_7; **Figure 3.4a**) with fine lapilli and a wavy ash layer. The lower part of the KrC_7 is laminated and organic-rich.

3.3 Field observations and sampling

The middle to lower part of the Kromberg type-section covers the volcanic stratigraphy of ca. 1.3 km above the Noisy Formation (from sample KrO-20 to Kr-Dun-65 in **Figure 3.2**). Grid mapping at high resolution was conducted along the Komati River for all exposed areas identified in the Kromberg type-section. The aim was to produce field outcrop maps of the volcanic, intrusive and volcano-sedimentary rock types and structures and to record the geology of the Kromberg type-section in the best possible detail. A total of 10 grid maps are presented. Three grid sections in selected areas, ca. 6m x 4m in size, were mapped on the eastern side of the Komati River (River pavement Area 1, see below), and an additional seven grid sections of similar size were mapped out on the western side (River pavement Area 2, see below).

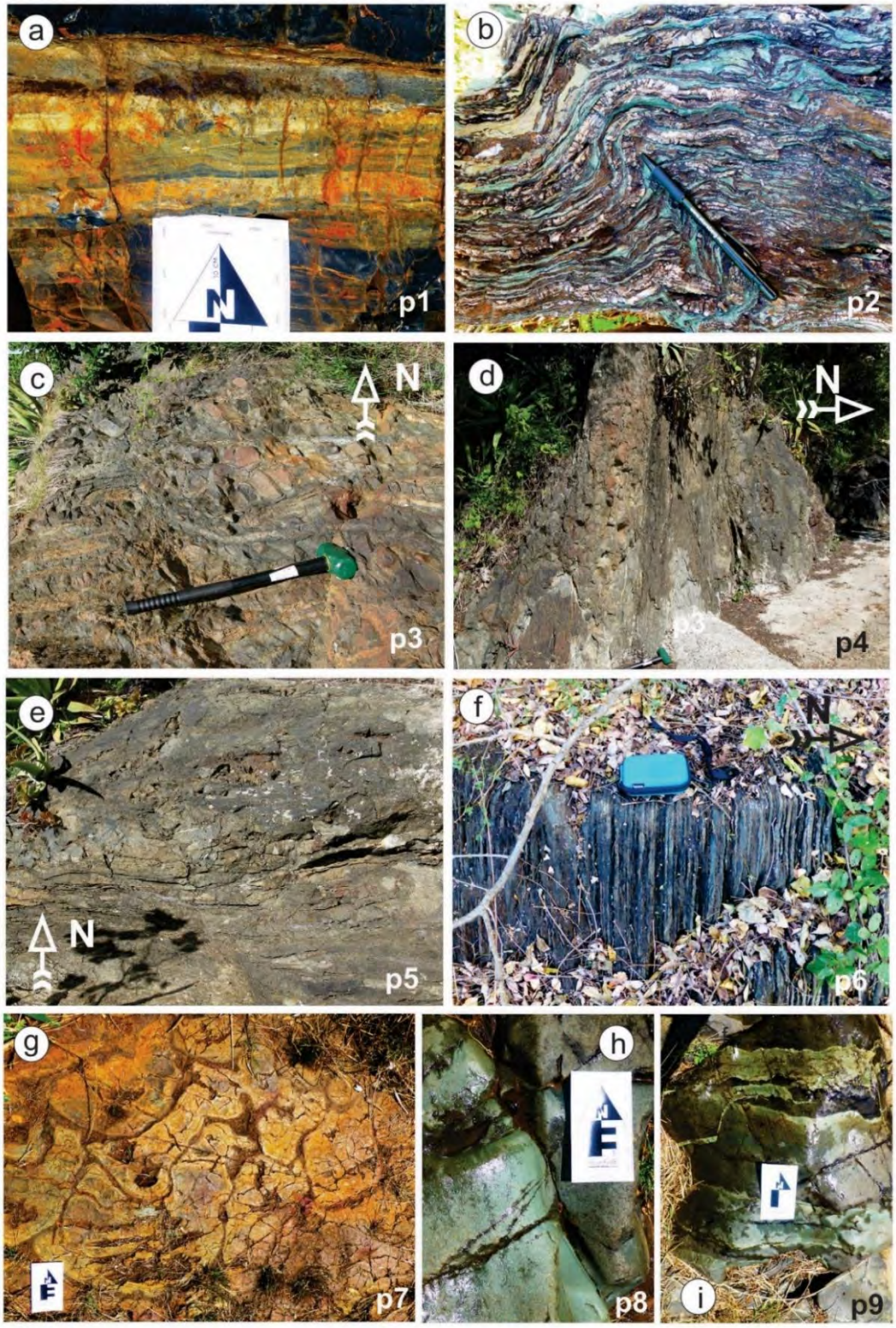

***Figure 3.4**: Field photos showing the different rock composition in the south-eastern limb of the Kromberg type-section. (a) Footbridge ferruginous chert located in the uppermost stratigraphy of the Kromberg type-section, (b) and (f) listvenitic tectonite, (c) and (d) sheared metapyroxenite, (e) deformed tholeiitic pillows, (g) pillowed tholeiite with pipe vesicles, (h) N-S trending feeder dyke and (i) E-W oriented sheet intrusions.*

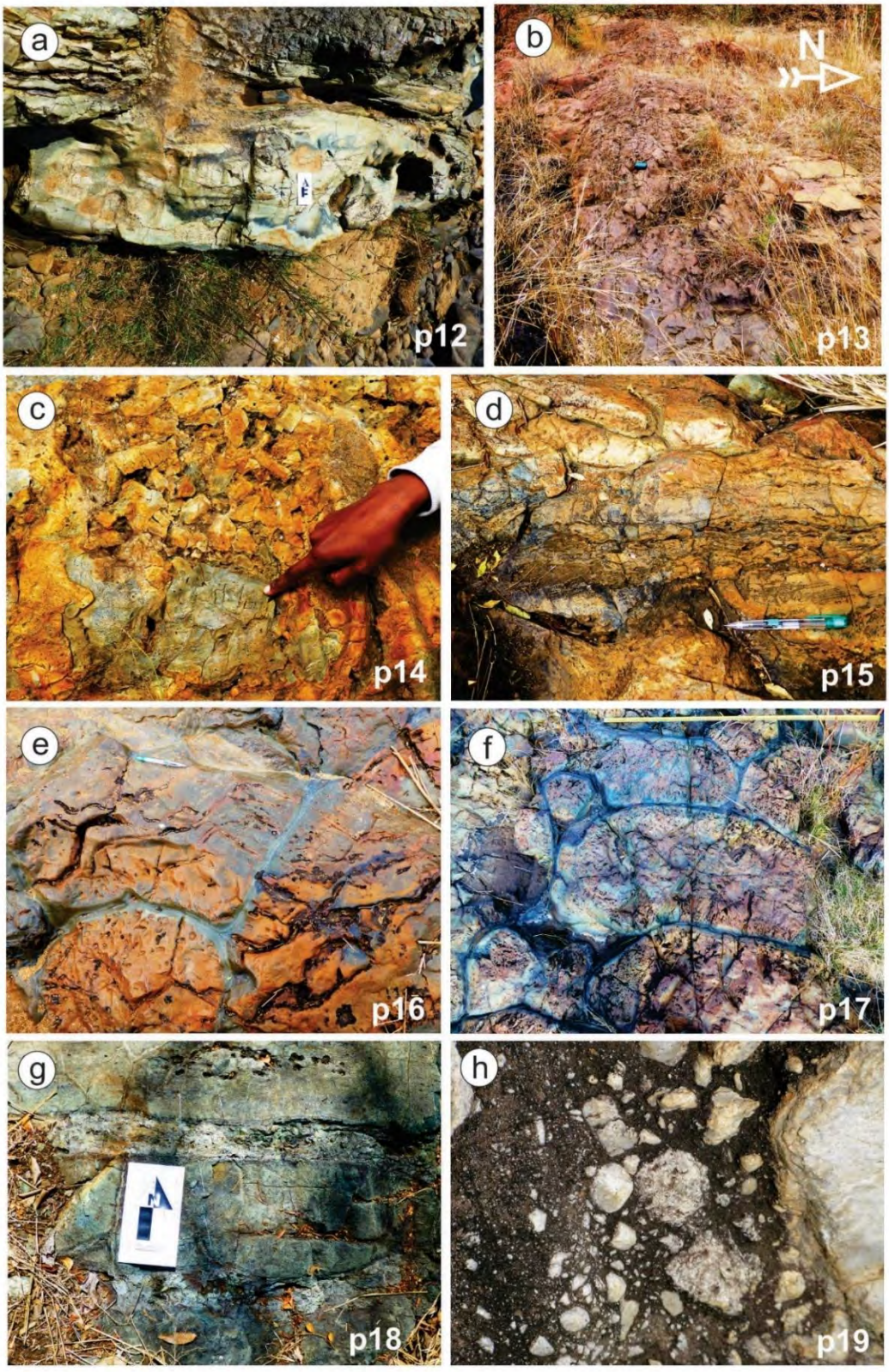

***Figure 3.5**: Field photos showing the different rock composition in the south-eastern limb of the Kromberg type-section. (a)pillowed tholeiitic lavas with magma mixing, (b)cumulate peridotite, (c)brecciated pillow, (d)sediment infill, (e) and (f) large vesicular lavas, (g)lowermost metadunite and (h)sedimentary rocks of the Noisy Formation.*

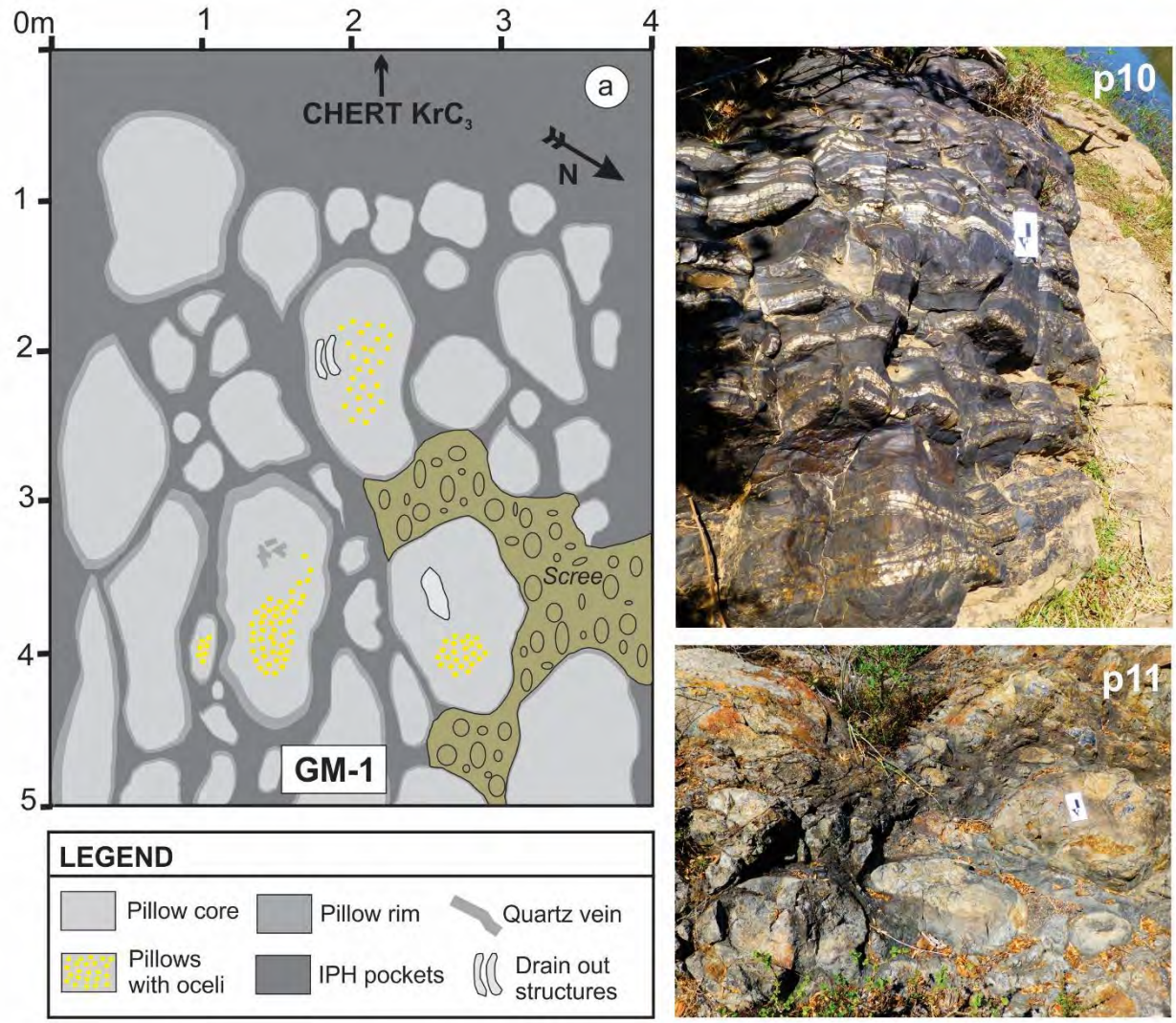

***Figure 3.5**: GM-1 showing silicified pillow lavas with ocelli and drainout structures. p10 and p11 are field photos taken from the Kromberg type-section. p10 is a banded ferruginous chert overlying silicified pillow lavas shown in p11 and mapped in GM-1.*

3.3.1 River pavement Area 1

Three grid maps were conducted along River pavement Area 1. For this section, grid mapping was conducted along the eastern bank of the Komati River. These grid maps, Grid map 1 (GM-1) and Grid map 2 (GM-2a and GM-2b), represent rocks directly beneath chert horizon, KrC_3. A key map that illustrates the location of GM-2a and 2b is presented in **Figure 3.7a**. GM-1 is not shown on the map since it is located further away and SE of GM-2.

3.3.1.1 Grid map 1 (GM-1)

GM-1 is a 5 m x 4 m grid representing highly weathered and largely silicified pillow lava flows (**Figure 3.6a**). It comprises both large pillow structures (up to ca. 1.7 m in length) and smaller pillow structures (ca. 0.1 m in length). The pillow structures in this area comprise pillow cores, pillow rims and are bounded by a hyaloclastite matrix. The pillow cores are brown with dark grey pillow rims and hyaloclastite matrix. These pillow lavas are loosely packed with individual pillows separated by a large gap. The cause of this large gap is intense metasomatic subseafloor hydrothermal silicification (Paris et al., 1985; Hofmann and Harris, 2008). Metasomatic silicification by seawater hydrothermal fluids in these rocks has also resulted in the rocks being extremely hard. This pavement of KrC3 and silicified and unsilicified pillow lavas has not been previously reported in the literature.

The pillow structures vary in shapes. Some pillows are rounded and sub-rounded, while others are elliptical. The pillow cores consist of silicified ocelli structures, quartz veins and drain-out structures in places. The drain-out structures (areas where hot lava has poured out from pre-existing pillows) are infilled with secondary quartz and carbonate. The pillows are semi-elliptical, have a grey interior and dark grey margins and are undeformed. The ocelli structures are spherical to subspherical and located within the pillow cores of the basaltic flow. They are light coloured compared to the host pillow basalt. Due to silicification and subseafloor weathering of the pillow lavas, there is no sharp contact observed between the ocelli and the pillow lavas. Generally, the height of GM-1 pillows is larger than their lengths. These dimensions are an indication of the geometry of these pillow structures. Most of the pillows in GM-1 are therefore sub-spherical and have average length of 0.97 m in the major axis and length of 0.52 m in the minor axis (**Figure 3.11**). Further away north from GM1, some massive and pillowed lavas become progressively less silicified.

3.3.1.2 Grid map 2 (GM-2a – GM-2b)

Two grid maps, GM-2a and GM-2b, have been constructed and shown in the key map in **Figure 3.7a**. The key map for GM-2 covers an area of 20 m x 30.5 m and comprises pillow lava flows. GM-2a-2b consist of very large elliptical pillow structures, reaching lengths above one metre along the major axis and lengths of approximately half a metre along the minor axis. They have pale green and dark green cores, as well as dark grey pillow rims.

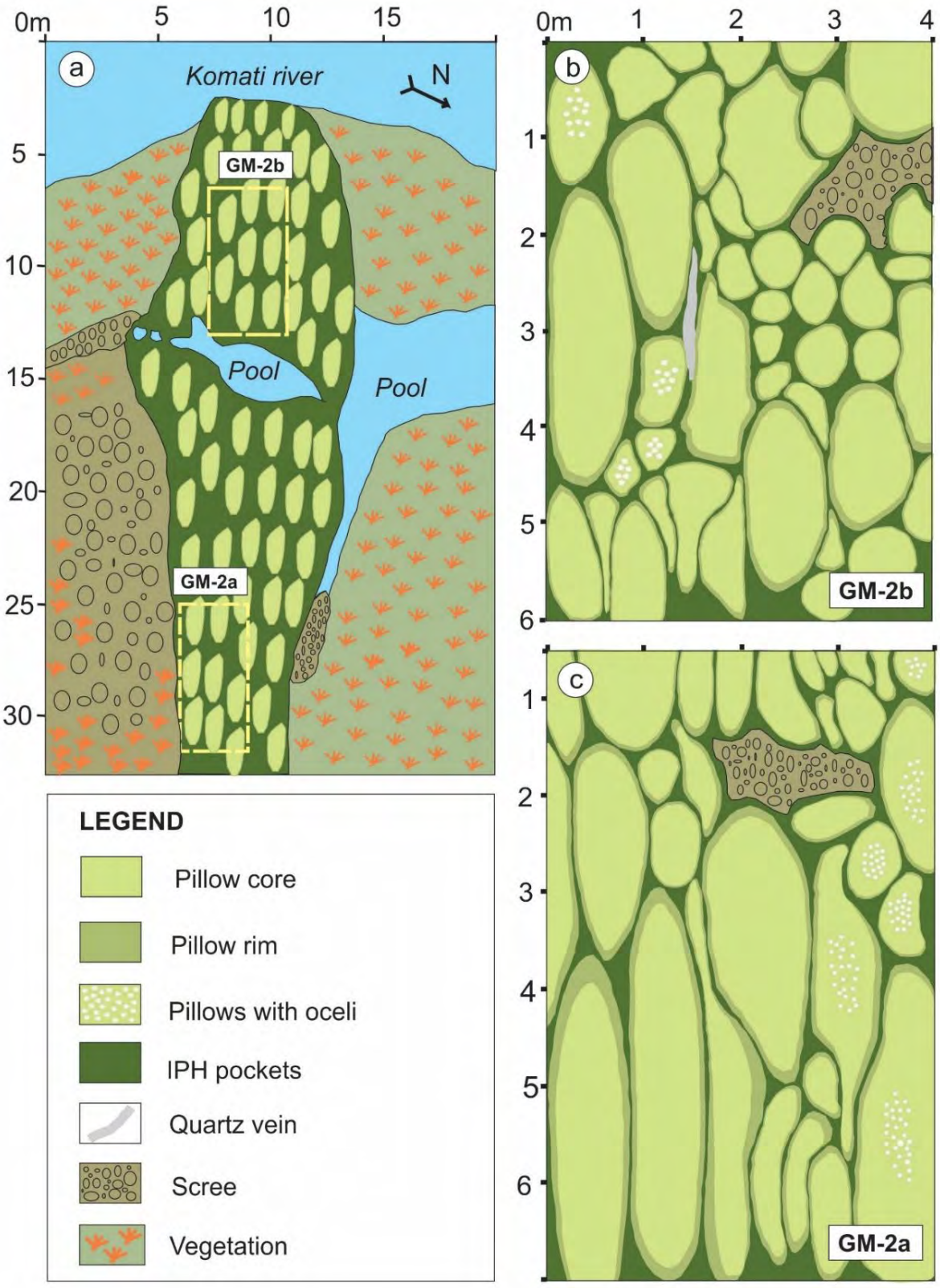

Figure 3.6: *(a) Key map showing the location of GM-2a-2b. (a) and (b) shows lobate pillow lavas. Some of these pillow lavas are ocelli-bearing.*

They lack pipe vesicles, but some pillows have ocelli in their cores. Different shades of green are observed within the pillow basalts with a dark green colour indicating a more mafic magma and a light green colour indicating a silica-rich (basaltic) magma. This suggests magma mingling processes (e.g. Robins et al., 2010, 2011).

GM-2a (**Figure 3.7c**) comprises very large pillow structures reaching lengths up to 3.4 m in the major axis and heights up to 1 m in the minor axis. The smallest pillow in this section has a height of ca. 0.3 m and a length of ca. 0.4 m. The pillow lavas in this section are elongate and lobate. Some contain ocelli within their cores. These ocelli structures are spherical, cream-white and leucocratic. GM-2b also comprise large lobate pillow structures, some of which have ocelli (**Figure 3.7b**). The smallest pillow in GM-2b has a major axis of ca. 0.3 m while the largest pillow is 2.2 m along the major axis. Quartz veinlets are evident in most of the pillow structures and one large quartz vein (ca. 1.1 m) is found in between the pillow structures near the central part of GM2a (**Figure 3.7b**). The quartz veining within these pillow basalts are an indication that these pillow lavas have been partially affected by silicification. The elongate pillow basalts of GM-2a-2b show no sign of deformation. The sphericity of the ocelli in the pillow cores, as well as the presence of small rounded pillows in parts, suggest a lack of deformation. The average length of the pillows in this location is 1.76 m in the major axis and the average length is 0.56 m in the minor axis (**Figure 3.11**). These dimensions coincide with the geometry of the pillows, which is in this case elongate.

3.3.2 River pavement Area 2

Figure 3.8 is a general map that illustrates the location of the grid maps GM-3, GM-4 (GM-4a-4c) and GM-5 (GM-5a-5c), very well exposed along the western bank of the Komati river. Grid map GM-3 is 32.5 m long and 13.5 m wide (only partly shown in **Figure 3.8**, see **Figure 3.9** for detailed grid map). Further representative areas of the river pavements in Area 2 were mapped at high-resolution and shown in GM 4a-4c and 5a-5c (**Figure 3.10**).

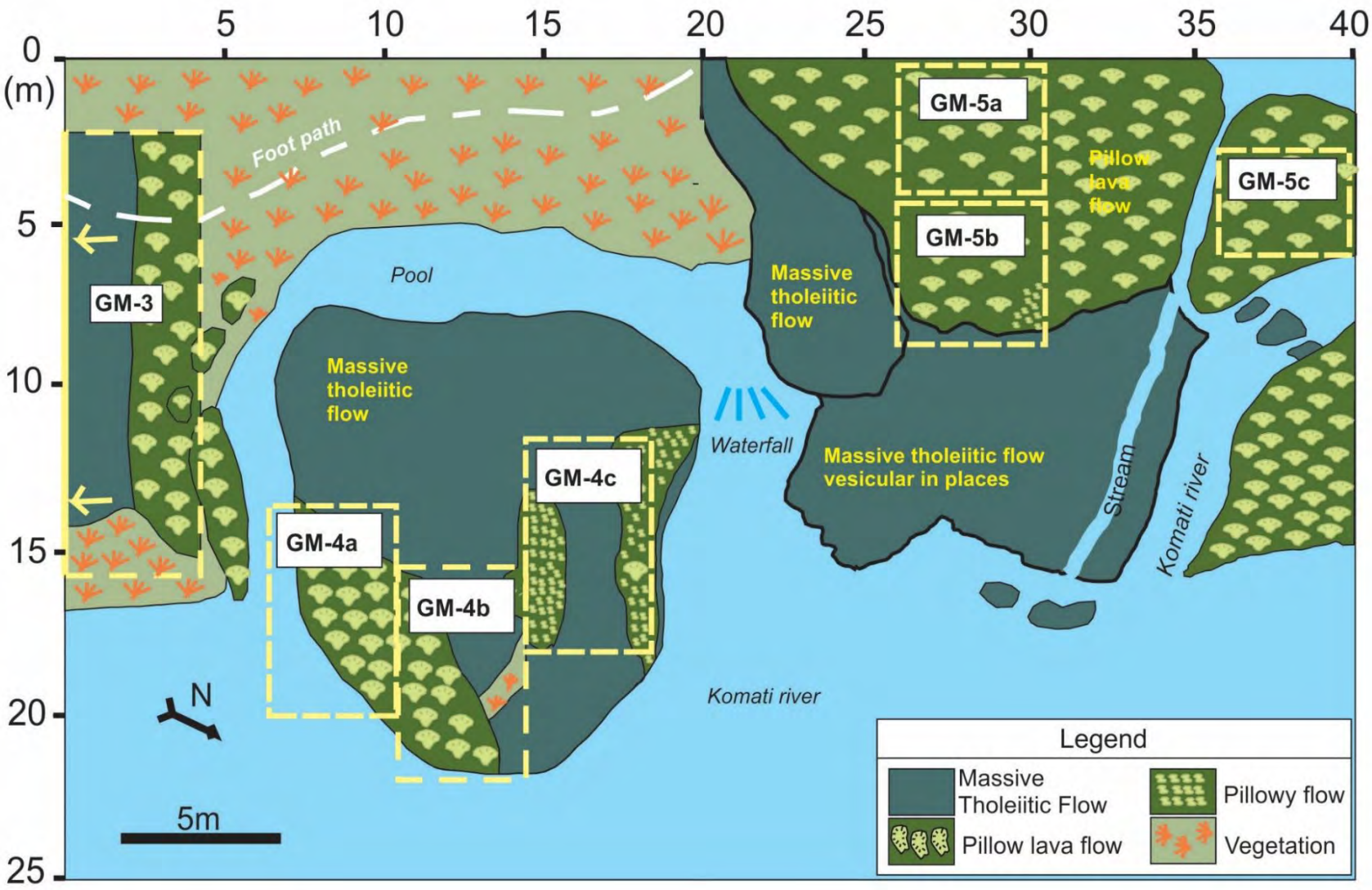

Figure 3.7*: Key map of Area 2 showing the different locations where grid mapping was conducted for GM-3, 4a-4c and 5a-5b.*

3.3.2.1 Grid map 3 (GM-3)

GM-3 is situated about 6m away from the Komati River (**Figure 3.8** and **3.9**). It covers an area of approximately (16m x 32.5m) 520 m^2 and has a footpath that cuts across it. From the southern side to northern side, the section consists of brecciated pillows, fragmented pillows, massive tholeiitic flows and vesicular pillow flows. Brecciated pillows are found further south of GM-3 (see **Figure 3.9**). They extend horizontally across from south to north for approximately 5m. They are angular with a fine-grained matrix dominated by glass shards in inter-pillow hyaloclastite (IPH) pockets. They have an uneven size distribution where the smallest pillow was measured to be approximately 9 cm and the biggest, approximately 50 m along their major axis.

Pipe vesicles are strongly exposed in the coherent pillows, while they remain poorly exposed or absent in the largely fragmented pillows. Subsequently, some glass breccia fragments are observed at approximately 10m away from pillow breccias, stratigraphically below fragmented pillows lavas. These angular fragments of glass breccias are bounded by a glassy hyaloclastite matrix and range in size from 1 cm to 6 cm. They extend for approximately a metre. Pillow fragments are observed in two localities in GM-3. One section of the pillow fragments is located 5m away from the pillow breccias (**Figure 3.9**). It extends from south to north for about 5 m. It comprises both large and small pillow fragments bounded by a glassy hyaloclastite matrix. These pillow lavas are up to 50 cm in size. Most of the pillows in this section have poorly developed pillow rims. The periphery of the pillow cores is fragmented while the inner core remains unfragmented. Pipe vesicles can be observed on the unfragmented parts of the pillow core whereas they remain poorly exposed in the fragmented parts. Other fragmented pillows form a thin unit less than a metre (GM-3, **Figure 3.9**). They form at 15.2 m, below a sediment infill unit (**Figure 3.9)**. These fragments are poorly formed. Above the sediment infill is a 2 m thick pillowy flow. These are about 30-60 cm in size. Some of these pillowy flows appear to be brecciated. The pillowy structures form when the lava solidifies quickly on the outside, preventing internal movement and thereby inhibiting the development of the typical pillow structures seen in the field. Lower viscosity lavas may also form pillowy structures. They have a low resistance to flow and therefore create smaller pillows. The effect of both viscosity and the cooling rate in basaltic lavas is therefore the probable cause of the pillowy structures observed in GM-3 (and GM-4c and GM-5b discussed below, **Figure 3.10**). Several sediment-infills occur between the

fragmented pillows and the pillowy flow. They are narrow, bulges at the centre and pinches out at both ends. Massive tholeiitic basaltic flows are

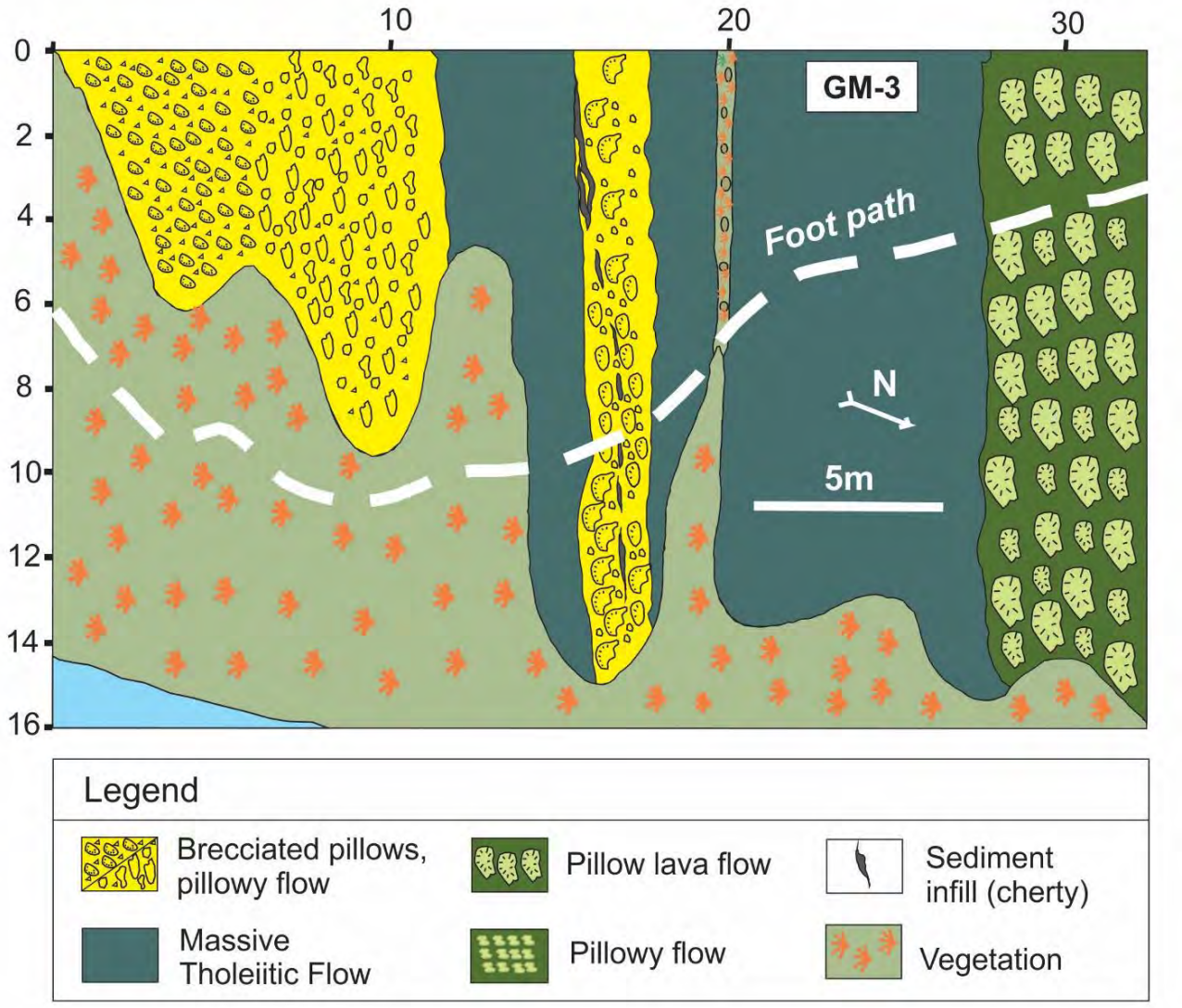

Figure 3.8: *GM-3 shown in Figure 8. A sedimentary infill can be observed within the pillow lavas of GM-3. In the same area there are also breciated pillows and massive flows. Pillow lava flows are lavas with pillow-shaped structures whereas in the pillowy flow, the pillow-shaped structure is not well-developed.*

found interlayered with brecciated and fragmented pillow lava flows. They are dark green in colour. They are found in two localities within GM-3 (**Figure 3.9**). The first massive flow is located at 11 m and extends from southwest to northeast for about 4 m. At about 17.5 m is another massive flow, through which the pathway crosses. This flow extends from south to north for about 10 m. It is massive and featureless for the first 2.5 m and becomes vesicular in

places for the next 7.5 m. Following the massive flows are well-developed pillow lavas. They are located at 27.5 m in GM-3 (**Figure 3.9**). These pillows are large with various shapes; that is, oval-shaped, mushroom-shaped, rounded and sub-rounded pillows. They range in sizes from 40 cm to 1.8 m. They have well developed grey-black glassy rims with widths of ca. 1-2 cm and pale-green cores (with brown weathering colour) with well-developed pipe vesicles. The pipe-vesicles are located near the rim-core boundary, towards the edges of the core. At the intersection of three or more pillows are inter-pillow hyaloclastite (IPH) pockets.

3.3.2.2 Grid map 4 (GM 4a-4c)

Grid maps 4a-4c represent outcrops along the Komati River, ca. 2m away from GM-3. It covers a distance of about 12 m to the north-westerly direction (see **Figure 3.10a**). It comprises a pillowy flow and pillow lava flow interlayered with a massive flow. Grid map GM 4a-4b (**Figure 3.10a**) comprises a 7 m wide pillow lava flow. The pillows have pillow cores and rims, and prominent IPH pockets. Some pillows are massive with no internal structures while others have pipe vesicles at the margins of their cores. The pillow lavas have different sizes, with the smallest pillow about a 25 cm on the maximum axis and 20 cm on the minimum axis in length. The largest pillow lava has dimensions of about 2 m along the maximum axis and 1.6 m on the minimum axis. Contrary to GM 4a-4b, GM-4c comprises of a pillowy flow, although a few well-developed pillows can be found.

From the data obtained, it is evident that the size distribution of pillow lavas in GM 4a -4c is not uniform (**Figure 3.10a**). While the sizes vary, pillow lava shapes vary too. Some pillow lavas have a mushroom-like shape, while others have sub-rounded, rounded and lobate shapes. The pillow structures in GM 4a-4c become less prominent towards the north-westerly direction with pillows becoming progressively pillowy from GM-4b to GM-4c. Only a few pillows are well-developed in GM-4c (**Figure 3.10a**). The term “pillowy” is used to describe pillow structures that are not fully developed. Pillow structures in GM 4a-4c have an average length of 0.94 m (major axis) and average height of 0.61 m (minor axis; **Figure 3.11**). This suggest that the average shape of the pillows in this location is subspherical, as shown in **Figure 3.10a**.

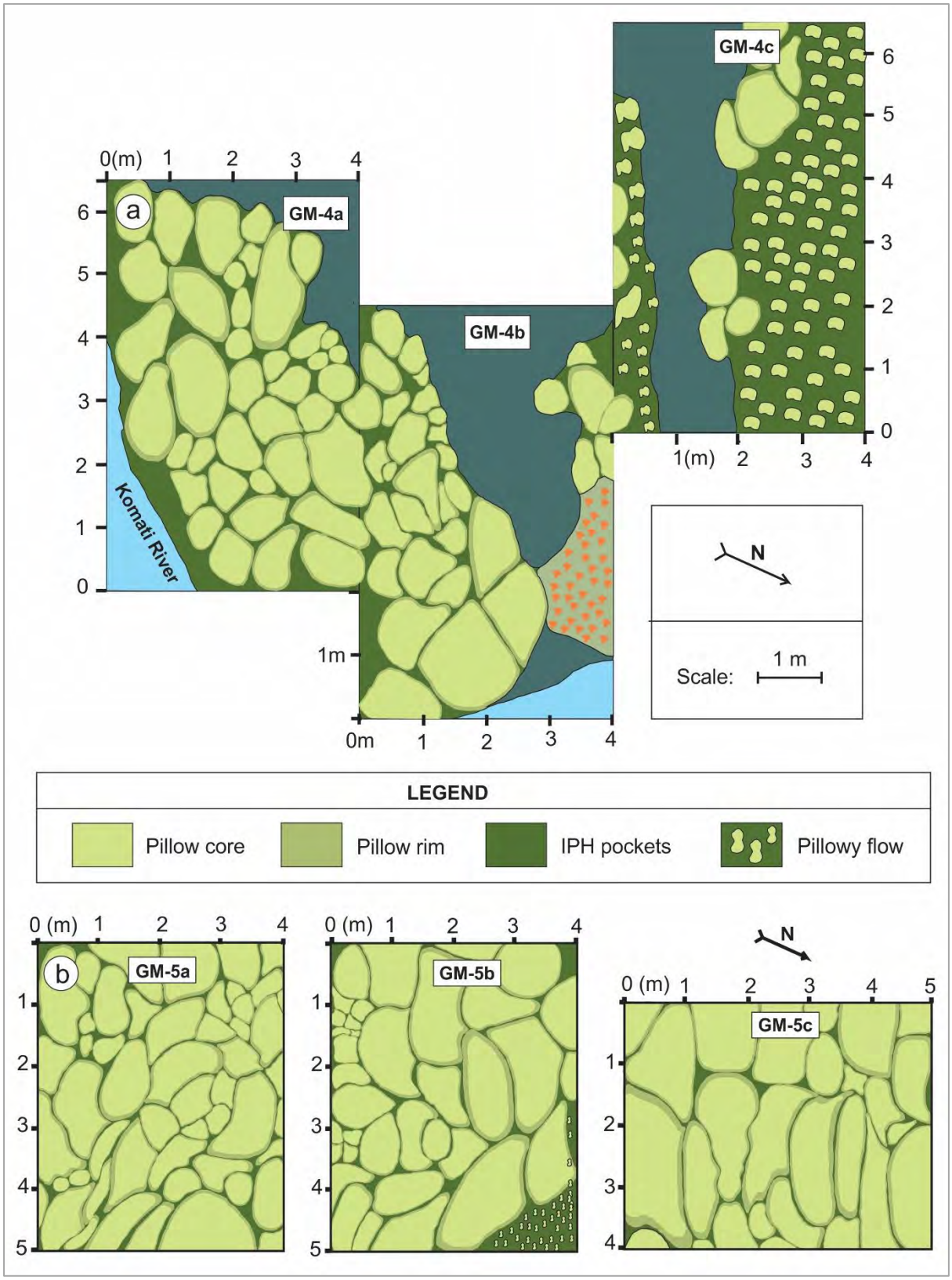

***Figure 3.9**: (a) GM 4a-4c showing different pillow structures. Some pillows are massive while others are vesicular. A pillowy flow is observed in GM-4c (b) GM 5a-5c showing pillow lavas with IPH pockets. Pillow lavas in (a) have an overall sub-rounded pillow shape, whereas pillow lavas in (b) have an overall elongate shape.*

3.3.2.3 Grid map 5a-5c

Grid map GM 5a-5c also covers an outcrop along the Komati river. This outcrop is dominated by pillow lavas and have some pillowy flows. Three sections have been mapped out namely, GM-5a, GM-5b and GM-5c (**Figure 3.10b**). All the pillows in GM 5a-5c differ in shapes, with some mushroom-shaped, rounded and sub-rounded. They all have pillow rims, pillow cores and pipe vesicles at the margin of their cores. GM-5b have some pillowy flow, but it is mostly dominated by well-formed pillow structures. The pillow lava flows in GM 5a-5c also range in sizes, where centimetre- and metre-sized pillow lavas can be observed. The smallest pillow is about 0.1 m in height (minor axis) and 0.25 m in length (major axis), while the largest pillow is 6 m along the major axis and 1 m along minor axis. Compared to GM-4 and GM-3, the pillow lavas in GM 5a-5c have more prominent pillow boundaries, pipe vesicles and IPH pockets. The pillow structures from GM 5a-5c have an average length of 1.53 m (major axis) and an average height of 0.62 m (minor axis). This suggests an average pillow basalt shape that is oval and lobate (**Figure 3.11**).

3.4 Reconstructed Geology of the Kromberg type-section volcanic stratigraphy and structure (summary)

The Kromberg type-section is made up of seven volcanic cycles interrupted by low-energy depositional environments represented by different volcano-sedimentary chert units. Each volcanic cycle is dominated by tholeiitic basalt flows, although mesocratic diabase intrusions, minor komatiitic basalts and cumulate peridotites are also evident. At least three different shear zones are evident, with one major shear zone (Kromberg Section Mylonites, KSM) found below the Footbridge chert. These shear zones are listvenitic consisting of fuschitic-chlorite-carbonate-quartz bands.

The grid maps of pillow lavas along the Kromberg type-section were drawn in selected areas where exposed river pavement outcrops were available on both the eastern and western side of Komati River. Along the eastern bank of the river, two localities were selected for grid mapping, GM-1 and GM-2a-2b, while in the western side of the river pavement, three were selected, GM-3, GM 4a-4c and GM 5a-5c. In river pavement areas,

Area 1 and Area 2, pillow lava flows of varying sizes and shapes were observed. All the pillow lavas comprise a pillow core, pillow rim and hyaloclastite matrix in between the pillows. Pillowy structures, brecciated pillows and massive flows interlayered with the pillow lavas were observed on the western side of Komati River while silicified pillow lavas, some with ocelli in their cores, were observed on the eastern side of the Komati River, in the mid Kromberg type-section.

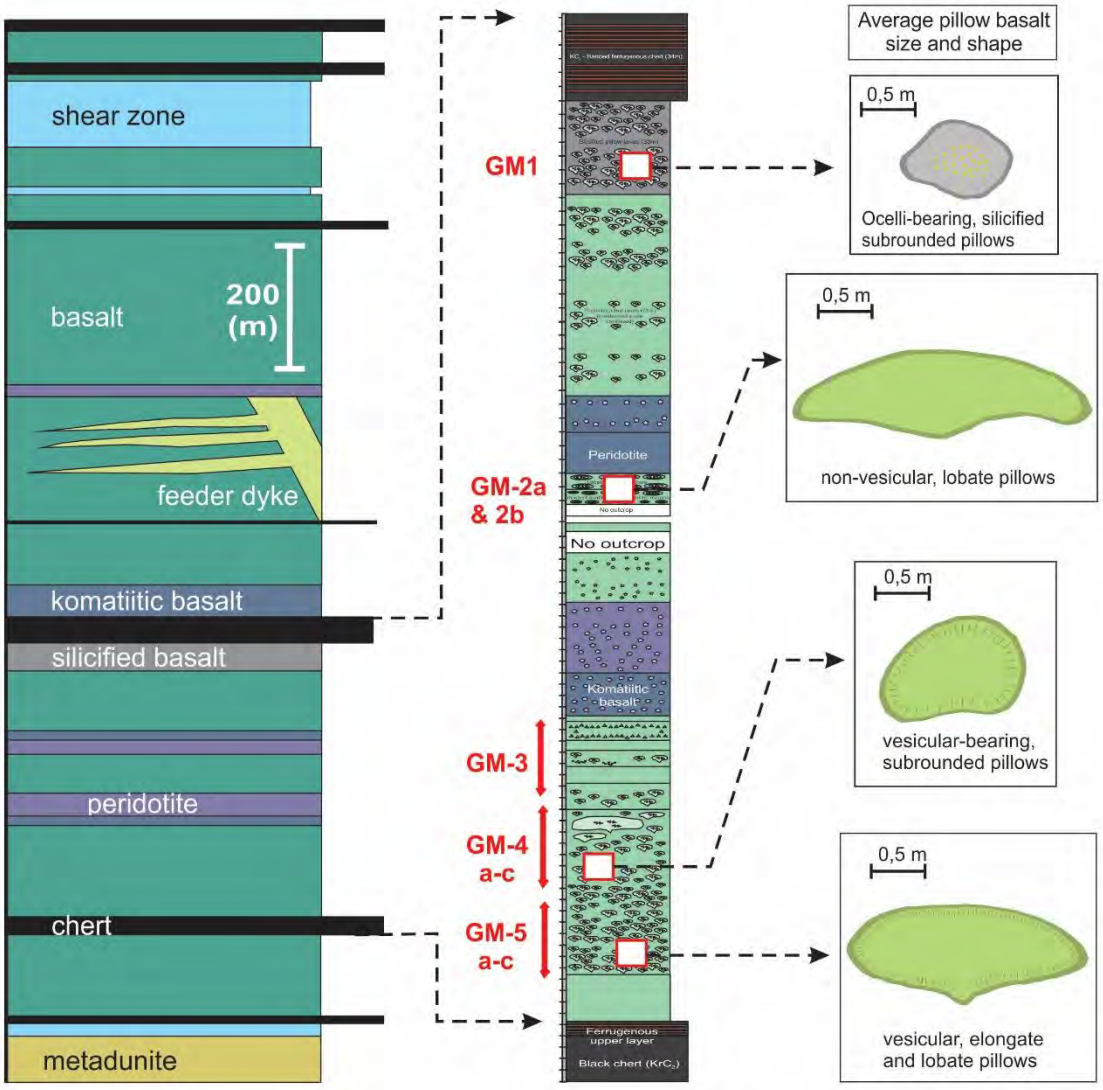

Figure 3.10: *A simplified section from the new geological profile of the Kromberg type-section (after Grosch et al., 2020) that shows the location from which the grid maps were conducted. The focus of this study is on the mid-lower section of the Kromberg, denoted by dotted lines with arrows. For each location, a representative basaltic pillow structure shown on the right-hand side. Their location is shown by white boxes with a red outline. The orientation of the pillow lavas is not cross-sectional.*

GM-1 pillow lavas are highly silicified and are found directly below a thick ferruginous chert unit (KrC_3). They have brown pillow cores and dark grey pillow rims. Their pillow rims are heavily silicified, forming part of the hyaloclastite matrix. These pillows are not tightly packed due to silicification with highly altered pillow rims and inter-pillow hyaloclastite. They are also very hard and on average form subspherical pillows with a maximum average axis of 0.97 m and minor average axis of 0.52m. Although in the same river pavement, grid maps GM-2a-2b differs from GM-1. Grid maps GM-2a-2b comprise large, elongate and lobate pillows with average maximum axis and minor axis of 1.76 m and 0.56 m, respectively (**Figure 3.11**). They are green with heterogenous pale green and dark green pillow cores and dark grey pillow rims. The different colours observed within the pillow cores are interpreted to be a result of magma mingling between light and dark coloured magmas (low and high silica tholeiitic magma). The pillow basalts are tightly packed and have various quartz veinlets running through them and indicating some partial silicification in places. Although they are affected by silicification, they are not as heavily silicified as pillow lavas from GM-1. There is no sign of deformation observed in both GM-1 and GM-2a-2b.

Grid map GM-3 comprises brecciated pillows and fragmented pillows interlayered with massive flows and pillowed lava flows. These breccias are formed by explosive phreatomagmatic processes. Grid maps GM 4a-4c and GM 5a-5c comprise pillow lava flows interlayered with massive basaltic flows. The pillow lavas on the western side of the river pavement are first observed in GM3 where up to 50 cm mushroom-shaped pillows are found. They further extend to GM 4a-4c up until the end of the outcrop near the Komati River where grid map GM 5a-5c is located. Pillow structures in grid maps GM 4a-4c and GM 5a-5c display no pattern in size or shape distribution. They all have well developed pillows rims and IPH pockets in between three pillow structures. These pillows structures are tightly packed with no sign of silicification and deformation. The difference between GM 4a-4c pillow lavas and GM 5a-5c pillow lavas are the massive pillow flows occurring with vesicular pillow lavas contrasted with the massive lava flows found in GM 4a-4c. Grid maps GM 5a-5c has large vesicular pillow lavas (up to 6m along the major axis) that become more elongate to the north. The pipe vesicles do not appear deformed thus ruling out any deformation. Pillow structures in grid maps GM 4a-4c have an average spherical to sub-spherical shape while those in grid maps GM 5a-5c are flat, oval and lobate on average

(**Figure 3.11**). The interlayering of massive and pillow lavas in GM 4a-4c are interpreted to be affected mainly by viscosity and effusion rate (Griffiths and Fink, 1992). The massive flows are favoured by high effusion rates whereas pillow flows are favoured by low effusion rate. The degree of vesicularity mainly indicates the water depth at which the pillow lavas formed (Moore, 1965). At greater depths pipe vesicles are not expected to form whereas at shallower submarine depths they may form. This means that the level of seawater under which these pillows lavas extruded was shallow.

4 X-ray Diffraction (XRD)

Geological mapping on the western bank of the Komati river, Kromberg Formation, in Songimvelo Nature Reserve.

4.1 Introduction

X-ray diffraction is a method used to identify the presence of minerals in rocks is especially useful in identifying fine-grained alteration minerals that are difficult to identify under the microscope (Tucker, 1988). This technique was used to screen for various sheet silicate and other alteration (as well as igneous) minerals in rocks across the Kromberg type-section. As a first order analysis, based on preliminary hand specimen observations showing alteration, samples were selected to investigate various types of alteration mineral assemblages in terms of silicification, chloritization, amphibole formation and albitization. X-ray Diffraction (XRD) analysis was conducted at Rhodes University where Dr. Jonathan Britton provided the

analytical setup and performed the analysis in the Chemistry department. The university utilizes a Bruker D8 Discover diffractometer with Cu-Kα radiation (λ = 1.5405 Å) and nickel (Ni) filter. Data was collected in a range from 2θ= 10º to 100º, scanning at 1.5 min^{-1} with filter time-constant of 0.38 s per step and a slit width of 6.0 mm. Samples were placed on a silicon wafer slide. The XRD data was treated using the EVA (Evaluation Curve Fitting) software. Baseline correction was performed on each diffraction pattern by subtracting a spline function fitted to the curved background. For each sample, the diffraction pattern obtained was used on Bruker software, CrystalSleuth, to identify the minerals present. A spectrum of X-ray intensity (in counts) versus peak position was obtained from each sample and was compared with a standard reference obtainable at an online database, namely the RRUFF project (Lafuente et al., 2015). If the peak position of the sample in the Kromberg type-section matches with that of a reference standard (**Figure 4.1**), that mineral is present in the rock sample. It is important to note that the CrystalSleuth software only picks up dominant peaks for each analysed sample. Some mineral peak positions are therefore not detected; they are masked by dominating minerals in the rock samples. For such minerals, mineral chemistry and more detailed petrography (**Chapter 7**) is required for their detection.

4.2 Mineral phases in the Kromberg type-section

Sample KrDun-65 (**Figure 4.2a**) is a serpentinized metadunite that occurs at the base of the geological stratigraphy for the Kromberg type-section (see **Figure 3.3**). Sample KrDun-65 has more than six peaks, with lizardite serpentine occupying peak positions at 12.2, 19.3, 24.2, 35.9 and 60.2 2-theta position. Chrysotile serpentine occupies peak positions at 12.2 and 24.2 2-theta position. Sample KrO-45 (**Figure 4.2b**) is a partially serpentinized cumulate (olivine and pyroxene) peridotite. The alteration minerals comprise a mixture of lizardite and chrysotile serpentine, also with magnetite present. Chrysotile occupies the 12.2 and 24.8 2-theta peak positions, lizardite occupies 12.1 ,19.4, 24.8 and 42.1 2-theta positions. Magnetite occupies the 35.5 and 43.1 2-theta positions. The intensity of lizardite and chrysotile have up to 3010 counts while magnetite has up to 1789 counts. Sample KrO-20 (**Figure 4.2c**) sample occurs below the intrusive rocks of the Kromberg type-section. This sample consists of the alteration minerals chlorite, lizardite and actinolite. Chlorite occupies peak positions at ca. 13.34, 18.73 and 24.94 2-theta. Actinolite amphibole has peak positions at ca. 10.54, 12.34,

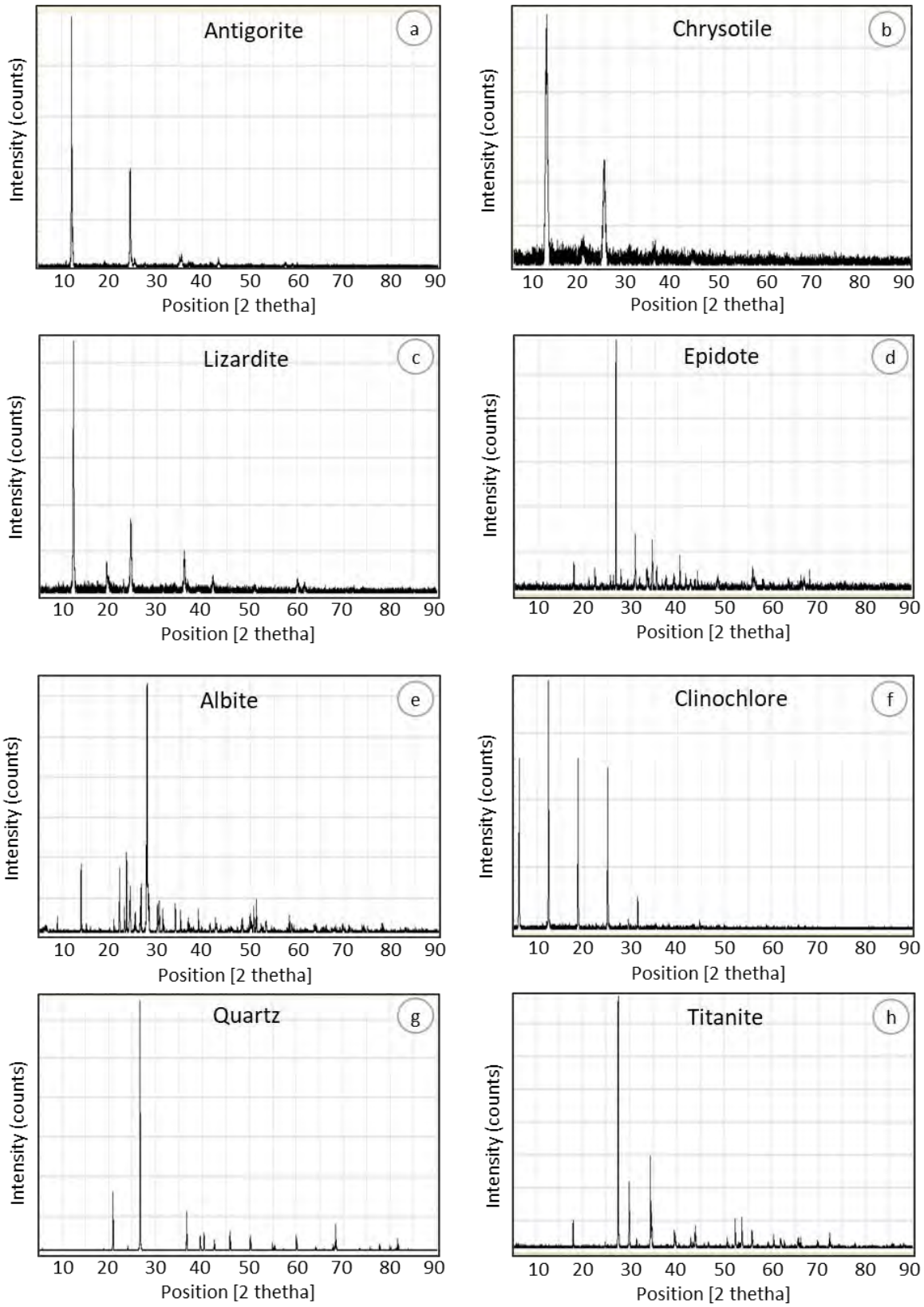

***Figure 4.1**: Reference spectra taken from an online database, namely the RRUFF project (Lafuente et al. 2015), showing peak positions corresponding to certain minerals. These were compared with the spectra obtained from different samples of the Kromberg type-section.*

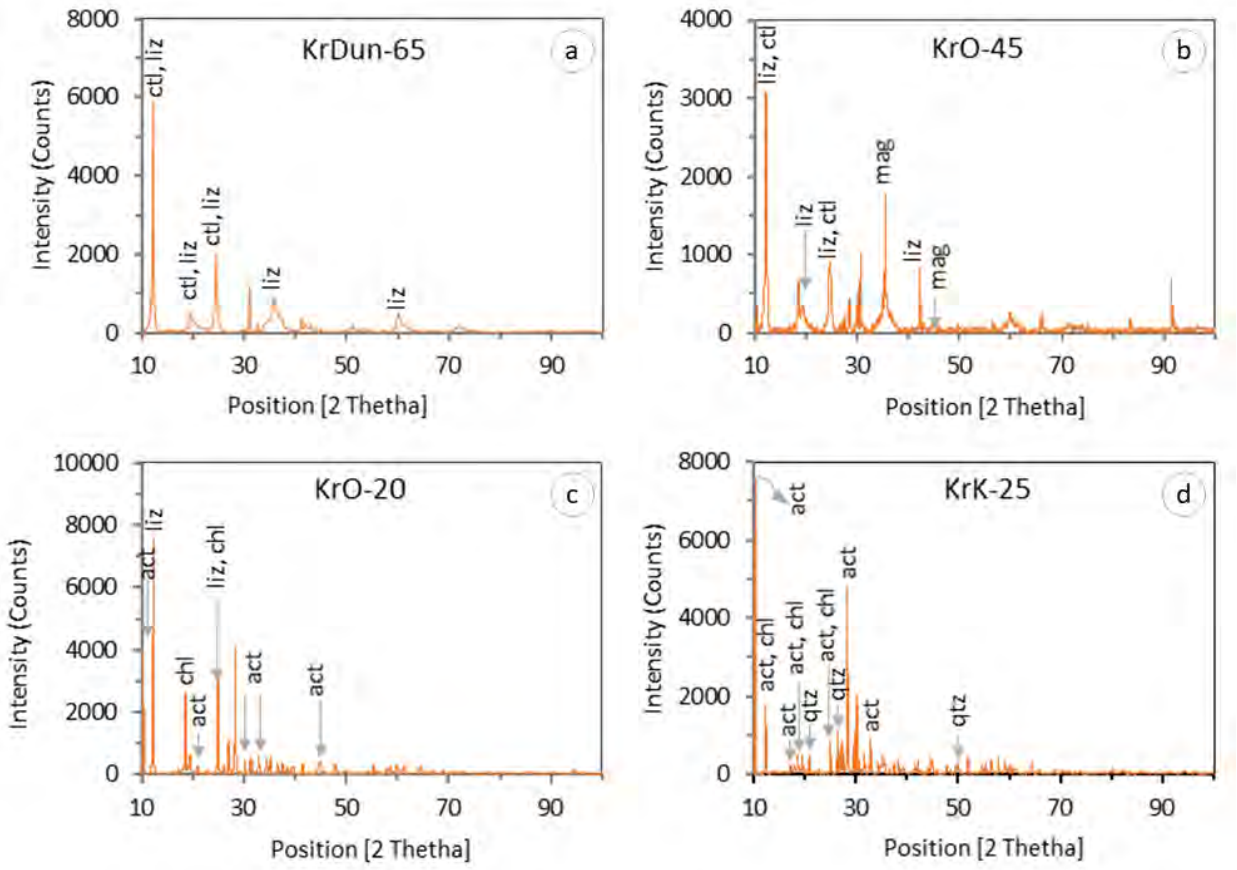

***Figure 4.2**: The XRD spectra for different samples in the Kromberg type-section. (a) is a metadunite sample, (b) and (c) a cumulate peridotite (d) a komatiitic basalt. See reference spectra in **Figure 4.1**.*

21.08, 30.30, 33.02 and 45.06 2-theta, and lizardite occupies two peak positions at ca. 12.34, 24.94 2-theta. Sample KrK-25 (**Figure 4.2d**) is a komatiitic basalt and consists of the alteration minerals actinolite, chlorite and quartz. Actinolite occupies peak positions at ca. 10.35, 12.34, 17.49, 19.59, 25.25, 28.53 and 33.12 2-theta position. Chlorite has peak positions at ca. 12.34, 19.59 and 28.53 2-theta, and quartz occupies peak positions at 21.27, 26.72 and 50.13 2-theta.

Sample KrT-42 (**Figure 4.3a**) is a massive tholeiite that comprises chlorite, quartz and epidote. In the sample, KrT-42, the spectrum indicates nine visible peak positions. Chlorite occupies 12.4, 18.7 and 25.1 2-theta positions with peaks less than 3000 counts. Epidote occupies 26.5, 27.9 and 34.6 2-theta positions while quartz occupies 21.1, 26.5, 36.5,

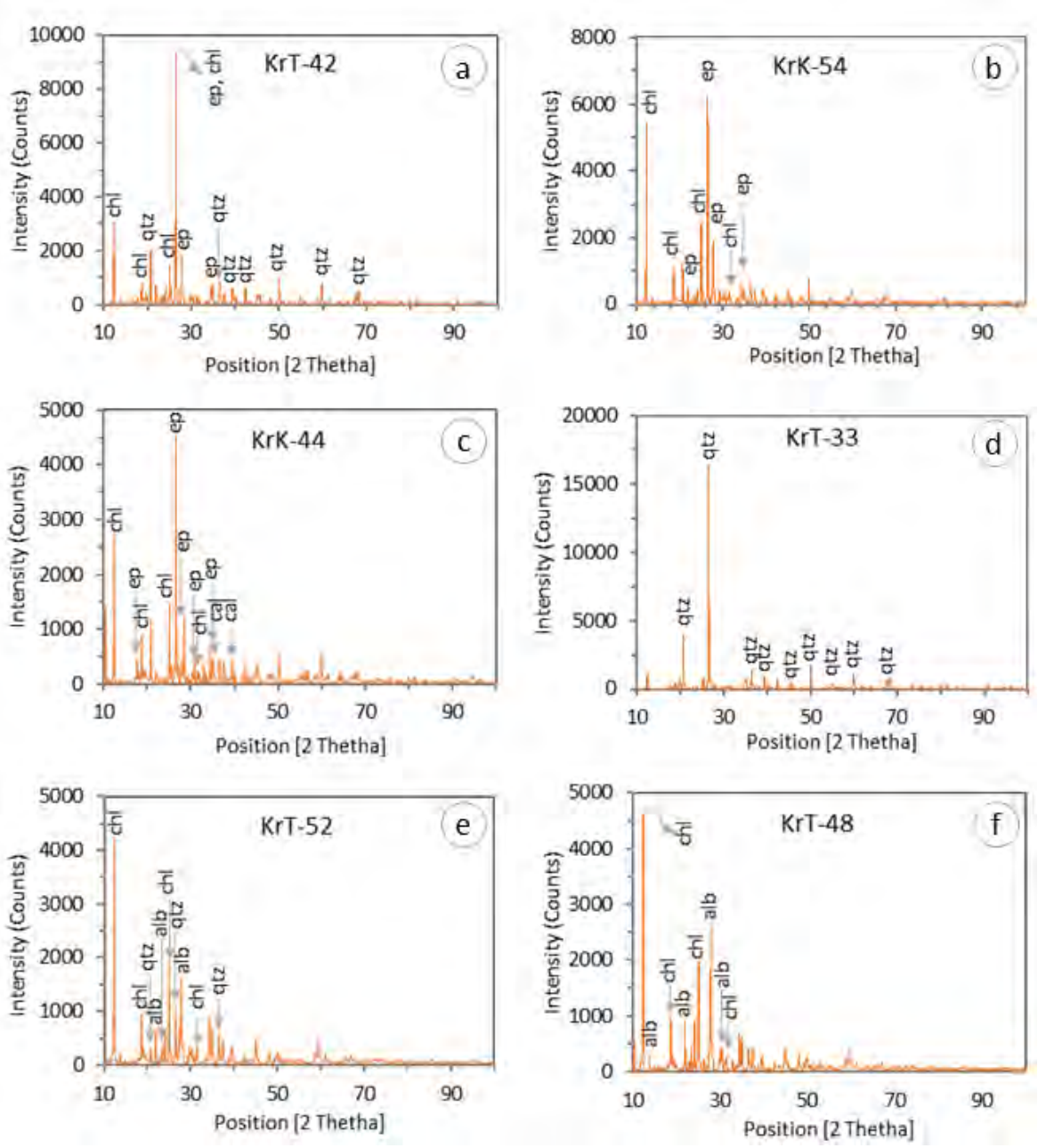

Figure 4.3: *XRD spectra for selected tholeiitic rocks of the Kromberg type-section. See reference spectra in* ***Figure 4.1****.*

39.5, 42.5, 50.1, 60.1 and 68.2 2-theta positions. The rock composition is thus silicified with little chloritization and amphibolization. Sample KrK-54 (**Figure 4.3b**) is a massive tholeiitic metabasaltic rock that comprises epidote, chlorite and titanite. Epidote peak positions are at 22.1, 26.3, 27.9 and 34.5 2-theta position, whereas chlorite peak positions are at 12.4, 18.7, 25.1 and 31.6 2-theta positions. Titanite has peak positions at 39.6 2-theta positions and shares two peak positions with epidote at 27.9 and 34.5 2-theta positions. Sample KrK-44

(**Figure 4.3c**) is a tholeiitic metabasalt composition that consists of epidote, chlorite and calcite. Peak positions are at 12.3, 18.6, 25.1 and 31.6 2-theta position and epidote occupy peak positions at 17.5, 26.7, 30.8 and 34.5 2-theta position. Epidote has the highest intensity, with up to 4526 counts whereas the highest intensity for chlorite is 12.4 counts. Calcite also alters the rock and records peak positions at 36.9 and 39.5 2-theta position. Sample KrT-33 (**Figure 4.3d**) is a silicified tholeiitic pillow lava. The XRD spectra revealed that this rock consists dominantly of quartz. The quartz mineral occupies peak positions at 20.9, 26.5, 36.6, 39.6, 42.4, 45.8, 50.2, 60.1 and 68.3 2-theta.

4.3 Summary

The rocks of the Kromberg type-section have been variably affected by low-grade alteration and metasomatic silicification processes. The extent to which the alteration presides cannot solely be determined by XRD analysis. Further petrographic studies, in Chapter 5, are required to assess the degree of alteration in these rocks. From the XRD analysis summarized in **Table 4.1**, different rock compositions display different mineralogical compositions. For instance, the metadunite sample and partially altered cumulate peridotite show serpentinization, whereas komatiitic basalts are affected by complex amphibolization and chloritization. All tholeiitic metabasalt rocks are variably affected by chloritization (to be discussed in the succeeding **Petrography Chapter 5**). Albitization and epidotization is also evident in tholeiitic metabasaltic rocks. The quartz peak positions in metasomatized tholeiitic basalt represents silicification, previously identified in the Local Geology Chapter 3, in grid map GM-1.

Table 4. 1*: A table showing different mineral phases found in different rock compositions in the Kromberg type-section.*

Sample name	**Rock name**	**Ctl**	**Liz**	**Mag**	**Act**	**Chl**	**Qtz**	**Ep**	**Alb**	**Cal**
KrDun-65	Metadunite	X	X							
KrO-45	Cumulate peridotite	X	X	X						
KrO-20	Cumulate peridotite		X		X	X				
KrK-25	Komatiitic basalt				X	X	X			
KrT-42	Tholeiitic basalt					X	X	X		
KrK-54	Tholeiitic basalt					X		X		
KrK-44	Tholeiitic basalt					X		X		X
KrT-33	Tholeiitic basalt					X				
KrT-52	Tholeiitic basalt					X	X		X	
KrT-48	Tholeiitic basalt					X			X	

5 Petrography

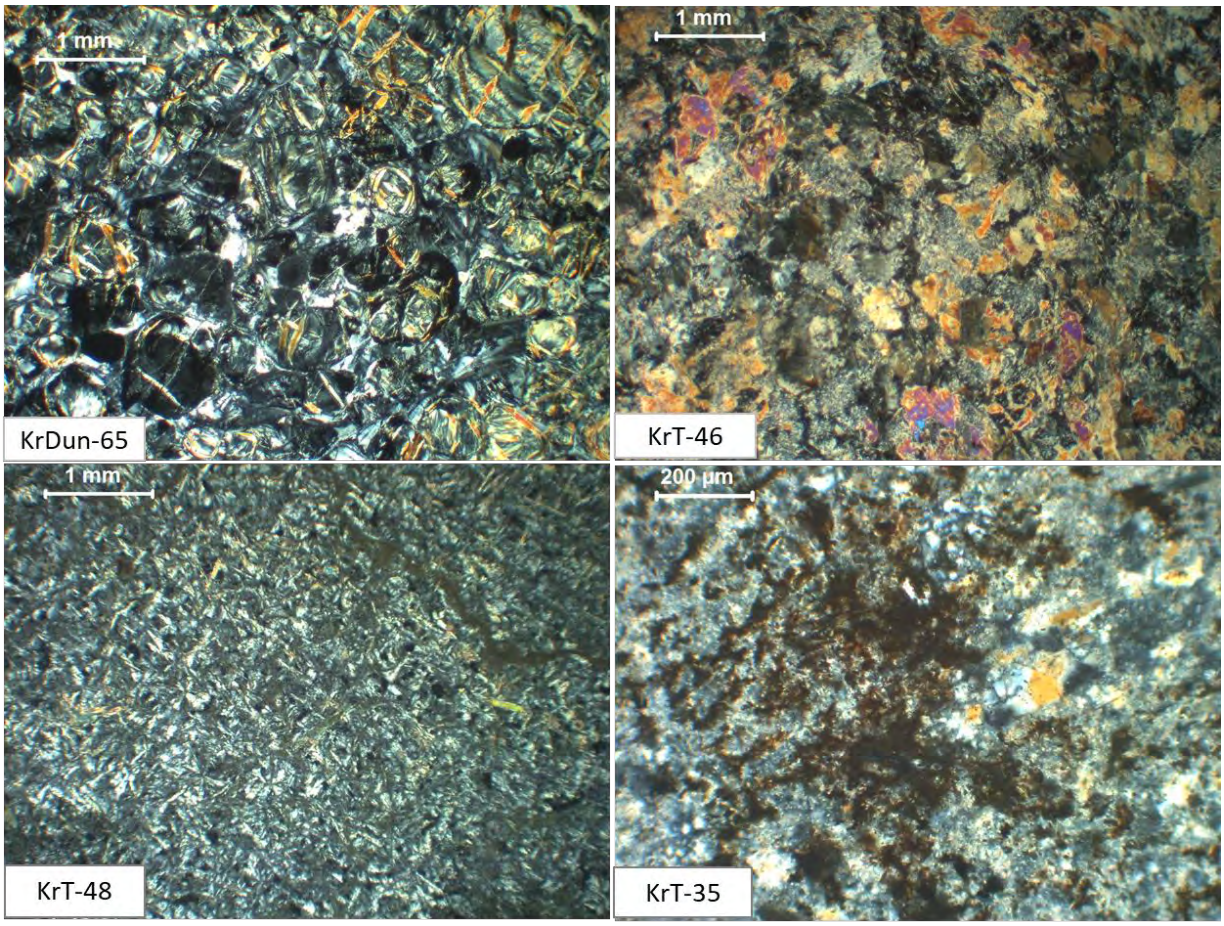

Different petrographic textures found in the Kromberg type-section. KrDun-65 represents a cumulate texture with serpentinized olivine forming a cumulus phase, KrT-46 an interstitial texture, KrT-48 a subophitic texture and KrT-35 an aphyric, silicified texture.

5.1 Introduction

A total of 33 thin sections were prepared for petrographic studies. A subtotal of 29 of the 33 thin sections are mafic-ultramafic rocks in the Kromberg type-section, whereas 4 thin sections included volcano-sedimentary chert. Petrographic analysis was conducted for all rock samples based on preliminary field observations (**Chapter 3**), hand specimen characteristics and XRD analysis **(Chapter 4)** for mineral identification. Additionally, thin section photomicrographs and descriptions not included in this chapter are presented in **Appendix A2**. A Leica Application Suite microscope connected to a camera was further used

for petrographic analyses and photomicrograph collection. The petrographic analysis, combined with the XRD results, field and hand specimen observations allowed for preliminary classification and rock grouping. Metavolcanics rocks have been grouped as: metadunite, olivine-pyroxene cumulate peridotite (wehrlite), komatiitic basalts, chloritized tholeiitic metabasalts and silicified tholeiitic metabasalts. The relatively fine-grained Kromberg rock samples appeared relatively fresh in hand specimen, but many of them also displayed different shades of grey or green colour due to variable degrees of seawater silicification and/or chloritization. As a result, some of the Kromberg mafic-ultramafic rocks are observed to have different low-temperature metamorphic/alteration replacement textures. The petrographic rock classification and groupings are tested and confirmed against whole-rock major and trace element geochemistry results in the subsequent **Geochemistry Chapter 7**.

5.2 Petrography of metavolcanics rocks

5.2.1 Komatiitic basalts

Komatiitic basalts are fine-grained, comprise interlocking pyroxene crystals and have an overall interstitial texture. They have been partially altered to actinolite and chlorite. Minor amounts of iron-oxides like magnetite or titanite, quartz and carbonate forms part of the matrix. Sample KrK-25 (**Figure 5.1a-c**) is a medium-grained rock that comprises ca. 80% interlocking pyroxene crystals, ca. 10% titanite and ca. 10% quartz. The pyroxene crystals are elongate in habit. They vary in crystal sizes with sizes ranging from ca. 0.125 mm to ca. 1.05 mm. They are colourless and pleochroic with a green tint in plane polarized light. They have a moderate relief and up to second order interference colours. Titanite is a brown alteration mineral that forms crystals between pyroxene crystals. Quartz is an alteration product and is found associated with chlorite. In places, quartz and calcite forms groundmass aggregates replacing the interstitial igneous matrix. Calcite is light pink – colourless with visible lamellae. Pyroxene is partially replaced by chlorite and actinolite. Chlorite results in dark-bluish interference colours while actinolite forms orange to yellow second order interference colours. A similar texture is observed in sample KrT-46 (**Appendix A3**).

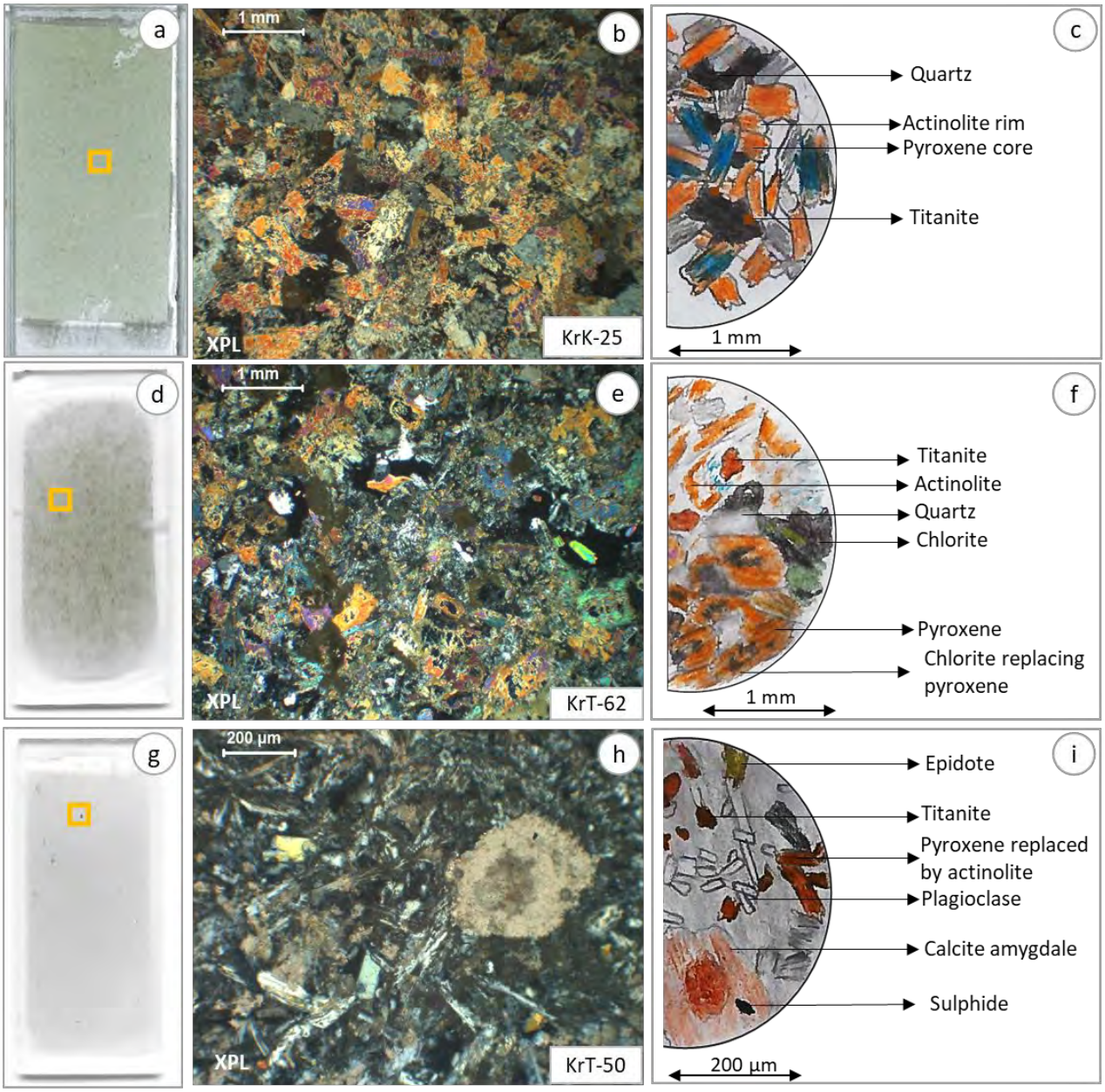

Figure 5. 1: *Representative samples for partially altered komatiitic basalt and tholeiite metabasaltic rocks in the Kromberg type-section that show their thin section, photomicrograph in crossed-polarised light (XPL) and the location from which the photomicrograph was taken (represented by orange boxes), and labelled sketch drawings. (a)-(c) shows a komatiitic basalt with an overall interstitial texture (d)-(f) Is a partially chloritized tholeiite rock sample with partially chloritized pyroxene cores and a groundmass completely replaced by chlorite, epidote and quartz. (g)-(i) is partially silicified amygdaloidal tholeiite with plagioclase replaced by epidote and sericite. Carbonate is also present.*

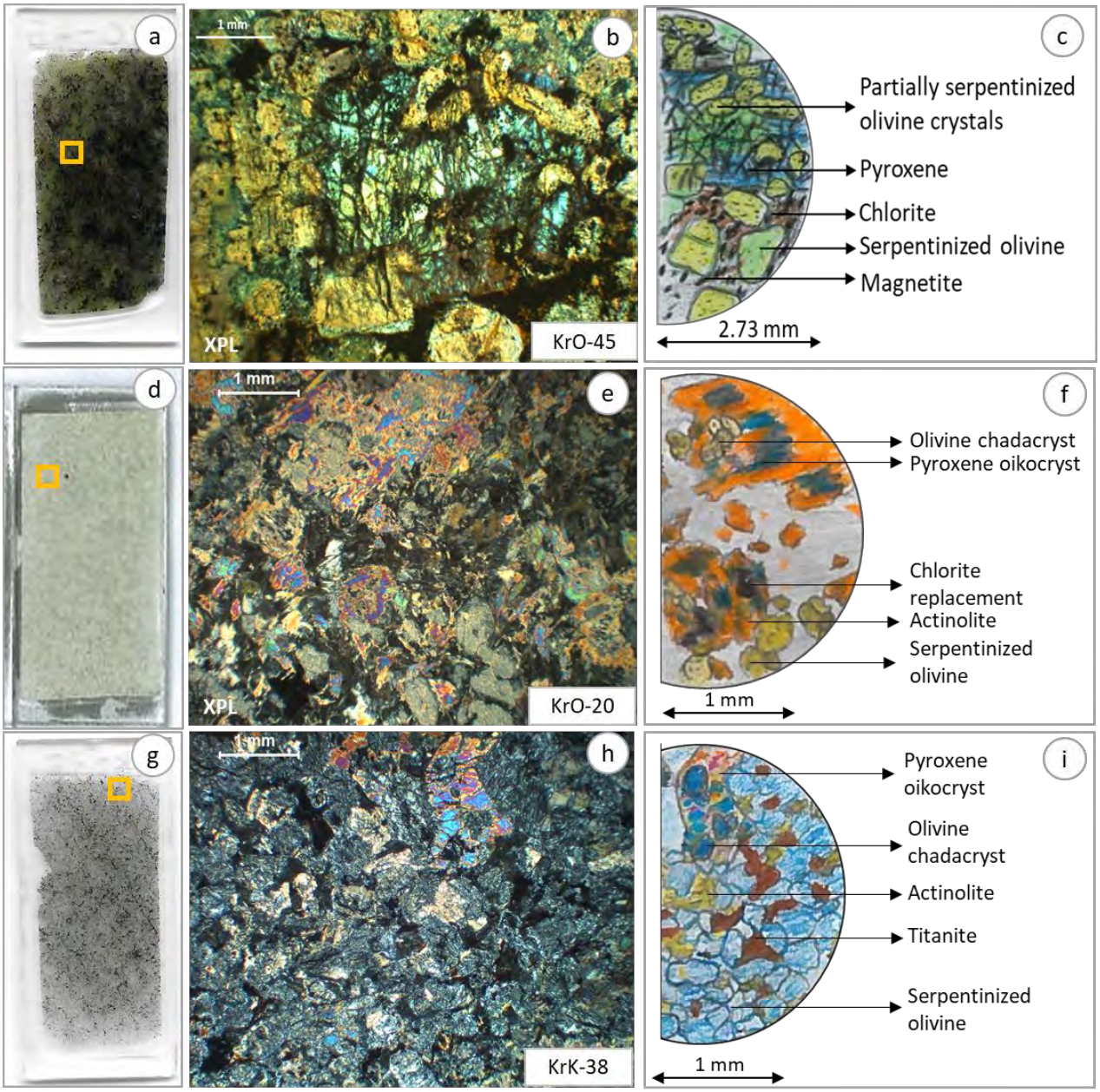

Figure 5. 2*: Thin sections slides, representative photomicrographs in crossed-polarised light and sketch drawings of poikilitic wehrlite (or cumulate peridotite) with olivine chadacrysts and pyroxene oikocrysts. (a)-(c) is partially serpentinized olivine crystals and relatively fresh pyroxene crystals. (d)-(i) is moderately altered cumulate peridotite with a few relatively fresh pyroxene crystals preserved.*

5.2.2 Cumulate peridotite

The cumulate peridotitic rocks in the Kromberg type-section are phaneritic and have an orthocumulate texture. They comprise ca. 50% olivine, ca. 20-40% pyroxene and ca. 10-20% alteration minerals such as actinolite, chlorite, titanite and/or magnetite. They have a poikilitic texture where olivine occurs as chadacrysts and pyroxene as oikocrysts. Cumulate peridotite rocks in the Kromberg type-section are altered to varying degrees depending on their localities. KrO-45 (489.5 m above the Noisy Formation; **Figure 5.2a-c**) display low degree alteration and comprises ca. 50% olivine, ca. 30% pyroxene, 10% chlorite and ca. 10% magnetite. Even after low temperature alteration the rock remains phaneritic and preserves relatively fresh pyroxene crystals. The rock has elongate pyroxene oikocryst that form lengths between ca. 1.25 mm and ca. 5.50 mm. They have a moderate relief, form two cleavages intersecting at slightly less than 90^0 and are weakly pleochroic with pale green pleochroism. The elongate crystals show large degree of fracturing and have pink-blue-green interference colours. Pyroxene crystals are replaced by Mg-rich chlorite along their margins giving the crystals the anomalous brown interference colours. Bright green chlorite is also found replacing the intercumulus mafic minerals of the rock. The smaller olivine chadacrysts have varying lengths from ca. 0.43 mm to ca. 1 mm. Olivine crystals are colourless, subhedral and non-pleochroic. They have a high relief and are moderately fresh with partially serpentinized rim forming a mesh texture. Relic olivine crystals have second order yellow interference colours. The opaque magnetite crystals occur as inclusions in olivine crystals and forms along pyroxene margins and fractures.

Samples KrK-38 and KrO-20 (580 m and 1063.5 m above the Noisy Formation, respectively; **Figure 5.2d-i**) are moderately altered, medium-grained and show less preservation of primary textures than KrO-45. KrO-20 (**Figure 5.2d-f)** comprises ca. 40% partially uralitized pyroxene crystals, ca. 40% serpentinized olivine crystals, 10% chlorite, 5% actinolite and 5% magnetite. Pyroxene oikocrysts are pale green and weakly pleochroic. They are tabular, have second order interference colours and have a moderate relief. They form lengths of up to ca. 2 mm. Along their margins, they have a low relief. Their low relief is a result of uralitization where they are replaced by actinolitic amphibole. The pyroxene crystals are also partially replaced by chlorite resulting in dark bluish-black interference colours. The sample has colourless and weakly pleochroic olivine chadacrysts. Olivine is pseudormorphed by serpentine resulting in grey, complex interference colours. The opaque

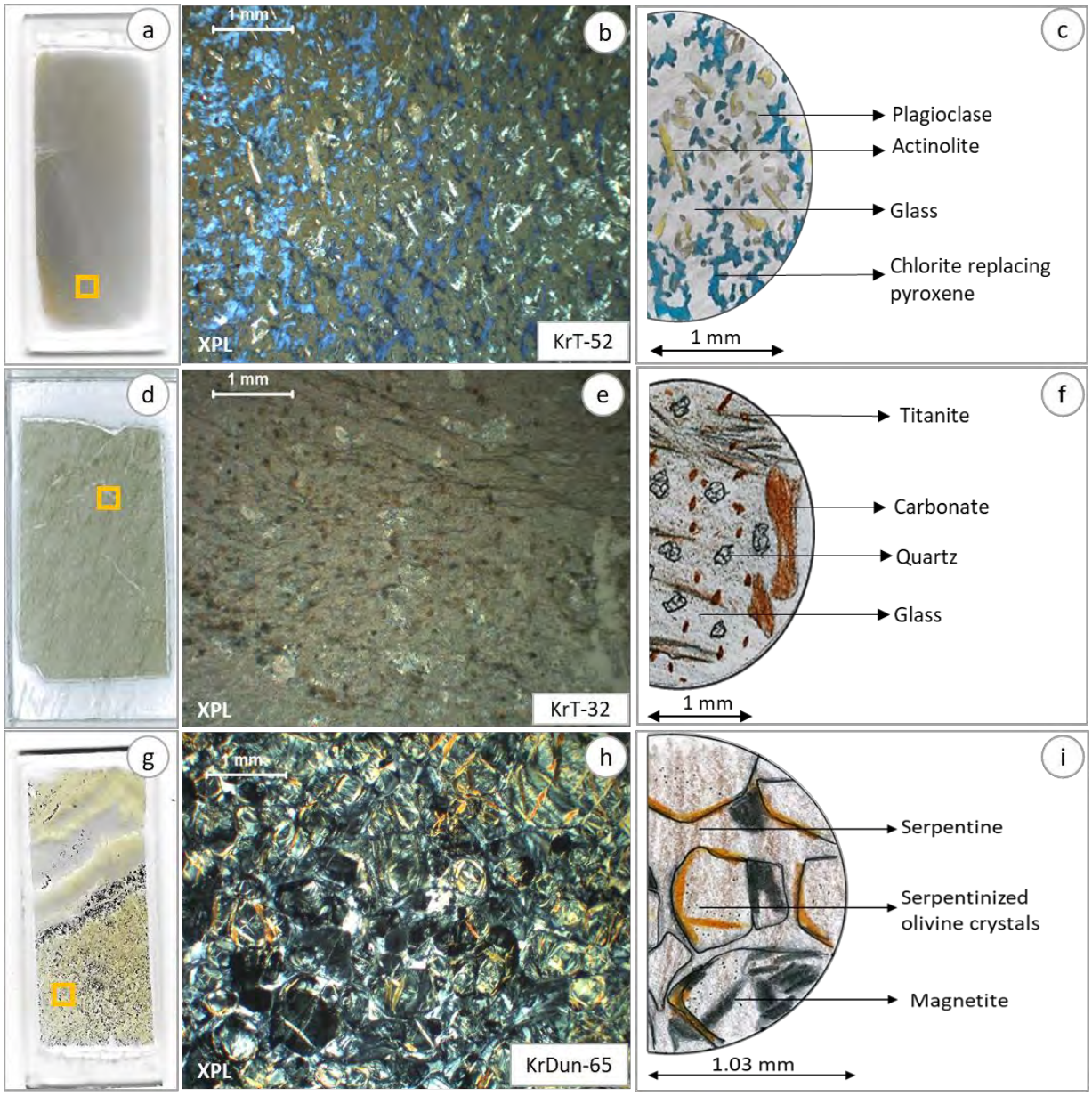

Figure 5. 3*: Thin sections slides, photomicrographs and sketch drawing of rock samples in crossed-polarised light that show high degree of alteration. (a)-(c) shows a highly chloritized tholeiitic metabasalt with chloritized pyroxene crystals and plagioclase in a glassy matrix. (d)-(f) is a highly silicified tholeiite with carbonization and (g)-(i) is a highly serpentinized metadunite cumulate.*

mineral, magnetite, is found as tiny crystals around the pyroxene grains and in between the olivine crystals. Sample KrK-38 (**Figure 5.2g-i**), on the other hand, comprises ca. 50% serpentinized olivine, ca. 30% partially altered pyroxene, ca. 10% titanite and ca. 10% magnetite. The olivine chadacryst are altered to serpentine and magnetite. They are green with grey-blue to white interference colours as a result of complete serpentinization. They are anhedral and comprise grains forming lengths of ca. 0.167 mm. The pyroxene oikocrysts are

relatively fresh with a few crystals converted to actinolite. Relatively fresh pyroxene oikocrysts are colourless, fractured, have a moderate relief and have two cleavages intersecting at c. 90^0. They have second order interference colours and display inclined extinction. In most part of the rock, olivine chadacrysts almost entirely encloses pyroxene crystals. Opaque magnetite is found along olivine fractures. Titanite is subhedral, brownish in plane polarized light and occurs in minor amounts as an alteration mineral. It is associated with magnetite and forms between olivine crystals.

5.2.3 Chloritized tholeiitic metabasalts

Chloritized tholeiitic metabasalts have been grouped in accordance with their mineralogy and type of alteration. In the Kromberg type-section, chloritized tholeiitic metabasalts are either highly or partially chloritized. Highly chloritized tholeiites are fine- to medium-grained. They comprise relic primary plagioclase and pyroxene. Alteration minerals include chlorite, titanite and epidote, and some samples have a chloritized glassy groundmass. They have an ophitic texture or a porphyritic texture. Highly chloritized tholeiitic metabasalt rock samples analysed for petrography are KrK-23 and KrK-53 (KrK-24 and KrT-54 are in **Appendix A2**), and partially chloritized tholeiitic metabasalt samples: KrK-21, KrK-62, KrST-22, KrT-47 and KrT-49 (KrT-48, KrT-51b, KrT-54 and KrT-61 are in **Appendix A3**). Partially chloritized tholeiites are fine- to medium-grained and comprise slightly uralitized pyroxene. Actinolite and minor chlorite replaced the pyroxene and epidote replaced the plagioclase. In general, these metabasalts display a subophitic, intersertal or porphyritic texture and some sample are affected by late-stage veining. Slightly, porphyritic partially chloritized tholeiites are medium-grained rocks that comprises pyroxene phenocrysts in a finer -grained groundmass.

Sample KrK-21 (**Figure 5.4a**) comprises ca. 60% relic igneous pyroxene altered partially along rims and fractures to actinolite, in an alteration matrix making up, 10% chlorite, ca. 10% quartz, 10% carbonate groundmass and ca. 10% titanite. Primary relic pyroxene crystals are colourless, subhedral and weakly pleochroic. Their length ranges between 0.125 mm and 1.05 mm. They have a moderate relief and two cleavages intersecting at c. 90. Under cross-polarized light (XPL) pyroxene crystals display second order purple-green-orange interference colours, with green being the highest interference colour. Pyroxene

is uralitized along its fractures and rims to actinolite. Actinolite is green and pleochroic with lower first order yellow interference colours. Titanite is anhedral as an alteration mineral, brown under plane polarized light (PPL) and becomes greyish brown under XPL. The groundmass is made up of quartz and carbonate. Carbonate is colourless and has a pale-brown interference colour, while quartz is colourless with first order grey-white interference colours. The groundmass is partially altered by Fe-rich chlorite resulting in blue interference colours. A late-stage carbonate veinlet is evident in the rock. Sample KrK-62 (**Figure 5.1d-f**) differs from KrK-21 in that it has no carbonate and has pyroxene crystals ranging from 0.69 mm to 1.20 mm in size. Fe-rich chlorite with blue interference colours partially replaces pyroxene crystals at their cores. Titanite is coarse-grained and anhedral. The groundmass is completely replaced by chlorite, quartz and epidote, masking primary igneous features. Epidote grains are colourless, and anhedral with a moderate relief. It has third order bright pink-orange interference colours.

Other partially chloritized tholeiites are fine-grained and comprise plagioclase, pyroxene and quartz. They display a subophitic texture where plagioclase does not completely enclose the pyroxene crystals. Sample KrST-22 (**Figure 5.4b**) comprises ca. 40% pyroxene, ca. 20% plagioclase, 10% actinolite, 15% chlorite, ca. 10% quartz and 5% titanite. Quartz is interstitial to pyroxene and plagioclase. Plagioclase crystals are tabular, colourless and non-pleochroic. They have first order white-grey interference colours with simple twinning. Plagioclase is altered to albitic feldspar and display a perthitic texture in places. Pyroxene crystals are anhedral, colourless and weakly pleochroic. They show second order interference colours and have a moderate relief. Along their margins, they are uralitized to actinolite. Actinolite is colourless to pale green, has a low relief and displays simple twins. Titanite forms as dusty stains in the rock and quartz forms the matrix. Chlorite partially replaces pyroxene and the matrix minerals. It is green, weakly pleochroic and has a low relief. It forms anomalous dark-blue interference colours, suggesting Fe-rich chlorite. Rock sample KrT-47 (**Figure 5.4c**) comprises ca. 40% plagioclase, ca. 40% pyroxene, ca. 10% titanite, 5% chlorite and 5% actinolite. Plagioclase has a low relief and form lengths of ca. 0.125mm to 0.363 mm. In places polysynthetic twinning and endulose extinction is observed. Pyroxene is completely replaced by chlorite and actinolite. They have second order bluish-black interference colours due to chloritization. Actinolite crystals are tabular and display simple twinning. Titanite is brown, forms around the plagioclase and actinolite crystals. The rock sample, KrT-49 (**Figure 5.4d**) comprises ca. 40% plagioclase crystals, ca. 30%

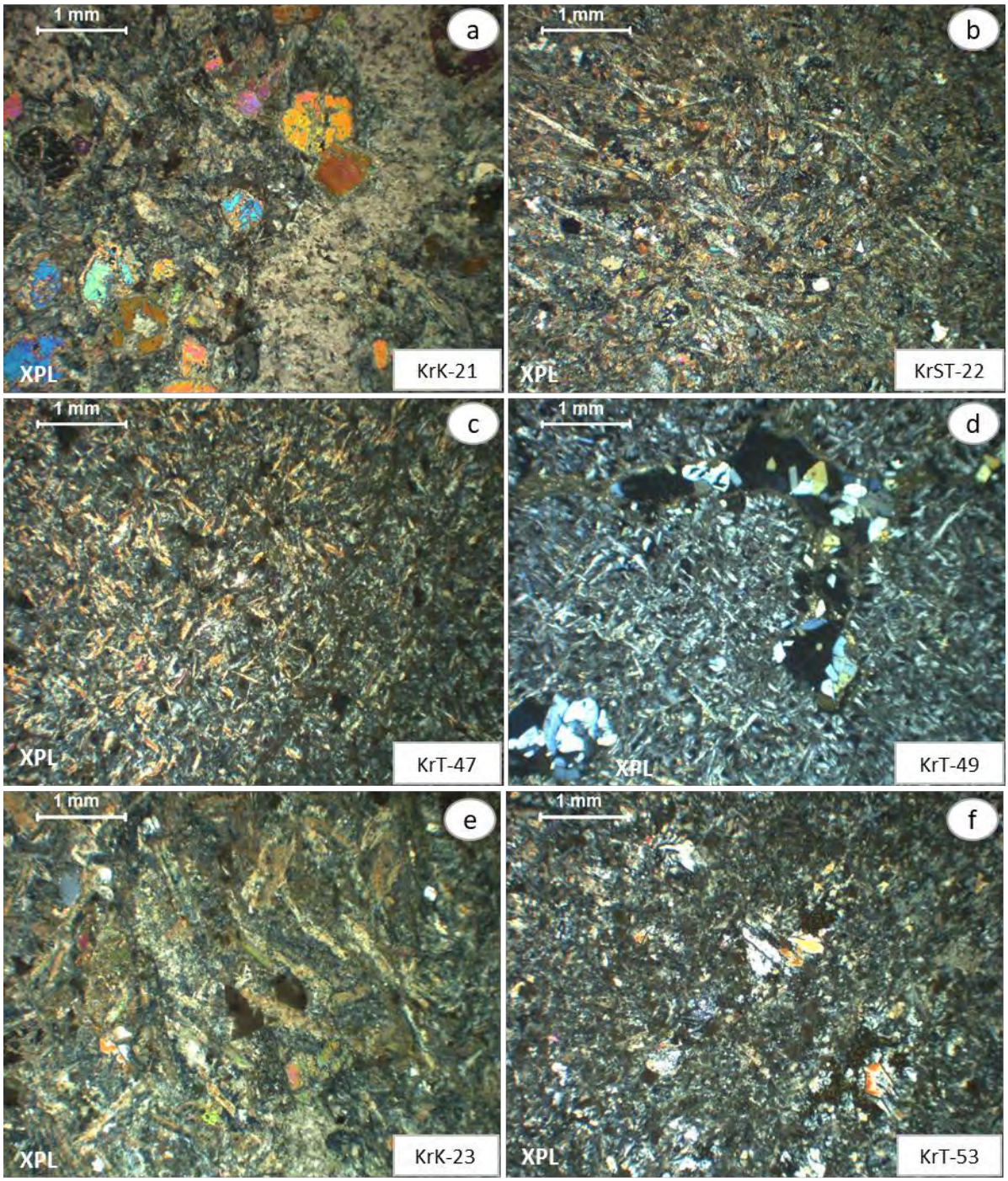

Figure 5. 4*: Photomicrographs of chloritized tholeiitic basalts in crossed-polarised light where (a)-(d) are partially chloritized and (e)(f) highly chloritized tholeiites.*

pyroxene, 10% actinolite, 10% chlorite and ca. 5% titanite and 5% epidote. Microdomains of chloritized glass occupy the interstices between plagioclase and pyroxene. Pyroxene crystals are colourless, have a pale green pleochroism and have a 93° extinction angle. They have been replaced by actinolite. Low relief plagioclase displays simple-twinning and interlocks

with other plagioclase crystals. An interstitial matrix is completely altered to chlorite and epidote, replacing all primary minerals. Chlorite is green in plane polarized light and displays anomalous dark-blue interference colours while epidote crystals are euhedral to subhedral, stubby and forms lengths of 0.05 mm to 0.25 mm. Epidote is colourless, has a moderate relief and have third order yellow and blue interference colours. Titanite is found in between the feldspar crystals, forming dusty stains throughout the thin section.

Sample KrK-23 (**Figure 5.4e**) is a subophitic, medium-grained rock that comprises ca. 40% pyroxene, ca. 30% plagioclase, ca. 20% titanite and 10% chlorite. Pyroxene is tabular, has a moderate relief and displays second order pink-green-yellow interference colours. Although a few relic pyroxene crystals remain preserved, most pyroxene crystals have been overprinted by Fe-rich chlorite resulting in blue interference colours. They have varying length that range between 0.22 mm and 2.27 mm. Plagioclase crystals are elongate with lower first order grey-orange interference colours. They form lengths between 0.45 mm and 1.36 mm. They are partially replaced by quartz and sericite, resulting in a pale-brown sheen. Brown titanite is anhedral and forms lengths between 0.22 mm and 0.68 mm. A similar texture is observed in KrK-24 (**Appendix A3**). KrK-53 (**Figure 5.4f**) is porphyritic with ca. 40% plagioclase and ca. 30% titanite phenocryst and a ca. 30% altered glassy groundmass. Elongate plagioclase has first order orange interference colours and is altered to quartz, resulting in first order grey-white interference colours. Quartz is associated with chlorite, which forms a fringe around plagioclase crystals. Al-rich chlorite is green, has a low relief and a mottled texture and has anomalous brown interference colours. Titanite forms up to 0.25 mm fine-grained spots throughout the rock. The groundmass is altered to chlorite displaying blue interference colours. It has also been carbonatized in minor quantities displaying fourth order pink-brown interference colours.

5.2.4 Silicified tholeiitic metabasalt

Silicified tholeiitic basalt rock specimens are also grouped according to their degree of silicification (that is, partially or highly silicified tholeiites). Highly silicified tholeiitic basalts comprise plagioclase, pyroxene and silicified igneous matrix. Due to the high degree of silicification, most primary minerals have been completely overprinted and very few primary igneous minerals are preserved, although igneous textures are preserved. Highly silicified

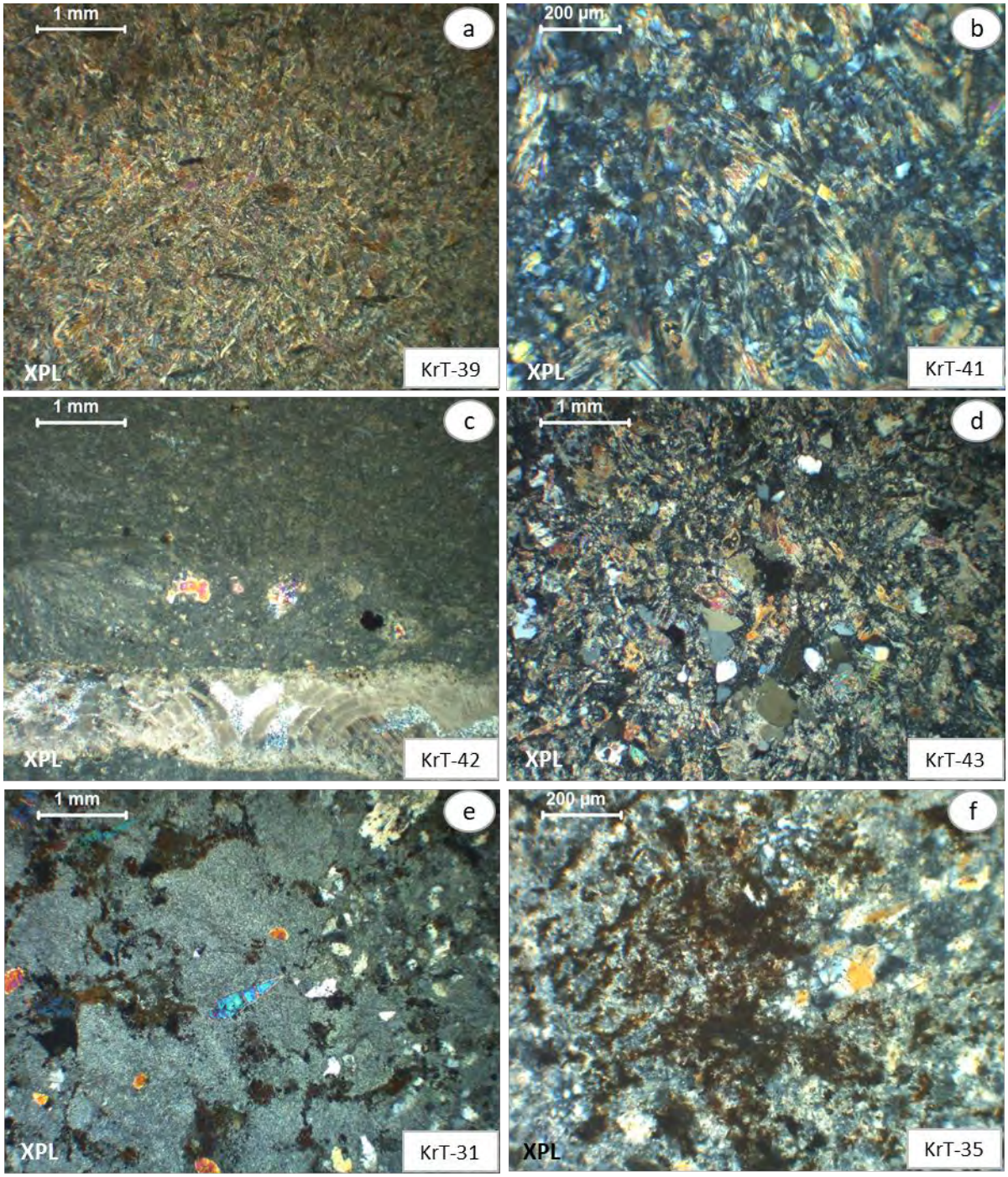

Figure 5. 5*: Photomicrographs (in crossed-polarised light) of silicified tholeiites where (a)-(d) represent partially silicified tholeiites and (e)-(f) represent highly silicified tholeiites. A carbonate-quartz vein runs through KrT-42 in (c).*

tholeiites that are petrographically described are KrT-31 and KrT-32 (KrT33, KrT-34 and KrT-35 are in **Appendix A2**). The protolith to these rocks are phaneritic but silicification has resulted in its fine-grained nature observed also in the field. Partially silicified tholeiites are

fine- to very fine-grained. They all comprise uralitized pyroxene and moderately sericitized plagioclase. Actinolite and chlorite replaces the pyroxene and sericite and epidote replaced the plagioclase. The samples are affected by late stage veining with quartz and carbonate or chloritized veins cross-cutting the rock. Other samples are amygdaloidal with carbonate replacing amygdales. In some samples, sulphide minerals are observed in minor quantities associated with amygdales and late-stage veins. Partially silicified tholeiites analysed for petrography are: KrT-41, KrT-39, KrT-42, KrK-43 and KrT-50 (KrT-36, KrT-40 and KrT-44 are in **Appendix A2**).

Rock samples that display a subophitic texture are KrT-39 and KrT-41 (**Figure 5.5a-b**). They comprise ca. 50% pyroxene, ca. 40% plagioclase and ca. 10% titanite. These rock samples have interlocking tabular pyroxene crystals. Pyroxene crystals in KrT-39 ranges in length from ca. 0.11 mm to 0.51 mm while in KrT-41 they range from 0.02 mm to 0.91 mm. The pyroxene crystals are replaced by actinolite and Fe-rich chlorite. The rock samples also comprise colourless and low relief plagioclase with simple twinning. Plagioclase forms lengths between 0.15 mm and 0.26 mm in KrT-39 and is almost completely replaced by epidote in KrT-41. In KrT-39, chloritized vein with anomalous blue interference colours runs through the rock. The rock also comprises quartz veinlets with first order grey-white interference colours. In KrT-41, epidote is stubby, colourless and has no cleavages. They have a high relief and have second order blue interference colours. Minor amounts of titanite crystals are observed in both samples. KrT-42 (**Figure 5.5c**) is cryptocrystalline with individual crystals not completely resolved using a microscope. It comprises ca. 40% pyroxene, ca. 40% glass and ca. 20% titanite. Pyroxene is completely replaced by actinolite with orange-yellow interference colours. The glassy matrix is silicified and therefore displays first-order interference colours. Epidote is colourless to pale green and ranges in length between 0.12 mm and 0.44 mm. It is found closer to the quartz-carbonate vein cross-cutting the rock and is therefore regarded as an alteration mineral. Samples with an intersertal texture (KrT-50 and KrK-43) comprise quartz interstitial to plagioclase and pyroxene. In KrK43 (**Figure 5.5d**), quartz abundance is ca. 20% while pyroxene is 30%, plagioclase 20% and titanite ca. 10%. Quartz crystals are anhedral and range in length between 0.20 mm and 0.62 mm. Titanite is fine-grained with up to 0.25 mm length. In both rock samples plagioclase is partially altered to sericite resulting into a pale-brown sheen. Sericite is colourless and has a low relief. KrT-50 (**Figure 5.2g-i**) is amygdaloidal with calcite amygdale ranging in size

between 0.318 mm and 1.10 mm. The amygdales have well developed rhombohedral cleavage with lamellae twins at the core and a reaction rim.

Sample KrT-31b (**Figure 5.5e)** is grey with ca. 50% groundmass, ca. 30% pyroxene phenocryst and ca. 20% titanite. The rock is heavily altered and has an aphyric texture. Pyroxene is colourless, pleochroic with second order interference colours. Pyroxene crystals have varying lengths that ranges from ca. 0.23 mm to ca. 1 mm. The groundmass is silicified with grey-white interference colours while titanite forms brown spots in the rock. KrT-32 (**Figure 5.3j-l**) comprises of ca. 40% silicified groundmass, ca. 20% titanite, ca. 25% pyroxene, ca. 15% carbonate. The rock is grey-brown due to silicification and carbonization. Pyroxene forms phenocrysts in a glassy groundmass. It is heavily altered by quartz, where quartz completely pseudormorphs pyroxene crystals. It is tabular and has first order grey-white interference colours due to silicification. Relic pyroxene crystals are however preserved. They have orange-yellow interference colours. Titanite is brown in XPL and PPL and forms dusty stains in the rock. Carbonate is light brown. It is found associated with quartz and pyroxene. The fine-grained nature of the rock is due to silicification and carbonization. Sample KrT-35 (**Figure 5.5f**) comprises ca. 50% groundmass, ca. 30% titanite and ca. 20% stubby crystals of epidote/clinozoisite with lengths of 0.01 mm to 0.2 mm. Titanite forms in clusters in places while the groundmass is grey-white from intense silicification.

5.2.5 Metadunite

The rock KrDun-65 (**Figure 5.3g-i**) is a phaneritic rock with a cumulate texture. It is holocrystalline with olivine crystals. The overall texture of the rock is therefore mesocumulate. The protolith of the rock is a coarse-grained dunite with interlocking olivine crystals. The dunite sample have been heavily serpentinized with late stage cross-cutting serpentine veins evident. As a result of secondary alteration processes, fine-grained olivine crystals with lengths ranging from ca. 0.14 mm to ca. 0.44 mm are observed. Serpentine (chrysotile and lizardite) and magnetite replaces olivine. Chrysotile forms a mesh texture resulting dark massive cores and light grey to white rims in crossed-polarised light. Lizardite (confirmed by XRD) occurs within olivine fractures and rims forming first order orange

interference colours. Black and opaque magnetite replaces olivine crystals from their rim inwards; in places it completely pseudomorphs olivine.

5.3 Petrography of volcano-sedimentary (chert) rocks

The lowermost chert, KC_1-64a, consists of ca. 70% massive silica-rich section, ca. 20% carbonaceous matter and ca. 10% carbonate grains. The carbonate grains are brown, rhombohedral and form lengths of ca. 0.219 mm. They are found in between the carbonaceous matter crosscut by late-stage silica-rich veins. The carbonaceous matter is black and comprises wispy grains and smaller peloids that have been amalgamated thus forming composite grains (**Figure 5.6a-c**). The composite grains vary in shape, from irregular to ellipsoidal, and form lengths of ca. 0.182 mm. A large ellipsoidal composite grain (ca. 1.24 mm) is observed crosscut by silica-rich veins. The wispy grains are observed forming a network in a silica-rich cement, parallel to the laminae. They have a ca. 0.021 mm short axis and ca. 0.212 mm long axis. The carbonaceous matter (including both the wispy grains and composite grains) is observed enclosed by botryoidal silica.

The chert, KC_2-56a (**Figure 5.6d**), is a microcrystalline black and laminated chert. It consists of silica-rich and carbonaceous laminae. The silica-rich laminae comprise disseminated peloids, whereas the carbonaceous laminae are massive in places and comprises carbonaceous matter, disseminated carbonate grains and disseminated magnetite in places. Magnetite is disseminated in the massive carbonaceous and silica-rich laminae with single, ca. 0.248 mm euhedral grain of magnetite observed disseminated in a thin wavy carbonaceous lamina. Carbonate grains are brown, rhombohedral and are concentrically zoned. They form lengths between ca. 0.229 mm and 0.408 mm. They are found embedded in a thick carbonaceous lamina. A cavity is observed in between the thick carbonaceous lamina. It comprises quartz crystals that coarsen towards the core. Carbonaceous matter is observed forming a composite grain with lengths of up to 0.2 µm.

KC_3-27 **(Figure 5.6e**) is a black and white layered chert comprising thick and thin carbonate bands, magnetite, siderite and various cross-cutting veins. The silica cement forms laminations where disseminated carbonate grains are found. A thick layer of carbonate is found forming a band. It is pinkish brown with black opaque magnetite, and siderite, a golden-brown mineral forming in between the carbonate band. A thick carbonaceous lamina

is observed. The carbonaceous bands are separated by quartz cavities. These cavities have coarse-grained quartz in their core. The cavities are also observed, in a much smaller scale, in the silica-rich cement. $KC_4$26 (**Figure 5.6f-g**) comprises disseminated organics and a thick band of organics in a silica-rich cement. The organics are black brown. A vein concentrated with organic carbonate grains runs through the rock. The rock is not laminated.

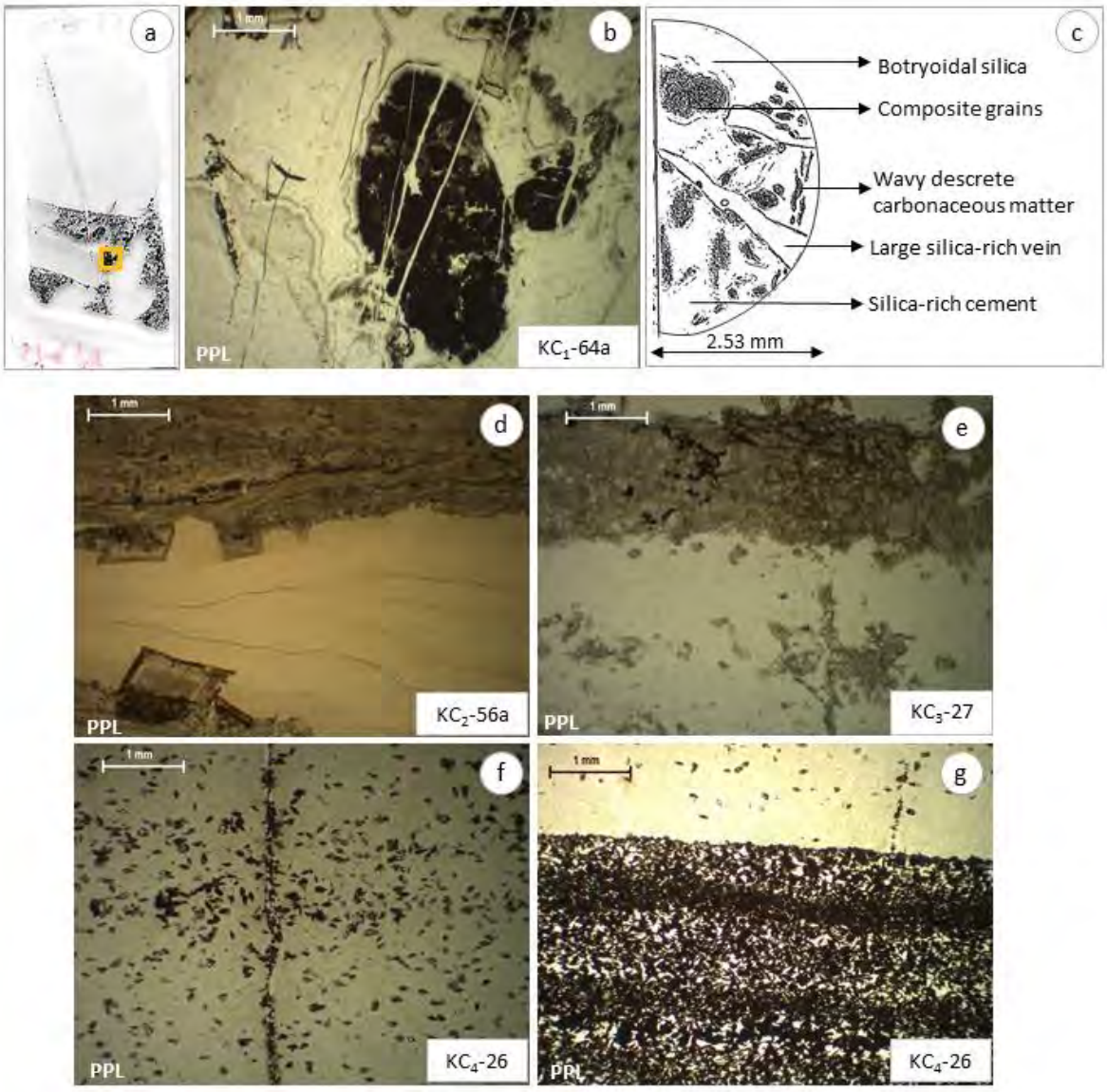

Figure 5. 6*: Photomicrographs of the four chert horizons of the Kromberg type-section in plain-polarised light. (a) shows a thin section of lowermost KC_1-64a chert and the location from which photomicrograph (b) was taken and (c) is its labelled sketch drawing. (d)-(g) shows photomicrographs of the upper chert horizons. Descriptions of these photomicrographs are provided in the text.*

5.4 Summary

Table 5. 1*: A summary of different rock groups that occur in the Kromberg type-section and the different textures observed.*

Rock name	Igneous minerals	Alteration minerals	Overall texture
Komatiitic basalt	pyroxene, iron-oxide (magnetite)	actinolite, chlorite, titanite, quartz ± carbonate	Interstitial
Partially chloritized tholeiitic basalt	pyroxene, plagioclase	chlorite, titanite, quartz ± carbonate ± epidote	Porphyritic and subophitic
Partially silicified tholeiitic basalt	pyroxene, plagioclase ± quartz	actinolite, titanite, chlorite, ± quartz ± epidote ± sericite ± carbonate	Intersertal and subophitic
Highly chloritized tholeiitic basalt	plagioclase ± pyroxene ± altered glass	Chlorite, titanite ± actinolite ± quartz ± carbonate	Ophitic, porphyritic and intersertal
Highly silicified tholeiitic basalt	pyroxene	quartz ± epidote	Aphyric
Poikilitic wehrlite (cumulate peridotite)	pyroxene, olivine, magnetite	actinolite, serpentine, chlorite ± titanite	Orthocumulate
Metadunite	olivine	magnetite, lizardite and chrysotile	Mesocumulate

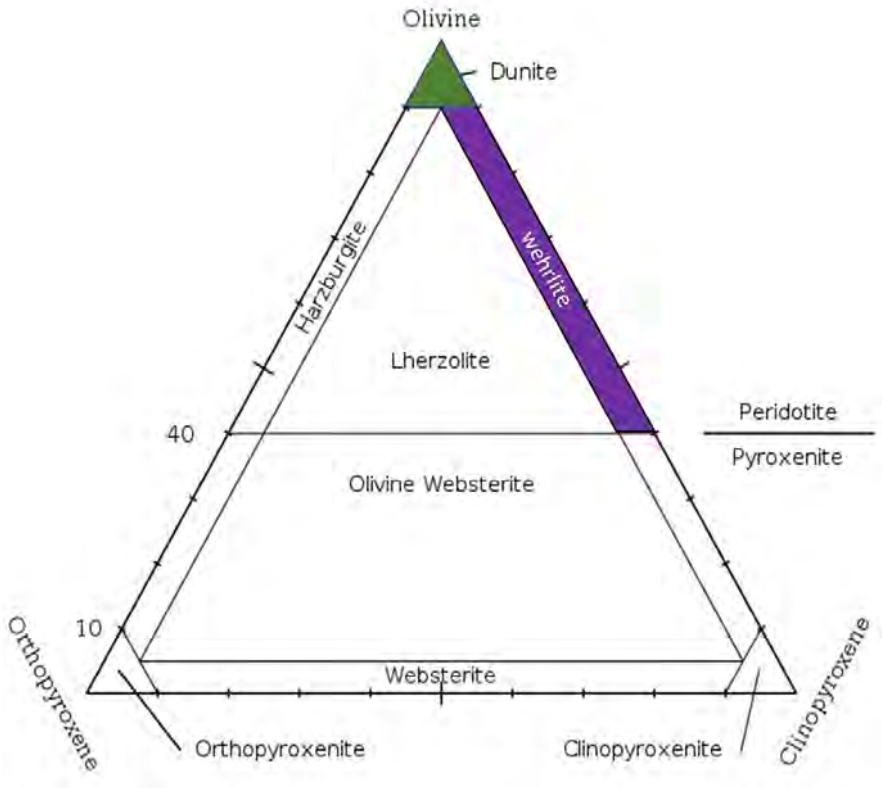

Figure 5. 7*: A classification diagram after (Le Maitre et al., 2002) that was used to classify cumulate rocks of the Kromberg type-section. The dunite field (in green) comprises more than 90% olivine crystals and the wehrlite comprises 40-90% olivine crystals.*

The silicified volcano-sedimentary rocks analysed for petrography are different chert horizons that cap volcanic rocks of the Kromberg type-section. These chert horizons display different textures depending on their locality in the volcanic architecture. The lowermost chert horizon, KC_1-64a comprises composite grains enclosed by botryoidal silica while KC_2-56a and KC_3-27 comprises organics and carbonate. KC_4-26 comprises organics forming a thick band and disseminated in a silica-rich cement. **Table 5.1** shows the different textures of the meta-igneous rocks observed in the mid-lower Kromberg type-section. These meta-igneous rocks are described based on the igneous textures preserved. Although low-grade metamorphism is recorded by the Kromberg type-section (see Grosch et al., 2012), more than 50% of the volcanic rocks have been affected by secondary alteration processes. Thus, depending on the extent of alteration, different rock samples are grouped in accordance with their protolith mineralogy, texture and alteration, e.g. highly chloritized tholeiitic metabasalts and partially chloritized tholeiitic metabasalts.

Komatiitic basalts are reported as medium-grained, interstitial rocks with a moderately low degree alteration. They have interlocking pyroxene crystals that are replaced by chlorite and actinolite. Quartz, calcite and titanite are interstitial forming groundmass aggregates replacing interstitial igneous matrix. Cumulate peridotites are orthocumulate rocks with a poikilitic texture where olivine forms smaller chadacrysts and pyroxene forms oikocrysts. They have ca. 50% olivine, ca. 40% pyroxene crystals and c. 10% alteration minerals. In a ternary classification diagram, after Le Maitre et al. (2002), the cumulate peridotites plot on wehrlite field (**Figure 5.7, Table 5.1**). Some cumulate peridotites are reported as affected by low degree of alteration while others are moderately altered.

Partially altered cumulate peridotites preserve most of their igneous textures while moderately altered cumulate peridotites preserve few primary igneous textures. All cumulate peridotitic rocks of the Kromberg type-section are partially serpentinized and chloritized. Partially chloritized tholeiitic metabasalts have either a subophitic, intersertal or a porphyritic texture. Their pyroxene crystals are partially replaced along its rims by actinolite. In places pyroxene is also replaced by chlorite. Epidote and sericite form alteration minerals replacing plagioclase. Highly chloritized tholeiites are either subophitic or slightly porphyritic. They are fine- to medium-grained and comprise plagioclase, pyroxene, chlorite, epidote and titanite. Some samples have an altered glassy groundmass. Partially silicified rocks are fine- to very fine-grained and comprise uralitized pyroxene, moderately sericitized plagioclase and epidote replacing plagioclase crystals, whereas while igneous minerals of highly silicified tholeiites are completely overprinted. Silicification and chloritization has resulted in their greyish colour and their fine-grained texture. The metadunite sample is also reported as highly serpentinized with very no igneous minerals preserved. It comprises more than 95% serpentinized olivine crystals (**Figure 5.7**).

6 Mineral chemistry

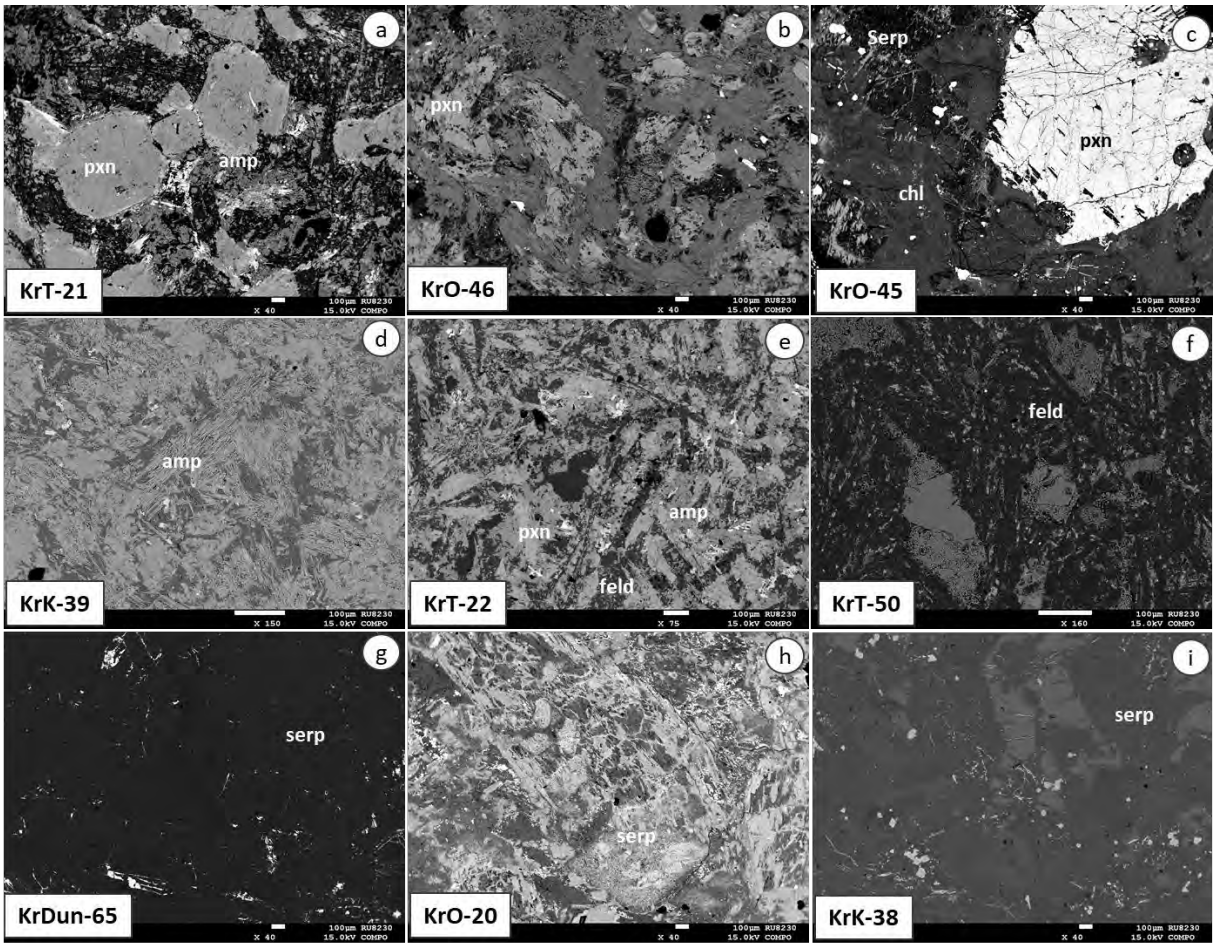

Backscattered images of the analysed rock samples for microprobe analyses. (a) A partially chloritized basalt which was analysed for relic pyroxene cores and amphibole replacing pyroxene along its rims. (b) A komatiitic basalt analysed for its interlocking pyroxene crystals. (c) A cumulate peridotite analysed for pyroxene, serpentine and chlorite, (d) and (f) are partially silicified tholeiitic basalts analysed for amphibole and feldspar. (e) A partially chloritized tholeiitic basalt analysed for pyroxene, amphiboles and feldspar. (g) A metadunite analysed for serpentine, and (h) and (i) are cumulate peridotites analysed for serpentine. Pxn=pyroxene, amp=amphibole, serp=serpentine, chlo=chlorite and feld=felspar.

6.1 Introduction and methods

Quantitative compositional analyses of minerals from selected altered mafic and ultramafic rocks were obtained using four wavelength dispersive spectrometers on a JEOL JXA-8230

electron probe micro-analyser at the Geology Department, Rhodes University. The analytical setup and technical assistance were provided for by Dr. Deon van Niekerk. The beam was generated by a Tungsten cathode, and excited with 15kV accelerating potentials at beam currents of either 2- or 20nA depending on the sensitivity of the minerals to beam damage. Beam sizes between 1 through 10 μm were used depending on the beam sensitivity of the material. All elements were measured on K-alpha peaks. Counting times on peak were 10s (except 15s for serpentine), and 10s total (except 15s for serpentine) on background. For intensity calibration, commercial "SPI" standards were used. The standards were Kaersutite (Al), Pyrope (Si, Mg, Fe), Albite (Na), Rhodonite (Mn), Rutile (Ti), Ni-metal (Ni), Olivine (Ni), Plagioclase (Ca), Cr_2O_3 (Cr), and Orthoclase (K). The data was collected with JEOL software (PC EPMA 1.9.2.0), and its ZAF matrix algorithm (Heinrich/Duncumb-Reed with FFAST-2005 MACs) was applied to correct for differential matrix effects. Oxygen was calculated by stoichiometry and H_2O by difference before the correction. Potential analytical drift was monitored for by interspersing secondary standards during the analyses. Samples were polished before analyses, and vacuum carbon coated to 25 nm (+/-5) thickness. The minerals analysed included olivine, pyroxene, felspar minerals, amphibole, chlorite and serpentine. The Kromberg type-section has a wide variety of minerals (see **Petrography Chapter 5**); due to laboratory time limitations, only the minerals, aforementioned, were analysed. The selected rock samples analysed are KrK-21, KrST-22, KrO-46, KrDun-65, KrT-39, KrO-45, KrT-50, KrK-38 and KrT-44.

6.2 Pyroxene

Rock samples analysed for pyroxene are KrO-45, KrO-46, KrK-21 and KrST-22. Their structural formula is calculated on the basis of 6 oxygen atoms (**Table 6.1**). The Fe^{3+} was calculated using a method by Droop (1987). Where a negative Fe^{3+} arose, all iron was assigned as ferrous (Fe^{2+}). As reported in the Petrography Chapter 6, pyroxene crystals are partially uralitized to amphibole. Relic igneous pyroxene was noted to usually be preserved in its crystal cores. It is therefore possible that the mineral compositions obtained for the pyroxene crystals analysed comprises mixed compositions because of the presence of amphibole (actinolite) alteration. A ternary diagram after Morimo (1988) is used for the classification of pyroxene mineral (**Figure 6.1a**). Pyroxene mineral composition analyses are

plotted based on three endmember compositions: Mg-rich enstatite, Fe-rich ferrosillite and Ca-rich wollastonite. On the ternary diagram, relatively fresh pyroxene crystals in the Kromberg type-section are augitic clinopyroxenes (**Figure 6.1a**). End-member compositions for KrO-45 are En (49.91-51.76%), Fs (9.89-11.05%) and Wo (38.27-39.17%); KrO-46: En (48.48-50.45%), Fs (8.68-10.39%) and Wo (39.14-40.83%); KrK-21: En (46.12-48.65%), Fs (12.45-14.85%) and Wo (36.30-41.43%); and KrST-22: En (32.79-38.92%), Fs (21.84-27.87%) and Wo (36.75-41.36%). Data comparison is compared to the study by Vennemann and Smith (1999) in the SE limb of the Kromberg type-section. In their study, the authors reported tholeiitic basalts, cumulate and komatiitic clinopyroxene as having sub-calcic augite and diopside compositions and concluded a basaltic magma origin. **Figure 6.1a** shows the compositions from this study as comparable with the study of Vennemann and Smith (1999), but a wider range in augitic compositions is observed in the current study.

6.3 Plagioclase

In this section KrT-50 and KrST-22 plagioclase crystals are analysed. The plagioclase crystals of the Kromberg type-section have been reported in preceding chapters as altered to albite. Structural formula is calculated based on 23 oxygen atoms (**Table 6.2, Appendix A3**). The Si content for sample KrT-50 is 11.78-12.33 apfu, the total Al 3.60-4.12 apfu, Na 3.43-3.88 apfu and Ca 0.06-0.12 apfu. Sample KrST-22 has Si compositions between 11.29 and 11.61 apfu, total Al between 4.15 and 4.77 apfu, Na between 3.00 and 3.80 apfu, and Ca between 0.11 and 0.42 apfu. A ternary diagram after Smith and Brown (1988) is plotted for the classification of plagioclase crystals analysed. The diagram makes use of three end-member compositions namely: Na-rich albite, Ca-rich anorthite and K-rich orthoclase (**Figure 6.1b**). The Kromberg type-section data have compositions between albite and orthoclase end-member compositions. They classify mineralogically as alkali feldspar. The An-Ab-Or end-member compositions for these rocks range between An = 2.81-10.90, Ab = 80.59-96.50 and Or = 0.69 -29.23 apfu for KrST-22 and An = 1.47-12.67, Ab =86.47-98.05 and Or = 0.44-6.77 for KrT-50. Sample KrT-50 comprises pure albite, plotting towards the apex in the albite field while KrST-22 data is distributed between albite and anorthoclase, a high potassian albite. These albitic compositions are due to hydrothermal alteration.

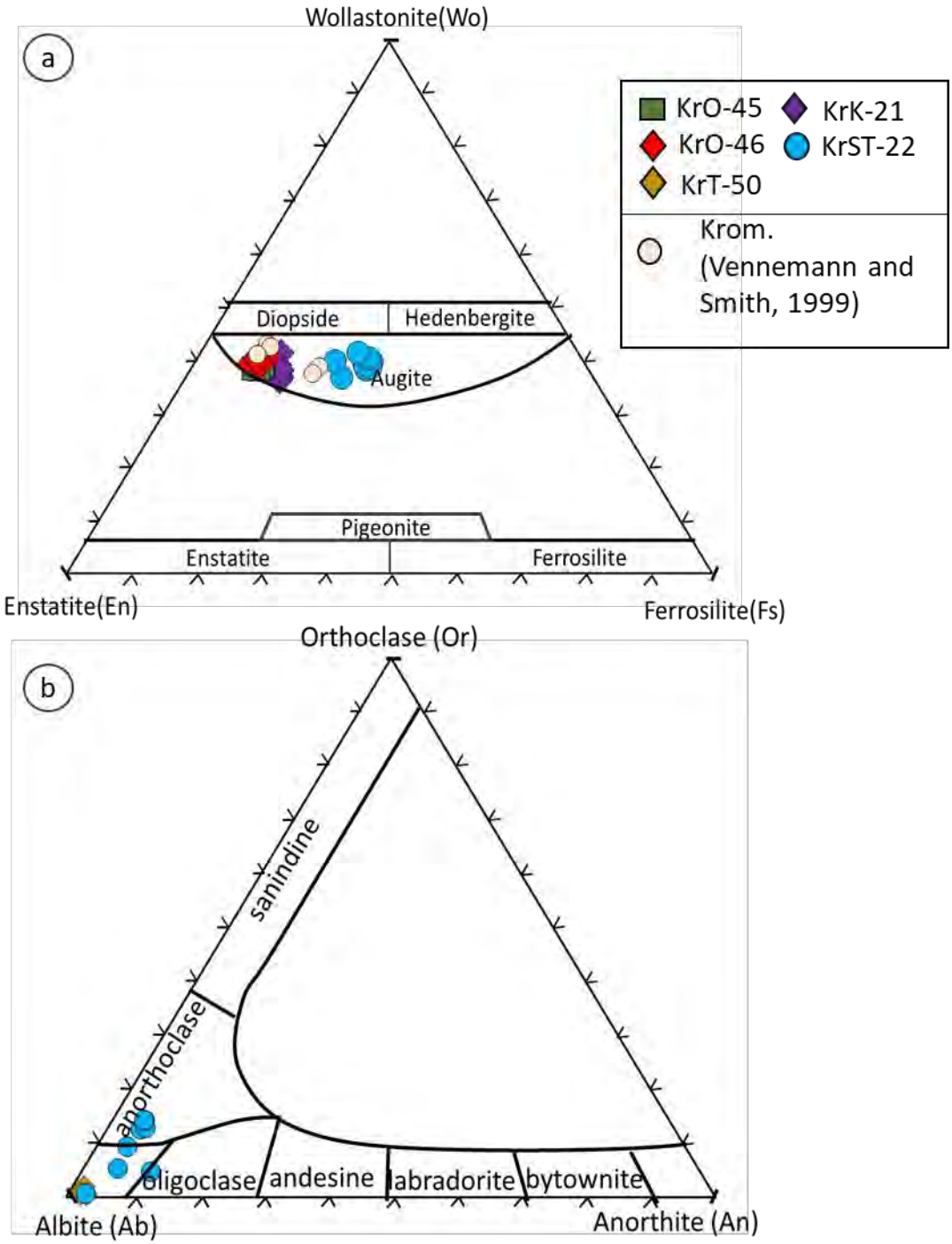

***Figure 6.1**: (a) A Mg-Ca-Fe pyroxene ternary diagram modified after Morimoto (1988). The pyroxene analysed in the Kromberg type-section is augitic. Data from Vennemann and Smith (1999) on their study in the Kromberg type-section is used and compared to data in this study. (b) An Ab-Or-An feldspar ternary diagram modified after Smith and Brown (1988) showing Kromberg type-section rocks plotting in the albite and anorthoclase field.*

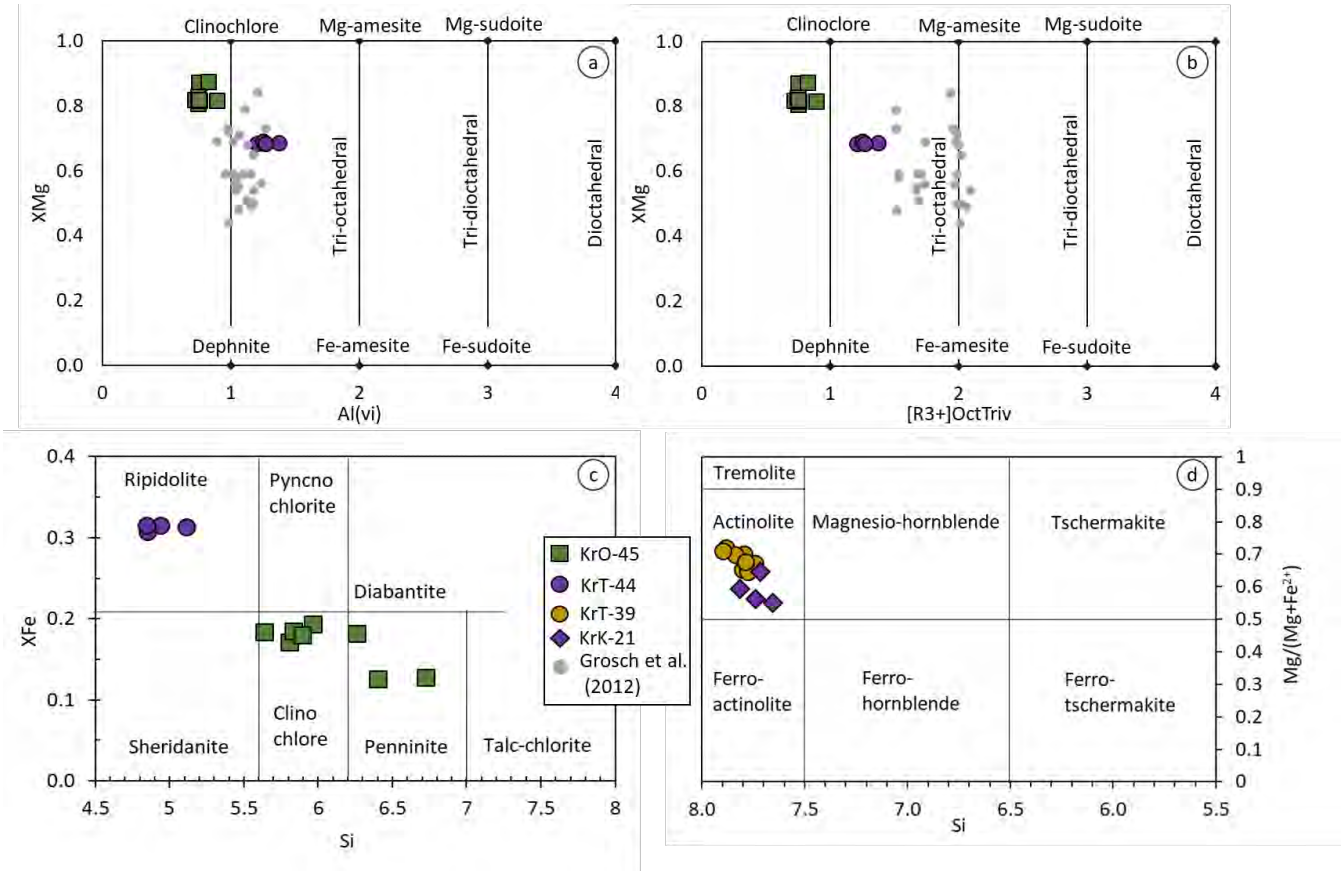

Figure 6.2*: (a)-(b) are classification diagrams for chlorite modified after Bailey (1988). Kromberg data in this study is compared to the study by Grosch et al. (2012) who studied the upper and lower part of the Kromberg type-section in the SE limb of the OAF. (c) a chlorite classification diagram modified after Hey (1954); chlorite fields from altered oceanic crust after et al. (1996). (d) is a classification diagram for calcic amphiboles modified after Leake et al. (1997).*

6.4 Chlorite

Two samples have been analysed for chlorite in the Kromberg type-section; sample KrO-45 (a partially altered cumulate peridotite) and sample KrT-44 (a tholeiitic metabasalt). Across the Kromberg type-section, chlorite is ubiquitous. The structural formula for chlorites was calculated based on 14 oxygen atoms (**Table 6.3, Appendix A3**). The sum of Ca, Na and K differs for both samples. Sample KrT-44 has a cationic sum less than 0.08 apfu, ruling out smectite and other clay mineral contamination, whereas KrO-45 has some analyses with cationic sum greater than 0.08 apfu. Sample KrK-44 has Si content between 2.83 and 2.98 apfu, Mg between 2.98 and 3.23 apfu and Fe^{2+} between 1.36 and 1.48. The Fe^{3+} calculation adopted for al chlorite analysis that by Droop (1987), and for all chlorite analyses all iron

present is ferrous. KrO-45 has Si content between 3.29 and 3.92 apfu, Fe^{2+} between 0.60 and 0.98 apfu and Mg between 4.03 and 4.20 apfu. Two classification

Table 6. 1*: Representative pyroxene compositional electron microprobe analyses in rocks of the Kromberg type-section. All oxides are in wt.%.*

	Kr21-12	**Kr21-14**	**Kr22-1**	**Kr22-2**	**Kr46-13**	**Kr46-14**	**Kr45-5**	**Kr45-6**
SiO_2	51.76	52.20	49.59	50.26	53.13	52.01	53.22	52.13
TiO_2	0.40	0.44	0.65	0.37	0.41	0.35	0.23	0.34
Al_2O_3	2.32	2.48	2.80	1.33	2.33	2.74	1.96	2.56
Cr_2O_3	0.53	0.28	0.02	0.05	0.44	0.71	1.04	0.90
Fe_2O_3	0.00	0.00	1.82	1.08	0.00	0.00	0.00	0.00
FeO	7.41	8.35	12.85	15.12	5.48	5.60	5.64	6.15
MnO	0.18	0.22	0.26	0.37	0.13	0.11	0.16	0.13
MgO	15.81	16.48	13.23	11.63	17.73	17.42	17.97	17.25
CaO	19.76	18.43	17.38	18.01	19.72	19.27	19.09	18.83
Na_2O	0.23	0.22	0.19	0.24	0.14	0.17	0.20	0.21
K_2O	0.03	0.03	0.02	0.02	0.04	0.03	0.00	0.03
NiO	0.00	0.05	0.00	0.00	0.00	0.04	0.08	0.00
Total	98.43	99.17	98.82	98.46	99.54	98.46	99.59	98.52
Formula			No. of cations on the basis of 6 oxygen atoms					
Si	1.94	1.94	1.90	1.95	1.95	1.93	1.95	1.94
Ti	0.01	0.01	0.02	0.01	0.01	0.01	0.01	0.01
Al	0.10	0.11	0.13	0.06	0.10	0.12	0.08	0.11
Cr	0.02	0.01	0.00	0.00	0.01	0.02	0.03	0.03
Fe(III)	0.00	0.00	0.05	0.03	0.00	0.00	0.00	0.00
Fe(II)	0.23	0.26	0.41	0.49	0.19	0.18	0.19	0.20
Mn	0.01	0.01	0.01	0.01	0.00	0.00	0.01	0.00
Mg	0.88	0.91	0.76	0.67	0.97	0.96	0.98	0.96
Ca	0.79	0.73	0.71	0.75	0.77	0.77	0.75	0.75
Na	0.02	0.02	0.01	0.02	0.01	0.01	0.01	0.02
K	0.00	0.00	0.00	0.00	0.00	0.00	0.00	0.00
Ni	0.00	0.00	0.00	0.00	0.00	0.00	0.00	0.00
tot.	4.00	4.00	4.00	4.00	4.00	4.00	4.02	4.01
End-member								
Fe	12.43	13.93	24.34	27.32	8.98	9.29	9.32	10.27
Ca	41.44	38.35	36.75	38.27	40.44	40.17	39.26	39.45
Mg	46.13	47.72	38.91	34.41	50.58	50.54	51.42	50.29
Total	100.00	100.00	100.00	100.00	100.00	100.00	100.00	100.00

***Table 6. 2**: Representative plagioclase compositional microprobe analyses in rocks of the Kromberg type-section. All oxides are in wt.%.*

	Kr50-1	**Kr50-2**	**Kr50-12**	**Kr50-14**	**Kr22-1**	**Kr22-6**	**Kr22-7**	**Kr22-9**
SiO_2	68.44	67.61	68.36	72.31	64.53	66.15	67.58	65.61
TiO_2	0.34	0.00	0.06	0.19	0.05	0.00	0.00	0.06
Al_2O_3	18.84	19.22	20.26	17.91	22.69	21.78	21.81	22.37
FeO	0.17	1.50	1.10	0.12	0.87	0.80	0.46	0.56
CaO	0.62	0.41	0.33	0.44	1.10	2.28	1.15	1.02
Na_2O	11.43	11.02	10.95	10.39	9.24	9.74	10.36	9.70
K_2O	0.11	0.20	0.20	0.18	2.15	0.82	0.91	1.61
MgO	0.00	0.55	0.37	0.02	0.26	0.06	0.10	0.17
BaO	0.03	0.00	0.00	0.00	0.00	0.01	0.00	0.02
F	0.00	0.00	0.07	0.04	0.00	0.00	0.00	0.00
SrO	0.33	0.32	0.40	0.43	0.34	0.40	0.40	0.40
Total	100.32	100.83	102.09	102.02	101.22	102.04	102.77	101.52
Formula			No. of cations on the basis of 32 oxygen atoms					
Si	11.98	11.84	11.79	12.33	11.34	11.49	11.61	11.45
Ti	0.04	0.00	0.01	0.02	0.01	0.00	0.00	0.01
Al	3.89	3.97	4.12	3.60	4.70	4.46	4.41	4.60
Fe(II)	0.03	0.22	0.16	0.02	0.13	0.12	0.07	0.08
Ca	0.12	0.08	0.06	0.08	0.21	0.42	0.21	0.19
Na	3.88	3.74	3.66	3.43	3.15	3.28	3.45	3.28
K	0.02	0.05	0.04	0.04	0.48	0.18	0.20	0.36
Mg	0.00	0.14	0.09	0.00	0.07	0.02	0.03	0.04
Ba	0.00	0.00	0.00	0.00	0.00	0.00	0.00	0.00
F	0.00	0.00	0.04	0.02	0.00	0.00	0.00	0.00
Sr	0.03	0.03	0.04	0.04	0.03	0.04	0.04	0.04
Total	19.99	20.07	20.02	19.59	20.12	20.01	20.01	20.06
An	2.89	2.00	1.63	2.27	5.38	10.90	5.49	4.95
Or	0.60	1.17	1.14	1.12	12.55	4.66	5.19	9.37
Ab	96.51	96.83	97.23	96.61	82.07	84.44	89.32	85.68

Table 6. 3*: Representative chlorite compositional microprobe analyses in rocks of the Kromberg type-section. All oxides are in wt.%.*

	Kr44-2	Kr44-5	Kr44-6	Kr44-7	Kr45-18	Kr45-19	Kr45-20	Kr45-21
SiO_2	28.84	30.32	28.39	28.26	34.16	35.14	35.79	35.34
TiO_2	0.00	0.00	0.00	0.00	0.00	0.00	0.00	0.00
Al_2O_3	19.75	20.62	20.62	20.73	14.13	11.97	11.07	11.92
Fe_2O_3	0.00	0.00	0.00	0.00	0.00	0.00	0.00	0.00
FeO	17.73	16.52	17.27	17.55	11.27	10.97	12.11	11.71
MnO	0.35	0.31	0.27	0.24	0.12	0.07	0.13	0.06
MgO	21.59	20.34	21.76	21.38	28.08	29.74	28.33	29.07
CaO	0.06	0.12	0.08	0.08	0.63	0.10	0.15	0.11
Na_2O	0.06	0.65	0.05	0.03	0.04	0.05	0.06	0.04
K_2O	0.05	0.06	0.03	0.02	0.13	0.07	0.20	0.25
Cr_2O_3	0.10	0.05	0.00	0.00	0.00	0.06	0.06	0.06
Total	88.52	88.98	88.47	88.28	88.55	88.17	87.89	88.56
Formula	No. of cations on the basis of 14 oxygen atoms							
Si	2.88	2.98	2.83	2.83	3.29	3.39	3.48	3.40
Al(iv)	1.12	1.02	1.17	1.17	0.71	0.61	0.52	0.60
T site	4.00	4.00	4.00	4.00	4.00	4.00	4.00	4.00
Al(vi)	1.20	1.37	1.25	1.27	0.89	0.75	0.75	0.76
Fe(III)	0.00	0.00	0.00	0.00	0.00	0.00	0.00	0.00
Ti	0.00	0.00	0.00	0.00	0.00	0.00	0.00	0.00
Mg	3.22	2.98	3.23	3.19	4.03	4.27	4.10	4.18
Fe(II)	1.48	1.36	1.44	1.47	0.91	0.88	0.98	0.94
Mn	0.03	0.03	0.02	0.02	0.01	0.01	0.01	0.00
Ca	0.01	0.01	0.01	0.01	0.06	0.01	0.02	0.01
Na	0.01	0.12	0.01	0.01	0.01	0.01	0.01	0.01
K	0.01	0.01	0.00	0.00	0.02	0.01	0.03	0.03
Cr(III)	0.01	0.00	0.00	0.00	0.00	0.00	0.00	0.00
O site	5.96	5.89	5.97	5.96	5.92	5.94	5.90	5.94
$[R^{3+}]$OctTriv	1.20	1.37	1.25	1.27	0.89	0.75	0.75	0.76
XMg	0.68	0.69	0.69	0.68	0.82	0.83	0.81	0.82
X Fe	0.32	0.31	0.31	0.32	0.18	0.17	0.19	0.18
non-interlayer	9.93	9.74	9.94	9.94	9.84	9.91	9.85	9.88
Al (tot)	2.32	2.39	2.42	2.44	1.60	1.36	1.27	1.35
Al(iv)	1.12	1.02	1.17	1.17	0.71	0.61	0.52	0.60
x (Chl)	0.94	0.76	0.95	0.95	0.85	0.92	0.86	0.89

[R3+]OctTriv = sum of trivalent cations in octahedral sites, XMg = (Mg^{2+}/Mg + Fe^{2+}), XFe = (Fe/Mg + Fe)

***Table 6. 4**: Representative amphibole (actinolite) compositional microprobe analyses in rocks of the Kromberg type-section. Oxides are in wt.%.*

	Kr39-1	**Kr39-2**	**Kr39-4**	**Kr21-10**	**Kr21-11**	**Kr21-6**
SiO_2	53.22	53.73	54.10	52.48	52.47	51.38
TiO_2	0.37	0.19	0.00	0.09	0.07	0.00
Al_2O_3	2.30	1.45	1.09	1.73	1.67	3.64
FeO	12.95	12.21	11.34	14.22	16.23	17.00
MnO	0.35	0.26	0.22	0.20	0.24	0.17
MgO	14.97	16.00	16.29	14.55	13.24	11.73
CaO	12.24	12.82	12.74	13.10	11.84	12.02
Na_2O	0.38	0.19	0.09	0.10	0.10	0.30
K_2O	0.23	0.07	0.06	0.05	0.08	0.16
Cr_2O_3	0.00	0.00		0.24	0.02	0.03
NiO	0.00	0.00		0.08	0.06	0.00
Total	97.01	96.92	95.92	96.82	96.01	96.43
Formula	No. of cations on the basis of 23 oxygen atoms					
Si	7.74	7.79	7.88	7.72	7.82	7.66
Al(iv)	0.26	0.21	0.12	0.28	0.18	0.34
T site	**8.00**	**8.00**	**8.00**	**8.00**	**8.00**	**8.00**
Al(vi)	0.14	0.04	0.07	0.02	0.11	0.30
Fe(III)	0.00	0.00	0.00	0.00	0.00	0.00
Ti	0.04	0.02	0.00	0.01	0.01	0.00
Mg	3.25	3.46	3.54	3.19	2.94	2.61
Fe(II)	1.58	1.48	1.38	1.75	1.94	2.10
Mn	0.00	0.00	0.00	0.00	0.00	0.00
Cr	0.00	0.00	0.00	0.03	0.00	0.00
Ni	0.00	0.00	0.00	0.01	0.01	0.00
C site	**5.00**	**5.00**	**4.99**	**5.00**	**5.00**	**5.00**
Fe(II)	0.00	0.00	0.00	0.00	0.08	0.02
Mn	0.04	0.03	0.03	0.02	0.03	0.02
Ca	1.91	1.99	1.99	2.06	1.89	1.92
Na	0.00	0.00	0.00	0.00	0.00	0.00
B site	**1.95**	**2.03**	**2.02**	**2.09**	**2.00**	**1.96**
Ca	0.00	0.00	0.00	0.00	0.00	0.00
Na	0.11	0.05	0.03	0.03	0.03	0.09
K	0.04	0.01	0.01	0.01	0.01	0.03
A site	**0.15**	**0.07**	**0.04**	**0.04**	**0.04**	**0.12**
Total	15.10	15.09	15.04	15.13	15.05	15.08
Mg/Mg+Fe	0.67	0.70	0.72	0.65	0.59	0.55

Table 6. 5*: Representative serpentine compositional microprobe analyses in rocks of the Kromberg type-section. All oxides are in wt.%.*

	Kr45-3	**Kr45-5**	**Kr65-1**	**Kr65-6**	**Kr38-1**	**Kr38-2**
SiO_2	41.23	41.05	41.76	42.72	42.31	42.65
Al_2O_3	2.15	2.28	1.64	1.75	1.28	1.75
TiO_2	0.00	0.00	0.00	0.00	0.00	0.17
MgO	30.12	32.29	39.32	39.79	36.34	35.64
FeO	12.39	11.51	3.94	3.19	8.70	7.17
MnO	0.18	0.16	0.00	0.00	0.25	0.08
CaO	0.14	0.00	0.00	0.08	0.05	0.18
Na_2O	0.14	0.00	0.00	0.00	0.07	0.00
K_2O	0.00	0.00	0.00	0.05	0.17	0.14
Cr_2O_3	0.17	0.14	0.35	0.51	0.00	0.15
NiO	0.62	0.32	0.00	0.20	0.00	0.58
Total	87.15	87.74	87.01	88.29	89.18	88.49
T site						
Si	33.52	32.97	32.57	32.73	32.99	33.26
Al	0.48	1.03	1.43	1.27	1.01	0.74
Total T	34.00	34.00	34.00	34.00	34.00	34.00
M site						
Al	1.58	1.12	0.07	0.31	0.17	0.86
Ti	0.00	0.00	0.00	0.00	0.00	0.10
Mg	36.51	38.66	45.72	45.45	42.24	41.43
Fe	8.43	7.73	2.57	2.05	5.67	4.67
Mn	0.13	0.11	0.00	0.00	0.17	0.05
Ca	0.13	0.00	0.00	0.06	0.04	0.15
Na	0.22	0.00	0.00	0.00	0.11	0.00
K	0.00	0.00	0.00	0.05	0.17	0.13
Cr	0.11	0.09	0.22	0.31	0.00	0.09
Ni	0.41	0.20	0.00	0.12	0.00	0.36
Total M	47.50	47.91	48.57	48.35	48.56	47.86

diagrams after Bailey (1988; **Figure 6.2a,b**) were used to determine the site occupancies of octahedral sites and chlorite end-members in the Kromberg type-section rocks. This diagram is a function of XMg [that is, Mg/(Mg+Fe)] against Al^{vi}, whereas the other is a function of XMg against $^{vi}[R^{3+}]$ (sum of trivalent cations in the octahedral site). Both samples have mineral compositions that classify as tri-octahedral chlorite. XMg is further used to determine whether they have Mg- or Fe-rich endmembers. Both rocks have Mg-rich endmember with KrO-45 consisting of Mg-clinochlore and KrK-44 comprising both Mg-clinochlore and Mg-amesite. When compared to the data by Grosch et al. (2012), chlorite in the lower part of the stratigraphy (this study) is more Mg-rich.

Hey's (1954) diagram was also used as a classification diagram for chlorite. This diagram is a function of XFe against Si (apfu). Hey's (1954) diagram assumes no ferric iron, classifies chlorite with ≥4.5 apfu Si content and calculates Si based on 24 oxygen atoms. Sample KrK-44 chlorite plots in the ripidolite field, whereas sample KrO-45 plots in the clinochlore and penninite field. The XFe [that is $Fe^{2+}/(Fe^{2+} + Mg)$] for sample KrK-44 chlorite is between 0.31 and 0.32, whereas that of KrO-45 is between 0.13 and 0.18. In Hey's (1954) diagram, amesite is not included. According to Bourdelle et al. (2013) three main substitutions occur in chlorites namely: Tschermak's Al^{iv} Al^{vi} – Si (Mg, Fe^{2+}), Fe^{2+} – Mg and di/trioctahedral 3(Mg, Fe^{2+}) – octahedral vacancy + 2 Al^{vi}. In sample KrK-44, the correlation coefficient between Mg and Al^{vi} is -0.94, between Al^{iv} and Si -1.00 and that between Mg and Fe^{2+} is 0.91. The reason for the 1:1 negative correlation between Si and tetrahedral Al is because Al^{iv} was obtained by difference. These correlation coefficients are in line with tschermak's substitution, where Al^{iv} substitute Si and Al^{vi} substitutes Mg and Fe^{2+} in the octahedral layer. This is different for sample KrO-45 which shows a weak negative correlation between Al^{vi} and Mg. A comparison was further conducted where data from the SE limb of the Kromberg type-section (Grosch et al., 2012) was plotted with data from this study. Chlorite compositional data from Grosch et al., (2012) has intermediate to high XMg, ranging between ca. 0.4 and 0.85 apfu and plotting in a trioctahedral field and a few samples plotting in a dioctahedral field (**Figure 6.2a-b**). The data from the current study is more Mg-rich plotting towards clinochlore, whereas the chlorite compositional data from Grosch et al. (2012) has a range of compositions between Mg-rich and Fe-rich chlorite.

6.5 Amphibole

Two rock samples were analysed for amphibole namely: KrT-39 and KrK-21. Structural formula was calculated on the basis of 23 oxygen atoms (**Table 6.4, Appendix A3**). The Fe^{3+} was calculated according to Leake et al. (1997). If this calculation yielded a negative value for ferric iron, all iron was assigned to Fe^{2+}. The Si (apfu) content in KrT-39 is between 7.74 and 7.79 apfu, Mg 3.02-3.54 apfu, Al^{vi} 0.04-0.28 apfu, Ca 1.81-2.03 apfu and Na 0.03-0.09. According to the amphibole nomenclature of Leake et al. (1997) the amphiboles classify as calcic with site B, Ca and Na greater than 1.00 apfu and site B, Ca greater than 1.50 apfu. Since the sum of site A, K and Ca is less than 0.5 apfu for all selected rock thin sections, an end-member classification diagram of actinolite, hornblende and tschermakite is used in **Figure 6.2**. This diagram is a function of XMg [that is Mg/(Mg+Fe)] against Si. All rock samples analyses have similar XMg plotting between 0.5 and 0.8. Both KrT-39 and KrK-21 amphibole compositions plot in the actinolite field. In the Kromberg type-section, the amphiboles present occur as replacing pyroxene. According to Howie et al. (1992) amphiboles have four main substitutions namely: Na – Ca, (Mg,Fe) – Al , A site introduction of Na(K) and Al – Si. In the analysed data, samples KrT-39 and KrK-21 show tschermak's substitution where a strong negative correlation exists between Al^{vi} and Mg and Al^{iv} and Si. The correlation coefficient of Al^{vi} and Si in both rocks is -1.00 due to structural formula calculation, whereas the correlation coefficient for Al^{vi} and Mg is -0.85 and -0.99 for KrT-39 and KrK-21. Sample KrK-21 with high correlation coefficients has completely been affected by tschermakite substitution; its correlation coefficient between Na and Ca is -0.38. Sample KrT-39, on the other hand, is also affected by Ca replacement by Na. In addition to its high negative correlation for Al and Mg that represent Al replacement for Mg, there is also high negative correlation between Na and Ca of -0.95.

6.6 Serpentine

Three rock samples were analysed for serpentine namely, KrK-38, KrDun-65 and KrO-45. Their structural formula was calculated on the basis of 116 oxygen atoms (**Table 6.5**, **Appendix A3**). KrO-45 serpentines has Si (apfu) compositions between 32.78 and 33.97

apfu, Fe of 6.13-8.43 apfu and Mg of 36.3-39.25 apfu. Sample KrDun-65 serpentine compositions record the range 32.57-33.05 Si (apfu), 1.69-2.57 apfu Fe and 45.16-46.17 apfu

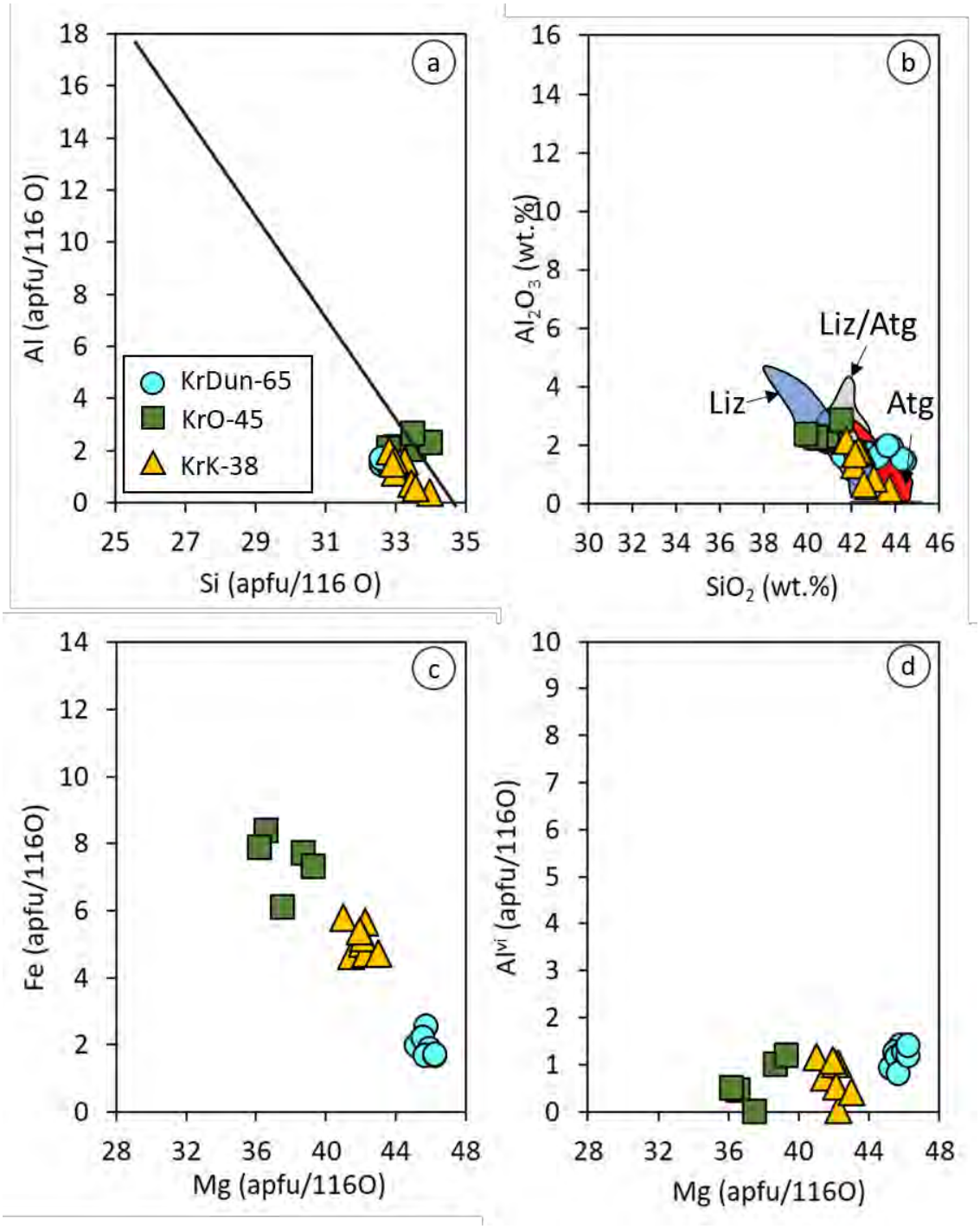

***Figure 6.3**: Binary plots that show serpentine compositions in altered rocks of the Kromberg type-section. Atg=antigorite field (in red), Liz=lizardite field (in blue) and Liz/Atg = mixture of antigorite and lizardite field (in grey). (a) is an Al versus Si plot and (b) Al_2O_3 versus SiO_2 plot which shows low Al and high silica for the serpentine minerals of the Kromberg type-section. (c)Shows Fe versus Mg plot and (d) shows an Al versus Mg plot.*

apfu Fe and 45.16-46.17 apfu Mg; and KrK-38 comprises 32.26-33.96 apfu Si, 4.72-5.80 apfu Fe and 40.98-42.99 apfu Mg. **Figure 6.3** shows binary plots for serpentine compositions. **Figure 6.3a** compares Al cation content to Si cation content. There is a negative correlation between Al and Si cation. All analysed compositions cluster in low Al content, less than 4 apfu. **Figure 6.3b** shows a binary plot of Al_2O_3 against SiO_2, and **Figure 6.3c-d** is a function of Fe and octahedral Al against Mg. A strong negative correction is observed in **Figure 6.3b,c**. According to Padrón-Navarta et al. (2013), in antigorite two Al cations substitute for Mg and Si cations through coupled exchanged, an exchange known as Tschermak's exchange. The strong negative correlation between octahedral Al and Mg accompanied by that of Fe and Mg indicates that as Al substitutes strongly for Mg and Fe. In **Figure 6.3b**, KrO-45, KrK-38 and KrDun-65 lie in the lizardite and antigorite mixed field with some KrO-45 data points plotting in the lizardite field and some KrDun-65 data points plotting in the antigorite field.

6.7 Summary

In this chapter, a microprobe analyses for pyroxene, feldspar, chlorite, amphiboles and serpentine was conducted. All pyroxene crystals analysed are augitic ranging from Mg-rich to intermediate Fe/Mg ratios. The feldspars analysed belong to the alkali feldspar group where all compositions are albitic. KrST-22 is reported having both pure albite and K-rich albite. Chlorite has Mg-rich compositions with KrO-45 comprising clinochlore and penninite and KrK-44 comprised ripidolite and a mixture of clinochlore and amesite. In comparison with chlorite compositional data from Grosch et al., (2012), the data in the current study from the mid-lower Kromberg type-section has more Mg-rich chlorite. The composition mixture between amesite and clinochlore represent Tschermakite substitution where Al substitutes for Mg and Fe. Tschermak's substitution is also present in calcic amphiboles with actinolitic compositions (KrT-39 and KrK-21). Serpentine was also analysed in KrDun-65, KrK-38 and KrO-45 in which a strong tschermak's substitution was observed between Al and (Mg, Fe). It was also discovered that the serpentine minerals altering KrO-45, KrK-38 and KrDun-65 is lizardite and antigorite. KrDun-65 is rich in SiO_2 and poor in Al_2O_3.

7 Geochemistry

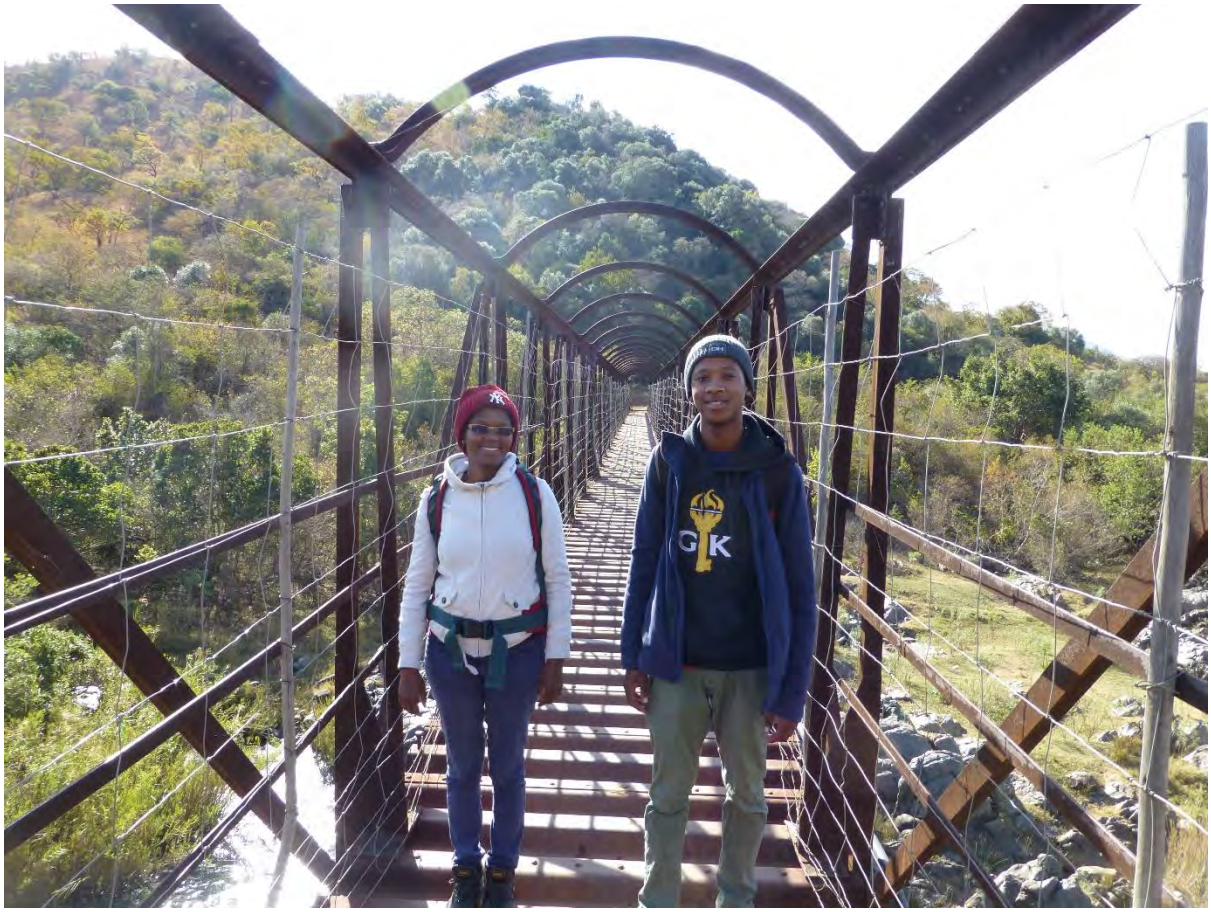

A bridge across the Komati river in the Songimvelo Nature Reserve. In the background of the photo are the mountains of the Kromberg type-section.

7.1 Major and trace elements analysis

7.1.1 Introduction

In this chapter major and trace element data are presented for 34 samples collected in the mid-lower part of the SE limb of the Kromberg type-section. Following fieldwork and petrography, different meta-igneous rock compositions of the Kromberg type-section are presented and screened for alteration. The mid-lower Kromberg type-section was estimated to preserve temperatures of the lowest sub-greenschist facies metamorphic conditions of T =

240 – 140 ºC (Grosch et al., 2012). Screening rocks for alteration assists in understanding protolith chemistry and igneous petrogenesis as once identified, relatively fresh rock compositions are used for classification and geodynamic modelling. Altered compositions are for this reason separated from relatively fresh compositions to (1) analyse the extent and style of alteration in the Kromberg type-section, (2) allow for geochemical classification and characterization using relatively fresh samples only, (3) observe crystallisation and geochemical history using relatively fresh compositions, and (4) to investigate the geodynamic setting of the Kromberg type-section rocks.

7.1.2 Analytical Methods

XRF analytical method: Analytical methodology and analysis courtesy of the Central Analytical Facilities laboratory manager, Riana Rossouw of Stellenbosch University. A total of 34 mafic-ultramafic samples of the mid-lower Kromberg type-section were crushed into a fine powder (particle size < 70 μm) with a jaw crusher and milled in a tungsten-carbide Zibb mill prior to the preparation of a fused disc for major and trace elements analysis. The jaw crusher and mill are cleaned with clean uncontaminated quartz between 2 samples to avoid cross contamination. Glass disks were prepared for XRF analysis using 7 g of high purity trace element and Rare Earth Element-free flux ($LiBO_2$ = 32.83%, $Li_2B_4O_7$ = 66.67%, LiI = 0.50%) mixed with 0.7g of the powder sample. Whole-rock major element compositions were determined by XRF spectrometry on a PAN analytical Axios Wavelength Dispersive spectrometer at the Central of Analytical Facilities, Stellenbosch University, South Africa. The spectrometer is fitted with a Rh tube and with the following analysing crystals: LIF200, LIF220, PE 002, Ge 111 and PX1. The instrument is fitted with a gas-flow proportional counter and a scintillation detector. The gas-flow proportional counter uses a 90% Argon-10% methane mixture of gas. Major elements were analysed on a fused glass disk using a 2.4kW Rhodium tube. Matrix effects in the samples were corrected for by applying theoretical alpha factors and measured line overlap factors to the raw intensities measured with the Super Q PANalytical software. The concentration of the control standards that were used in the calibration procedures for major element analyses fit the range of concentration of the samples. Amongst these standards were NIM-G (Granite from the Council for Mineral Technology, South Africa) and BE-N (Basalt from the International Working Group).

Laser Ablation ICP-MS: A Resolution 193nm Excimer laser from ASI connected to an Agilent 7700 ICP-MS is used in the analysis of trace elements in bulk rock samples as well as on single mineral grains. Ablation is performed in He gas at a flow rate of 0.35L/min, then mixed with argon (0.9L/min) and Nitrogen (0.004L/min) just before introduction into the ICP plasma. For traces in fusions, 2 spots of 100μm is ablated on each sample using a frequency of 10Hz and fluence of ~5J/cm2. Fusion disks prepared for XRF analysis by an automatic Claisse M4 Gas Fusion instrument and ultrapure Claisse Flux, using a ratio of 1:10 sample:flux, were coarsely crushed and a chip of sample mounted along with up to 12 other samples in a 2.4cm round resin disk. The mount was mapped, and then polished for analysis. Trace elements are quantified using NIST 612 for calibration and the % SiO_2 from XRF measurement as internal standard, using standard – sample bracketing. Two replicate measurements are made on each sample. The calibration standard was run every 12 samples. A quality control standard is run in the beginning of the sequence as well as with the calibration standards throughout. BCR-2 or BHVO 2G, both basaltic glass certified reference standards produced by USGS (Dr Steve Wilson, Denver, CO 80225), is used for this purpose. A fusion control standard from certified basaltic reference material (BCR-2, also from USGS) is also analysed in the beginning of a sequence to verify the effective ablation of fused material. Data processing was done using the LA-ICP-MS data reduction software package Iolite v.3.2 (Paton et al., 2011).

7.1.3 Alteration effects and integrated data screening

This section investigates alteration trends observed in the Kromberg type-section. Following fieldwork and petrography, four different rock compositions are classified in the Kromberg type-section namely: metadunite, cumulate peridotite, komatiitic basalt and tholeiitic basalt (**Table 7.1**). In this subsection komatiitic basalts are investigated with tholeiitic basalts to demonstrate the effect of alteration in the Kromberg type-section. Komatiitic basalts are shown in the subsequent subsections in classification diagrams specific for mafic to ultramafic greenstones (see subsection 7.1.4 and **Figure 7.5**). The metadunite composition (KrDun-65) is a heavily serpentinized ultramafic cumulate rock found in the lowermost Kromberg type-section stratigraphy (see **Petrography Chapter 5**) while cumulate peridotites (KrO-20, KrK-38 and KrT-45) are ultramafic sill intrusions with MgO content between 14 and 21 wt.% (**Figure 7.1**). Tholeiitic basalt compositions are extrusive rocks with MgO

contents between 4 and 12 wt.% (**Figure 7.1**). The tholeiitic basalt compositions have been sub-divided according to their alteration type and extent of alteration (based on field observations and petrography). Four sub-categories of tholeiitic compositions are classified namely: highly silicified tholeiites, partially silicified tholeiites, highly chloritized tholeiites and partially chloritized tholeiites. Highly silicified tholeiites are KrT-31B, KrT-32, KrT-33, KrT-34 and KrT-35. They are located directly beneath a ca. 50 m thick chert horizon KrC_3. Beneath the highly silicified tholeiites are partially silicified tholeiites (KrT-36, KrT-42, KrT-50, KrT-39, KrT-40, KrT-41, KrT-43 and KrT-44). They are also exposed in the western bank of the Komati River (see **Local Geology Chapter 3**).

To assess the effects of alteration in the Kromberg type-section rocks, major element diagrams are plotted in **Figure 7.1** to investigate the potential mobility of major elements. This is followed by trace element versus trace element plots (**Figure 7.2**) to assess potential changes in trace element compositions. In **Figure 7.1** mobile major elements (SiO_2, FeO total or FeO^T, K_2O, CaO and Na_2O) and one plot of an immobile major element (TiO_2) are plotted against MgO. Tholeiitic metabasalt compositions have the lowest MgO compositions compared to the metadunite and cumulate peridotites (**Figure 7.1**). Tholeiitic metabasalts are therefore more evolved than the other two rock compositions. According to **Figure 7.1a** highly silicified tholeiites have the highest SiO_2 (above 65 wt.%) content while partially silicified compositions have SiO_2 between 60 and 65 wt.%. Highly chloritized tholeiites have SiO_2 (wt.%) compositions between 45 and 52 wt.% while partially chloritized tholeiites have compositions between 42 and 53 wt. %. From this figure, the highly silicified tholeiites have the lowest MgO (wt.%) between 0 and 4 wt.% while highly chloritized tholeiites have MgO (wt.%) contents between 5 and 10 wt.%. The partially chloritized and partially silicified tholeiitic basalts have MgO compositions between 1 and 12 wt.% with partially silicified basaltic compositions having MgO contents between 3.0 and 10.4 wt.%. In this subsection, basaltic compositions are grouped according their geochemical alteration signatures. Partially chloritized tholeiitic basalts have MgO (wt.%) contents ranging between 3.6 and 20.5 wt.%, but this range includes komatiitic basalts (classified separately as a relatively fresh rock group and discussed in subsection 7.1.4). Silicification has therefore resulted in MgO mobility in some samples, depleting silicified basalts of MgO and enriching them with SiO_2. The SiO_2 content in chloritized basalts has not been heavily affected by chloritization (**Figure 7.1a**).

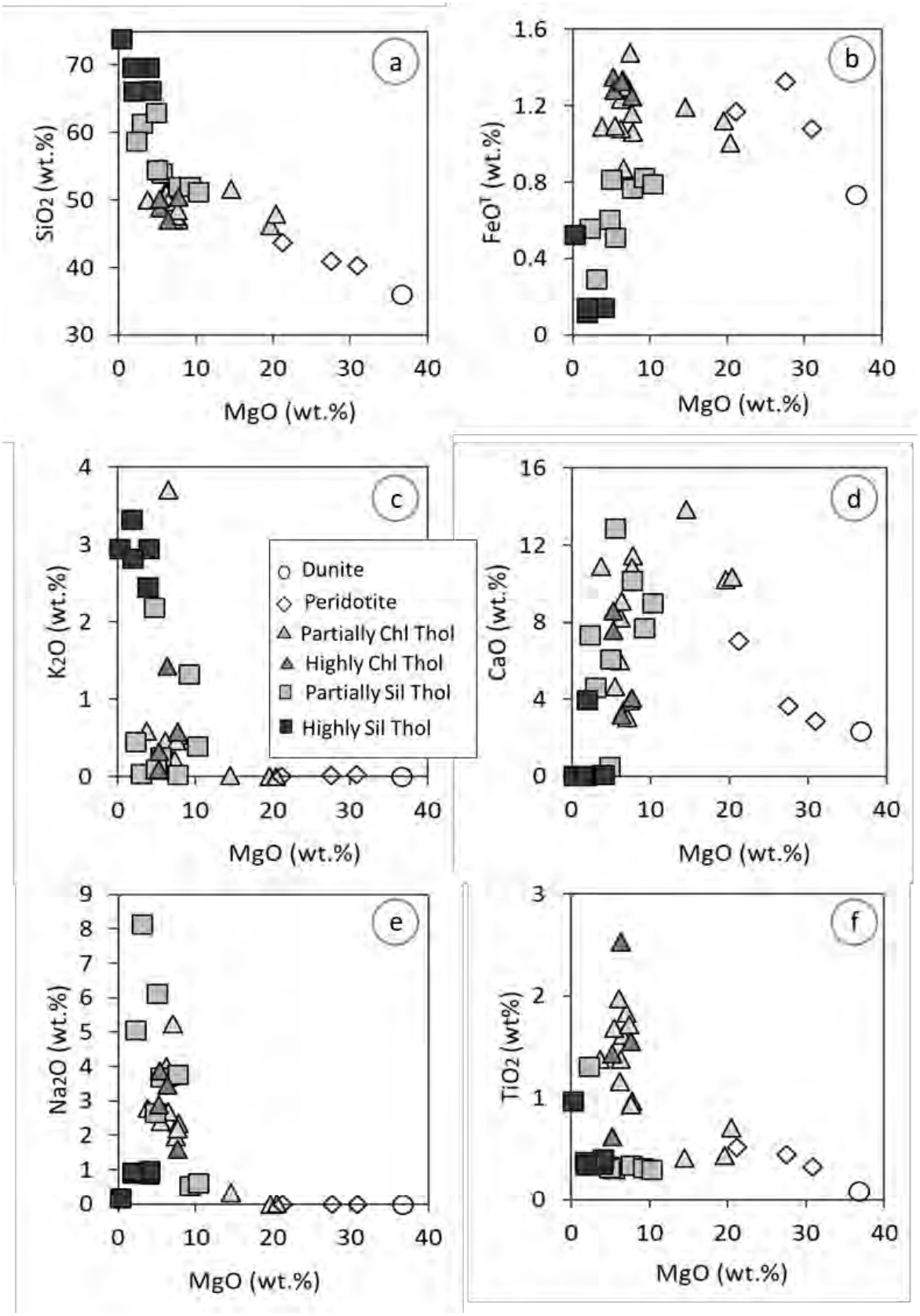

Figure 7. 1*: Major element versus MgO (wt.%) binary diagrams for all rock compositions of the Kromberg type-section. All major elements are recorded in weight percentage (wt.%). The 'Dunite' is a serpentinized metadunite rock. The cumulate peridotite consists of altered pyroxene and olivine.*

The MgO-FeO^T plot (**Figure 7.1b**) shows highly chloritized tholeiites to have high FeO^T compositions between 1.1 and 1.4 wt.% and highly silicified tholeiites to have contents between 0.1 and 0.5 wt.%. Partially silicified tholeiites have compositions between 0.3 and 0.9 wt.% and partially chloritized tholeiites have compositions between 1.0 and 1.5 wt.%. Samples directly beneath the chert horizons KrC_2 and KrC_3, samples Kr-31B and KrK-61b, have relatively higher FeO^T compositions compared to similar tholeiites of their groups. This means that the general trend observed is a depletion in FeO^T in highly silicified tholeiitic basalts and an enrichment in FeO^T in highly chloritized tholeiitic basalts. The MgO-K_2O plot (**Figure 7.1c**) shows highly silicified tholeiites to have high K_2O compositions between 2.2 and 3.2 wt.%. Highly chloritized tholeiites have low K_2O contents between 0 and 0.6 wt.% while partially silicified tholeiitic basalts have compositions between 0 and 2.1 wt.%. Partially chloritized compositions have K_2O contents between 0 and 3.8 wt.%. In partially chloritized tholeiitic basalts, one sample (KrT-47) has the highest K_2O content. Some partially chloritized tholeiites have K_2O contents below 0.9 wt.% and overlapping with highly chloritized tholeiites. It is evident therefore that silicification has resulted in K_2O enrichment, whereas K_2O remained relatively immobile during the process of chloritization.

There is a large scatter observed in the MgO-CaO (**Figure 7.1d**) plot. Highly silicified tholeiites have the lowest CaO compositions between 0 and 4 wt.%, whereas highly chloritized tholeiites have contents between 3 and 7 wt.%. Partially silicified tholeiites have CaO contents between 4.5 and 14 wt.% while partially chloritized tholeiites have contents between 3 and 15 wt.%. Chloritization has not significantly changed the CaO content in the tholeiitic metabasalt compositions, whereas silicification has resulted in the relative depletion of CaO. The same trend is observed in the MgO-Na_2O binary plot (**Figure 7.1e**) where highly silicified tholeiites are depleted in Na_2O and highly chloritized tholeiites have not significantly changed in Na_2O. Highly silicified tholeiites have Na_2O contents between ranging between 0 and 1 wt.%, whereas highly chloritized tholeiites have Na_2O contents between 1 and 4 wt.%. Partially chloritized tholeiites have Na_2O contents between 0 and 5.5 wt.%, whereas partially silicified tholeiites have contents between 0.5 and 8.5 wt.%.

In the MgO-TiO_2 plot, the highly silicified tholeiites haves TiO_2 contents between 0.2 and 1 wt.%, highly chloritized tholeiites: 1.5-2.5 wt.%, partially chloritized tholeiites: 0.5-2 wt.% and partially silicified tholeiites: 0.1 to 1.2 wt.%. The change in TiO_2 contents in silicified tholeiites is very small. Majority of the silicified tholeiites have low TiO_2 contents below 0.5 wt.%.

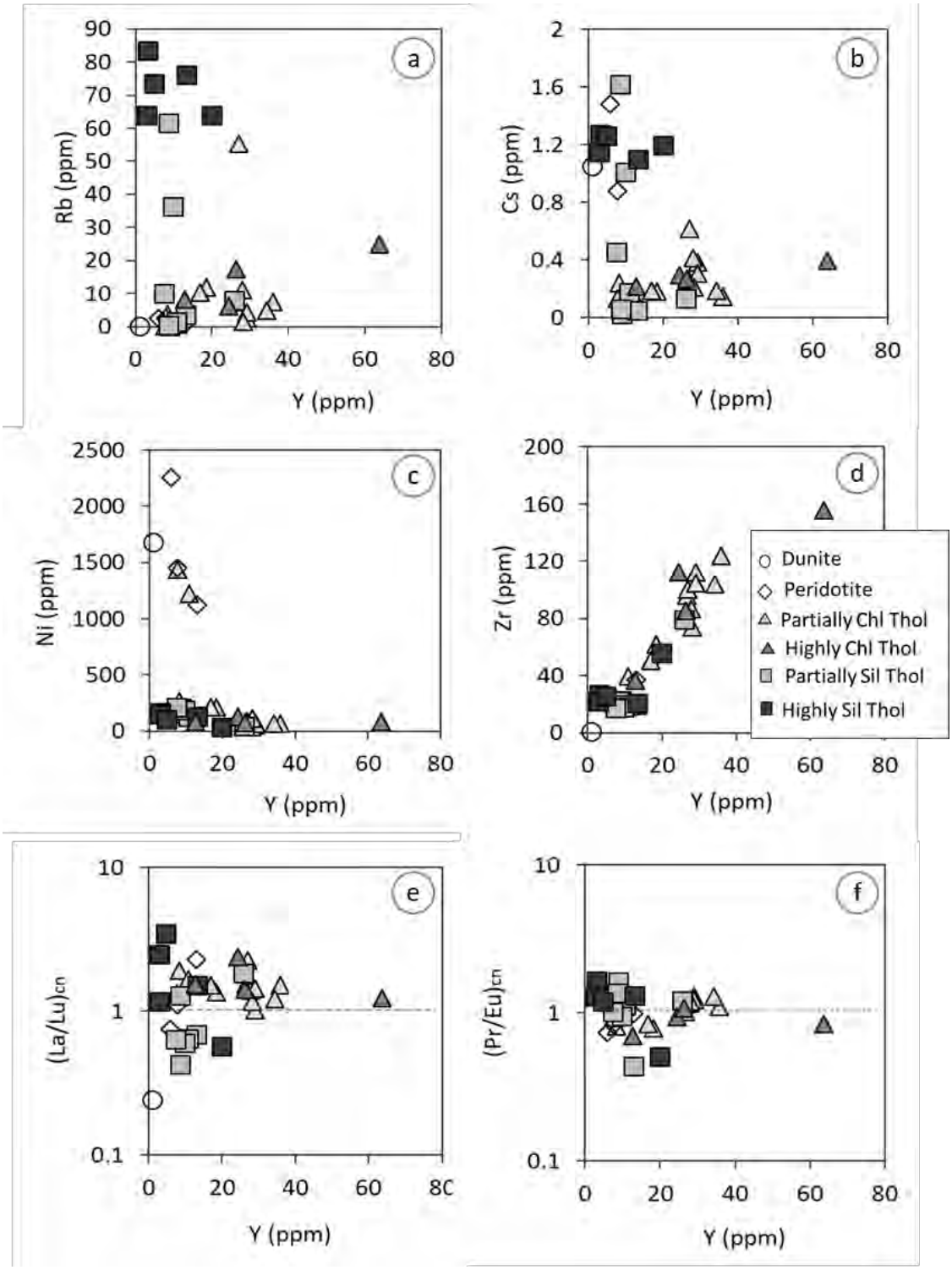

Figure 7. 2*: Trace element versus trace element binary plots of all rock samples collected in the Kromberg type-section. All trace elements are recorded in part per million (ppm). (e) and (f) are C1chondrite normalized (Sun and McDonough, 1989) ratios against Y.*

Table 7. 1*: Major (in wt.%) and trace (in ppm) element data of different rock compositions in the Kromberg type-section. Below dl= below detection limit, Depth =depth above Noisy Formation (in m), Mg # = Mg-number.*

Rock	Highly silicified tholeiitic basalts					Highly chloritized tholeiitic basalts				Cumulate peridotite		
Depth	714	704	699.5	694	681.5	924	783.5	402	385	580	489.5	1063.5
Sample	**KRT-31B**	**KRT-32**	**KRT-33**	**KRT-34**	**KRT-35**	**KRK-23**	**KRK-24**	**KrT-52**	**KrK-53**	**KRK-38**	**KrT-45**	**KR0-20**
SiO_2	73.92	69.72	69.63	66.26	66.12	48.88	50.14	46.94	50.40	40.20	40.93	43.69
TiO_2	0.97	0.37	0.35	0.40	0.34	1.43	0.62	2.53	1.55	0.32	0.44	0.51
Al_2O_3	10.33	18.62	16.83	18.80	16.01	13.71	14.71	17.34	13.83	3.63	5.05	7.25
Cr_2O_3	0.76	0.09	0.03	0.03	0.03	bdl	bdl	bdl	0.01	0.73	0.64	0.40
Fe_2O_3	5.84	1.30	1.58	1.58	1.58	14.99	14.25	14.73	13.87	12.01	14.73	12.99
FeO	4.78	1.06	1.29	1.29	1.29	12.26	11.65	12.04	11.34	9.82	12.04	10.62
FeO^T	0.53	0.12	0.14	0.14	0.14	1.35	1.28	1.32	1.25	1.08	1.32	1.17
CaO	0.06	0.06	0.07	0.09	3.98	7.55	8.58	3.19	4.07	2.84	3.62	7.01
Na_2O	0.18	0.90	0.87	0.98	0.93	2.88	3.88	3.46	1.60	bdl	bdl	bdl
K_2O	2.94	3.32	2.45	2.94	2.82	0.33	0.10	1.43	0.58	0.03	0.02	0.01
MgO	0.29	1.83	3.91	4.05	1.90	5.28	5.32	6.36	7.70	30.90	27.54	21.17
Mg #	0.10	0.75	0.84	0.85	0.72	0.43	0.45	0.48	0.55	0.85	0.80	0.78
MnO	0.02	0.01	0.01	0.02	0.11	0.20	0.19	0.23	0.18	0.18	0.20	0.23
P_2O_5	0.01	0.03	0.02	0.05	0.03	0.15	0.05	0.19	0.13	0.03	0.04	0.06
L.O.I.	3.69	3.12	3.65	4.47	6.80	4.13	2.00	3.95	6.15	10.79	7.92	6.73
Sum Of Conc.	99.01	99.37	99.40	100	101	100	100	100	100	102	101	100
Sc	14.52	50.40	43.60	49.30	42.30	26.91	28.86	54.90	26.70	19.48	21.13	30.35
V	216	261	242	265	192	264	211	511	329	119	135	174
Cr	5245	670	647	697	610	25.21	18.42	25.00	84.00	4966	3789	2784
Co	6.35	9.92	21.70	21.96	25.70	66.80	57.66	44.60	23.83	132	107	99.00
Ni	31.20	161	150	106	129	127	81.80	78.30	69.30	2257	1453	1122
Cu	33.27	13.33	15.02	13.75	25.90	58.50	60.50	280	18.50	33.41	20.70	66.60
Zn	50.10	14.80	71.50	48.10	34.80	95.40	76.00	167	82.00	96.00	69.80	78.90
Rb	63.90	83.50	63.80	73.60	76.10	6.23	8.21	24.87	17.24	2.63	2.53	0.89
Sr	22.27	25.40	25.10	34.40	50.30	150	267	113	47.50	6.77	6.59	11.35
Y	19.89	3.08	2.87	4.80	13.20	24.38	12.76	63.70	26.36	5.88	7.79	13.02
Zr	55.67	26.69	22.20	25.82	21.20	113	36.55	156	85.60	17.78	23.32	37.30
Nb	2.16	1.12	0.92	0.92	0.76	4.17	1.35	7.18	4.03	0.68	1.04	1.46
Mo	1.47	0.48	0.48	0.30	0.51	0.53	0.26	0.72	0.25	0.60	0.32	0.26
Cs	1.19	1.27	1.15	1.26	1.10	0.29	0.22	0.40	0.27	1.48	0.88	0.09
Ba	344	153	133	226	217	85.60	66.90	114	90.50	14.30	33.80	73.60
La	1.44	1.57	1.41	3.14	3.66	7.53	2.80	12.19	5.72	1.08	1.25	4.13
Ce	3.09	3.99	3.44	3.60	5.95	15.74	6.63	27.78	14.14	2.44	3.44	7.70
Pr	0.40	0.65	0.58	0.58	0.91	2.15	0.93	3.87	2.17	0.40	0.42	1.00
Nd	2.13	3.05	1.97	2.00	4.76	11.15	5.34	19.40	9.84	1.70	2.62	5.19
Sm	0.95	0.57	0.66	0.53	1.21	3.31	1.70	5.61	3.14	0.71	1.07	1.54
Eu	0.48	0.24	0.27	0.29	0.42	1.40	0.82	2.81	1.23	0.33	0.31	0.62
Gd	1.91	0.71	0.70	0.78	1.64	4.46	2.11	8.60	3.75	1.06	1.29	2.14
Tb	0.44	0.28	0.27	0.16	0.30	0.72	0.34	1.56	0.69	0.27	0.20	0.35
Dy	3.49	0.81	0.67	0.96	2.30	4.75	2.43	11.40	4.94	1.22	1.52	2.37
Ho	0.74	0.35	0.31	0.23	0.52	0.94	0.52	2.35	0.98	0.29	0.29	0.51
Er	1.97	0.41	0.45	0.61	1.52	2.51	1.32	7.66	2.81	0.76	0.82	1.32
Tm	0.29	0.21	0.16	0.11	0.23	0.36	0.19	1.05	0.41	0.11	0.11	0.20
Yb	1.83	0.46	0.57	0.74	1.69	2.20	1.26	6.53	2.68	0.68	0.70	1.22
Lu	0.27	0.07	0.13	0.10	0.26	0.34	0.19	1.06	0.43	0.15	0.12	0.19
Hf	1.80	0.83	0.90	0.89	0.66	3.11	1.09	4.46	2.52	0.67	0.78	1.15
Ta	0.13	0.18	0.23	0.09	0.07	0.30	0.10	0.44	0.25	0.10	0.06	0.10
Pb	14.62	1.78	1.97	1.88	1.84	2.39	2.63	6.51	2.04	2.87	1.17	1.09
Th	0.25	0.30	0.17	0.18	0.16	1.08	0.24	0.90	0.47	0.19	0.13	0.43
U	0.63	0.17	0.24	0.05	0.04	0.22	0.09	0.21	0.18	0.18	0.01	0.12

***Table 7.1**: (continued)*

Rock	Partially silicified tholeiitic basalts								Metadunite
Depth	606	556.5	434	572	565.5	563.5	540.5	533	18
Sample	**KRT-36**	**KrT-42**	**KrT-50**	**KRT-39**	**KRT-40**	**KrT-41**	**KrT-43**	**KrT-44**	**Kr Dun 65**
SiO_2	61.33	62.91	58.75	53.95	54.44	52.00	51.96	51.19	36.02
TiO_2	0.36	0.33	1.31	0.30	0.31	0.34	0.31	0.29	0.08
Al_2O_3	17.19	16.03	13.40	16.27	15.10	15.20	14.57	14.69	2.23
Cr_2O_3	0.03	0.08	bdl	0.07	0.08	0.08	0.06	0.09	0.25
Fe_2O_3	3.27	6.70	6.18	5.66	9.04	8.54	9.16	8.79	8.15
FeO	2.67	5.48	5.05	4.63	7.39	6.98	7.49	7.19	6.66
FeO^T	0.29	0.60	0.56	0.51	0.81	0.77	0.82	0.79	0.73
CaO	4.59	0.49	7.32	12.87	6.09	10.14	7.72	8.98	2.36
Na_2O	8.14	2.67	5.05	3.69	6.13	3.77	0.54	0.61	bdl
K_2O	0.04	2.19	0.45	0.26	0.10	0.03	1.33	0.40	bdl
MgO	3.01	4.78	2.26	5.53	4.94	7.70	9.19	10.33	36.67
Mg#	0.67	0.61	0.44	0.68	0.54	0.66	0.69	0.72	0.91
MnO	0.08	0.20	0.13	0.15	0.31	0.19	0.15	0.15	0.12
P_2O_5	0.05	0.03	0.13	0.03	0.04	0.03	0.03	0.03	0.00
L.O.I.	2.26	4.09	5.32	2.06	4.17	2.30	5.88	4.83	15.10
Sum Of Conc.	100	101	100	101	101	100	101	100	101
Sc	46.10	42.19	27.50	40.60	42.80	39.60	38.30	39.40	10.04
V	244	204	324	200	236	204	190	186	37.70
Cr	635	511	22.30	481	567	513	373	609	1491
Co	48.50	36.30	23.80	35.30	47.50	44.80	44.00	47.76	57.70
Ni	163	156	43.40	132	128	206	186	211	1678
Cu	34.70	39.50	131	11.31	15.08	200.60	25.00	28.50	8.55
Zn	36.90	69.50	62.00	30.50	67.60	63.70	47.50	50.70	18.10
Rb	0.28	61.50	7.94	3.54	1.46	0.38	36.30	10.14	0.28
Sr	154	20.20	77.50	130	90.70	108	66.70	84.90	7.53
Y	8.85	8.53	25.89	12.97	10.72	8.66	9.77	7.36	0.96
Zr	22.60	22.27	79.60	19.66	19.01	19.52	18.22	17.46	1.25
Nb	0.83	0.80	3.95	0.78	0.71	0.72	0.77	0.58	0.04
Mo	0.30	0.18	0.42	0.35	0.38	0.26	0.18	0.29	0.23
Cs	0.03	1.62	0.13	0.05	0.18	0.06	1.01	0.46	1.05
Ba	22.10	106	44.10	75.00	40.00	28.30	28.40	16.80	8.90
La	1.11	1.76	5.99	1.54	1.32	0.81	1.08	0.89	0.07
Ce	2.94	3.51	14.10	3.43	2.91	2.23	2.47	2.08	0.09
Pr	0.42	0.48	2.05	0.46	0.37	0.33	0.35	0.30	bdl
Nd	2.24	2.34	9.81	2.27	1.92	1.73	1.81	1.73	bdl
Sm	0.75	0.75	3.34	0.74	0.58	0.51	0.52	0.57	0.03
Eu	0.16	0.22	1.03	0.65	0.20	0.15	0.22	0.18	bdl
Gd	1.23	0.99	4.04	1.27	0.98	0.75	1.16	0.76	0.03
Tb	0.21	0.16	0.70	0.25	0.20	0.15	0.20	0.13	0.02
Dy	1.60	1.57	4.78	1.90	1.57	1.30	1.46	1.16	0.14
Ho	0.38	0.31	0.91	0.49	0.40	0.37	0.36	0.27	0.04
Er	1.04	0.98	2.73	1.40	1.21	1.16	1.10	1.04	0.13
Tm	0.17	0.12	0.38	0.21	0.19	0.18	0.17	0.14	0.02
Yb	1.19	0.92	2.37	1.54	1.42	1.26	1.30	0.89	0.11
Lu	0.19	0.15	0.35	0.24	0.22	0.20	0.19	0.15	0.03
Hf	0.68	0.62	2.28	0.54	0.59	0.61	0.51	0.48	bdl
Ta	0.06	0.06	0.21	0.04	0.05	0.05	0.05	0.03	bdl
Pb	1.64	2.93	1.61	1.91	1.38	1.56	0.94	1.12	0.99
Th	0.12	0.32	0.43	0.11	0.12	0.12	0.12	0.12	bdl
U	0.03	0.11	0.14	0.04	0.03	0.05	0.03	0.03	bdl

***Table 7.1**: (continued)*

Rock	Partially chloritized tholeiitic basalt												
Depth	1009.5	996.5	487	455	439	426	376	343.5	222	1004	748.5	591	475.5
Sample	**KRK-21**	**KRST-22**	**KrT-47**	**KrT-48**	**KrT-49**	**KrT-51b**	**KrK-54**	**KrK-61b**	**KrK-62**	**ICK-X**	**KRK-25**	**KR0-37**	**KrT-46**
SiO_2	47.10	51.50	51.22	46.96	50.98	50.06	54.58	47.70	49.70	48.38	51.55	46.23	47.88
TiO_2	0.97	1.16	1.61	1.83	1.97	1.38	1.68	1.72	1.38	0.93	0.41	0.43	0.70
Al_2O_3	11.95	12.48	17.08	17.29	15.06	13.27	14.56	13.31	13.76	12.46	3.65	5.62	4.85
Cr_2O_3	0.06	0.01	bdl	bdl	bdl	bdl	0.01	bdl	0.01	0.07	0.11	0.59	0.33
Fe_2O_3	11.77	13.70	9.65	14.45	12.01	12.11	12.18	16.40	14.84	12.90	13.25	12.47	11.16
FeO	9.62	11.20	7.89	11.82	9.82	9.90	9.96	13.41	12.13	10.55	10.83	10.20	9.13
FeO^T	1.06	1.23	0.87	1.30	1.08	1.09	1.10	1.48	1.33	1.16	1.19	1.12	1.00
CaO	11.42	8.20	3.42	3.03	6.01	10.87	4.67	3.93	9.09	10.84	13.86	10.20	10.33
Na_2O	2.35	3.70	3.72	5.24	3.99	2.79	2.41	1.96	2.69	2.19	0.34	bdl	0.02
K_2O	0.53	0.37	3.70	0.15	0.46	0.59	0.16	0.21	0.09	0.47	0.02	bdl	0.01
MgO	7.77	6.22	6.55	7.02	6.17	3.73	5.48	7.40	6.40	7.63	14.52	19.57	20.41
Mg#	0.59	0.50	0.60	0.51	0.53	0.40	0.50	0.50	0.48	0.56	0.70	0.77	0.80
MnO	0.18	0.21	0.16	0.17	0.17	0.21	0.14	0.11	0.20	0.20	0.25	0.18	0.16
P_2O_5	0.08	0.13	0.17	0.15	0.17	0.13	0.17	0.18	0.12	0.08	0.05	0.03	0.07
L.O.I.	5.37	1.91	3.42	4.10	3.16	5.69	4.05	6.99	2.45	4.65	1.94	6.02	4.05
Sum Of Conc.	100	100	101	100	100	101	100	100	101	101	100	101	100
Sc	43.30	35.81	38.40	36.60	39.70	30.30	27.70	32.20	32.12	43.00	41.20	27.71	23.13
V	267	286	392	369	415	334	337	428	375	261	186	167	149
Cr	409	84	42	22	24	20	99	44	107	466	801	4150	2064
Co	59.90	49.05	41.44	49.60	39.30	27.40	29.40	41.60	46.90	54.80	69.80	127	77.20
Ni	209	83.70	79.80	52.80	62.00	37.30	66.20	64.00	113	213	266	1438	1224
Cu	207	75.40	8.60	30.10	263	148	173	125	126	123	122	213	34.30
Zn	76.80	70.70	92.50	72.20	109	88.30	98.70	108	88.90	75.60	91.30	67.60	58.20
Rb	11.79	7.33	55.40	2.42	7.41	11.08	4.26	4.75	1.51	10.35	3.78	0.26	0.74
Sr	157	205	47.60	27.89	65.60	214	113	38.00	138	162.40	16.43	6.39	6.11
Y	18.36	26.61	27.00	29.06	35.84	27.88	29.11	34.29	28.21	16.85	8.28	7.61	10.88
Zr	61.90	96.40	100	112	124	86.60	105	104	73.60	50.48	20.68	20.85	39.40
Nb	2.21	3.29	4.68	5.13	5.58	4.00	4.73	4.31	2.94	2.20	0.79	0.82	1.68
Mo	0.48	0.61	0.39	0.29	0.72	0.41	0.51	0.25	0.79	0.46	0.38	0.28	0.21
Cs	0.18	0.26	0.61	0.38	0.15	0.42	0.31	0.19	0.21	0.19	0.24	0.13	0.16
Ba	69.30	167	185	58.20	54.60	79.00	35.30	20.40	23.70	93.60	46.10	19.50	13.90
La	3.59	5.24	7.72	4.16	8.34	5.42	5.93	6.43	4.42	2.99	2.32	1.49	1.78
Ce	8.23	11.81	18.80	11.56	19.49	14.34	14.78	16.19	11.46	7.36	5.29	3.60	4.58
Pr	1.20	1.71	2.66	1.75	2.89	2.18	2.23	2.25	1.75	1.05	0.65	0.48	0.74
Nd	6.37	9.47	13.49	9.68	13.89	10.09	10.96	12.14	8.82	5.57	3.51	2.48	3.90
Sm	2.09	3.07	3.87	3.35	4.58	3.37	3.29	3.63	2.91	1.61	1.08	0.94	1.54
Eu	0.93	1.03	1.42	0.83	1.60	1.14	1.11	1.07	0.90	0.76	0.49	0.31	0.41
Gd	3.07	4.50	4.49	4.14	5.28	4.05	4.60	4.81	4.07	2.59	1.45	1.30	1.91
Tb	0.53	0.73	0.78	0.64	0.87	0.72	0.75	0.82	0.67	0.50	0.27	0.22	0.32
Dy	3.44	5.05	4.97	5.17	6.76	4.73	5.26	5.79	4.82	3.12	1.69	1.51	2.04
Ho	0.76	1.05	1.05	1.02	1.41	1.07	1.13	1.21	0.97	0.64	0.34	0.34	0.42
Er	2.12	2.72	3.00	3.14	3.95	3.20	3.04	3.70	2.94	1.77	0.95	0.83	1.17
Tm	0.26	0.38	0.38	0.45	0.64	0.44	0.46	0.56	0.44	0.25	0.12	0.10	0.16
Yb	1.75	2.51	2.40	2.91	3.81	2.77	2.74	3.57	2.97	1.42	0.80	0.72	0.81
Lu	0.28	0.36	0.36	0.44	0.59	0.42	0.44	0.57	0.41	0.21	0.13	0.12	0.12
Hf	1.83	2.81	2.77	3.09	3.40	2.51	2.96	2.86	2.22	1.60	0.60	0.92	1.17
Ta	0.17	0.24	0.24	0.33	0.29	0.24	0.30	0.22	0.17	0.13	0.06	0.05	0.09
Pb	1.18	1.88	1.49	1.31	2.09	2.06	2.35	1.68	1.47	1.94	3.81	1.45	1.43
Th	0.42	0.65	0.64	0.61	0.72	0.56	0.62	0.47	0.36	0.36	0.19	0.28	0.15
U	0.10	0.15	0.17	0.16	0.22	0.13	0.18	0.10	0.08	0.10	0.06	0.05	0.04

With decreasing MgO content, TiO_2 increases in chloritized tholeiites. Highly chloritized tholeiites have overlapping compositions with partially chloritized tholeiites. This means that during chloritization, TiO_2 content did not change significantly; it remained conservative. These diagrams indicate that MgO and TiO_2 were not mobile in the partially chloritized tholeiitic basalts. Thus, they record a primary magmatic differentiation trend. On the other hand, MgO and TiO_2 have been mobile to some extent in the partially silicified tholeiites, indicating a metasomatic alteration trend.

Trace element versus trace element diagrams are plotted in **Figure 7.2**. In these plots trace elements such as Cs, Rb, La, Lu, Pr, Eu, Zr, and Ni are plotted against Y, a relatively immobile incompatible element. The plots include large-ion lithophile element (LILE) Rb and Cs, high-field strength element (HFSE) such as Zr, rare earth elements (REE) La, Lu, Pr and Eu, and a siderophile element Ni. The REE ratios are plotted against Y (**Figure 7.2e,f**) to show their degree of enrichment and/or depletion in the Kromberg type-section rocks. The Y-Rb binary diagram (**Figure 7.2a**) shows a poor correlation between Y (ppm) and Rb (ppm) for rock compositions of the Kromberg type-section. Highly silicified tholeiites have Rb values ranging between 60 and 85 ppm, whereas partially silicified tholeiites have values between 0 and 60 ppm. Highly chloritized tholeiites have Rb values between 0 and 15 ppm, whereas partially chloritized tholeiites have Rb values between 10 and 25 ppm. Highly silicified compositions form a compositional cluster in the Y-Rb binary diagram and have the highest Rb values compared to other rock compositions of the Kromberg type-section. This means that the process of hydrothermal alteration and silicification resulted in an enrichment of Rb. As opposed to high concentrations of Rb in the silicified samples, highly chloritized tholeiites plot and overlap with partially chloritized tholeiites in the Y – Rb diagram with lower concentrations. Chloritization appears not to have resulted in Rb mobility in the partially chloritized and highly chloritized tholeiites. Similar trends are observed in Y-Cs space. **Figure 7.2b** shows a Y-Cs diagram where highly chloritized compositions low values compared to highly silicified tholeiites. Highly chloritized and partially chloritized tholeiites have overlapping quantities with Cs values between 0.1 and 0.6 ppm. Highly silicified tholeiites have Cs contents between 1 and 1.4 ppm while partially silicified tholeiites have Cs compositions between 0 and 1.7 ppm. Both Rb and Cs have been mobile during alteration. are mobile and incompatible. Their poor correlation is evidence for the secondary metasomatic process, silicification. The Y-Ni plot (**Figure 7.2a**) shows tholeiitic metabasalt

compositions of the Kromberg type-section to be depleted of Ni, whereas the ultramafic metadunite and cumulate peridotites are enriched. Ni is enriched the metadunite and cumulate peridotite samples because of the minerals present in the samples namely, olivine and pyroxene. The three tholeiitic metabasalts (KrO-20, KrO-37 and KrT-46) showing Ni content above 1000 ppm are observed (in the petrography chapter), to comprise pyroxene and olivine crystals. This accounts for their high Ni compared to other tholeiitic compositions. All other tholeiitic compositions show a depletion in Ni content, with values less than 200 ppm.

There is a strong positive correlation observed between Y and Zr (**Figure 7.2d**). Silicified tholeiites have low Zr compositions, whereas partially silicified tholeiites have less than 20 ppm and highly silicified tholeiites have contents between 20 and 60 ppm. Partially chloritized and highly chloritized tholeiites have Zr contents above 30 ppm. The Zr compositions are moderately affected by silicification in the silicified samples. **Figure 7.2e,f** shows a Y-$(La/Lu)_{cn}$ and Y-$(Pr/Eu)_{cn}$ plot to assess the degree of alteration in comparison to the chondritic compositions. The y-axis in these plots have been represented using a log scale. In these plots it is observed that the rock compositions of the Kromberg type-section have REE element ratios above the chondritic concentrations. In **Figure 7.2e** the majority of highly silicified tholeiites have $(La/Lu)_{cn}$ of more than 1 while partially silicified tholeiites plot below 1. There is no clear compositional distinction observed between partially chloritized and highly chloritized tholeiitic metabasaltic rocks. In **Figure 7.2f** the behaviour of MREE (mid-REE) is assessed where the majority of highly silicified and partially silicified tholeiites have $(Pr/Eu)_{cn}$ ratios greater than 1. This is different from the partially chloritized tholeiitic metabasalts that have $(Pr/Eu)_{cn}$ ratios of less than 1. Partially chloritized tholeiites are depleted in MREE, whereas variation is observed in MREE of different samples of highly silicified and partially silicified tholeiites indicating metasomatic alteration effects of silicification.

Binary plots of immobile elements versus immobile elements have been plotted in **Figure 7.3** to investigate how metasomatism and chloritization has potentially affected immobile elements. **Figure 7.3a** shows no significant changes for most tholeiitic compositions. In exception to KrT-31B, these tholeiites have Cr_2O_3 contents less than 0.2 ppm and Al_2O_3 more than 10 wt.%. KrT-31B, a highly silicified tholeiite sample directly beneath the chert, is more enriched in Cr_2O_3 compared to any other highly silicified tholeiites. Some partially chloritized tholeiites have higher Cr_2O_5 and lower Al_2O_3 contents compared to others. This could account for the absence of pyroxene in the mineral assemblage of some

tholeiitic rocks (confirmed by petrography). **Figure 7.3b** shows a Mg-number-TiO_2 plot with partially and highly silicified tholeiites having low TiO_2 contents of less than 1 wt.% and partially and highly chloritized tholeiites showing a spread in TiO_2. The Mg-number of tholeiitic compositions is approximately the same, between ca. 0.4 and 1 wt.%.

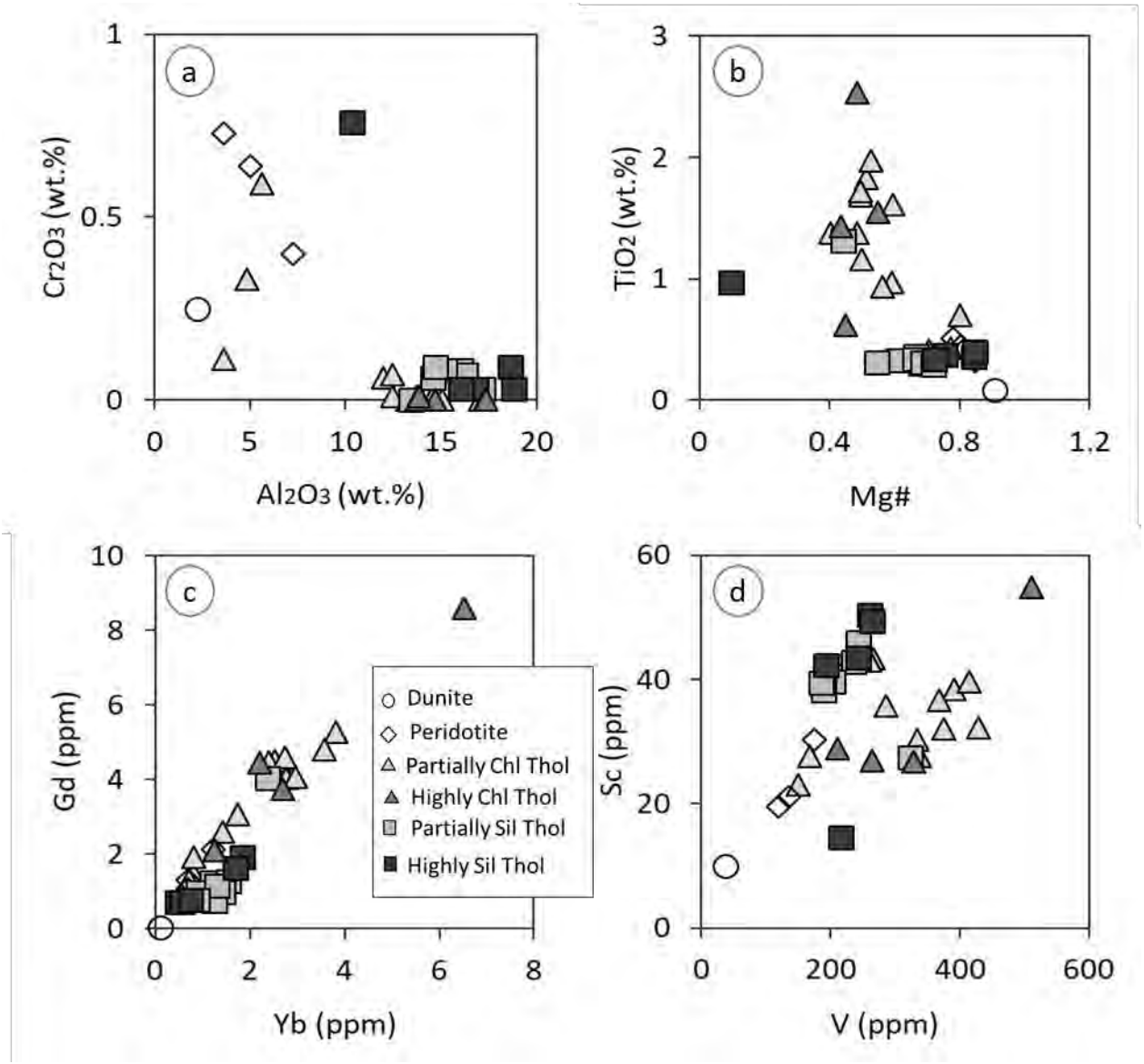

Figure 7. 3*: Binary plots of immobile versus immobile elements. All trace elements are recorded in ppm and major elements recorded in wt.%.*

There is, however, a spread observed in the Yb-Gd and V-Sc (**Figure 7.3c,d**) plot. A positive correlation is observed where highly and partially silicified tholeiites have low Gd and Yb and the highly and the partially chloritized tholeiites have higher concentrations. There is no correlation observed in the V-Sc plot. Majority of highly and partially silicified tholeiites

have high Sc whereas majority of partially and highly chloritized tholeiites show lower concentrations. There is no significant change observed in V contents. From **Figure 7.3** it is therefore observed that immobile elements like Mg-number, V, Yb and Gd are unaffected by either chloritization or silicification.

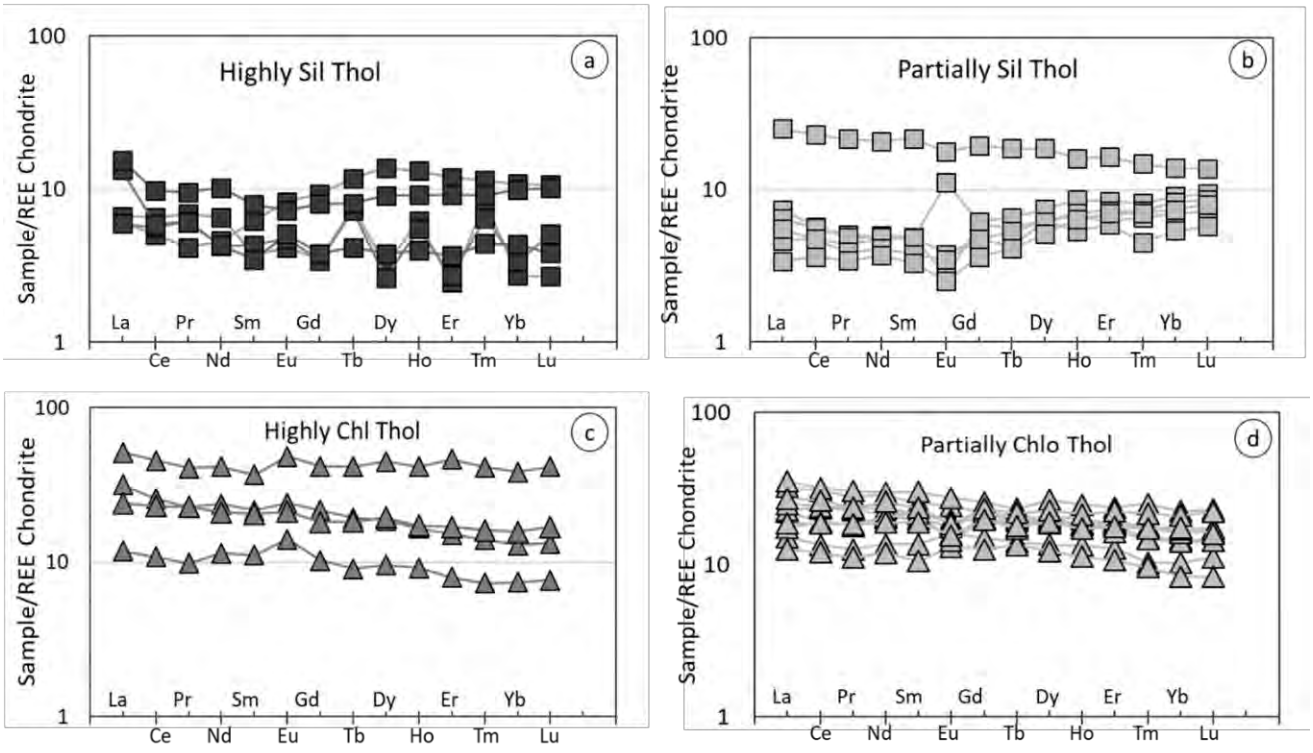

Figure 7. 4*: C1-Chondrite normalized (Sun and McDonough, 1989) REE plots of (a) highly silicified tholeiites, (b) partially silicified tholeiites, (c) highly chloritized tholeiites and (d) partially chloritized tholeiites*.

C1-chondrite normalized (Sun and McDonough, 1989) REE plots are provided to assess the REE patterns with regards to metasomatic alteration. From these plots, partially chloritized tholeiitic rocks are compared to highly chloritized tholeiitic rocks while partially silicified tholeiites are compared to highly silicified tholeiites to assess the degree of chloritization and silicification. From **Figure 7.4a.b** partially silicified tholeiites have a different pattern from highly silicified tholeiites. All, but one sample of partially silicified tholeiites have chondrite normalized REE concentrations that lie below 10. All partially silicified samples have negatively sloping LREE and are therefore enriched in LREE. A

positive slope is observed for HREE, for samples that have concentrations below 10, whereas one sample, KrT-50, with chondrite normalized REE concentration of more than 10, have a negative slope. KrT-50 shows enrichment in HREE, whereas all other samples are depleted in HREE. All partially silicified tholeiites have a strong negative Eu anomaly except for KrT-39 with a strong positive anomaly. Highly silicified tholeiites, like most partially silicified tholeiites have an overall negative slope for LREE. HREE have varying patterns where KrT-32, KrT-33, and KrT-33 show mobility in HREE and KrT-31 and KrT-35 have an overall positive slope. It is evident that silicification has heavily affected the LREE and the HREEs to some extent. **Figure 7.4c,d** also shows different REE patterns for highly and partially chloritized tholeiites. Partially chloritized tholeiite are enrichment in both LREE and HREE. Highly chloritized tholeiites also show a slight enrichment in LREE and HREE but differ from partially chloritized tholeiites by a small positive Eu anomaly. It can therefore be deduced that chloritization has not significantly changed the REE contents of chloritized tholeiitic metabasalt rocks in the Kromberg type-section. This is in line with the observations from the binary plots where significant elemental change is observed in silicification. The partially and highly silicified tholeiitic metabasalts have been affected by metasomatism and their bulk geochemistry does not reflect their igneous protolith compositions. They can therefore not be reliably used in protolith classification diagrams. Some highly chloritized tholeiitic metabasalts also appear to have been slightly affected, but not to the extent that the silicified samples have been. Highly chloritized tholeiitic basalts are also excluded in the rock classification and petrogenesis, sub-section 7.14, for high precision results. Furthermore, petrographic examination reveals that cumulate peridotites and metadunite are altered, but that alteration has not significantly affected the geochemistry of these rocks.

7.1.4 Rock classification and Petrogenesis (geochemical characterization)

The geochemical analysis in section 7.1.3 indicates that hydrothermal metamorphism affected many of the rocks in the Kromberg type-section. This is particularly true for silicified basalts and highly chloritized basalts. After conducting petrography, mineral chemistry, XRD analysis, and geochemical screening, 10 tholeiitic metabasaltic samples were deemed as relatively fresh. These include only the relatively fresh, partially chloritized samples. Alteration did not significantly change the protolith geochemistry of these rocks; therefore,

they can be used for igneous petrogenetic and geochemical classification. These samples together with the cumulate peridotite samples were geochemically classified according to the mafic-ultramafic geochemical criteria of Viljoen and Viljoen (1969c), Williams and Furnell, (1979), Viljoen et al., (1983), Smith and Erlank, (1982). Komatiites have MgO content between 23 and 36 wt.%, komatiitic basalts have MgO content between 11 and 24 wt.% and tholeiites have MgO content between 4 and 9 wt.%. In order to accurately classify these rock compositions, a Ti+Fe-Al-Mg plot modified after Jensen (1973) was used. Four rock compositions exist in the Kromberg type-section namely, partially chloritized tholeiites (KRK-21, KRST-22, KrT-47, KrT-48, KrT-49, KrT-51b, KrK-54, KrK-61b, KrK-62 and ICK-X), komatiitic basalts (KrK25, Kr0-37, KrT-46), cumulate peridotites (KrO-20, KrK-38, KrT-45) and metadunite (KrDun-65; **Table 7.2**). The partially chloritized tholeiites plot in the high Fe-rich tholeiitic basalt field in the Jensen (1973) diagram (**Figure 7.5a**), whereas the komatiitic basalts plot in the komatiitic basalt field. Two peridotitic cumulates plots in the komatiitic basalt field and one plots in the komatiite field. According to field evidence, these rock compositions are sill intrusions, thereby differ from both komatiites and komatiitic basalts. They have a poikilitic texture with pyroxene oikocrysts and olivine chadacrysts. The rock is further classified as a poikilitic wehrlite based on petrography studies. Petrographic evidence also reveals the metadunite sample to be a cumulate with serpentinized olivine crystals. These geochemical, textural and field differences differentiate metadunite, peridotitic cumulates, komatiitic basalts and tholeiitic basalts.

Further diagrams were plotted to compare the different rock compositions of the Kromberg type-section with similar rock compositions within the Onverwacht Group, BGB (**Figure 7.5b,c**). The different fields marked in **Figure 7.5b,c** were marked according to Viljoen et al. (1982). In these plots normal tholeiites are distinguished from Fe-rich and Mg-rich tholeiites. Komatiitic basalts are divided into three groups, Geluk-type (BK-1), Badplaas-type (BK-2) and Barberton-type (BK-3) komatiitic basalts, and an area marked K represents komatiite (after Viljoen et al., 1982). **Figure 7.5b** shows the tholeiitic metabasalt compositions of the Kromberg type-section as plotting within the tholeiitic basalt field. **Figure 7.5c** shows tholeiitic compositions as plotting within the normal tholeiitic basaltic field and a few plotting in the Fe-rich tholeiitic field. This differs from Jensen (1973) plot where all tholeiitic compositions are classified as Fe-rich tholeiites. Two komatiitic basalts (KrT-46 and KrO-37) plot within the Geluk-type komatiitic basalts and one sample (KrK-25) plots within the Badplaas-type komatiitic basalt field (**Figure 7.5b,c**). According to Viljoen

et al. (1982) Geluk-type komatiitic basalts vary in mineralogy from tremolite-chlorite and Badplaas-type varieties include tremolite-chlorite-actinolite assemblages. Petrographic studies reveal the two samples plotting in the Geluk-type field as comprising actinolite and chlorite and the sample plotting in the Badplaas-type field as comprising actinolite. Two cumulate peridotite samples and the metadunite rock plots in the komatiite field in **Figure 7.5b,c**. These are cumulate ultramafic rocks and are not komatiite *senso-stricto*.

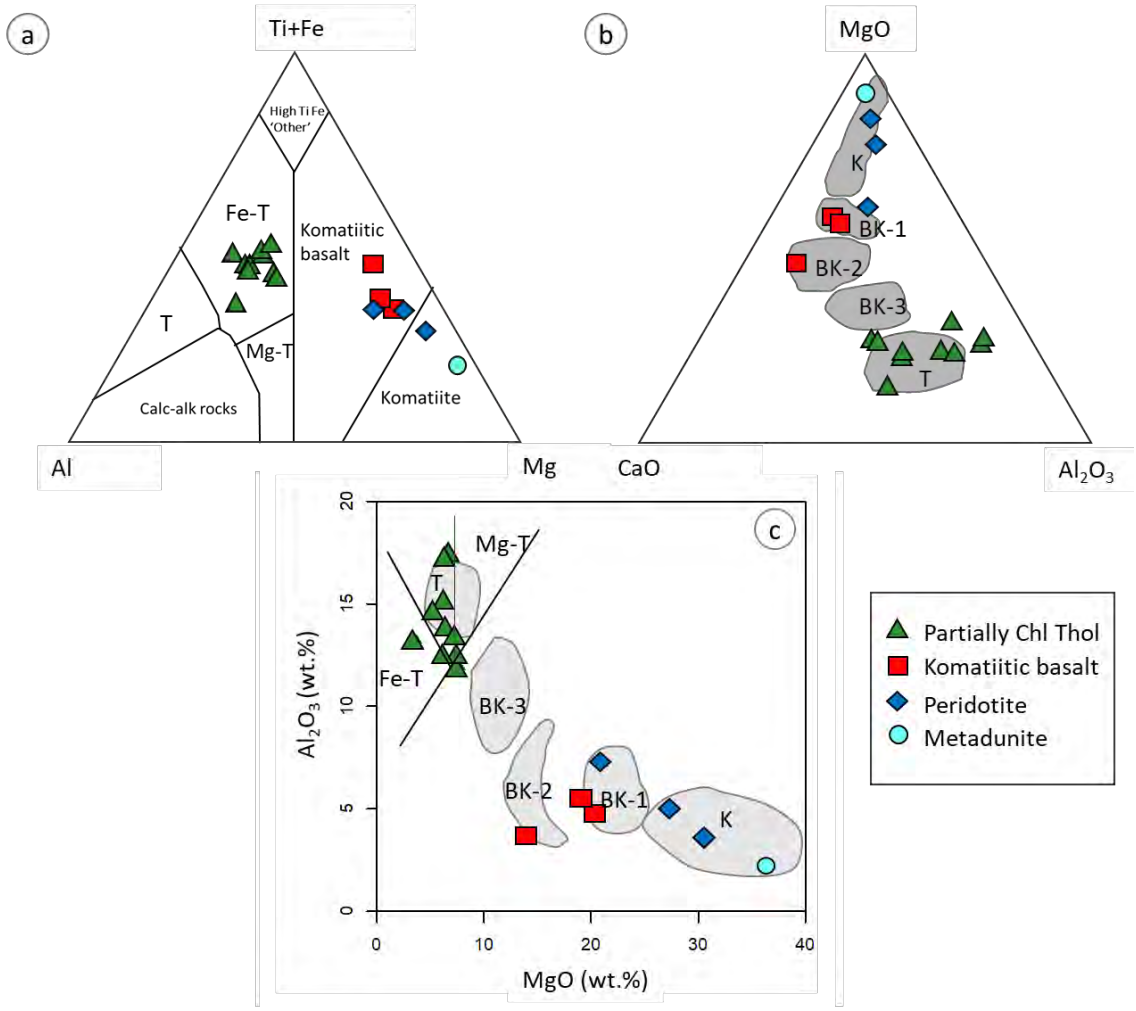

Figure 7. 5*: Classification diagrams (a) modified after Jensen (1973), (b) and (c) modified after Viljoen et al. (1982). (a) shows a ternary diagram where tholeiitic rocks are differentiated as calc-alkaline, Fe-rich and Mg-rich, and komatiitic rocks are differentiated as komatiites and komatiitic basalts. (b) shows a ternary plot and (c) a binary diagram that differentiates komatiitic basalts as BK-1 (Geluk-type), BK-2 (Badplaas-type) and BK-3 (Barberton-type); K=komatiites.*

Harker diagram binary plots of major elements versus MgO (wt.%) were plotted in **Figure 7.6**. In these plots MgO is used as an abscissa because it shows a fractional

crystallisation trend where the most evolved compositions, partially chloritized tholeiites, have lower MgO and the most primitive compositions, metadunite, have the highest MgO. **Figure 7.6a** shows a MgO-SiO_2 plot where SiO_2 supports the fractional crystallization trend. Partially chloritized tholeiites have the highest SiO_2 and the most primitive metadunite has the lowest SiO_2. Although komatiitic basalts have a higher MgO content compared to partially chloritized tholeiites, they show overlapping silica SiO_2 contents with partially chloritized tholeiites. **Figure 7.6b** shows a MgO-Al_2O_3 plot with a strong negative trend. The metadunite have the lowest Al_2O_3 compositions followed by peridotitic cumulates, komatiitic basalts and lastly partially chloritized tholeiites. This agrees with fractional crystallisation where more primitive rocks have low Al_2O_3 contents and evolved rock compositions have high Al_2O_3 contents. The large compositional gap in the diagram observed suggest crystallisation of partially chloritized tholeiites at much lower pressure conditions compared to komatiitic basalts (Herzberg, 1992).

Figure 7.6c,d shows a MgO-TiO_2 binary plot and a MgO-P_2O_5 plot. Both these plots show a strong negative trend with metadunite have the lowest TiO_2 and P_2O_5 contents, followed by cumulate peridotites, komatiitic basalts and lastly partially chloritized tholeiites. A near horizontal trend is observed in **Figure 7.6e** between MgO and Fe_2O_3. The binary plot shows overlapping quantities between different rock compositions of the Kromberg type-section. In **Figure 7.6f** partially chloritized tholeiitic basalts have overlapping compositions with all rock groups of the Kromberg type-section. Komatiitic basalts have the highest CaO compositions compared to other serpentinized rocks (metadunite and peridotitic cumulate) of the Kromberg type-section. This is possibly due to differences in mineralogical compositions of the different rock groups. The MgO-L.O.I. (loss on ignition) plot (**Figure 7.6g**) shows a positive trend where the most primitive rock, metadunite, has the highest loss on ignition (L.O.I.) contents compared to the most evolved rock compositions, the partially chloritized tholeiites. The L.O.I. content is correlated with the amount of alteration assemblages and the amount of water contained in each the rock. The metadunite and olivine-pyroxene peridotitic cumulates have high L.O.I. compositions because they are altered and contain low-temperature H_2O-rich alteration minerals, such as serpentine, chlorite and actinolite. There is an overlap observed between L.O.I. values of partially chloritized tholeiites and komatiitic basalts. This could be because both these rock compositions are affected by low-grade metamorphism and have hydrous mineral assemblages including chlorite and actinolite.

Table 7. 2: *Screened data showing compositions of relatively fresh rocks including major (in wt.%) and trace (in ppm) elements of different rock compositions in the Kromberg type-section. bdl= below detection limit, Depth =depth above Noisy Formation (in m), Mg# = Mg-number.*

Rock	Partially chloritized tholeiitic basalt									
Depth	1009.5	996.5	487	455	439	426	376	343.5	222	1004
Sample	**KRK-21**	**KRST-22**	**KrT-47**	**KrT-48**	**KrT-49**	**KrT-51b**	**KrK-54**	**KrK-61b**	**KrK-62**	**ICK-X**
SiO_2	47.10	51.50	51.22	46.96	50.98	50.06	54.58	47.70	49.70	48.38
TiO_2	0.97	1.16	1.61	1.83	1.97	1.38	1.68	1.72	1.38	0.93
Al_2O_3	11.95	12.48	17.08	17.29	15.06	13.27	14.56	13.31	13.76	12.46
Cr_2O_3	0.06	0.01	bdl	bdl	bdl	bdl	0.01	bdl	0.01	0.07
Fe_2O_3	11.77	13.70	9.65	14.45	12.01	12.11	12.18	16.40	14.84	12.90
FeO	9.62	11.20	7.89	11.82	9.82	9.90	9.96	13.41	12.13	10.55
FeO^T	1.06	1.23	0.87	1.30	1.08	1.09	1.10	1.48	1.33	1.16
CaO	11.42	8.20	3.42	3.03	6.01	10.87	4.67	3.93	9.09	10.84
Na_2O	2.35	3.70	3.72	5.24	3.99	2.79	2.41	1.96	2.69	2.19
K_2O	0.53	0.37	3.70	0.15	0.46	0.59	0.16	0.21	0.09	0.47
MgO	7.77	6.22	6.55	7.02	6.17	3.73	5.48	7.40	6.40	7.63
Mg#	0.59	0.50	0.60	0.51	0.53	0.40	0.50	0.50	0.48	0.56
MnO	0.18	0.21	0.16	0.17	0.17	0.21	0.14	0.11	0.20	0.20
P_2O_5	0.08	0.13	0.17	0.15	0.17	0.13	0.17	0.18	0.12	0.08
L.O.I.	5.37	1.91	3.42	4.10	3.16	5.69	4.05	6.99	2.45	4.65
Sum Of Conc.	100	100	101	100	100	101	100	100	101	101
Sc	43.30	35.81	38.40	36.60	39.70	30.30	27.70	32.20	32.12	43.00
V	267	286	392	369	415	334	337	428	375	261
Cr	409	84	42	22	24	20	99	44	107	466
Co	59.90	49.05	41.44	49.60	39.30	27.40	29.40	41.60	46.90	54.80
Ni	209	83.70	79.80	52.80	62.00	37.30	66.20	64.00	113	213
Cu	207	75.40	8.60	30.10	263	148	173	125	126	123
Zn	76.80	70.70	92.50	72.20	109	88.30	98.70	108	88.90	75.60
Rb	11.79	7.33	55.40	2.42	7.41	11.08	4.26	4.75	1.51	10.35
Sr	157	205	47.60	27.89	65.60	214	113	38.00	138	162.40
Y	18.36	26.61	27.00	29.06	35.84	27.88	29.11	34.29	28.21	16.85
Zr	61.90	96.40	100	112	124	86.60	105	104	73.60	50.48
Nb	2.21	3.29	4.68	5.13	5.58	4.00	4.73	4.31	2.94	2.20
Mo	0.48	0.61	0.39	0.29	0.72	0.41	0.51	0.25	0.79	0.46
Cs	0.18	0.26	0.61	0.38	0.15	0.42	0.31	0.19	0.21	0.19
Ba	69.30	167	185	58.20	54.60	79.00	35.30	20.40	23.70	93.60
La	3.59	5.24	7.72	4.16	8.34	5.42	5.93	6.43	4.42	2.99
Ce	8.23	11.81	18.80	11.56	19.49	14.34	14.78	16.19	11.46	7.36
Pr	1.20	1.71	2.66	1.75	2.89	2.18	2.23	2.25	1.75	1.05
Nd	6.37	9.47	13.49	9.68	13.89	10.09	10.96	12.14	8.82	5.57
Sm	2.09	3.07	3.87	3.35	4.58	3.37	3.29	3.63	2.91	1.61
Eu	0.93	1.03	1.42	0.83	1.60	1.14	1.11	1.07	0.90	0.76
Gd	3.07	4.50	4.49	4.14	5.28	4.05	4.60	4.81	4.07	2.59
Tb	0.53	0.73	0.78	0.64	0.87	0.72	0.75	0.82	0.67	0.50
Dy	3.44	5.05	4.97	5.17	6.76	4.73	5.26	5.79	4.82	3.12
Ho	0.76	1.05	1.05	1.02	1.41	1.07	1.13	1.21	0.97	0.64
Er	2.12	2.72	3.00	3.14	3.95	3.20	3.04	3.70	2.94	1.77
Tm	0.26	0.38	0.38	0.45	0.64	0.44	0.46	0.56	0.44	0.25
Yb	1.75	2.51	2.40	2.91	3.81	2.77	2.74	3.57	2.97	1.42
Lu	0.28	0.36	0.36	0.44	0.59	0.42	0.44	0.57	0.41	0.21
Hf	1.83	2.81	2.77	3.09	3.40	2.51	2.96	2.86	2.22	1.60
Ta	0.17	0.24	0.24	0.33	0.29	0.24	0.30	0.22	0.17	0.13
Pb	1.18	1.88	1.49	1.31	2.09	2.06	2.35	1.68	1.47	1.94
Th	0.42	0.65	0.64	0.61	0.72	0.56	0.62	0.47	0.36	0.36
U	0.10	0.15	0.17	0.16	0.22	0.13	0.18	0.10	0.08	0.10

***Table 7.2**: (continued)*

Rock	Komatiitic basalt			Cumulate peridotite			Metadunite
Depth	748.5	591	475.5	580	489.5	1063.5	18
Sample	**KRK-25**	**KR0-37**	**KrT-46**	**KRK-38**	**KrT-45**	**KR0-20**	**Kr Dun 65**
SiO_2	51.55	46.23	47.88	40.20	40.93	43.69	36.02
TiO_2	0.41	0.43	0.70	0.32	0.44	0.51	0.08
Al_2O_3	3.65	5.62	4.85	3.63	5.05	7.25	2.23
Cr_2O_3	0.11	0.59	0.33	0.73	0.64	0.40	0.25
Fe_2O_3	13.25	12.47	11.16	12.01	14.73	12.99	8.15
FeO	10.83	10.20	9.13	9.82	12.04	10.62	6.66
FeO^T	1.19	1.12	1.00	1.08	1.32	1.17	0.73
CaO	13.86	10.20	10.33	2.84	3.62	7.01	2.36
Na_2O	0.34	bdl	0.02	bdl	bdl	bdl	bdl
K_2O	0.02	bdl	0.01	0.03	0.02	0.01	bdl
MgO	14.52	19.57	20.41	30.90	27.54	21.17	36.67
Mg#	0.70	0.77	0.80	0.85	0.80	0.78	0.91
MnO	0.25	0.18	0.16	0.18	0.20	0.23	0.12
P_2O_5	0.05	0.03	0.07	0.03	0.04	0.06	0.00
L.O.I.	1.94	6.02	4.05	10.79	7.92	6.73	15.10
Sum Of Conc.	100	101	100	102	101	100	101
Sc	41.20	27.71	23.13	19.48	21.13	30.35	10.04
V	186	167	149	119	135	174	37.70
Cr	801	4150	2064	4966	3789	2784	1491
Co	69.80	127	77.20	132	107	99.00	57.70
Ni	266	1438	1224	2257	1453	1122	1678
Cu	122	213	34.30	33.41	20.70	66.60	8.55
Zn	91.30	67.60	58.20	96.00	69.80	78.90	18.10
Rb	3.78	0.26	0.74	2.63	2.53	0.89	0.28
Sr	16.43	6.39	6.11	6.77	6.59	11.35	7.53
Y	8.28	7.61	10.88	5.88	7.79	13.02	0.96
Zr	20.68	20.85	39.40	17.78	23.32	37.30	1.25
Nb	0.79	0.82	1.68	0.68	1.04	1.46	0.04
Mo	0.38	0.28	0.21	0.60	0.32	0.26	0.23
Cs	0.24	0.13	0.16	1.48	0.88	0.09	1.05
Ba	46.10	19.50	13.90	14.30	33.80	73.60	8.90
La	2.32	1.49	1.78	1.08	1.25	4.13	0.07
Ce	5.29	3.60	4.58	2.44	3.44	7.70	0.09
Pr	0.65	0.48	0.74	0.40	0.42	1.00	bdl
Nd	3.51	2.48	3.90	1.70	2.62	5.19	bdl
Sm	1.08	0.94	1.54	0.71	1.07	1.54	0.03
Eu	0.49	0.31	0.41	0.33	0.31	0.62	bdl
Gd	1.45	1.30	1.91	1.06	1.29	2.14	0.03
Tb	0.27	0.22	0.32	0.27	0.20	0.35	0.02
Dy	1.69	1.51	2.04	1.22	1.52	2.37	0.14
Ho	0.34	0.34	0.42	0.29	0.29	0.51	0.04
Er	0.95	0.83	1.17	0.76	0.82	1.32	0.13
Tm	0.12	0.10	0.16	0.11	0.11	0.20	0.02
Yb	0.80	0.72	0.81	0.68	0.70	1.22	0.11
Lu	0.13	0.12	0.12	0.15	0.12	0.19	0.03
Hf	0.60	0.92	1.17	0.67	0.78	1.15	bdl
Ta	0.06	0.05	0.09	0.10	0.06	0.10	bdl
Pb	3.81	1.45	1.43	2.87	1.17	1.09	0.99
Th	0.19	0.28	0.15	0.19	0.13	0.43	bdl
U	0.06	0.05	0.04	0.18	0.01	0.12	bdl

The MgO-K_2O diagram (**Figure 7.6h**) shows a depletion in K_2O for almost all the rock compositions in the Kromberg type-section, besides partially chloritized tholeiites. The partially chloritized tholeiites have high K_2O contents whereas komatiitic basalts, peridotitic cumulates and metadunite plot with low K_2O contents near the x-axis. The MgO-Cr_2O_3 plot (**Figure 7.6i**) shows a positive correlation where partially chloritized tholeiitic metabasalts have the lowest Cr_2O_3 contents and peridotitic cumulates have the highest contents, reflecting primary igneous compositions. Trace element versus Zr (ppm) binary diagrams has been plotted in **Figure 7.7** to show the relationship between high field strength elements (HFSEs) and rare earth elements (REEs). High field strength elements (Y, Sm, Th, Nb, Hf, Ce) and rare earth elements REE (La, Lu, Pr, Eu) have been plotted against a HFSE, namely Zr. HFSE against HFSE (**Figure 7.7a-d**) shows a strong positive correlation. In **Figure 7.7a** the Zr-Y plot shows the metadunite as having the lowest Y and Zr contents followed by peridotitic cumulates and komatiites, then lastly partially chloritized tholeiites. This is also observed in Zr-Sm and Zr-Nb (**Figure 7.7b,d**) plot and Zr-Hf and Zr-Ce (**Figure 7.7f,g**).

There is an overlap observed between komatiitic basaltic rocks and partially chloritized tholeiitic rocks regarding Th concentration in **Figure 7.7c**. The REE-normalized ratios also show similar pattern, where a positive correlation is observed in the Zr-Lu plot with the metadunite having the lowest content and partially chloritized tholeiites having the highest contents (**Figure 7.7eb)**. **Figure 7.7h,i** shows a Zr-$(La/Lu)_{cn}$ and Zr-$(Pr/Eu)_{cn}$ plots. These ratios are C1-chondrite normalized (Sun and McDonough, 1989) and thereby used to compare Kromberg type-section geochemical signatures with chondritic signatures. All samples show an enrichment relative to the chondritic concentrations. In **Figure 7.7h** the $(La/Lu)_{cn}$ ratio is used to assess the behaviour of LREE for komatiitic rocks and tholeiitic metabasaltic rocks of the Kromberg type-section. Both komatiitic basalts and partially chloritized tholeiites are enriched in LREE, whereas cumulate peridotites vary. The **Figure 7.7i** is used to assess the MREE of the komatiitic rocks and tholeiitic rocks in the Kromberg type-section. Cumulate peridotites and komatiitic basalts are depleted in MREE while majority of partially chloritized tholeiites are slightly enriched in these elements.

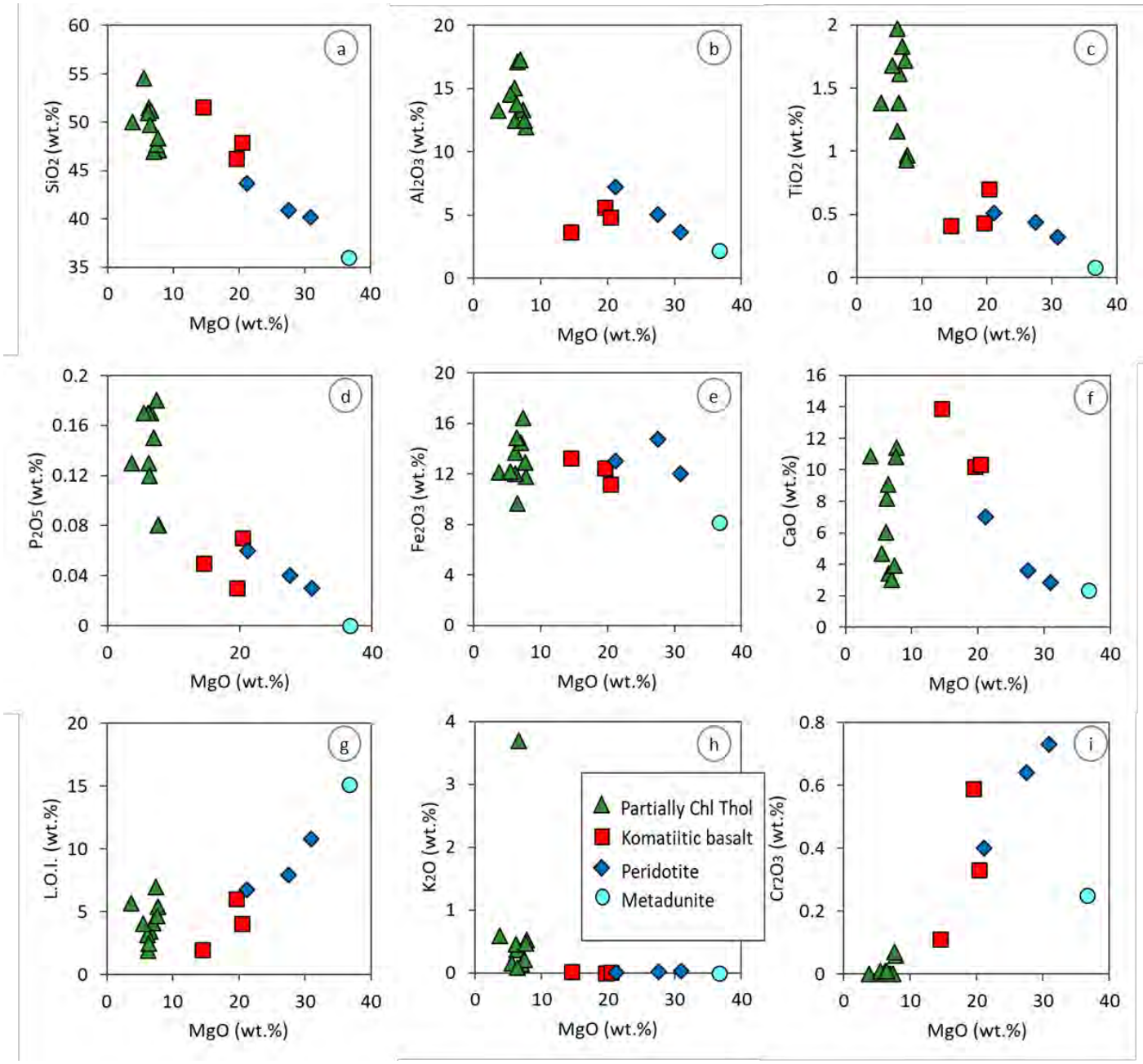

***Figure 7. 6**: Major element versus MgO (wt.%) binary plots of relatively fresh samples.*

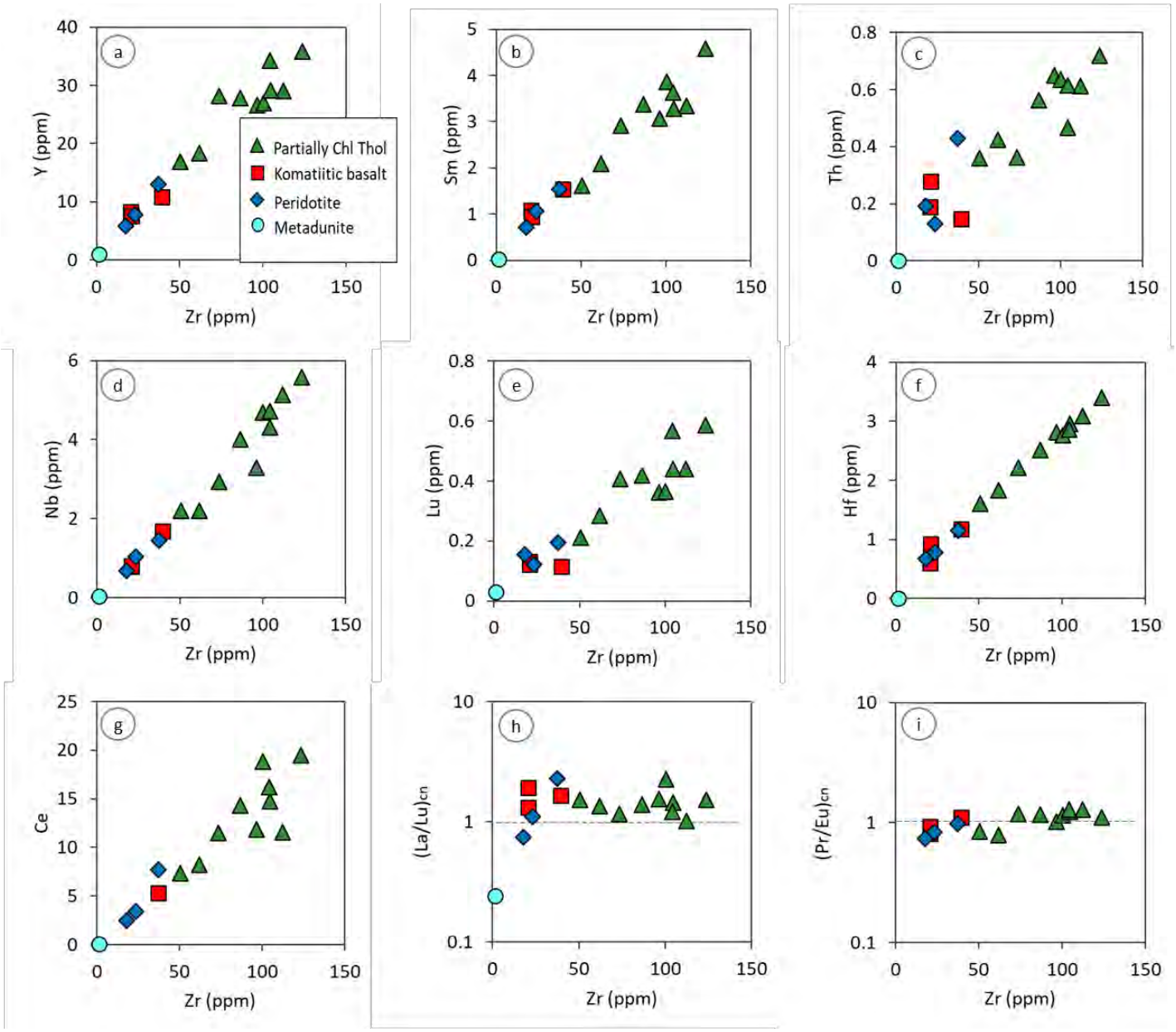

Figure 7. 7*: Trace elements versus Zr (in ppm) binary plots. (h) and (i) are C1-chondrite normalized (Sun and McDonough, 1989).*

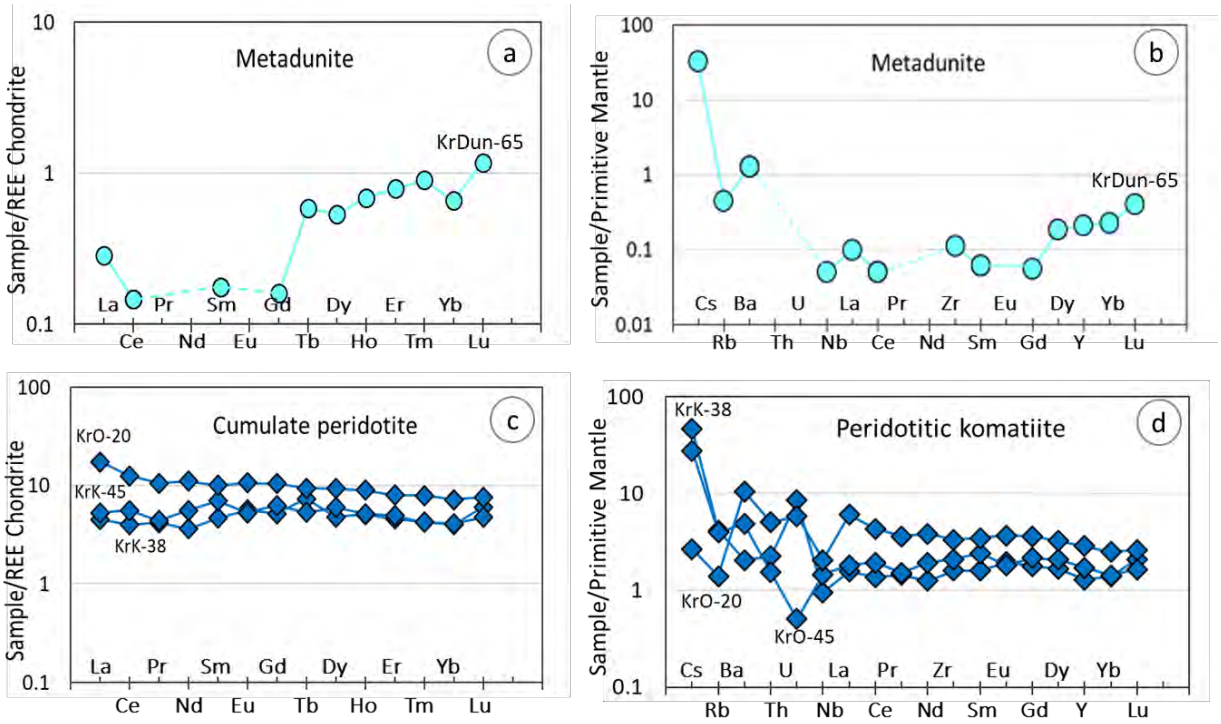

Figure 7. 8*: Normalised incompatible element diagrams for the metadunite and cumulate peridotite samples. (a) and (c) shows the C1-Chondrite normalized (Sun and McDonough, 1989) diagrams while (b) and (d) show primitive mantle normalized (Sun and McDonough, 1989) plots.*

Normalised incompatible element diagrams for different rock compositions in the Kromberg type-section have been plotted to investigate the trace element variation for each rock type. **Figure 7.8** shows chondrite-normalized REE plots and primitive mantle-normalized plots for peridotitic cumulate and metadunite, respectively. The highly serpentinized metadunite sample is depleted in LREE with $(Ce/Yb)_{cn}$ of 0.22 (Figure 7.8a). On a primitive mantle normalised plot, the metadunite has a concave upward shaping curve with positive Cs, Ba, La, Zr and Dy anomalies and negative Rb, Nb, Ce and Yb anomalies. Peridotitic cumulates (**Figure 7.8c**) have an overall negative slope for HREE and have positive and negative slope for LREE for different samples. They are depleted in LREE with $(Ce/Yb)_{cn}$ of 0.99-1.74 and enriched in HREE. KrK38 has a small positive anomaly for La, Pr and Ho and a large positive anomaly for Tb and Lu. The peridotitic cumulate sample KrK-45 has a positive anomaly for Ce, Sm, Gd and Dy and a negative anomaly for Tb and Nd (**Figure 7.8c**). The peridotitic cumulate sample KrO-20 has an overall negative slope for both LREE and HREE. It is enriched in LREE and HREE. It has a small negative Pr, Sm and Yb anomaly. On a primitive mantle normalised plot, peridotitic cumulates have concave

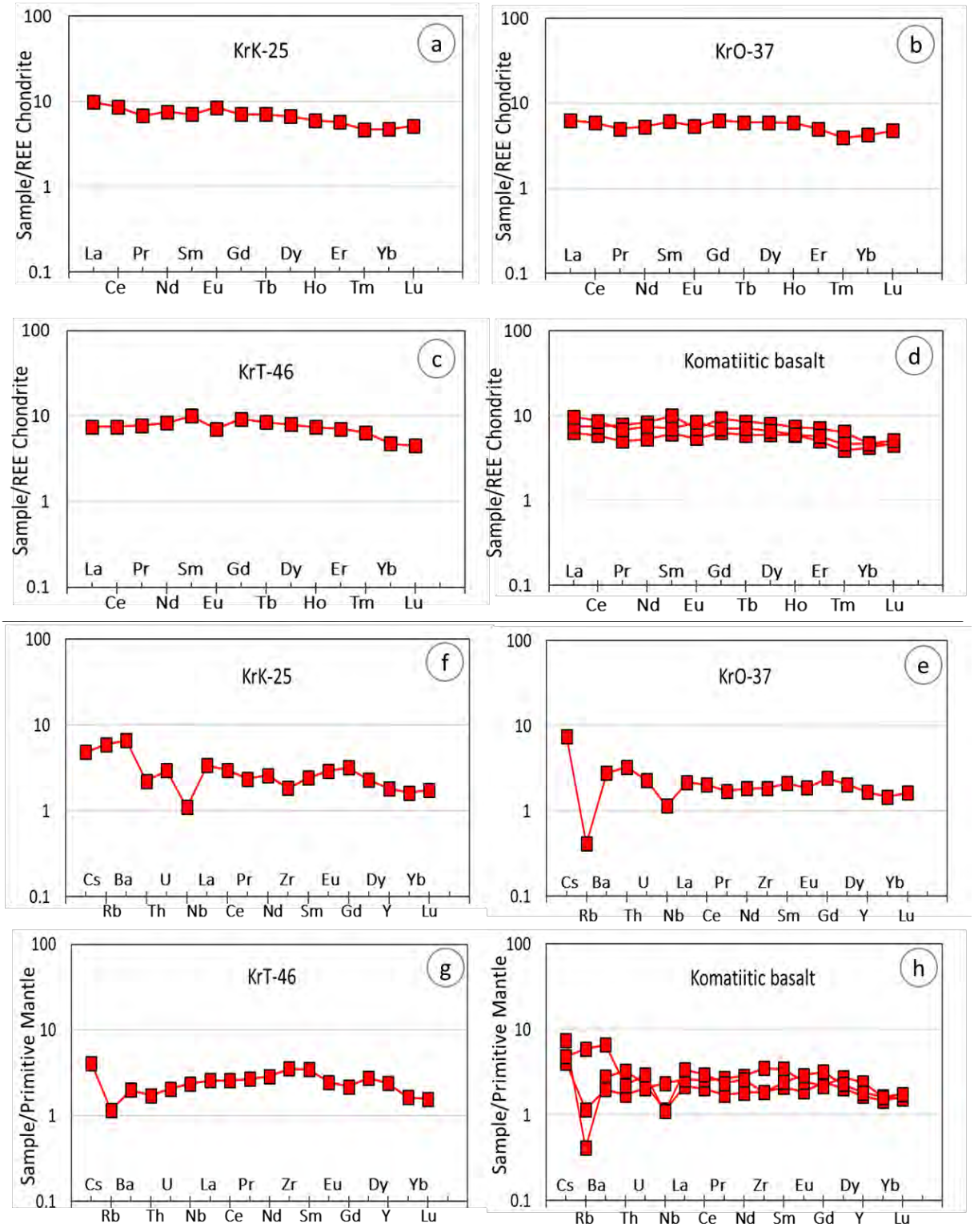

Figure 7. 9*: Normalised incompatible element diagrams for komatiitic (a) and (d) shows the C1-Chondrite normalized (Sun and McDonough, 1989) REE diagrams while (e) and (h) show primitive mantle normalized (Sun and McDonough, 1989) plots. (d) and (h) shows normalised incompatible elements for all komatiitic basalts in the Kromberg type-section.*

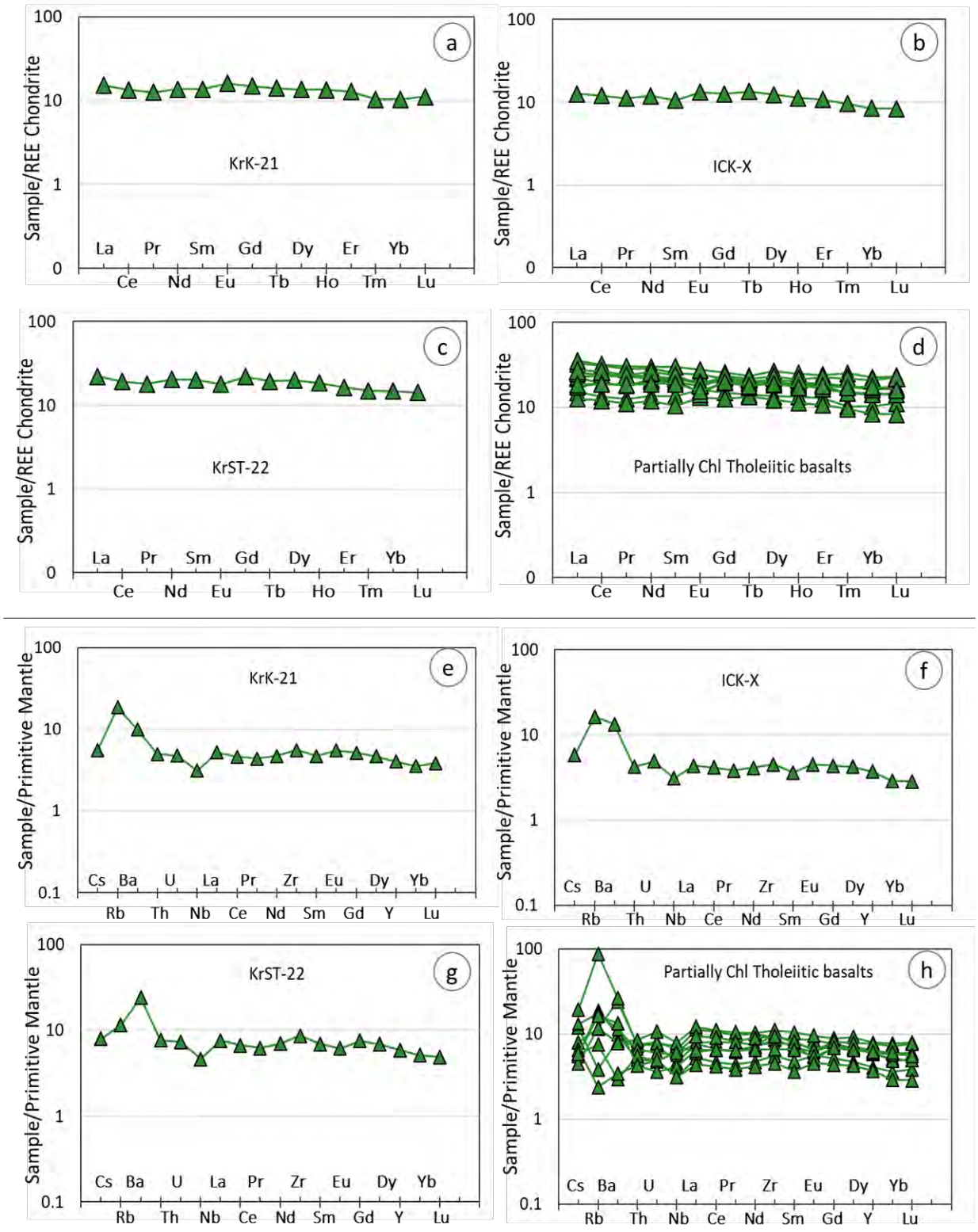

Figure 7. 10*: Normalised incompatible element diagrams for komatiitic (a) and (d) shows the C1-Chondrite normalized (Sun and McDonough, 1989) REE diagrams while (e) and (h) show primitive mantle normalized (Sun and McDonough, 1989) plots. (d) and (h) shows normalised incompatible elements for all komatiitic basalts in the Kromberg type-section.*

upward-shaped curve with a relatively flat slope for REE and varying Ba and U anomalies (**Figure 7.8d**).

Komatiitic basalts (**Figure 7.9d**) have a relatively flat slope for all REE, they are slightly enriched in LREE with $(Ce/Yb)_{cn}$ of 1.38-1.83. On primitive mantle-normalised plot, komatiitic basalts have relatively flat patterns with small negative Nb and Yb anomalies and a positive La anomaly (**Figure 7.9h**) observed in some of the samples. Partially chloritized tholeiites (**Figure 7.10d**) have a relatively flat REE pattern. All tholeiitic basalt samples, except for two, show a slightly negative slope for both LREE and HREE. Their LREE are not enriched relative to relative to the middle REE (Sm, Eu, Gd, Tb). The tholeiitic metabasalt samples have (Ce/Yb)cn ratios of 1.07-2.17 and they are depleted in HREEs. Tholeiitic metabasaltic samples KrT-21 (**Figure 7.10a**) and ICK-X (**Figure 7.10b**) have a positive slope for LREE and a negative slope for HREE. They are depleted in LREE and depleted in HREE. On primitive mantle-normalised plots, partially chloritized tholeiites have a relatively flat slope with small negative Nb and Yb anomaly (**Figure 7.10h**). Variation is observed in the large ion lithophile elements (LILEs) such as Rb and Ba, where some partially chloritized tholeiites exhibit positive anomalies and others exhibit negative anomalies.

Figure 7.11 shows binary plots for komatiitic rocks of the Onverwacht Group. Komatiitic basalts are compared to komatiitic rocks of the Mendon Formation, a formation directly above the Kromberg Formation. M2v, M1v, M4v-l and M4vu data from Byerly (1999) has been plotted to investigate and compare the type of magma that produced the high MgO rocks in the Kromberg type-section. **Figure 7.11a,b** shows the TiO_2 against V and Al_2O_3 for komatiitic rocks of the Kromberg type-section and the Mendon sequence (Byerly, 1999). Komatiitic basalts of the Kromberg type-section have TiO_2 compositions between 0.4 and 0.8 wt.% and V compositions between 100 and 200 ppm (**Figure 7.11a**). High MgO rocks of the Kromberg type-section plot in the region where M2v and M1v (of the Mendon) plot. They are further away from M4v-l and M4v-u contents. This means that the magma source of M1v-u and M2v could be similar to the magma source type for the Kromberg type-section komatiitic rocks. **Figure 7.11b** shows a TiO_2-Al_2O_3 plot that is divided according to the Al_2O_3/TiO_2 ratios. In this diagram, high MgO rocks of the Kromberg type-section also plot with the M2v and M1v-u of the Mendon Formation, a similar pattern to that observed in **Figure 7.11a**. They have Al_2O_3/TiO_2 ratios between 5 and 20.

There are two types of komatiites: Al-depleted and Al-undepleted komatiites (Nesbitt and Sun, 1976). The Al-undepleted komatiites are further classified as Munro-type komatiites (locality in Abitibi greenstone belt) while the Al-depleted komatiites were classified as Barberton-type komatiites (Arndt, 2003). According to Gruau et al. (1990), Al-undepleted komatiites have Al_2O_3/TiO_2 ratios between 15 and 30, Al-depleted komatiites have Al_2O_3/TiO_2 ratios less than 15 and another group of komatiites, the Al-enriched komatiites, is recognised with ratios exceeding 30. Al-undepleted komatiites form by extreme melting of the mantle at shallower depth, in the absence of garnet, leaving olivine as a residual phase and Al-depleted komatiites melt at a greater depth with garnet forming the residual phase (Arndt, 2003). According to Ohtani et al. (1989) Al-undepleted komatiites melt at <450 km and Al-depleted komatiites at depths between 450-650 km. Al-enriched komatiites are recognised to form through multi-stage melting with residual garnet in the source (Gruau et al., 1990). Al-depleted komatiites have low Al_2O_3/TiO_2 (less than 16; **Figure 7.11c**) and high CaO/Al_2O_3 (greater than 1; **Figure 7.11d**) while Al-undepleted komatiites have higher Al_2O_3/TiO_2 (greater than 20) and lower CaO/Al_2O_3 (less than 1). **Figure 7.11c,d** makes use of CaO/Al_2O_3, Al_2O_3/ TiO_2 and (Gd/Yb)pm ratios to constrain the mantle source characteristics of komatiitic rocks found in the Kromberg type-section. In these plots, melting in the presence of garnet as a residual phase is attributed to komatiitic rocks with high CaO/Al_2O_3 and (Gd/Yb)pm (greater than 1) and low Al_2O_3/TiO_2 (less than 16) in accordance to Jahn et al. (1982) and Gruau et al. (1992).

The binary plot in **Figure 7.11b** reveals that the komatiitic basalts are Al-depleted having ratios Al_2O_3/TiO_2 ratios less than 15. According to Al_2O_3/TiO_2-$(Gd/Yb)_{pm}$ plot (**Figure 7.11c**), komatiitic basalts of the Kromberg type-section plot in the garnet fractionation field. Similarly, in **Figure 7.11d** komatiitic basalts plots in the garnet fractionation field in a CaO/Al_2O_3-$(Gd/Yb)_{pm}$ diagram. In the **Petrography Chapter 5**, komatiitic basalt were discovered to be partially altered by quartz and carbonate in their matrix. This potentially may have resulted in significantly high CaO compositions for komatiitic basalts. It is proposed that **Figure 7.11c** is therefore more reliable for investigating Al-depletion or -enrichment for the Kromberg type-section komatiitic basalts. The komatiitic rock samples in the Kromberg type-section are Al-depleted and requires garnet in equilibrium with the melt in the mantle source region. Garnet in the source region requires deep mantle melting depths of between 450 – 650 km (e.g. Jahn et al. 1982; Ohtani et al., 1989 and Gruau et al. 1992; Byerly et al., 1999).

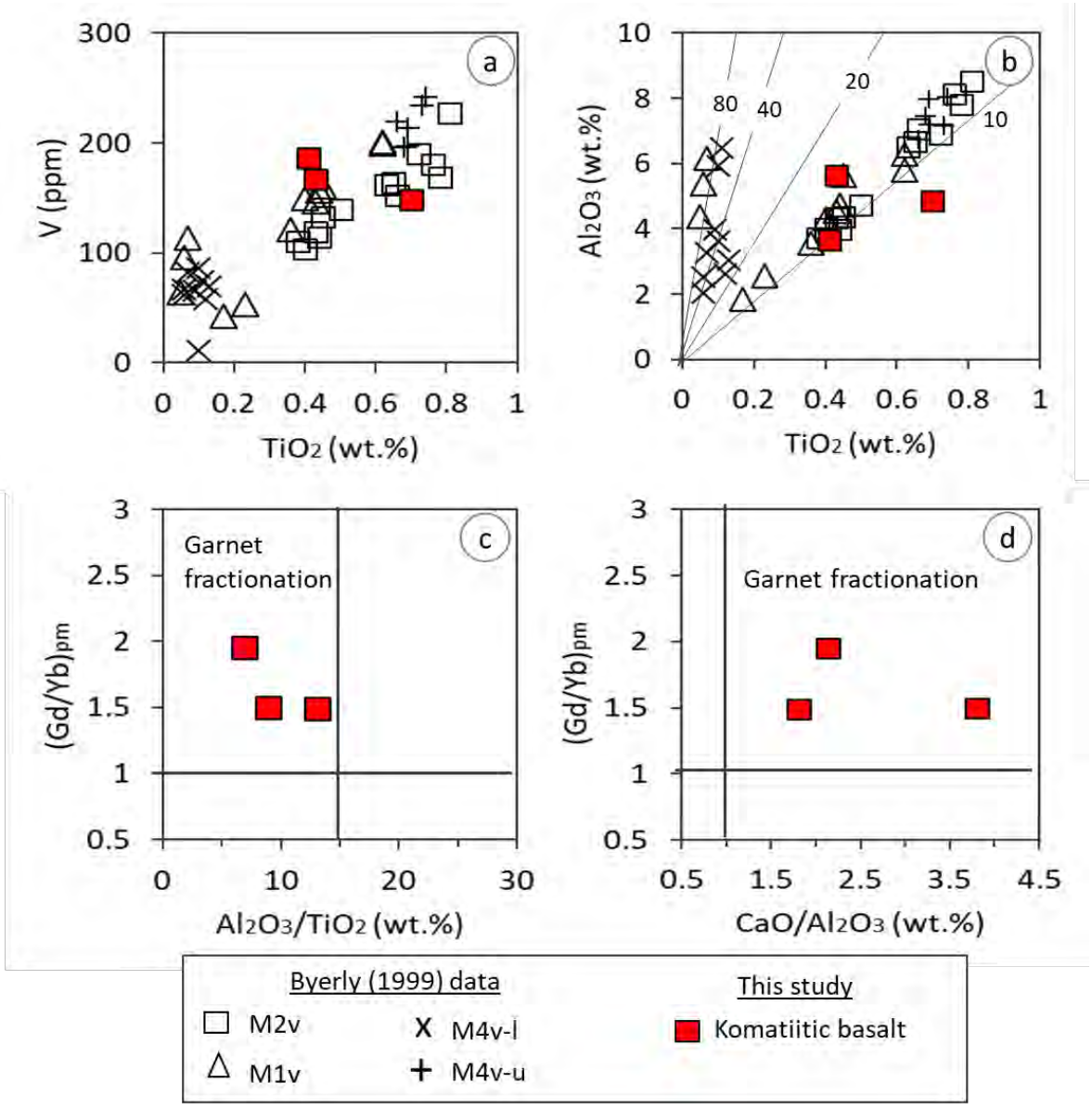

Figure 7. 11*: (a)and (b) Binary plots of with the Kromberg type-section data and Mendon Formation komatiite rock data (Byerly, 1999), used to investigate the magma type for komatiite rocks. The numbers in (b) represent Al_2O_3/TiO_2 ratios. (c) and (d) Komatiitic basalts plot in the garnet fractionation fields of the $(Gd/Yb)_{pm}$ vs Al_2O_3/TiO_2 and $(Gd/Yb)_{pm}$ vs CaO/Al_2O_3 binary diagrams in accordance to Jahn et al. (1982) and Gruau et al. (1992).*

To investigate further the petrogenesis of the Kromberg type-section, partially chloritized tholeiitic rocks were plotted on binary geochemical plots and compared to Mariana arc boninites (Reagen et al., 2010) and crustally contaminated boninites associated

with the Bushveld complex (Hatton and Sharpe, 1989). In this diagram (**Figure 7.12a**) partially chloritized tholeiites are plotted in the Nb versus La/Nb plot where a region for Mariana forearc boninites and crustally contaminated boninites is drawn. From this plot a data point that represents Stolzberg felsic trondhjemite (Stolz TTG; Kleinhanns et al., 2003) is included together with a datapoint showing an average composition of the Archean Upper Continental Crust (AUCC; Rudnick and Gao, 2004). It is observed that partially chloritized tholeiites of the Kromberg type-section increases in Nb contents as La/Nb decreases. However, the decrease in La/Nb is small compared to the increase in Nb. It is noted that partially chloritized tholeiites have slightly higher La/Nb values than N-MORB at the same Nb concentration. The data also plot further away Mariana forearc boninite field. The La/Nb versus Nb diagram, illustrates that the tholeiitic metabasalts and komatiitic basalts do not plot in the crustal contamination and subduction arc fields. The tholeiitic metabasalts plot closer to the primitive mantle and N-MORB compositions (**Figure 17.12a**). This suggests that the Kromberg type-section rocks did not form in the forearc subduction basin and is not affected by crustal contamination. Further plots are required to investigate the result for high Nb contents.

The **Figure 7.12b** shows a La/Ta versus La/Sm diagram (modified after Lassiter and DePaolo, 1997) where partially chloritized tholeiites and komatiitic basalts of the Kromberg type-section ar plotted. In this plot, the rock compositions of the Kromberg type-section have low La/Sm ratios where a positive trend is observed between La/Ta and La/Sm. Partially chloritized tholeiitic metabasalts have slightly higher La/Sm ratios compared to komatiitic basalts. The metabasalts all plot along the plume or sub-lithospheric mantle mixing trend. The Stolzberg TTG datapoint and crustal contamination field is farther away from the Kromberg data, ruling out the possible effect of crustal contamination. Furthermore, the Kromberg tholeiitic metabasalt compositional data plots near the primitive mantle composition in the diagram (**Figure 7.12b)**. From both plots in **Figure 7.12 (a, b)** it can be deduced that the Kromberg type-section did not form in a forearc subduction zone setting and the Nb contents are not due to crustal contamination.

To investigate further whether the Kromberg type-section rocks formed in an oceanic arc or in a different setting, data from different Archean greenstones belts was selected for global comparison. These greenstones either had an oceanic arc setting or an oceanic plateau setting and also have different ages: the Abitibi greenstone belt formed at ca. 2.7 Ga (Laflèche et al., 1992), Isua greenstone belt at ca. 3.7 Ga (Polat et al., 2002), Sumozero

greenstone belt at ca. 2.9 Ga (Puchtel et al., 1999); Holenarsipur greenstone belt at ca. 3.3 Ga (Khanna et al., 2018) and Koolyanobbing greenstone belt at ca. 3.0 Ga (Angerer et al., 2013). The **Figure 7.13** contains plots where these different greenstone belts are compared to the Kromberg type-section rocks. In these plots, greenstone belts with an oceanic arc origin are assigned a blue colour whereas those that have an oceanic plateau origin are assigned a pink colour; partially chloritized tholeiites of the Kromberg type-section remain the same colour used throughout the thesis, namely dark green. **Figure 7.13a** shows a MgO (wt.%) versus Nb/Th plot where greenstone belts with an oceanic arc setting have lower Nb/Th ratios compared to those with an oceanic plateau origin. There is a spread in MgO (wt.%) values for oceanic arc greenstone belts and a tighter cluster of compositions for oceanic plateau greenstone belts (**Figure 7.13a**). The Kromberg type-section metabasalt data shows a tight cluster with low MgO and high Nb/Th. The Kromberg type-section metabasalt data points plot in the same compositional region as greenstone belts with the oceanic plateau setting (**Figure 7.13a**).

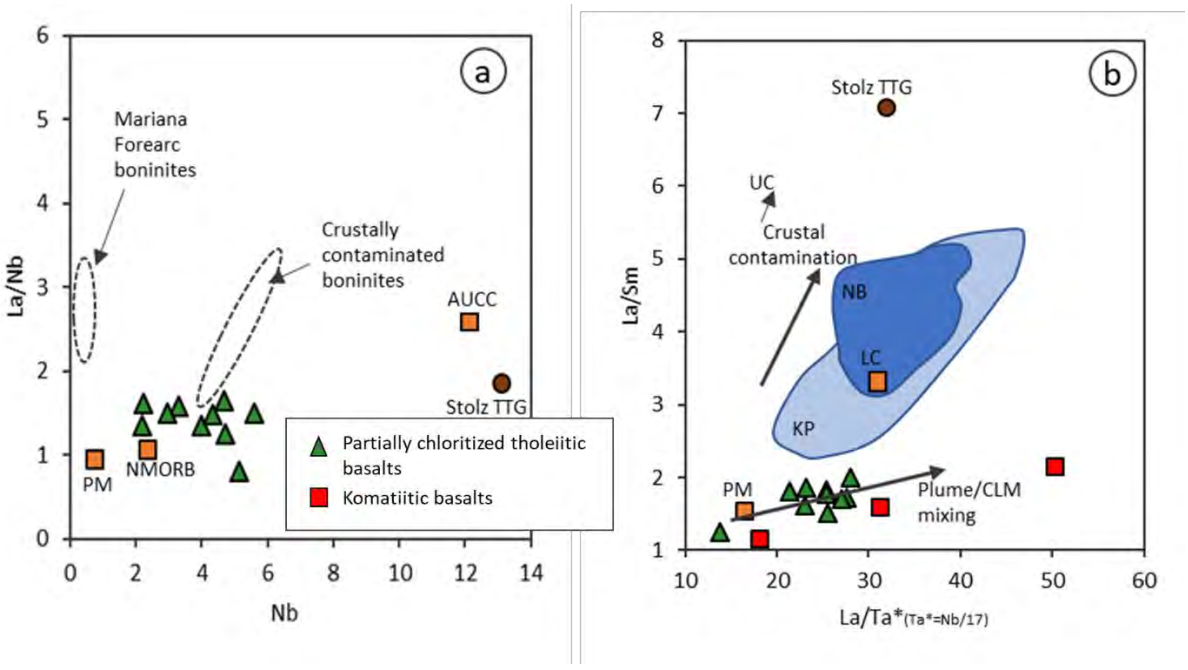

Figure 7. 12*: Global discriminant diagrams where (a) partially chloritized tholeiites are compared to Mariana forearc boninite (Reagen et al., 2010) and crustally contaminated boninites (Hatton and Sharpe, 1989); and (b) komatiitic basalts are compared to Karoo Picrites (KP; Lassiter and DePaolo, 1997) and Nadezhdinsky lavas (NB) in a La/Ta-La/Sm plot (modified after Lassiter and DePaolo, 1997). AUCC=Archean Upper Continental Crust (Rudnick and Gao, 2004), Stolz TTG= Stolzberg TTG (Kleinhanns et al., 2003); PM=Primitive mantle and NMORB=Normal Mid-Oceanic Ridge*

Basalt (Sun and McDonough, 1989); UC=Upper continental crust and LC=Lower continental crust (Taylor and McLennan, 1985); CLM=Continental Lithosphere Mantle.

Figure 7.13b is a TiO_2-Zr plot where both the oceanic plateau and oceanic arc greenstone belts have a positive correlation. The Kromberg type-section tholeiitic metabasalt data plots with the oceanic plateau greenstone belts but overlaps with the oceanic arc greenstone belts (**Figure 13b**). This overlap occurs with the oceanic arc related 2.7 Ga Abitibi greenstone belt. **Figure 7.13c** shows a Mg-number-$(Gd/Yb)_{pm}$ plot where Gd and Y concentrations are normalized to the primitive mantle (Sun and McDonough, 1989). In this diagram, there is a clear distinction between oceanic arc greenstone belts ($(Gd/Yb)_{pm} < 1$) and oceanic plateau greenstone belt ($(Gd/Yb)_{pm} > 1$). The oceanic arc greenstone belts have higher Mg-number and lower $(Gd/Yb)_{pm}$ compositions compared to the oceanic plateau greenstone belts. The Kromberg type-section metabasalt data plots within the oceanic plateau greenstone belt field in this diagram (**Figure 7.13c)**.

The **Figure 7.13d** is a Y (ppm) versus primitive mantle normalized (Sun and McDonough, 1989) Gd/Yb diagram. There is a spread observed for $(Gd/Yb)_{pm}$ values in the oceanic arc greenstone belts and a tight cluster observed for oceanic plateau greenstone belts. Partially chloritized tholeiitic metabasalts of the Kromberg type-section have overlapping trace element signatures with oceanic plateau greenstone belts (**Figure 7.13d)**. From these plots in **Figure 7.13**, the Kromberg type-section shows a strong geochemical correlation with oceanic plateau greenstone belts and not oceanic arc-related greenstone belts. This observation agrees with **Figure 7.12a** where partially chloritized tholeiitic basalts show very little geochemical relation to Mariana forearc boninites. A Pearce (2008) diagram is also plotted in **Figure 7.14** to evaluate the geodynamic setting of the 3.3 Ga Kromberg type-section rocks. **Figure 7.14a** is the plot which includes the Stolzberg TTG composition (Kleinhanns et al., 2003), N-MORB, Primitive Mantle (PM), enriched-MORB and ocean island basalt (OIB; Sun and McDonough, 1989). The light green triangle represents the average composition of the partially chloritized tholeiitic basalts (**Figure 7.14a)**. Partially chloritized tholeiites plot slightly above the mantle array near the primitive mantle composition (**Figure 7.14a)**. They plot in the tholeiitic field, away from the active continental margin and oceanic arc field. The Stolzberg TTG data point represents the Archean continental crust. The Kromberg type-section tholeiitic metabasalt rock compositions plot

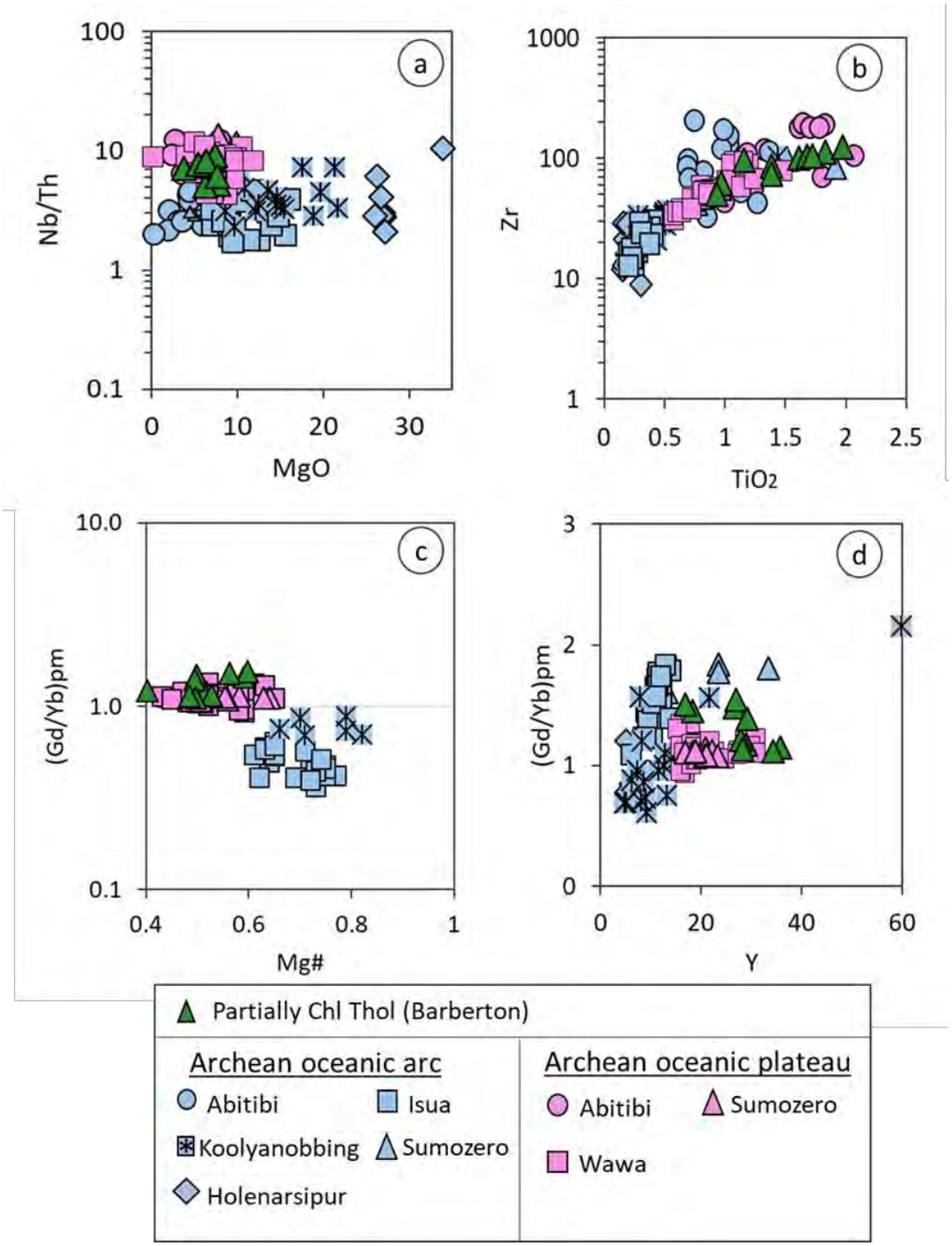

Figure 7. 13: *Geochemical binary plots where Archean oceanic arc greenstone belts and oceanic plateau greenstone belts are compared to the Kromberg type-section. Reference data include that of the. Abitibi greenstone belt formed at c. 2.7 Ga (Lafléche et al., 1992), the Isua greenstone belt at 3.7 Ga (Polat et al., 2002), the Sumozero greenstone belt at 2.9 Ga (Puchtel et al., 1999); the Holenarsipur greenstone belt at 3.3 Ga (Khanna et al., 2018) and the Koolyanobbing greenstone belt at 3.0 Ga (Angerer et al., 2013). (a) Is a logNb/Th-MgO plot, (b)a logZr-TiO_2 plot, (c) a log $(Gd/Yb)_{pm}$-Mg-number plot and (d) $(Gd/Yb)_{pm}$-Y plot. (c) and (d) are normalized to the primitive mantle (Sun and McDonough, 1989).*

outside the backarc and forearc fields and away from the Archean continental crust (**Figure 7.14a,b)**. They do not record subduction zone geochemical signatures (**Figure 7.14a)**. Furthermore, comparison with Archean oceanic arc and oceanic plateau greenstone belts was conducted in the Pearce (2008) plot in **Figure 7.15**. **Figure 7.15a** shows the metabasalt datasets of different greenstone belts and **Figure 7.15b** shows the average compositions of different greenstone belt metabasalts. The oceanic arc greenstones have a widespread in Th/Yb and Nb/Yb ratios, spreading towards the active continental margin and oceanic arc field. The Isua greenstone belt average in **Figure 7.15b** lies above the backarc field together with the Holenarsipur and Koolyanobbing greenstone belt average compositions overlapping in the backarc and forearc fields. The oceanic plateau greenstone belts plot in the tholeiitic field with the primitive mantle and with a slight overlap in the mantle array (**Figure 15b**). The oceanic plateau greenstone belt metabasalt datasets overlap with Kromberg type-section metabasalt compositional data points. Their average compositions in **Figure 7.15b** lie below the backarc region and slightly overlap the mantle array. Wawa and Abitibi greenstone belts with an Archean oceanic plateau origin have average geochemical signatures that overlap with the average composition of the Kromberg type-section metabasalts and the primitive mantle. From **Figure 7.14** and **7.15** it can be deduced that Kromberg type-section tholeiitic metabasalts has an oceanic plateau origin and is possibly associated with primitive mantle plumes and is not affected by crustal contamination or Archean subduction zone processes. It is not geochemically related to oceanic arc greenstone belts but records strong geochemical similarities with other Archean oceanic plateau greenstone belts.

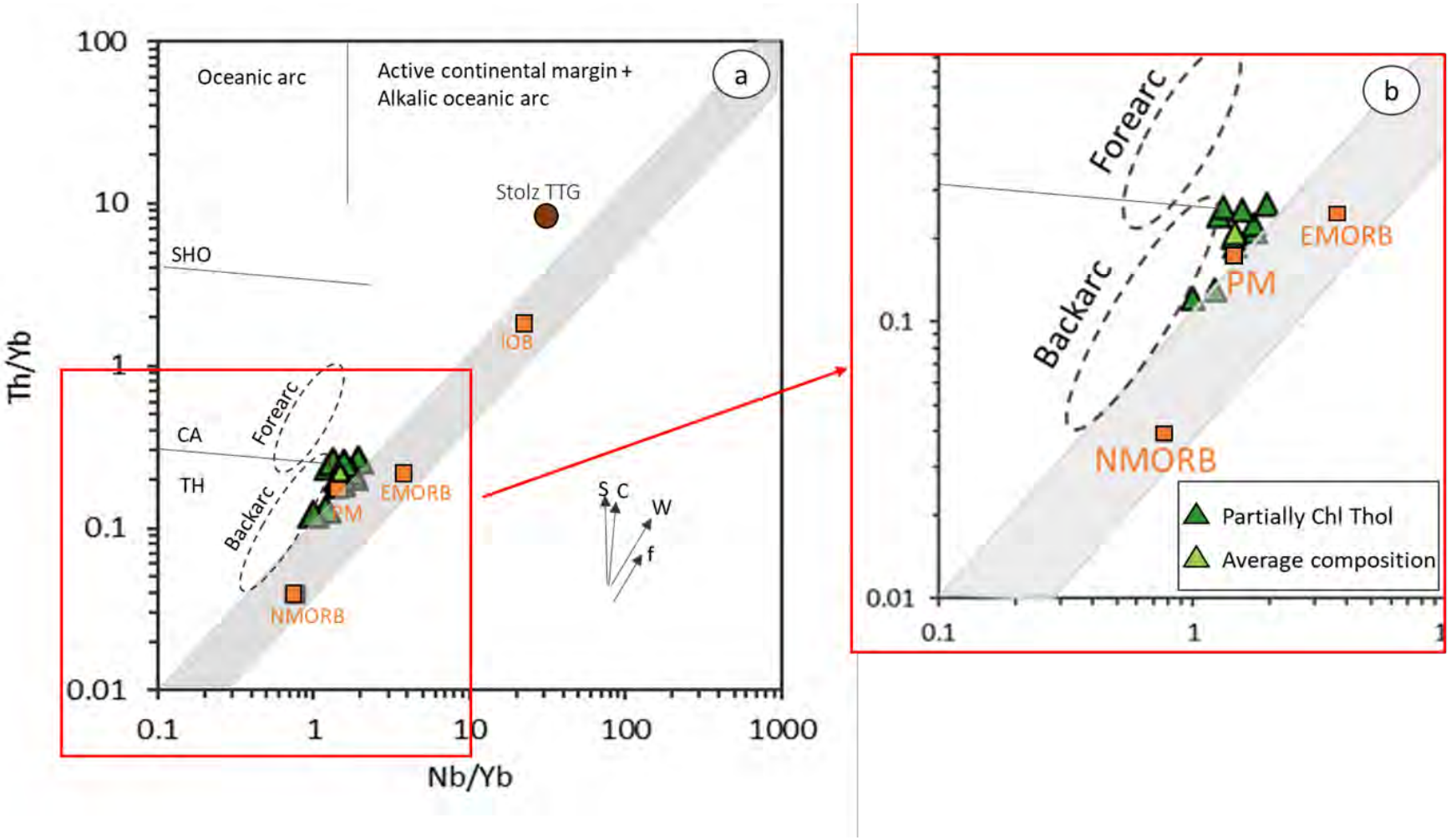

Figure 7. 14*: Nb/Yb-Th/Yb plot (modified after Pearce, 2008). S=subduction, C=crustal contamination, W=within plate and f=fractional crystallisation vectors. (b) is the insert magnification of (a). A field for backarc and forearc is included in the diagram. The light green triangle represents the average composition of the partially chloritized tholeiites.*

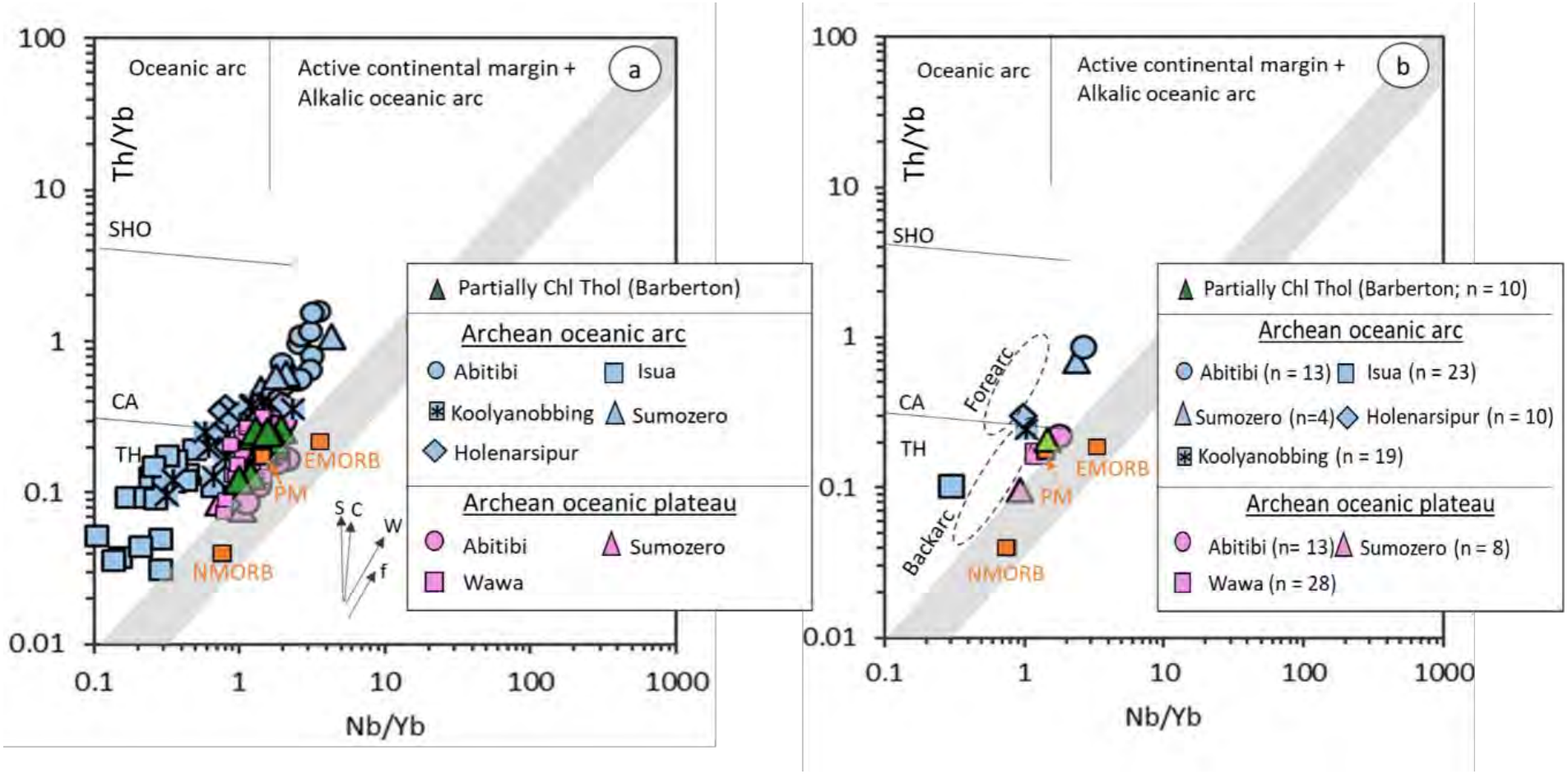

Figure 7. 15*: Nb/Yb-Th/Yb plot modified after Pearce (2008). (a) shows that different datasets for different greenstone belts and (b) shows their average composition. Abitibi greenstone belt formed 2.7 Ga (Lafléche et al., 1992), Isua greenstone belt: 3.7 Ga (Polat et al., 2002), Sumozero greenstone belt: 2.9 Ga (Puchtel et al., 1999); Holenarsipur greenstone belt: 3.3 Ga (Khanna et al., 2018) and Koolyanobbing greenstone belt: 3.0 Ga (Angerer et al., 2013).*

7.1.5 Comparison to previous geochemical work on the Kromberg type-section

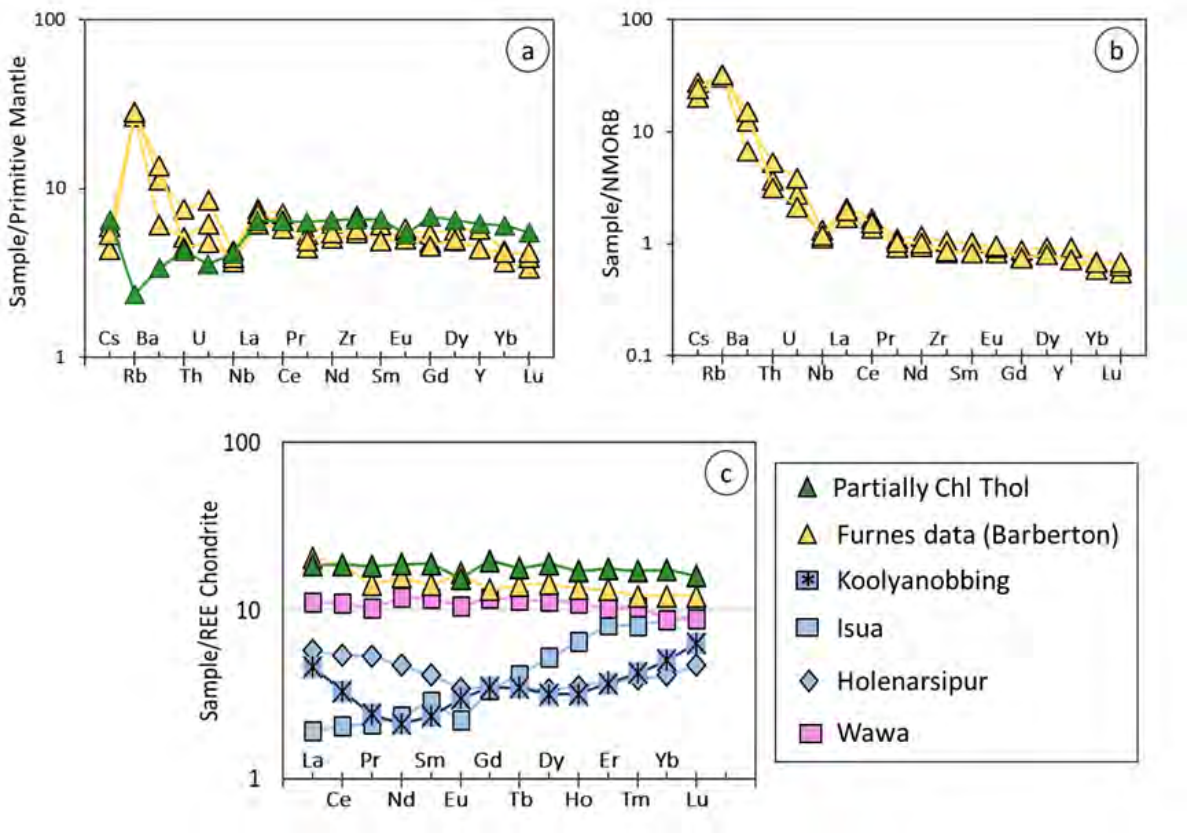

Figure 7. 16: *(a)Primitive-mantle normalized and (b) N-MORB normalized multi-element diagrams comparing the Kromberg type-section data to published data of Furnes et al.,2012)..(c) Shows C1-normalized REE diagram comparing data from the Kromberg type-section to other greenstone belts, i.e. Koolyanobbing (Angerer et al., 2013), Isua (Polat et al., 2002), Holenarsipur (Khanna et al., 2018) and Wawa greenstone belt (Polat et al., 1999). Only selected representative samples plotted for clarity in all diagrams.*

After screening for alteration, partially chloritized tholeiitic metabasalts of the Kromberg type-section are plotted with metabasaltic data from other greenstone belts in **Figure 7.16** for comparative purposes. In addition to the data from this study, published data on the south-eastern limb of the Kromberg type-section from Furnes et al. (2012) is plotted on N-MORB and primitive mantle-normalised diagrams (Sun and McDonough, 1989). In **Figure 7.16a** only Kromberg type-section data from this study and Furnes et al. (2012) study are plotted. Data from this current study is not plotted in the N-MORB normalized diagram in **Figure**

7.15b as unlike in the Furnes et al. (2012) case, this current study argues against N-MORB normalization for the Archean 3.3 Ga Kromberg type-section rocks (see succeeding discussion). Furnes et al. (2012) data shows a prominent positive Rb anomaly and a negative Nb anomaly in the primitive mantle normalized diagram (**Figure 7.15a**), this is not observed in the relatively fresh chloritized tholeiitic metabasalt in the current study (**Figure 7.15a**). The negative Nb anomaly is not pronounced in the primitive mantle normalized plots for metabasalts in the current study. The N-MORB normalized diagram displays a positive Rb anomaly and a negative Nb anomaly (**Figure 7.15b**). There are also differences in U and Th abundances between Furnes et al. (2012) data and data from this current study, metabasalts in this study have lower abundances in U and Th. These differences are proposed to have formed as a result of different analytical methods applied in Furnes et al. (2012) compared to this study. Furnes et al. (2012) deduced, based on the small negative Nb anomaly (in N-MORB and primitive mantle diagrams) and other trace element data, that the Kromberg type-section has a back-arc setting with a subduction zone signature. In this study based on trace element data, the back-arc subduction origin is not favoured as the small negative Nb anomaly is not adequately prominent for subduction and other elemental abundances, for instance, high U, could cause an apparent negative Nb anomaly. In this study, it is also noted that the small negative Nb anomaly and large ion lithophile element (LILE) enrichment is more prominent in the N-MORB normalized diagram than in the primitive mantle normalized diagram (**Figure 7.15a,b**). Since the Kromberg type-section rocks have more primitive Archean compositions (see **Figure 7.14**), the primitive mantle normalization approach is suggested as reliable for the Kromberg type-section rocks. Furthermore, a comparison in chondrite normalized REE patterns is conducted for different greenstone belt rocks (**Figure 7.16c**). In this diagram, the Kromberg type-section metabasalts has a relatively flat pattern, similar to the Wawa greenstone belt (Polat et al., 1999); it is not w-shaped like the pattern observed in subduction-related Koolyanobbing (Angerer et al., 2013) and Holenarsipur (Khanna et al., 2018) greenstone belt and is not s-shaped like the REE pattern observed in Isua greenstone belt (Polat et al., 2002). The Kromberg type-section metabasalts thus have similar compositions to proposed Archean oceanic plateau greenstone belts and does not record strong geochemical evidence of subduction zone processes (**Figure 7.16c**).

7.1.6 Summary

In this chapter, whole-rock major and trace elements are used for geochemical classification and to assess alteration effects on the geochemistry of rocks. Highly altered rock compositions are separated from partially altered compositions to track geochemical changes and element mobility during secondary alteration processes. It is observed that silicification has significantly changed the geochemistry of the rocks, whereas chloritization did not largely affect the protolith rock chemistry in the Kromberg type-section. Silicified tholeiitic metabasalts are enriched in SiO_2, K_2O, Rb and LREE, and depleted in MgO, CaO and Na_2O. The elements V, Yb and Gd are immobile and remain unaffected by both chloritization and silicification, whereas the HREE of silicified tholeiites are show mobility during alteration and a highly variable pattern in REE plots (see summary of geochemical signatures in **Table 7.3**). Silicified (both highly and partially silicified) tholeiitic metabasalts and highly chloritized tholeiitic metabasalts have been screened from geochemical classification and petrogenetic interpretation to increase precision for classification and magmatic interpretation.

After filtering and geochemically classifying the least altered rock compositions, the Kromberg type-section was discovered to comprise partially chloritized tholeiitic basalts, metadunite, poikilitic wehrlite (peridotitic cumulate) and Geluk-type and Badplaas-type komatiitic basalts. The rock compositions of the Kromberg type-section display a fractional crystallisation trend, where the most primitive rock, the metadunite, has the highest MgO and lowest SiO_2 while the most evolved rocks have the lowest MgO and highest SiO_2 (**Table 7.3**). The same rocks reveal a large compositional gap in Al_2O_3 (wt.%) compositions between komatiitic basalts and partially chloritized tholeiitic metabasalts. The Al_2O_3 compositional gap is interpreted as representing the different pressure conditions in the mantle source of komatiitic basalts and tholeiitic metabasalts. The chondrite normalized REE plots revealed a depletion in LREE for metadunite and peridotitic cumulates and a slight enrichment in LREE for komatiitic basalts and partially chloritized tholeiitic basalts. Their primitive mantle-normalized diagrams revealed a very small negative Nb and Yb anomaly for komatiitic basalts and partially chloritized tholeiitic basalts. The metadunite has a positive Cs, Ba, La, Zr and Dy and a negative Rb, Nb, Ce and Yb. The komatiitic basalts are Al-depleted with Al_2O_3/TiO_2 ratios less than 15. The small negative Nb anomaly is less pronounced in

primitive mantle normalized diagrams and is not pronounced enough to represent subduction related processes.

Table 7. 3*: Summary of selected geochemical signatures of different rock compositions in the Kromberg type-section.*

Rock name	**MgO (wt.%)**	**FeO total (wt.%)**	**Al_2O_3 (wt.%)**	**Ba (ppm)**	**Rb (ppm)**
Highly silicified tholeiitic basalt	0.29 - 4.05	0.12 - 0.53	10.30 - 18.80	133 - 344	63.80 - 83.50
Highly chloritized tholeiitic basalt	5.28 - 7.70	1.28 - 1.38	13.71 - 17.34	66.90 - 113.70	6.23 - 24.87
Partially silicified tholeiitic basalt	2.26 - 10.33	0.29 - 0.82	13.40 - 17.19	16.80 - 105.60	0.28 - 61.50
Partially chloritized tholeiitic basalt	3.73 - 7.77	0.87 - 1.48	11.95 - 17.29	23.70 - 185.10	1.51 - 55.40
Komatiitic basalt	14.52 - 20.41	1.00 - 1.19	3.65 - 5.62	13.90 - 46.10	0.26 - 3.78
Cumulate peridotite	21.17 - 30.90	1.08 - 1.32	7.25 - 3.63	14.30 - 73.60	0.89 - 2.63
Metadunite	36.67	0.73	2.23	8.9	0.28

Various geochemical plots were also used to investigate the petrogenesis of the volcanic rocks in the Kromberg type-section. Partially chloritized tholeiites have similar geochemical compositions to the primitive mantle composition and plots close to, but mainly away from crustally contaminated boninite field (see Hatton and Sharpe, 1989) and Mariana Forearc boninites (Reagan et al., 2010). In addition, different geochemical plots are used to investigate the geodynamic setting by comparing the Kromberg type-section rocks globally to different greenstone belts with oceanic arc or oceanic plateau setting (Abitibi, Isua, Sumozero, Holenarsipur and Koolyanobbing greenstones). The Kromberg type-section tholeiitic metabasalt rocks have similar compositions to Archean greenstone belts with a proposed oceanic plateau setting (see **Figure 7.13**). In the Pearce (2008) Th/Yb-Nb/Yb diagram, Kromberg type-section data plots in the oceanic region, slightly above the mantle

array, near the primitive mantle composition and below (outside) the back-arc and fore-arc fields. This means that the mantle source for the Kromberg type-section metabasalts are primitive and that the geodynamic setting for the Kromberg type-section, most likely, does not involve a back-arc or fore-arc subduction zone setting.

7.2 Lu-Hf isotope geochronology and application

7.2.1 Background to the Lu-Hf isotope system and application to Archaean rocks/minerals

Hafnium (Hf) is a lithophile element. It has an atomic number of 72 and six isotopes, ^{174}Hf, ^{176}Hf, ^{177}Hf, ^{178}Hf, ^{179}Hf and ^{180}Hf, of which one, ^{176}Hf, is radiogenic. It is geochemically similar to Zr and Ti in terms of ionic radius. ^{176}Hf is a daughter isotope formed by radioactive decay of ^{176}Lu. The Lu-Hf radiogenic isotope system is a very useful tool in the Earth Sciences in the fields of geochronology and tracer isotopic applications (Vervoort, 2015) because both Hf (as a HFSE) and Lu (as a HREE) are highly immobile during alteration and low-medium grade metamorphism. By convention, for the Lu-Hf system the reference stable isotope is ^{177}Hf. Lutetium (Lu) with time and with the half-life of 37.12 Gyr decays to Hf, and consequently they are both different from each other, thereby geochemically behaving very differently. Lu is a Rare-Earth-Element (REE), has a valence of +3 and is lighter (with an atomic mass of 174.967 u) than Hf. Hf is heavier (with an atomic mass of 178.49 u) than Lu and has a valence of +4. Since the daughter element, Hf, is more incompatible than the parent element, the residual solid after melting (depleted mantle) has higher Lu/Hf ratios compared to the melt. Because Hf partitions into the melt, Hf is relatively abundant in the continental crust (5.3 ppm; Rudnick and Gao, 2003) and less so in the Earth's mantle (0.28 ppm; McDonough and Sun, 1995). The radiogenic Hf isotope is produced by Lu through beta decay:

$$^{176}\text{Lu} \rightarrow {}^{176}\text{Hf} + \beta^{-}.$$

The general decay equation is given by:

$$R(p) = R(t) + K(p) * (e^{\lambda t} - 1),$$

where R is an isotopic ratio of a daughter element and K is a ratio of a parent to daughter isotope, $R_{(p)}$ and $K_{(p)}$ are measurable ratios, $R_{(t)}$ is the isotopic composition of daughter

element at the time of formation and λ is a decay constant. For Lu-Hf system, the decay equation is given by:

$$^{176}Hf\,(p) = {}^{176}Hf(t) + {}^{176}Lu(p) * (e^{\lambda t} - 1)$$

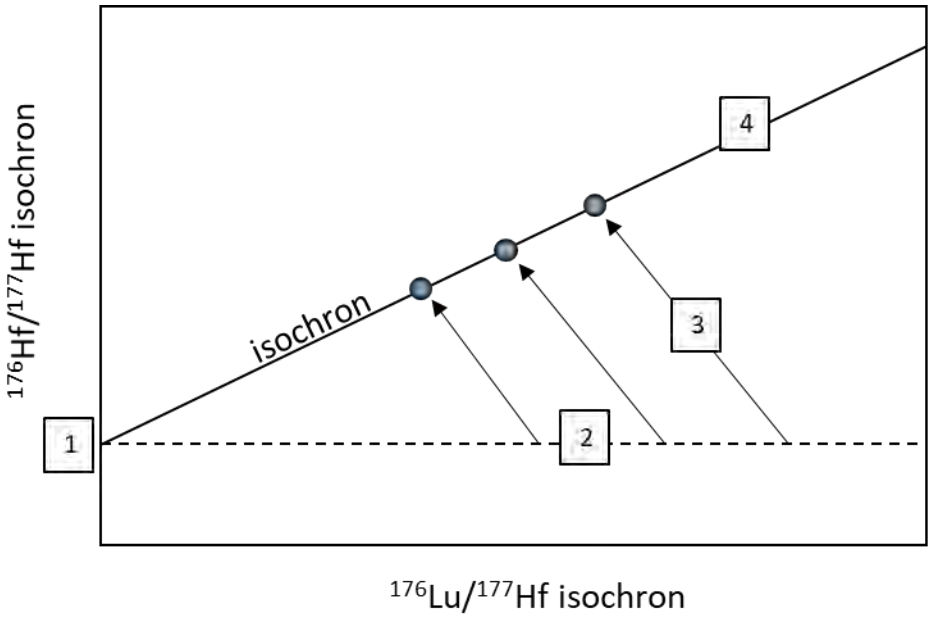

Figure 7. 17*: An example of an isochron diagram where (1) is a Hf isotopic composition at t=0, (2) shows that the initial $^{176}Hf/^{177}Hf$ for phases in the rock is the same, (3) shows that Hf compositions evolve with time as a function of Lu/Hf ratios and (4) shows that rocks in a closed system will have compositions plotting along the isochron line.*

It shows how radiogenic ^{176}Hf in a rock or mineral will decay over time. The amount of ^{176}Hf present today is given by the amount of the amount of ^{176}Hf present at some time in the past, the amount of radiogenic ^{176}Lu isotope present, the time elapsed since formation and the decay constant. When the above equation is referenced to a stable isotope, ^{177}Hf, it becomes:

$$^{176}Hf / {}^{177}Hf\,(p) = {}^{176}Hf / {}^{177}Hf\,(t) + {}^{176}Lu / {}^{177}Hf\,(p) * (e^{\lambda t} - 1)$$

An isochron diagram is a bivariate plot of measured parent-daughter isotope ratios for a suite of cogenetic samples (Rollinson, 1993). Lu-Hf geochronology makes use of the isochron method to determine the absolute ages (Vervoort, 2015). There are abundant daughter isotopes present in Lu-Hf system. Its' geochronology relies thus on the isochron approach which makes use of coexisting rocks and minerals to determine an age (Vervoort, 2015). The isochron approach assumes the following: (1) all minerals formed at the same time (they have

the same age), (2) all samples are cogenetic (they have the same initial isotopic composition i.e. ^{176}Hf / ^{177}Hf (t)) and (3) all dated samples are in a closed system. The isochron diagram in **Figure 7.17** shows that in (1) prior crystallization, the bulk rock has low parent-daughter ratios (Lu/Hf ratio) and a uniform daughter (Hf) isotopic composition, (2) as crystallization commences, different phases form with different Lu/Hf compositions, but they all had the same initial daughter isotope ratios ($^{176}Hf/^{177}Hf$), (3) the isotopic compositions of different components evolve as a function of their Lu/Hf ratio and (4) in a closed system, all components will plot on a line whose slope is function of time, called an isochron. Minerals or rocks having high Lu/Hf ratios will evolve more quickly to higher $^{176}Hf/^{177}Hf$ ratios than minerals or rocks with low Lu/Hf ratios (**Figure 7.17**; Vervoort, 2015). From the isochron, the igneous crystallisation age can thus be calculated using the following formula:

$$Age = \ln (slope + 1) / \lambda^{176}Lu$$

Where slope in the equation represents the slope of an isochron and $\lambda^{176}Lu$ represents the Lu decay constant. In this thesis, a decay constant of $1.8648 * 10^{-11} year^{-1}$ after Scherer et al. (2001) is used.

7.2.2 Methodology

About 0.5 g of powder of each sample was weighted and mixed with the ^{176}Lu-^{180}Hf tracer solution. The samples were digested in the labs of the Geological Institute of the Czech Academy of Sciences by Dr. Jiri Slama in closed 30ml Savillex teflon vials using combined acid attack (HF-HNO_3-$HClO_4$-HCl). First, 1 ml HNO_3 + 10 ml HF (concentrated acids) was added to each sample and left to stand cold in closed vial for 3 hours. Subsequently the bombs were opened and warmed on the hotplate to 90 ºC to evaporate Si and all acids. During this step the major minerals of the sample are attacked by the acids, most of the Si evaporates with the excess HF and the acids used in the following step thus can attack any resistant minerals without being depleted by reaction with major silicate phases. The same quantities of fresh HNO_3 and HF were then added to the vial with sample, closed tight and placed inside the 125ml digestion Parr bombs that were left in the oven at 180 ºC for 5 days. The samples were then evaporated to dryness at 90 ºC on a hotplate. To break down fluorides, 2 ml of $HClO_4$ were added to the sample and evaporated for a few days at 250°C until all the $HClO_4$ was gone. The samples were then taken up several times in 1 ml of 6M

HCl and evaporate to dryness to get rid of the last traces of $HClO_4$. Since Archean mafic-ultramafic rocks can usually be rich in Cr and $HClO_4$ is a strongly oxidizing acid, the mixture of 0.5 ml 6M HCl and 0.2 ml 3% H_2O_2 was added to the sample and evaporated at hotplate to reduce Cr^{6+} back to Cr^{3+}. After treating the sample a few times with 1 ml of 6M HCl, 2 ml of 1M HCl was added for subsequent column chemistry.

The ion exchange column chemistry follows closely that of Anczkiewicz et al. (2004), which is a down-scale modification of the original setup of Patchett and Tatsumoto (1980). The separation of Hf (+ Ti) and Lu (+ Yb and LREE) fractions is first carried out on a standard cation exchange column using AG50W-X8 resin (200–400 mesh size) and 1M HCl-0.06 M HF (HFSE elution) and 2.5 M HCl (REE elution). The final purification of Hf from other HFSE and potentially interfering Lu and Yb takes place on a second column with Eichrom LN resin (50–100 μm) using a technique based on Lee (1999) employing the mixture of 2M HCl–0.1 M. The same column is then used for purification of Lu from other REEs and reduction of Yb in the Lu cut using 4M HCl. All measurements of Lu and Hf fractions were carried out using a THERMO Neptune multi-collector (MC) ICP MS in the labs of the Czech Geological Survey in Prague. Hafnium isotopic compositions were analyzed in a static mode using Faraday cups with the following configuration: L4 – ^{172}Yb, L3 – ^{174}Yb, L2 – ^{175}Lu, L1 – ^{176}Hf, C – ^{177}Hf, H1 – ^{178}Hf, H2 – ^{179}Hf, H3 – ^{180}Hf, H4 – ^{182}W. Samples were aspirated to the instrument in 0.5 M HNO_3–0.25 M HF mixture using CETAC Aridus II desolvating nebulizer. The data acquisition procedure consisted of 40 integration cycles acquired over a period of ca. 6 min, followed by ca 5 min of washout with a mixture of 1.2 M HNO3–0.5 M HF composition. The raw data were processed off-line using on-purpose-built calculation EXCEL spreadsheet. Repeated measurements of 50 ppb JMC-475 standard over the period of analyses yield ^{176}Hf/^{177}Hf =0.282157 ± 4 (2SE, n=7), which is in agreement within the error with the reference data (Chu et al., 2002). The spike stripping routine employing the ratio of ^{179}Hf/^{177}Hf iteratively deconvoluting to the natural value of 0.7325 (Patchett and Tatsumoto, 1980) and exponential mass-bias correction were used to obtain Hf isotopic composition and Hf concentration of the spiked samples.

For Lu isotopic analyses, Faraday cup configuration was as follows: L3 – ^{171}Yb, L2 – ^{172}Yb, L1 – ^{173}Yb, C – ^{174}Yb, H1 – ^{175}Lu, H2 – ^{176}Lu, H3 – ^{177}Hf. The sample aspiration was identical to the Hf measurements with the difference that HF-free acids were used for sample introduction (0.5 M HNO_3) and washout (1.5 M HNO_3). The data acquisition procedure consisted of 40 integration cycles acquired over a period of ca. 3 minutes, followed by 4 min

of washout. The raw data were processed off-line using on-purpose-built calculation EXCEL spreadsheet. Repeated measurements of natural Lu and Yb standard solutions were carried out to check the accuracy of the isotopic ratio measurements. The mass-bias correction (exponential law) of the spiked $^{176}Lu/^{175}Lu$ ratio was done using the natural Yb present in the sample (reduced in the 3rd step of column chromatography to be ca. 1/10 of the amount of Lu to be suitable for mass bias correction while not causing excessive interference on ^{176}Lu mass) and the true ratio of $^{174}Yb/^{172}Yb = 1.45198$ (Thirlwall and Anczkiewicz, 2004). The value of $^{176}Lu/^{175}Lu$ was then used to calculate the concentration of Lu in the samples. The accuracy of the method was checked by measurement of spiked aliquot of BCR-2 reference material, which gave $^{176}Hf/^{177}Hf = 0.282856 \pm 20$, Hf = 4.82 ppm and Lu = 0.52 ppm, which are in good agreement with published values of 0.282866 ± 11 (Jweda et al., 2016), 4.8 ± 0.2 and 0.51 ± 0.02 (U.S. Geological Survey Certificate of Analysis, online source) respectively.

7.2.3 Results on the Kromberg samples and calculation of an isochron age

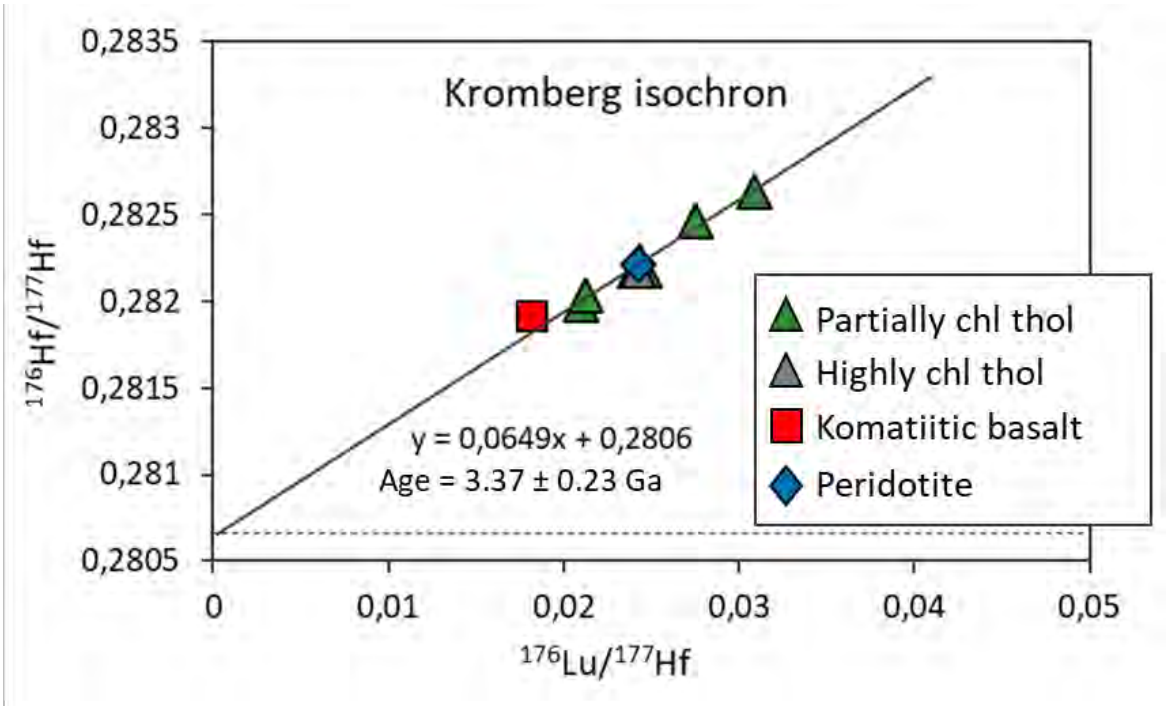

***Figure 7. 18**: (a) An isochron diagram for the least altered mafic-ultramafic rocks of the Kromberg type-section. The whole-rock isochron of the Kromberg type-section yields ages of 3.37 ± 0.23 Ga. This Lu-Hf isochron age agrees with published zircon ages from the Footbridge Chert of 3.33 ± 8.7 Ga (see Grosch and Slama, 2017).*

In the Kromberg type-section, an analysis of bulk Hf isotopic composition has been performed on 15 selected volcanic rocks. The analysed rock samples are KrT-41, KrT-42, KrT-43, KrT-44, KrT-50, KrT-48, KrT-49, KrK-54, KrK-61b, KrK-62, ICK-X, KrT-52, KrK-53, KrT-45 and KrT-46. According to the rock classification scheme used in the study, the rocks analysed are partially silicified tholeiites, partially chloritized tholeiites, highly chloritized tholeiites, peridotitic cumulates and komatiitic basalts. These rock samples were further filtered for high precision geochronology results. Therefore, out of 15 samples, 8 samples were determined as isochemical (remained closed system) thereby fitting for use in isochron and geochronology studies. These rock samples are: KrT-48, KrT-49, KrK-54, KrK-61b, KrK-62, KrK-53, KrT-45 and KrT-46. The remaining rock samples, for example the highly metasomatic and silicified samples were also analysed to see effects of alteration on the Lu-Hf and as control samples. Only the least altered samples were used to derive meaningful $\varepsilon_{Hf(t)}$ values, Hf model ages and an isochron age.

A whole-rock isochron was constructed for the relatively fresh samples of the Kromberg type-section (**Figure 7.18**). The partially chloritized and partially silicified rock samples (e.g. see **Table 7.5**) open to metasomatic processes were omitted from the isochron calculations because they are not in a closed system (see **Table 7.5**). It is possible that the rocks samples omitted have been reset by metamorphic, metasomatic or thermal processes thereby producing erroneous values. For high-precision geochronology and earth-crust and mantle melting evolution, the highly altered rocks are excluded from the data (in **Table 7.5** the excluded data is shown). They have $^{176}Hf/^{177}Hf$ ranging between 0.281915 and 0.282629 and $^{176}Lu/^{177}Hf$ of 0.018-0.031.

The Kromberg type-section whole-rock isochron has a slope of 0.0649 and a y-intercept of 0.2806. The y-intercept represent the initial $^{176}Hf/^{177}Hf$ prior to crystallisation. The slope of the isochron yields an age of 3.37 ± 0.23 Ga. This calculated isochron age on the freshest, least altered samples is in good agreement with zircon ages for the Kromberg Footbridge Chert zircons (e.g. Grosch and Slama, 2017, Byerly et al., 1996). This corresponds to the Pb/Pb evaporation dates yielded by the Footbridge Chert of 3334 ± 3 Ma (Byerly et al., 1996).

7.2.4 Calculation of $\varepsilon_{Hf(t)}$ and Hf model ages for Kromberg samples

The Earth's crust was formed from a silicate melt that was extracted from the mantle. The crust was enriched in incompatible elements, whereas the mantle remained depleted. Crustal rocks have lower Lu/Hf ratios relative to the bulk Earth, therefore their daughter isotopes, $^{176}Hf/^{177}Hf$, evolve slowly. Depleted mantle components, however, have relatively higher Lu/Hf ratios thus their daughter isotopes evolve more quickly compared to the bulk Earth (CHUR). Hf is approximated by average chondritic compositions known as Chondritic Uniform Reservoir model (CHUR) since in the solar nebular Hf was assumed as homogenous. Hf, measured in epsilon (parts per 10 000 from CHUR reference), expressed in present-day compositions is:

$$\varepsilon_{Hf(0)} = [(^{176}Hf/^{177}Hf_{(sample,\ 0)} - {}^{176}Hf/^{177}Hf_{(chur,\ 0)}) / (^{176}Hf/^{177}Hf_{(chur,\ 0)})] \times 10^4$$

and expressed at any time in the past, t, is:

$$\varepsilon_{Hf(t)} = [(^{176}Hf/^{177}Hf_{(sample,\ t)} - {}^{176}Hf/^{177}Hf_{(chur,\ t)}) / (^{176}Hf/^{177}Hf_{(chur,\ t)})] \times 10^4$$

The present-day $^{176}Hf/^{177}Hf$ and $^{176}Lu/^{177}Hf$ CHUR values used are those provided by Bouvier et al. (2008). In his study of chondrites, the present-day CHUR values are $^{176}Lu/^{177}Hf$ of 0.0336 ± 1 and $^{176}Hf/^{177}Hf$ of 0.282705 ± 11. Relative to the bulk Earth (CHUR), enriched crust evolves towards negative epsilon and depleted mantle towards positive epsilon (**Figure 7.19**). Time is an important factor for Hf isotope evolution and all radiogenic isotopes (Vervoort, 2015). It can be used to investigate the separation time from different reference reservoirs. These are called "model ages". The model age technique can be used by measuring the daughter isotopic compositions, $^{176}Hf/^{177}Hf$, and tracing back in time the parent-daughter ($^{176}Lu/^{177}Hf$) ratio of that sample until it intersects the reservoir of interest. In this study, the reservoir of interest is the depleted mantle reservoir; its model age is termed 'mantle model age' or 'crust-formation age' The reservoir of interest in this study is the depleted mantle which is used to identify the magmatic source for the Kromberg type-section rocks.

The **Figure 7.19** shows epsilon Hafnium values versus age (in Ga). Epsilon Hf values were calculated for different rock types at the t=0 Ga and t=3.33 Ga (the crystallization age). The $\varepsilon_{Hf(0)}$ are all less than zero, lying below the CHUR (or Bulk Silicate Earth). They range

from -30.77 to -5.513. They yield $\varepsilon_{Hf(3.33)}$ at crystallisation age that range from -0.615 and +4.1803 (**Figure 7.19**). For the depleted mantle, the initial value used for $^{176}Hf/^{177}Hf$ is 0.2833 and $^{176}Lu/^{177}Hf$ is 0.0384 (Chauvel and Blichert-Toft, 2001). For the given $^{176}Lu/^{177}Hf$ of the depleted mantle, the $\varepsilon_{Hf(0)}$ is +16.444. Mantle model ages were calculated for different rock samples in the Kromberg type-section. Partially chloritized tholeiites have $^{176}Lu/^{177}Hf$ that range from 0.021 and 0.031 and mantle model ages between 3.70 Ga and 4.27 Ga while cumulate peridotite with $^{176}Lu/^{177}Hf$ of 0.024 yields a mantle model age of 3.86 Ga. Komatiitic basalt have $^{176}Lu/^{177}Hf$ of 0.018 and a model mantle age of 3.43 Ga, whereas highly chloritized tholeiitic metabasalts yielded a mantle model age of 3.82 Ga with $^{176}Lu/^{177}Hf$ of 0.024 (**Table 7.4, Figure 7.19**). All mantle model ages are older than estimated crystallisation ages. According to Vervoort (2015), Hf mantle model ages older than crystallisation ages signifies an old magma source or sources that separated from the mantle in the past. The reason for the older varying ages in rocks could be because of sources that separated from the mantle in the past, and possibly recycled older crust, and probably mafic-ultramafic crust (given the flat REE patterns recorded).

***Table 7. 3**: Lu-Hf isotope data for selected relatively fresh rock samples of the Kromberg type-section.*

Sample	Rock type	Weight (g)	Lu (ppm)	Hf (ppm)	176Lu/177Hf	2SE	176Hf/177Hf	2SE	176Hf/177Hf_3.33Ga	Epsilon Hf 3.33Ga	2SE	Model age (Ga)
KrT-45	Peridotite	0.11	0.127	0.725	0.02	3.77E-06	0.282204	3.75E-06	0.280643	0.37	0.13	3.86
KrT-46	Komatiitic basalt	0.09	0.158	1.204	0.02	5.88E-07	0.281915	2.32E-06	0.280750	4.18	0.08	3.43
KrT-48	Partially chl thol basalt	0.05	0.521	3.443	0.02	4.99E-07	0.281978	3.37E-06	0.280633	0.02	0.12	3.78
KrT-49	Partially chl thol basalt	0.05	0.633	3.612	0.02	1.29E-06	0.282173	2.94E-06	0.280615	-0.62	0.10	3.95
KrK-54	Partially chl thol basalt	0.06	0.479	3.118	0.02	1.36E-06	0.282028	2.31E-06	0.280662	1.07	0.08	3.70
KrK-61b	Partially chl thol basalt	0.06	0.610	3.071	0.03	9.05E-07	0.282464	1.96E-06	0.280699	2.36	0.07	3.75
KrK-62	Partially chl thol basalt	0.07	0.482	2.163	0.03	1.13E-06	0.282629	2.04E-06	0.280649	0.58	0.07	4.27
KrK-53	Highly Chl thol basalt	0.07	0.446	2.549	0.02	7.83E-07	0.282206	2.87E-06	0.280651	0.65	0.10	3.82

***Table 7. 4:** Lu-Hf isotope data (excluded data) of highly altered samples affected by thermal or metasomatic processes in the Kromberg type-section.*

Sample	Rock type	Weight (g)	Lu (ppm)	Hf (ppm)	176Lu/177Hf	2SE	176Hf/177Hf	2SE	176Hf/177Hf_3.33Ga	Epsilon Hf 3.33Ga	2SE	Model age (Ga)
ICK-X	Partially chl thol basalt	0.11	0.254	1.540	0.02	1.72E-06	0.281263	1.72E-05	0.279800	-29.66	0.61	6.44
KrT-50	Partially sil thol basalt	0.07	0.372	2.114	0.02	7.04E-07	0.282186	3.10E-06	0.280623	-0.34	0.11	3.93
KrT-41	Partially sil thol basalt	0.10	0.201	0.505	0.06	1.40E-06	0.284035	4.69E-06	0.280500	-4.72	0.17	2.45
KrT-42	Partially sil thol basalt	0.10	0.175	0.691	0.04	1.30E-06	0.282868	3.67E-06	0.280622	-0.37	0.13	5.80
KrT-43	Partially sil thol basalt	0.11	0.197	0.477	0.06	2.65E-06	0.284060	4.60E-06	0.280381	-8.97	0.16	2.23
KrT-44	Partially sil thol basalt	0.12	0.155	0.476	0.05	3.78E-06	0.283468	3.13E-06	0.280580	-1.87	0.11	1.72

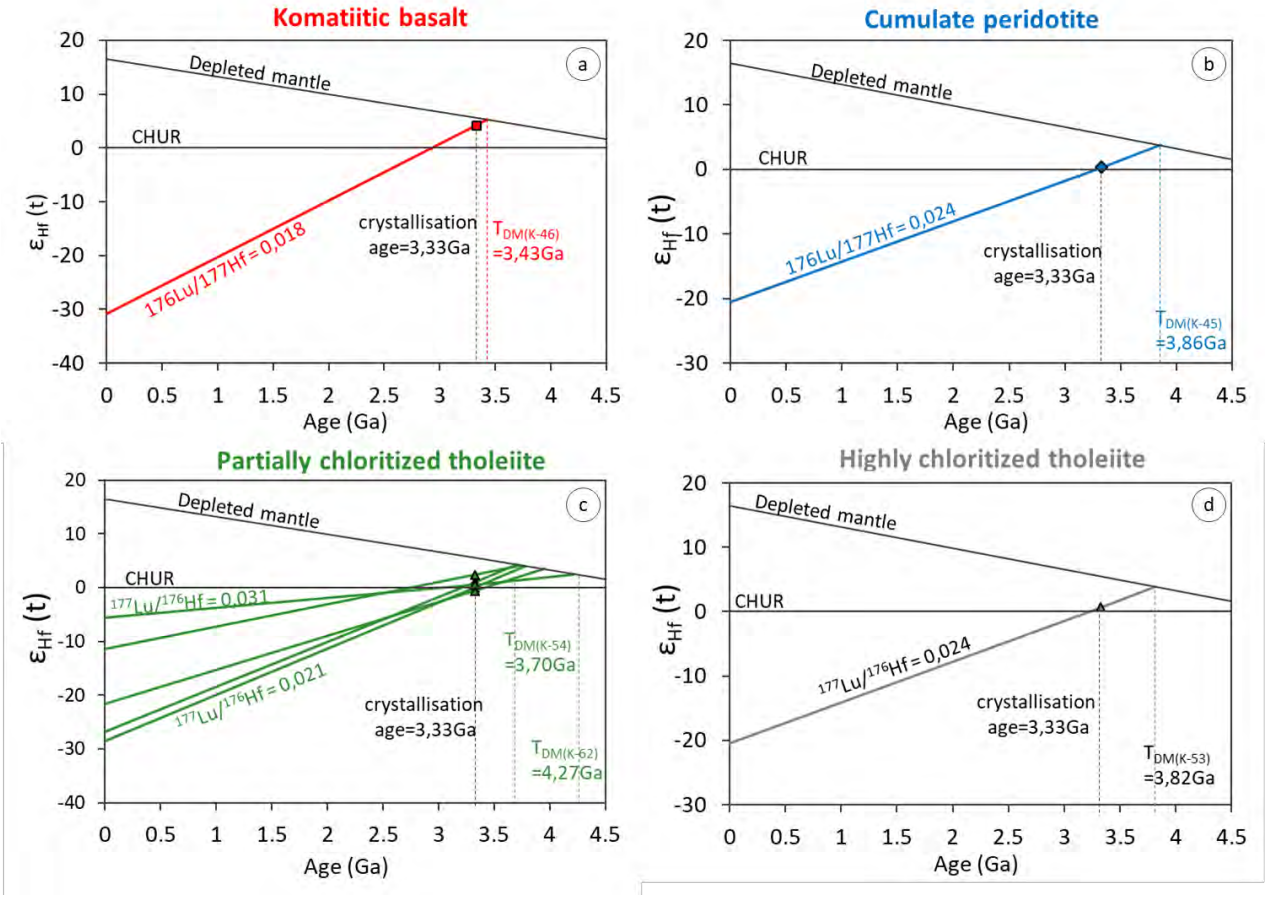

Figure 7. 19: *Epsilon Hf – Age binary plots for the Kromberg type-section for (a) komatiitic basalt, (b) peridotitic cumulate, (c) partially chloritized tholeiitic metabasalt and (d) highly chloritized tholeiitic metabasalt. DM = depleted mantle and K-46 = Kromberg type-section rock sample-number 46.*

7.2.5 Summary

In the Kromberg type-section 8 least-altered samples out of 15 were determined as isochemical and fitting for use in reliable isochron age calculation and geochronology. The altered silicified samples yielded erroneous values and therefore interpreted to have been reset by metasomatic hydrothermal processes. A whole-rock isochron study showed rock compositions of the Kromberg type-section as having $^{176}Hf/^{177}Hf$ of 0.281915-0.282629 and a $^{176}Lu/^{177}Hf$ of 0.018-0.031. They yield initial $^{176}Hf/^{177}Hf$ of 0.2806 and isochron ages of 3.37 ± 0.23 Ga. This is similar to the zircon ages from the Footbridge Chert of 3.33 ± 8.7 Ga

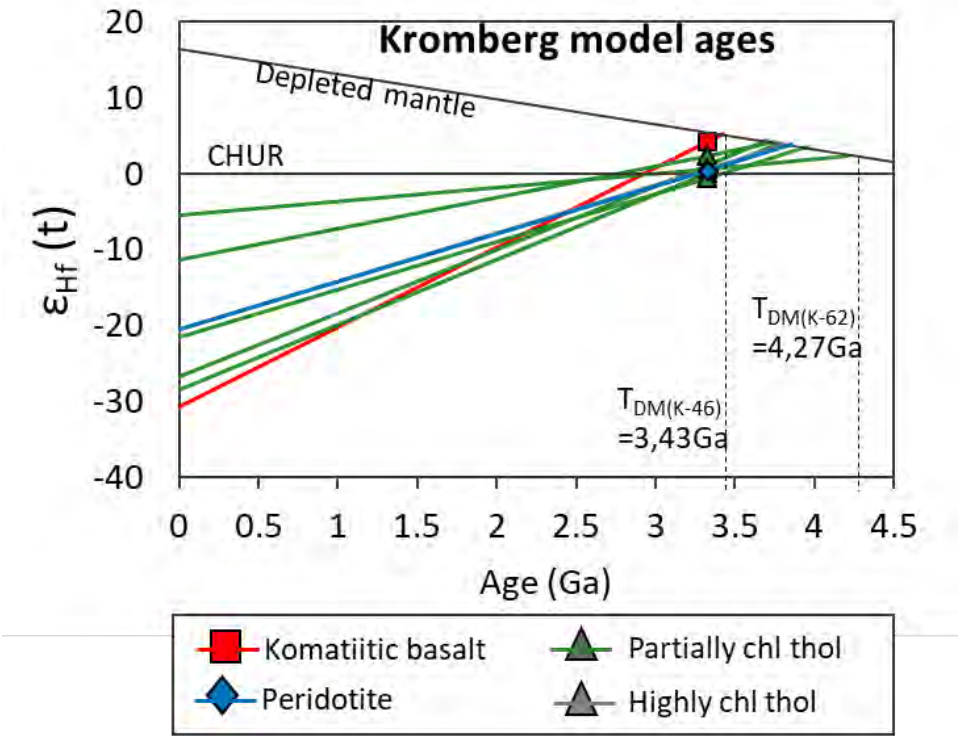

***Figure 7. 20**: A summary plot of ε_{Hf}-Age of the Kromberg type-section. Different colours are assigned to different rock compositions. The calculated Hf model ages range from 3.43 Ga to 4.27 Ga.*

(Grosch and Slama, 2017) and Pb/Pb evaporation dates yielded by the Footbridge Chert of 3334 ± 3 Ma (Byerly et al., 1996). An $\varepsilon_{(Hf)}$-Age diagram showing all least altered rocks of the Kromberg type-section analysed for geochronology is shown in **Figure 7.20**. The $\varepsilon_{Hf(0)}$ for the Kromberg type-section rocks have below CHUR values and range between -30.77 and -5.513. They have $\varepsilon_{Hf(3.33)}$ that lie between -0.615 and +4.1803. They yield calculated Hf mantle model ages older than their 3.33 Ga crystallization age. Their calculated Hf mantle model ages range between 3.43 Ga and 4.27 Ga (see Discussion and Interpretation section 8).

8 Discussion and interpretation

8.1 High-resolution volcanic architecture of the mid – lower Kromberg type section

In this study high-resolution geological mapping, petrography, mineralogy and whole-rock geochemistry are integrated to characterize rock compositions in the Kromberg type-section and to reconstruct an accurate geological profile (Chapter 3 Local Geology and Grosch et al., 2020). The new proposed geological stratigraphy is compared with geological interpretations of previous geology workers and to investigate the origin and evolution of the Kromberg mafic-ultramafic sequence. This study focusses on the mid-lower part of the Kromberg type-section stratigraphy, on the SE limb of the Onverwacht Anticline. Thus, to produce accurate fieldwork results, high-resolution geological mapping was conducted along both the eastern and western banks of the Komati River, which revealed some new river outcrop pavements. Outcrop exposure on the eastern side of the Komati river is poor, but results were compared to observations on the western side. The Kromberg type-section is noted in this study to comprise seven volcanic/igneous cycles each cycle capped by a chert horizon (KrC_1 to KrC_7). It is dominated by extrusive massive and pillowed tholeiitic lavas and comprises minor intrusions namely metadunite, cumulate metapyroxenite and coarse-grained mafic intrusions. The stratigraphy is dismembered by at least three listvenitic (fuchsite-chlorite-carbonate-quartz) shear zones with one major shear zone found in the upper stratigraphy below the uppermost Footbridge Chert (labelled KrC_7, see **Figure 8.1**). The lowermost and heavily serpentinized metadunite structurally overlies the conglomerates and sandstones of the Noisy Formation. A shear zone and chert horizon (KrC_1) occur immediately above the lowermost layered metadunite.

The Kromberg type-section comprises altered massive and vesicular tholeiitic pillow lavas, pillow breccias, komatiitic basalt and sediment infill representing extrusive volcanic. The geology and petrology of the records appear to record submarine eruption and phreatomagmatic processes. Minor intrusions are noted, such as cumulate olivine-pyroxene peridotites and a metadunite unit. The cumulate peridotite rocks are interpreted to represent cumulate sill intrusions with a fining upwards sequence. After a series of grid mapping exercises was conducted on the pillow lavas of the Kromberg type-section it was observed that pillow sizes vary across the stratigraphy. The smallest pillow is ca. 0.1 m in height and 0.25 m in length and the largest pillow is 6 m in length (major axis) and 1 m in height (minor

axis). Pillow metabasalt shapes also vary from sub-rounded pillows to elongate pillows (see **Figure 8.1**). Pillow lavas exposed along the eastern bank of the Komati river have quartz and carbonate filled drain-out structures and ocelli structures in their cores. There is also evidence for secondary metasomatic silicification and chloritization of basaltic flows. Pillow lavas directly beneath the c. 30 m thick KrC_3 chert horizon are heavily silicified, whereas those away from the chert show partial silicification. Evidence for mingling of two different magmas, one more Mg-rich than the other, is observed on the partly silicified lobate pillow lavas (see grid map 2a and 2b). There is also evidence for thin (cm-scale), tholeiitic sheeted sill intrusions and a north-south trending tholeiitic feeder dyke. Sheeted sills have been previously reported by de Wit (1987) while the presence of the feeder dyke is a new observation.

It was observed in thin section and geochemically that c. 50% of the protolith rock composition in the type-section classify as altered, namely highly chloritized or metasomatized by silica-rich hydrothermal seawater fluids. Chlorite compositions in the metabasalts record amesitic and clinochlore compositions with XFe ratios ranging between 0.13 and 0.32. Olivine alteration in the metadunite sample led to formation of mixed lizardite and chrysotile serpentine compositions. Low temperature alteration in the peridotitic cumulate rocks record partial alteration of olivine to serpentine (chrysotile, lizardite) and augitic clinopyroxene to fine-grained actinolite. Generally, in the mid-lower Kromberg type-section, alteration mineralogy corresponds to sub-greenschist facies to lower greenschist facies conditions, in contrast to higher metamorphic temperatures experienced in the upper shear zone part of the Kromberg type-section (within and below the main shear zone). Rock samples were thus screened for alteration wherein partially altered rocks that displayed a relatively fresh, original igneous geochemical protolith signature had not changed by alteration were used for petrology and geochemical classification. A geochemical classification after Jensen (1973) and Viljoen et al. (1982) revealed the Kromberg type-section rocks as comprising Fe-rich tholeiitic basalts, peridotitic cumulates, metadunite and minor komatiitic basalts (**Figure 7.5**). Komatiitic basalts have similar compositions to Badplaas and Geluk komatiitic basalts. The rock compositions of the Kromberg type-section have relatively flat REE patterns, a small negative Nb anomaly in primitive mantle normalized spider diagrams, low Th and high Nb values. After comparing the Kromberg type-section geochemical data with data from other Archean greenstones, the Kromberg type-section rocks displayed similar compositions with greenstones with an oceanic plateau origin

(such as Abitibi, Sumozero and Wawa greenstone belts), and does not display a typical subduction zone related geochemical signature. In a global comparative plot, partially chloritized tholeiites plot away from crustally contaminated boninites (**Figure 7.12**) and away from the Stolzberg TTG. Furthermore, in the La/Nb-Nb binary plot, La/Sm-La/Ta plot (**Figure 7.12**) and the Th/Yb-Nb/Yb plot (**Figure 7.14**) these rocks showed similar compositions to the primitive mantle, followed a plume mixing trend and does not plot in the backarc region in the Th/Yb-Nb/Yb plot (**Figure 7.14**). Geochemical data reveals melting in the presence of garnet for some komatiitic basalts thereby supporting high pressure melting for high Mg-rich melts. A Lu-Hf isotope study revealed Hf model ages of relatively fresh samples of the Kromberg type-section as older than their crystallisation age of 3.33 Ga (see Lowe et al., 1999). Their Hf model ages range between 3.43 - 4.27 Ga. The ε_{Hf} at t = 3.33 Ga are all positive except for one sample, KrT-49, with a slightly negative near chondritic value. Chloritized tholeiitic metabasalts have close to chondritic uniform reservoir (CHUR) ε_{Hf} (t = 3.33 Ga) values of -0.62 to +2.36, whereas komatiitic basalts have ε_{Hf} (t = 3.33 Ga) of ca. +4.18. Trace element and Lu-Hf isotope signatures of the mafic-ultramafic rocks indicates significant heterogeneity in the mantle source regions. The Lu-Hf data reveals derivation of Kromberg lavas from a mantle source that interacted with much older, Eoarchean recycled mafic crust, and less likely to have been contaminated by felsic crust, felsic volcaniclastics or subduction related mantle processes.

8.2 Comparison to previous geological work and interpretations

Since the work of Viljoen and Viljoen (1969), controversies centred on the stratigraphy models of the SE limb of the Kromberg type-section have since emerged. Although it has been ca. 50 years since the discovery of the type-section, there remain significant differences in stratigraphic interpretation between different workers. In this section the currently existing geological logs for the NW and SE limb of the Kromberg Formation are presented and compared to the newly reconstructed geological log of the Kromberg type-section on the SE limb of the OAF (this study and Grosch et al., 2020). It is important to point out that some of the differences may be due to poor exposure of rock outcrop, due to vegetation cover in places and to previous workers only working on the western side of the Komati River. Contrary to previous geological work, this current study provides geological mapping at

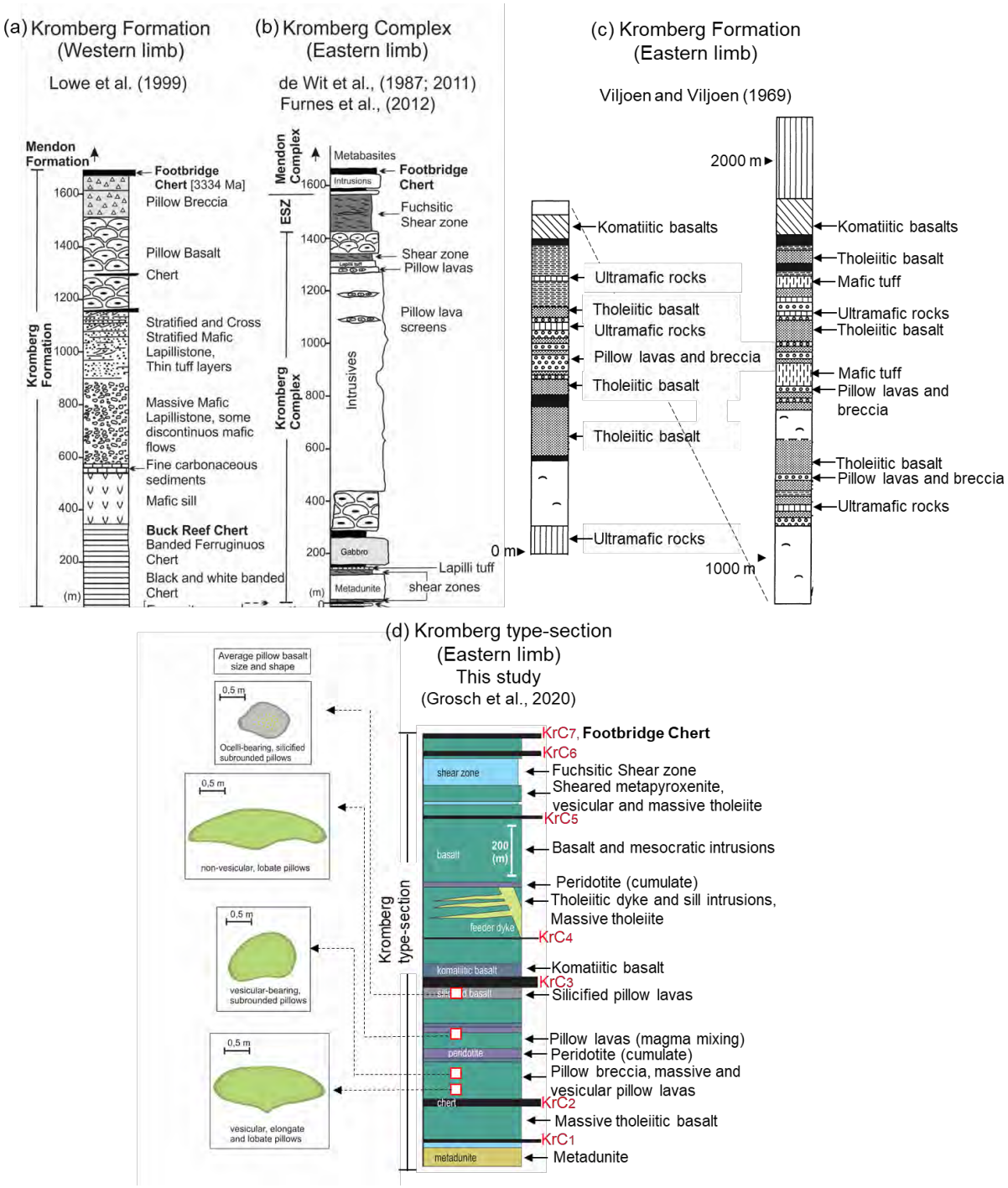

Figure 8. 1: *Different geological stratigraphic models for the mafic-ultramafic Kromberg Formation and Kromberg type-section. Geological logs (a) from the NW limb and (b)-(d) from the SE limb of the Kromberg Formation. (a) is modified after Lowe et al. (1999), (b) de Wit et al. (1987, 2011) and Furnes et al. (2012) (c) Viljoen and Viljoen (1969) and (d) Grosch et al. (2020) and this study geological interpretation for the Kromberg type-section. In (d) average pillow sizes and shape are included to show the distribution of pillow lavas across the Kromberg type-section.*

high-resolution of rock outcrops exposed on both the eastern and western banks of the Komati River in the Kromberg type-section (SE limb). As a result of the current high-resolution study, new outcrop exposures have become available providing a more complete geological record for the Kromberg type-section. In addition, high-resolution grid mapping was conducted for robust field results whereas, in the study by previous geology workers (e.g. de Wit et al., 2011; Furnes et al., 2011, 2012), geological mapping was presumably conducted at a macro-scale. In their work, only field photographs of tholeiitic lavas are produced; no photographs or descriptions of metagabbros are provided (de Wit et al., 2011; Furnes et al., 2011, 2012). In this current integrated study, petrographic descriptions, field photographs, mineralogy, and bulk rock compositions of all rock types are provided at high-resolution across the Kromberg type-section. On this basis, it is proposed that the geological profile presented in this study for the Kromberg type-section is preferred. For example, the previously proposed 'metagabbros' are interpreted here in this study as vesicular metabasalts or peridotitic cumulate rocks (see Petrography Chapter).

Viljoen and Viljoen (1969a) proposed a simplified continuous 'layer cake' stratigraphy for the SE limb of the Kromberg type-section. Vennemann and Smith (1999), in their study in the SE limb of the Kromberg type-section, used the stratigraphy model of Viljoen and Viljoen (1969a) for geochemical sampling and stratigraphic height of samples. The differences in stratigraphy observations between Viljoen and Viljoen (1969a) and the new stratigraphy proposed in this current study are outlined below (**Figure 8.1c,d**):

- In the stratigraphy model by Viljoen and Viljoen (1969a) only five chert horizons are identified. The geological log in this study reveals seven chert horizons (KrC_1 to KrC_7, the Footbridge Chert)
- Viljoen and Viljoen (1969a) classify felsic to intermediate rocks in the SE limb of the Kromberg type-section based on field observations only. Vennemann and Smith (1999) further distinguishes the rocks as geochemically different from other rocks in the Kromberg stratigraphy and suggest them having been formed from a distinctly different magma than the rocks of the Kromberg type-section. In this study the high SiO_2 (ca. 90 wt.%) and greyish colour of these rocks is attributed to secondary silica alteration processes (hydrothermal seawater metasomatism) thereby classifying as highly silicified tholeiitic pillow metabasalts.
- Viljoen and Viljoen (1969a) reports a mafic tuff in their stratigraphy model. In this study a felsic lapilli ash is reported.

- Viljoen and Viljoen (1969a) classifies some horizons in the stratigraphy as ultramafic rocks. Furthermore, Vennemann and Smith classify some of these 'ultramafic rocks' as komatiites. In this study the 'ultramafic rocks' represents a variety of rock types, e.g. peridotitic cumulate and a metadunite. In the current study, no massive or spinifex textured komatiites are identified in the new geological profile of the Kromberg type-section (SE limb). Minor komatiitic basalts are identified.
- In a stratigraphy model by Viljoen and Viljoen (1969a) no shear zones are identified, whereas in the current study fuchsite-chlorite-carbonate-quartz shear zones are identified.

The results presented in this study also differ from the recently proposed tectono-stratigraphy model of de Wit et al. (2011) and Furnes et al. (2011, 2012) for the Kromberg type-section (SE limb). The following are the observed differences (**Figure 8.1b,d**):

- According to de Wit et al. (2011) and Furnes et al., (2012; 2013) the 'tectono-stratigraphic' model of the SE limb of the Kromberg type-section or 'Kromberg Complex' is dominated by mainly 'undifferentiated' mafic to ultramafic intrusions (ca. 85%) with minor basalt and chert (ca. 15%). In this study, the Kromberg type-section is dominated by ca. 80% volcanic rocks (i.e. extrusive tholeiitic basalt and komatiitic basalt) with minor proportions, namely ca. 15% of intrusive rocks such as metadunite, cumulate metapyroxenite and coarse-grained mafic intrusions, intercalated by 7 different chert horizons making up ca. 5% of the reconstructed geological profile.
- De Wit et al. (2011) and Furnes et al. (2012) also reports a ca. 105 m thick metagabbro and diabase with a chert screen. The presence of the metagabbro is further reported in the upper stratigraphy beneath the Footbridge chert (de Wit et al., 2011). No metagabbro is reported in this study. The gabbroic intrusions reported by de Wit et al. (2011) are classified as extrusive volcanic rock in this study (e.g. vesicular metabasalts, pillow lavas, etc.).
- Wit et al. (2011) and Furnes et al. (2012) reports in their KV1 section as comprising massive and vesicular pillow lavas pillow grading from large pillow lavas to smaller pillow lavas and breccias. In this current study no pillow lava size variation is

observed with height in the stratigraphy (see average pillow size with depth in **Figure 8.1d**).

- In the middle of the stratigraphy de Wit et al. (2011) and Furnes et al. (2012) reports a 900 m KV3 section as comprising undifferentiated intrusions with chert and pillow lava screens. In this study, only a small fraction of the Kromberg represent intrusive rocks, most of the type-section is extrusive in nature due to the presence of dominantly volcanic rocks.
- Only east-west oriented sheeted sills are reported by de Wit et al. (2011). The north-south oriented tholeiitic feeder dyke reported in this study represents a new observation.
- This study also reports a major ca. 35 m thick ferruginous chert horizon in the mid-Kromberg sequence previously unrecognized by de Wit et al., (2011) and Furnes et al., (2012). This chert horizon KrC3, found on the eastern side of the Komati River (Grid map 1), is underlain by highly silicified pillow lavas.

There are also major differences found between the SE limb and the NW limb of Kromberg Formation (**Figure 8.1a,d**) attributed to diachroneity in the stratigraphy. The north-western limb of the Kromberg sequence has transitional evaporates between the Kromberg and the underlying Buck Ridge Volcano-Sedimentary Complex, BR-VSC (see de Vries et al., and others, de Wit et al., 2011). The lowermost part of the NW limb comprises evaporites, a 150 m Buck Ridge (black and white laminated) chert forming a subdivision K1 section (Lowe and Byerly, 1999). In the SE limb of the Kromberg type-section, there are no evaporites. At ca. 600 m to 800 m above BR-VSC, K2 of the NW limb comprises massive mafic lapilli tuff and lapillistone (Lowe and Byerly, 1999). A mafic tuff and lapillistone is not present in the SE Kromberg type-section; instead there are horizons of felsic lapilli ash. The upper part of the NW limb, K3, comprises ca. 500-600 m silicified pillow lavas and pillow breccia. This is different from the SE limb which comprises massive vesicular basalts, pillowed basalts, mesocratic intrusions, metapyroxenite and major and minor shear zones in the upper stratigraphy (see **Figure 8.1a,d**). In the SE Kromberg type-section, only a thin layer of brecciated pillows is observed in the lower parts of the stratigraphy.

8.3 Local volcanic evolution model for the Kromberg type-section sequence

In this section an eruptive model is discussed at a local scale for the Kromberg type-section. The model is discussed as per volcanic cycle present in the Kromberg type-section (**Figure 8.2**). Each volcanic cycle is followed by periods of quiescence where chert horizons (total of 7 volcanic/magmatic cycles) are deposited. The main aim of this section is to present igneous protolith processes operating in the Kromberg type-section, prior to tectonic dismemberment during accretion. In the Kromberg type-section, the presence of vesicular pillow metabasalts, komatiitic metabasalts and metabasaltic flows supports an extrusive model, with lavas erupting under submarine conditions. Additionally, low Th and Nb values in the Nb/Yb-Th/Yb plot modified after Pearce (2008) revealed an oceanic setting for the Kromberg type-section. Magmatic extrusion in a small oceanic basin or oceanic plateau setting is thus favoured for the eruption of the Kromberg type-section.

The Kromberg type-section sequence is heterogeneous comprising mafic to ultramafic rocks such as cumulate peridotite, metadunite, komatiitic basalts and Fe-rich tholeiitic metabasalts. Tholeiitic metabasaltic rocks have MgO (wt.%) compositions ranging between 0.29 and 10.33 wt.%, komatiitic basalts between 14.52 and 20.41 wt.% and cumulate peridotite between 21.17 and 30.90 wt.%. The high-Mg komatiitic basalts are Al-depleted thus possibly derived at deep mantle depths between 450 and 650 km (Ohtani et al., 1989) with melting occurring in the presence of garnet at high pressures in the mantle source region. At a lower pressure garnet melts near the solidus and is removed from the residue (Arndt, 2003). Production of the melts may have taken place in the deep part of a mantle plume. The tholeiitic metabasaltic rocks of the Kromberg type-section have higher Al_2O_3 compared to the basaltic komatiite rocks in the Kromberg type-section (**Figure 7.4b**). The Al_2O_3 (wt.%) content can be used to detect the pressure conditions of rocks; lower Al_2O_3 denotes higher pressure while rocks with higher Al_2O_3 were produced at a much lower pressure (Herzberg, 1992). In addition, a fractional crystallisation trend is observed between the Kromberg type-section rocks where the more evolved rocks have lower MgO and the more primitive rocks have higher MgO (**Figure 7.4a**).This means that tholeiitic melts in the Kromberg type-section were produced in two ways, either (a) at a lower pressure through low to intermediate partial melts or (b) as a result of crystal fractionation of a high-Mg melt. Both partially chloritized tholeiites and komatiitic metabasalts of the Kromberg type-section have similar geochemical composition to the primitive mantle (e.g. in La/Nb-Nb plot, La/Sm-La/Ta plot, **Figure 7.12**,

and the Th/Yb-Nb/Yb plot, **Figure 7.14**) suggesting melts were initially derived from the primitive mantle via plume melting. Furthermore, ε_{Hf} values indicate a spread of -0.62 to +4.18 and Hf-model ages (ranging between 3.43 – 4.27 Ga) much older than their crystallization age of 3.33 Ga. This is interpreted to represent heterogeneous assimilation of the magma source by older, Eoarchean recycled mafic crust and/or by mafic lower crust as the lavas ascended through the pre-existing Onverwacht Group rocks (e.g. mafic to ultramafic Komati and Hooggenoeg Formations).

The first volcanic/magmatic cycle comprises a basaltic komatiite flow. Komatiitic basalt flows are Mg-rich and therefore derived from a deep-seated magma chamber at a high pressure and erupting on the sea floor, or deep parts of a mantle plume. The komatiite flow overlies the lowermost metadunite, a sliver of accreted mantle peridotite. The metadunite comprises cumulate olivine crystals (serpentinized) and represent a cumulate coarse-grained mantle rock. The second eruptive cycle characterized by massive and vesicular lava flows was derived from low to intermediate pressure melts (**Figure 8.2a**) or possibly shallower and compositionally more heterogeneous parts of a mantle plume head. The Hf mantle model ages of the partially chloritized tholeiites in this eruptive cycle are Eoarchean to Hadean (3.75 to 4.27 Ga). The formation of tholeiitic melts thus resulted from the mixing of the plume magma with partial melts derived from a much older, recycled mafic crust in the mantle at a low to intermediate pressure.

The third eruptive cycle (**Figure 8.2b**) is characterized by changing sea level conditions. In this volcanic cycle both vesicular and non-vesicular pillow lavas are observed. There are also interlayered pillowed and massive lava flows, brecciated pillows, pillowy flows and pillow lava cooling fractures. Lobate pillow lavas that are both dark green and light green show evidence for magma mingling between two different magmas with different Mg/Fe compositions. The two magma compositions are interpreted to represent two different magma chambers, one possible produced at a low pressure (basaltic magma) and the other at a higher pressure (Mg-rich magma), as recorded by the compositional heterogeneity. The Mg-rich magma is produced by the partial melting and assimilation of an ancient oceanic crust. The ancient oceanic crustal material that assimilated and partially melted in the mantle is interpreted to have been derived from older lower oceanic crust that had undergone delamination and recycled into the mantle. The basaltic magma erupts at shallow sea levels and produces interlayered massive and pillowed flows as well as brecciated pillows. Brecciated pillows were formed by phreatomagmatic processes under shallow seawater

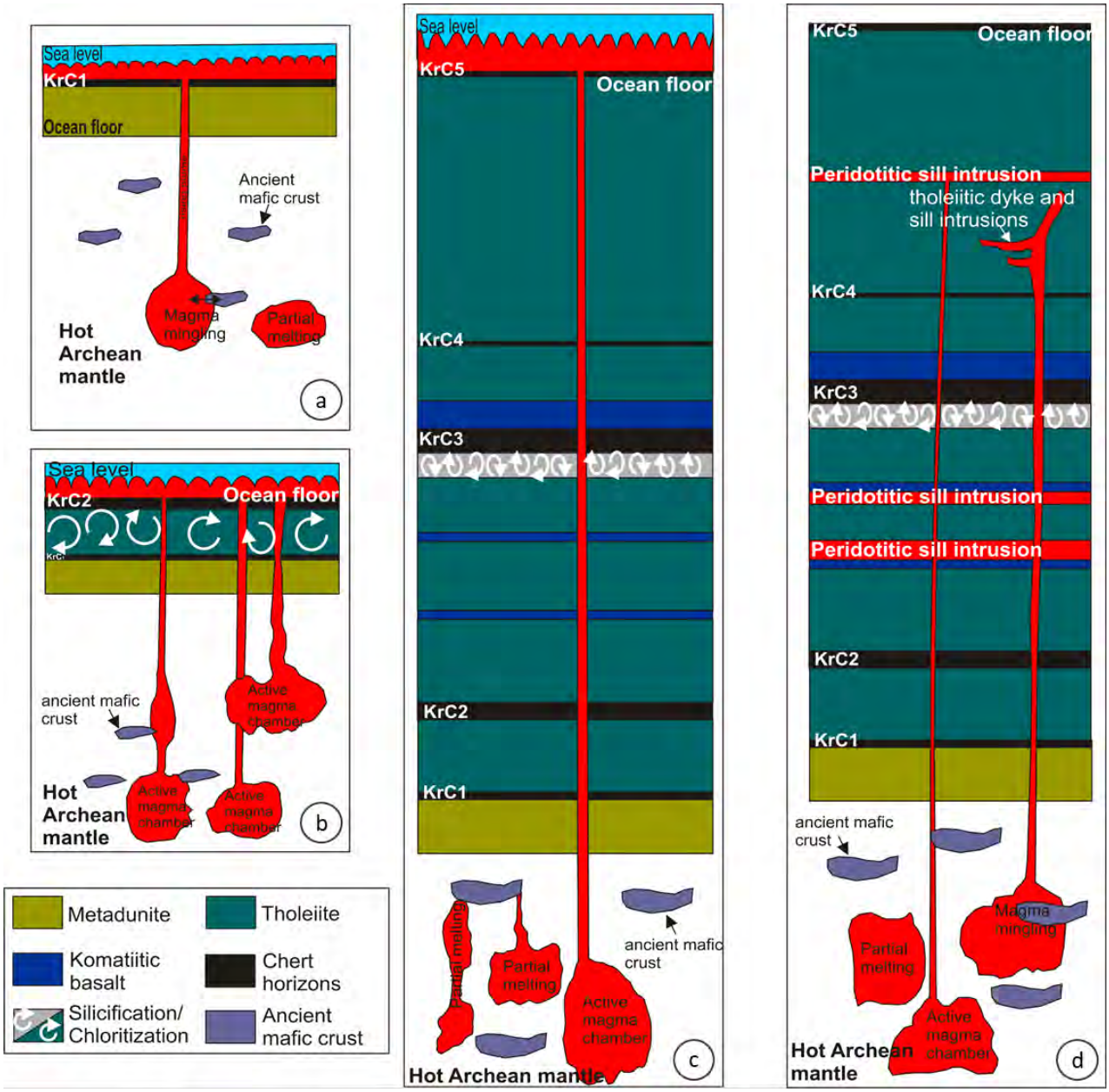

Figure 8. 2*: An eruptive model for the Kromberg type-section. This model is made up of various eruptive episodes characterized by different magma chambers with melt generated at different depths. In some eruptive episodes the is magma mingling between an older mafic crust and a rising magma chamber. The older, early Paleoarchean – Eoarchean, recycle mafic crust is given a purple colour on the diagram and its interaction with an active magma chamber is shown by a left-right arrow. Sections affected by secondary silicification are also shown in this diagram in grey. (a) Represents eruption of the second volcanic cycle, after chert deposition, KrC$_1$, (b) third volcanic cycle eruption, (c) sixth volcanic cycle eruption and (d) peridotitic sill intrusion through the volcanic and volcano-sedimentary sequence of the Kromberg type-section.*

conditions wherein magma interaction with shallow water results in explosive extrusive activity. Also, the vesicularity of pillow lavas indicates eruption at shallow water submarine conditions. The magma chamber at a much deeper depth produces ultramafic melts that differentiates through crystal fractionation to tholeiitic melts. As it erupts, it interacts with the basaltic magma to produce the magma mingling texture in pillow lavas exposed along the eastern bank of the Komati River (Grid map 2a and 2b). The pillow lavas beneath the chert horizon, KrC_3, are grey, rheologically hard and silicified. They are enriched in SiO_2, Rb and LREE and depleted in Na_2O and FeO^T. Silicification has also resulted in high mobility of HREE (**Figure 7.4a**). Hofmann and Haris (2008) suggested low temperature (50-150^{0}C) sea water hydrothermal alteration for the Barberton greenstone belt beneath chert horizons. Due to similarities in REE mobility in this study with the study by Harris and Hofmann (2008), the same hydrothermal processes hold for the Kromberg type-section. Contrary to metasomatic silicification, chloritization, occurring across the lower part of the stratigraphy, does not significantly change the geochemical signatures of tholeiitic metabsaltic rocks.

The fourth eruptive cycle (**Figure 8.2c**) consists of komatiitic basalts and tholeiites. The tholeiites in this cycle are interpreted to have been produced by fractional crystallization of a high-Mg lava after the crystallization of komatiitic basalts. The fifth eruptive cycle is produced by eruption of both low to intermediate melts as well as deep seated melts. The deep-seated melts produced the metapyroxenites while the shallow melts produced tholeiites. Across a few parts of the stratigraphy of the Kromberg type-section are intrusive rocks (**Figure 8.2d**). These include peridotitic sill intrusions. The olivine-pyroxene peridotitic (wehrlite) cumulate sill intrusions are Mg-rich and have a fining upward grain-size variation. The feeder dyke and sheeted sill intrusions are tholeiitic in composition and thereby interpreted to have been produced from a heterogeneous basaltic magma chamber(s).

8.4 Proposed regional geodynamic model for the Kromberg mafic-ultramafic sequence

This subsection briefly reviews geodynamic models proposed for the Kromberg type-section regionally, specifically reviewing models by Vennemann and Smith (1999), Byerly (1999c), Lowe et al., 1999; de Wit et al. (2011, 2018) and Furnes et al. (2012, 2013), van Kranendonk (2009) and Grosch and McLoughlin (2013). Based on data in the current study, a new

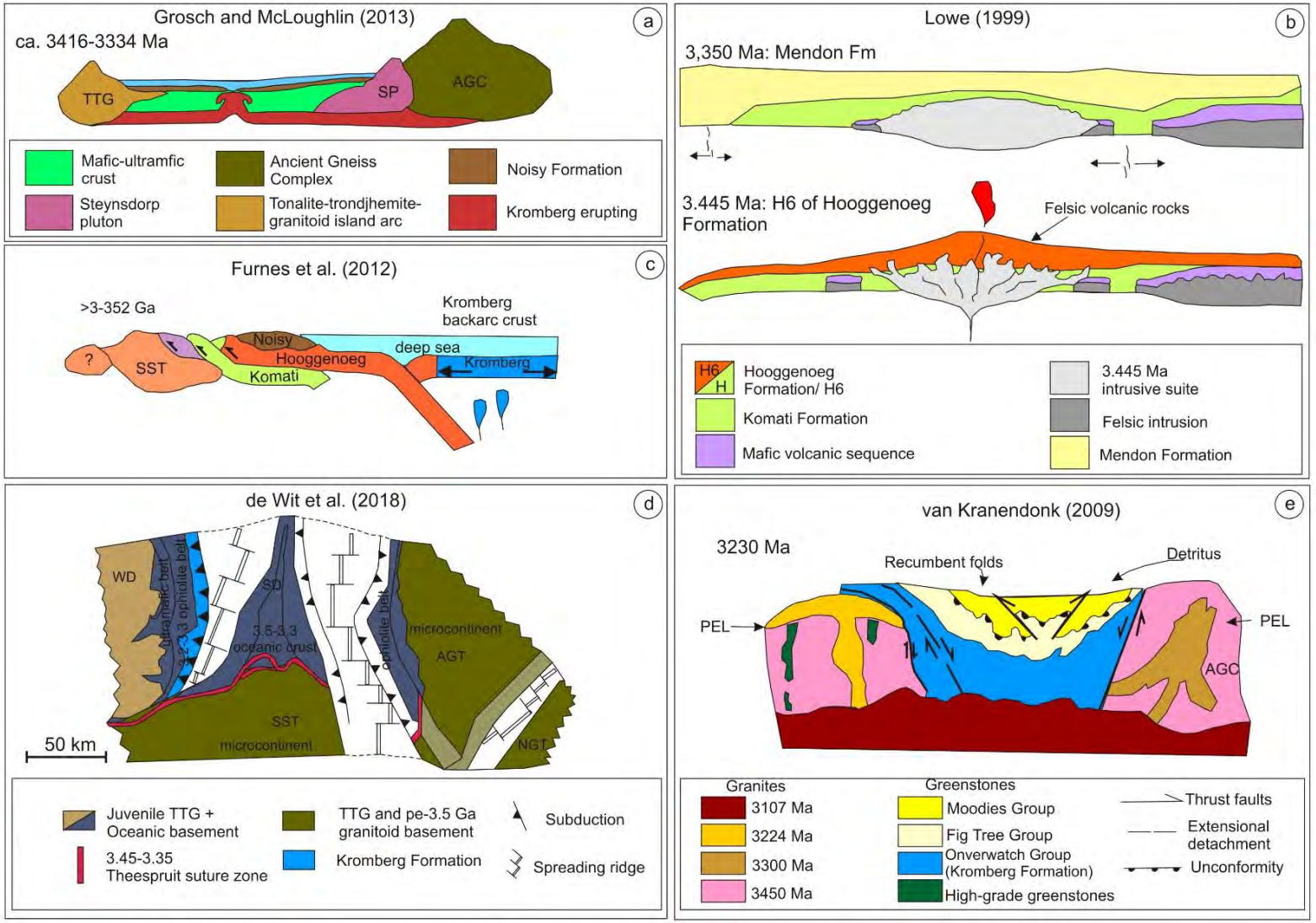

Figure 8. 3: *Proposed geodynamic models in the Onverwacht Group with (a) modified after Grosch and Mcloughlin (2013), (b) Lowe, 1999 (c) Furnes et al. (2012), (d) de Wit et al. (2018) and (e) van Kranendonk (2009).*

geodynamic model is proposed for the early evolution of the Kromberg mafic-ultramafic sequence and this model is also compared to previous geodynamic interpretations. Findings from Grosch et al. (2020) are briefly presented to address the later accretion of the Kromberg type-section oceanic crust. Geodynamic models based on previous interpretations are discussed first, followed by a comparative discussion of a proposed geodynamic setting for the Kromberg type-section. The geodynamic models discussed for the Kromberg type-section from previous geology workers indicates a continuous sequence (Viljoen and Viljoen, 1969; Vennemann and Smith, 1999; Lowe and Byerly, 1999) or a tectono-stratigraphy model with major structural breaks in the form of shear zones (de Wit et al., 2011, 2018; Furnes et al., 2012).

The geodynamic model by Lowe and Byerly (1999a) explains formation of the Onverwacht Group through the evolution of the Steynsdorp and Songimvelo crustal blocks where it is characterized by early eruption and late orogeny at ca. 3.2 Ga (**Figure 8.3b**). The Komati Formation forms the oldest unit in the Songimvelo Block (Byerly, 1999c). It is formed by rifting of the Steynsdorp Block produced by rapid effusive eruptions that resulted in thick flows with little or no sedimentary layers. Komatiitic flows were rapid and where individual komatiite eruptions were, they were terminated by phreatomagmatic process forming komatiitic ash beds (Lowe, 1999a, c) while basaltic eruptions together with thin sedimentary interflows were deposited in subaqueous, quiet and deep-water settings (Lowe, 1999a, c). Byerly (1999c) in his model, does not specify the volcanic setting of the Kromberg Formation regionally. However, the author suggests an extensional setting related to the Songimvelo Block and states that further investigation is required to construct the geodynamic setting for the Kromberg Formation (Byerly, 1999c).

In the model by Vennemann and Smith (1999), the interlayering of tholeiitic basalts and basaltic komatiites in the Kromberg type-section occurred as a result of fractional crystallisation of a magma chamber where komatiitic rocks are parental to tholeiitic rocks. It was proposed that the multi-element ratios, such as CaO/Al_2O_3 and TiO_2/P_2O_5, of komatiitic rocks resemble that of chondrites reflecting a chondritic mantle type. A geodynamic setting proposed by Vennemann and Smith (1999) involves melting of chondritic-type mantle at a high-pressure resulting in parental komatiitic melts. The melt is injected into a large magma chamber resulting into a low-density tholeiitic liquid and crystallization of chromite and

olivine cumulates that settled to the bottom of the magma chamber (Vennemann and Smith, 1999). Vennemann and Smith (1999) argue for komatiites which, in this current study, are not observed.

Van Kranendonk et al., 2009 proposed an intracratonic setting and eruption of the Onverwacht lavas including the Kromberg sequence which was based on the concept that the Onverwacht Group has a younging upward stratigraphy from the Komati Formation and also based on the thick (>10 km) greenstone stratigraphy (van Kranendonk et al., 2009, 2011; **Figure 8.3e).** The author suggested the BGB to have formed by partial convective overturn of felsic TTG middle crust and that igneous processes in the middle to upper part of the continental crust triggered the vertical movement causing proposed cooler greenstone 'drips' to sink down. In this study we question the thickness of Kromberg sequence, which is relatively thin compared to other formations of the Onverwacht Group and argue whether it is autochthonous or allochthonous. The different shear zones in the SE limb of the Kromberg type-section and the lowermost shear zone separating the Noisy Formation from the Kromberg type-section are not explained by the model of van Kranendonk et al. (2009, 2011). A model of Kromberg mafic-ultramafic volcanism through a felsic crust does not explain the low Th values (between 0.13 and 0.72 ppm) for the Kromberg type-section rocks. Consequently, it does not explain why the Kromberg type-section rocks display no trace element of Hf-isotope signature of felsic crustal contamination (**Figure 7.12a**).

The tectonic model by de Wit et al. (2011) and Furnes et al. (2012, 2013; **Figure 8.3c**) was based on geochemical data and structural re-interpretations of volcanosedimentary rocks of the Onverwacht Group. The geodynamic model for the Onverwacht Group involves obduction of oceanic crust slices that formed in volcanic arcs and back-arc basins (Furnes et al., 2013). This horizontal accretion process is argued to have resulted in tectonic stacking of 'complexes' and a uniformitarian modern-style plate tectonic model. Data from the Komati, Hooggenoeg and Kromberg 'Complexes' and the proposed Ncakini section (Kromberg and Mendon Complexes) were compared to data from the literature of Iceland, Cape Verde Islands and Hawaii (oceanic island volcanic provinces), Ontong Java and Kerguelen (oceanic plateau), and Izu-Bonin-Mariana-IBM- and Indonesian island arc (subduction setting). With the aid of MORB-normalized spider diagrams, the Onverwacht Group data revealed a negative Nb and Ta anomaly, Cs and Pb enrichment and relatively flat REE patterns (Furnes et al., 2012, 2013). A "piggyback" tectonic model is proposed for the upper Onverwacht Group (de Wit et al., 2011, 2018; Furnes et al., 2012). The Kromberg 'Complex' is proposed

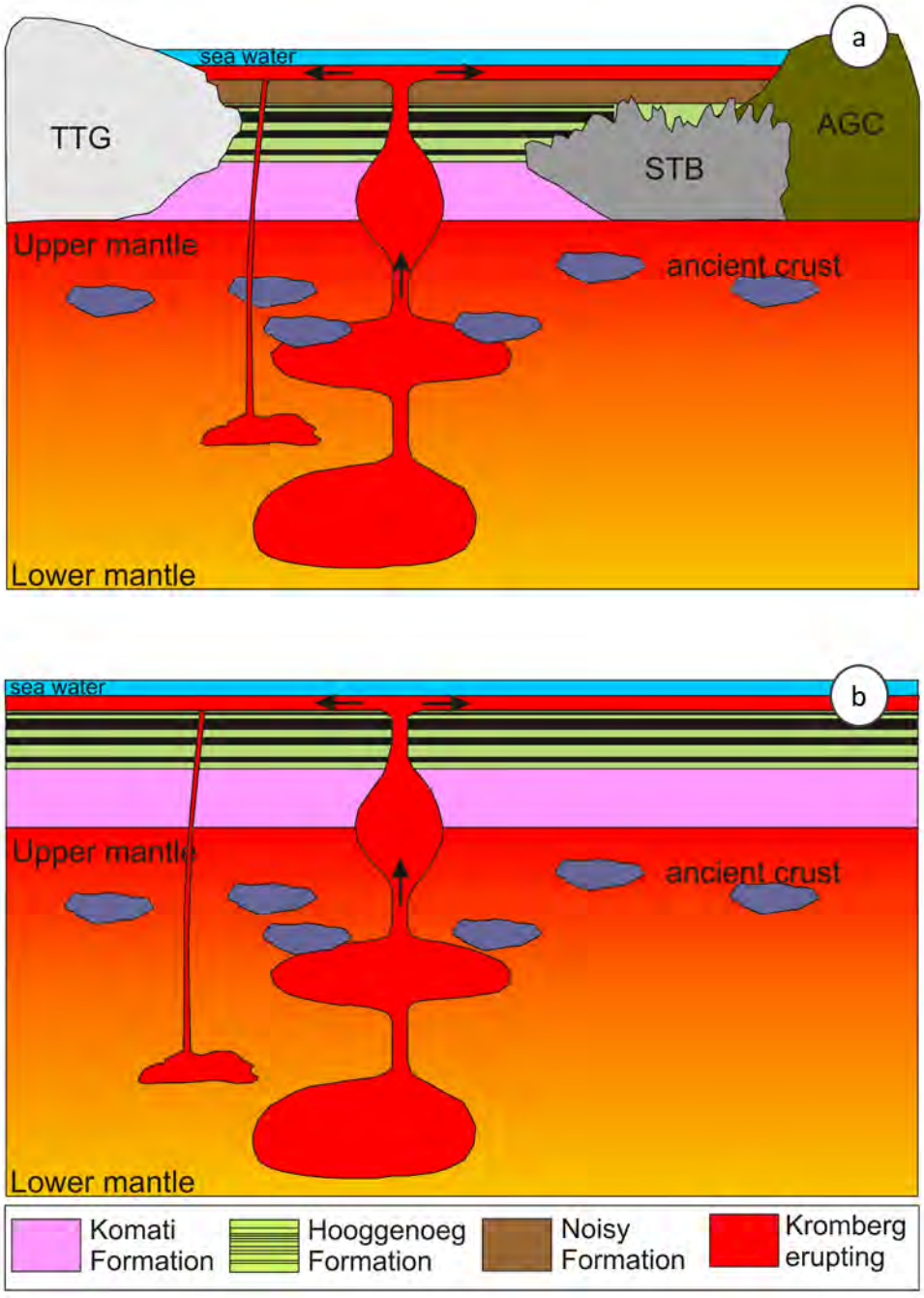

Figure 8. 4*: Propose geodynamic model for the Kromberg type-section. (a) Represents the first model with eruption onto the Noisy Formation and (b) represents the second model with eruption in a distal basin away from the Noisy, and the felsic rocks associated with the Noisy Formation. TTG = tonalite-trondhjemite-gneiss, STB = Stolzberg pluton and AGC = ancient gneiss complex.*

to be characterized by subalkaline basalts, Cs/Th and Ba/Th ratios comparable to MORB and negative Nb and Ta anomalies in MORB-normalised spider diagrams representing subduction-related processes (Furnes et al., 2012, 2013). A spreading ridge in the back-arc basin is proposed for the Kromberg sequence of rocks that generated MORB, with subduction modification (Furnes et al., 2012). In this study, it was revealed that MORB normalization leads to a more pronounced Nb anomaly than primitive mantle normalization (**Figure 7.16a,b**). The Kromberg type-section rocks are discovered to have similar compositions to the primitive mantle. Therefore, normalization of multi-element diagrams to the primitive mantle is more suitable for the Archean rocks and not MORB normalization. In addition, the small Nb anomaly observed in the Kromberg type-section rocks is argued to not be pronounced enough to represent a typical subduction zone signature as proposed by de Wit et al. (2011) and Furnes et al. (2012, 2013). Their model (de Wit et al., 2011 and Furnes et al., 2012, 2013) is similar to a model by de Wit et al. (2018) where accretion of Songimvelo Domain with Weltevreden and Malalotsha at 3227-3222 Ma and 3228-3223 Ma (Schoene and Bowring, 2010) was followed by subduction zones that created felsic volcanism and granitic magmatism (**Figure 8.3d**).

Grosch and McLoughlin (2013) in their sulphur isotope study proposed that the Kromberg Formation formed as a result of tectonic rifting forming an intra-cratonic basin, shortly after a tectonic accretion that occurred in less than ca. 3432 Ma that formed the Noisy Formation (**Figure 8.3a**). According to this model, the Hooggenoeg Formation oceanic crust and the Stolzberg TTG island arc developed in a supra-subduction zone setting at ca. 3460-3437 Ma (Grosch et al., 2011). The Archean subduction was followed by convergence of the Songimvelo Block onto the older Steynsdorp Block and Ancient Gneiss Complex. This resulted into a major uplift, obduction and erosion of the Hooggenoeg oceanic crust into the Songimvelo Block followed by Noisy Formation sediment exposure into the Archean atmosphere at <ca. 3432 Ma (Grosch et al, 2011; Grosch and McLoughlin, 2013). Grosch and McLoughlin (2013) further proposes a geodynamic setting change where rifting through the Komati, Hooggenoeg and Noisy Formation resulted in the eruption of the Kromberg mafic-ultramafic sequence. However, in this study the rifting process proposed by Grosch and McLoughlin (2013) does not explain the low Th values and absence of crustal contamination (e.g. by the Noisy Formation felsic rocks) in the Kromberg type-section.

In this current study, two possible end-member regional geodynamic models are proposed for the Kromberg type-section sequence of rocks; (1) one model involves rifting of

the oceanic basin through the Noisy Formation and (2) the other represents eruption at a distal, purely juvenile oceanic basin. The onset of eruption begins at 3.37 ± 0.23 Ga – evidence obtained from the whole-rock Lu-Hf isochron diagram for least altered rocks of the Kromberg type-section. Mantle melting is characterized by different magma chambers forming at different depths, with some deep partial melting in magma chambers interacting and assimilating with an ancient early Archean (Eoarchean) recycled, mafic crust in the mantle source. Eruption was episodic resulting in the deposition and hydrothermal silicification of different chert horizons observed in the Kromberg Formation. In the first model (**Figure 8.4a**), it is proposed that rifting occurred after the Noisy Formation was deposited (see Grosch and McLoughlin, 2013). At 3.37 ± 0.23 Ga the oceanic basin opened, and the magma chamber ascended through the Theespruit, Komati, Hooggenoeg and Noisy Formations. This model favours a small oceanic basin or plateau flanked by TTG felsic crust locally on either side of the basin, which is represented by eruption through volcanic and possible intra-cratonic deposits (from Noisy Formation). The flat REE patterns, very small negative Nb anomaly and the low Th values are suggested to be a result of limited crustal contamination of basaltic lavas with the felsic Noisy Formation sediments through which the magma erupted. However, it is argued that the Nb anomaly does not strongly represent crustal contamination or subduction-related processes. Also, the model fails to explain the relatively thin 1.5km thick stratigraphy of the Kromberg type-section. The lack of geochemical evidence for felsic crustal contamination, suggests that the model presented in Figure 8.4a, namely involving eruption through the felsic 3.43 Ga Noisy Formation, is probably unlikely.

In the second proposed model (**Figure 8.4b**), at 3.37 ± 0.23 Ga the oceanic basin opens through the Theespruit, Komati and Hooggenoeg Formations. In this model the Kromberg type-section is proposed to have formed in a juvenile oceanic basin or oceanic plateau, distal to the felsic TTG, the Noisy Formation and the Ancient Gneiss Complex (AGC). A juvenile, oceanic basin is supported by the detrital zircon U-Pb ages of the Footbridge Chert of 3.33 ± 8.7 Ga (Grosch and Slama, 2017) corresponding to gabbros regionally of similar age and the whole rock Lu-Hf isochron age of 3.37 ± 0.23 Ga (this study). Both these ages do not overlap with the ages of the Steynsdorp pluton and the older formations of the Onverwacht Group, except for the mafic gabbro age in the Komati Formation (Kamo and Davis, 1994). In addition to U-Pb and Lu-Hf ages, the major and traces elements of partially chloritized tholeiites of the Kromberg type-section have similar compositions to juvenile oceanic plateau

greenstone belts (e.g. Sumozero and Abitibi greenstone belts) further supporting a juvenile basin as opposed to a continental/intra-cratonic basin for the Kromberg sequence. It is proposed that the small negative Nb anomaly and flat REE profiles of the metabasalts observed is a result of magmatic assimilation of older, recycled mafic oceanic crust during ascent of primitive mafic magma through the mantle. Interaction of magmas with altered, lower crustal mafic-ultramafic rocks cannot be excluded. The highly silicified pillow lavas along the eastern bank of the Komati river represent a less dense crust compared to the underlying crust due to silicification. Density contrast between the upper crust and the lower crust may have resulted in delamination of the lower crust (see Grosch et al., 2020, see abstract in **Appendix A4**). The delamination and break off of the older, denser, lower Archean crust from silicified upper oceanic crust resulted in the preservation of relatively thin, accreted dismembered stratigraphy of the Kromberg type-section sequence (Grosch et al., 2020; see abstract in **Appendix A4**). In addition to this model, Grosch et al. (2012) proposed a thrust and accretion model for the Kromberg type-section that formed at ca. 3230 Ma during a regional transpressional crustal accretion event. The Kromberg type-section sequence of oceanic mafic-ultramafic rocks structurally overlies the Noisy Formation and represents accreted, juvenile oceanic crust (Grosch and Slama, 2017) with listvenitic shear zones forming at ca. 3230 Ma (Grosch et al., 2012). In this model the Kromberg mafic-ultramafic sequence represents a juvenile, allochthonous oceanic crust (initially formed in an oceanic basin or oceanic plateau setting) that was tectonically accreted over the older rocks of the Onverwacht Group. The Kromberg type-section rocks is argued not to have formed in a modern-style subduction zone setting, nor in a back-arc setting, due to the lack of a pronounced subduction zone signature.

Considering the two models proposed, the second distal, juvenile oceanic basin model is preferred over the oceanic basin flanked by TTG model 1. This is because the thin, dismembered geological section (ca. 1.65 km) of oceanic crust and the small, flat REE profiles of the metabasalts, low Th, small negative Nb anomaly representing limited crustal contamination is explained by the second model and not the first. In addition, the second model explains the oceanic crust origin for the Kromberg type-section. The dismembered stratigraphy of the SE limb of the Kromberg type-section supports the horizontal accretion of juvenile Archean oceanic crust at ca. 3.23 Ga, that followed the earlier eruption of the Kromberg type-section rocks (Grosch and Slama, 2017, Grosch et al., 2012).

9 Conclusions

The SE limb of the Kromberg type-section sequence has received limited geological attention since its discovery. Previous geological work on the construction of the geological architecture for the SE limb of the Kromberg type-section sequence has been based on outcrop igneous textures and rock colour in the field. As a result, contrasting geological logs and interpretations exist for the SE limb of the Kromberg sequence. In this study, geological mapping is conducted at high-resolution and is integrated with, petrographic, mineralogical and geochemical characterization to reconstruct the volcano-sedimentary architecture of the Kromberg type-section (SE limb). The SE Kromberg type-section is dismembered with at least three fuchsite-chlorite-carbonate-quartz shear zones and is dominated by volcanic extrusive rocks with minor mafic to ultramafic intrusions. It comprises seven chert horizons which are interpreted to represent the end of different volcanic cycles in the Kromberg sequence. Contrary to previous work on the Kromberg sequence, the sequence is dominated by tholeiitic metabasalts exposed along the eastern and western bank of the Komati River. The mid to lower part of the Kromberg sequence, the focus of this study, comprises four rock types namely: metadunite, peridotitic cumulate, komatiitic metabasalt and tholeiitic metabasalt. The Kromberg type-section comprises extrusive massive and vesicular pillow lava metabasalts, extrusive komatiitic metabasalts, minor intrusive cumulate peridotite sill and metadunite, sheeted tholeiitic sill intrusions and a newly discovered tholeiitic feeder dyke. The volcanic rocks of the Kromberg type-section represent seven eruptive cycles intercalated by chert horizons (KrC_1 -KrC_7, Footbridge Chert) marking periods of quiescence. More than 50% of these rocks are affected by secondary alteration processes where basaltic lavas are chloritized and some showing evidence for extensive seafloor hydrothermal silicification. Alteration mineralogy corresponds to sub-greenschist to lower greenschist facies with chloritized compositions comprising amesite and clinochlore chlorite.

Rock compositions in the Kromberg type-section record flat REE pattern, a small Nb anomaly and low Th values. Komatiitic basalts and peridotitic cumulate rocks are high Mg and Al-depleted rocks. Komatiitic basalts have similar geochemical compositions to Badplaas and Geluk komatiitic basalts. No massive or spinifex-textured komatiites are discovered in the Kromberg sequence (SE limb). Major and trace element compositions of the Kromberg type-section greenstone rocks show similar compositions to oceanic plateau greenstone belts and not subduction-related greenstone belts. The Kromberg type-section mafic-ultramafic

sequence, shows no strong geochemical evidence in support of Archean subduction-related processes. Furthermore, Lu-Hf isotope studies for the Kromberg type-section rocks are presented herein for the first time. Whole-rock isochron ages for the Kromberg type-section yielded 3.37 ± 0.23 Ga, similar to zircon ages on the Footbridge Chert of 3.33 ± 8.7 Ga (Grosch and Slama, 2017). There is heterogeneity in the mantle source where mantle Hf model ages ranges from Mesoarchean to Hadean. There is thus evidence for an ancient, recycled mafic crust in the heterogeneous mantle source to the Kromberg type-section rocks. A geodynamic model favoured for the Kromberg type-section thus involves initial formation of juvenile oceanic crust (in an oceanic rift basin or oceanic plateau) with partial melting of a heterogeneous mantle source involving a mantle plume. The mafic-ultramafic Kromberg sequence was then dismembered and accreted, by horizontal tectonic processes in an oceanic flake tectonic geodynamic process at ca. 3230 Ma (Grosch et al., 2020).

10 Reference list

Abbott, D., Drury, R. and Smith, W.H., 1994. Flat to steep transition in subduction style. *Geology*, *22*(10), pp.937-940.

Anczkiewicz, R., Platt, J.P., Thirlwall, M.F. and Wakabayashi, J., 2004. Franciscan subduction off to a slow start: evidence from high-precision Lu–Hf garnet ages on high grade-blocks. *Earth and Planetary Science Letters*, *225*(1-2), pp.147-161.

Angerer, T., Kerrich, R. and Hagemann, S.G., 2013. Geochemistry of a komatiitic, boninitic, and tholeiitic basalt association in the Mesoarchean Koolyanobbing greenstone belt, Southern Cross Domain, Yilgarn craton: implications for mantle sources and geodynamic setting of banded iron formation. *Precambrian Research, 224*, pp. 110-128.

Anhaeusser, C.R., 1973. A Discussion on the evolution of the Precambrian crust-The evolution of the early Precambrian crust of Southern Africa. *Philosophical Transactions of the Royal Society of London. Series A, Mathematical and Physical Sciences*, *273*(1235), pp.359-388.

Anhaeusser, C.R., 1981. The Barberton mountain land, South Africa. *Precambrian plate tectonics*, p.137.

Anhaeusser, C.R., 1984. Structural elements of Archaen granite-greenstone terranes as examplified by the Baberton Mountain Land, Southern Africa. In: *Precambrian tectonics illustrated*. pp. 57-78.

Anhaeusser, C.R. and CR, A., 1978. The geological evolution of the primitive earth-evidence from the Barberton Mountain Land.

Armstrong, R.A., Compston, W., De Wit, M.J. and Williams, I.S., 1990. The stratigraphy of the 3.5-3.2 Ga Barberton Greenstone Belt revisited: a single zircon ion microprobe study. *Earth and Planetary Science Letters*, *101*(1), pp.90-106.

Arndt, N., 2003. Komatiites, kimberlites, and boninites. *Journal of Geophysical Research: Solid Earth*, *108*(B6).

Bailey, S.W., 1988. Hydrous phyllosilicates. *Reviews in mineralogy*, *19*, p.725.

Bourdelle, F., Parra, T., Chopin, C. and Beyssac, O., 2013. A new chlorite geothermometer for diagenetic to low-grade metamorphic conditions. *Contributions to Mineralogy and Petrology*, *165*(4), pp.723-735.

Brandl, G., Cloete, M. and Anhaeusser, C. R., 2006. Archaean greenstone belts. *The Geology of South Africa,* pp.9-56.

Byerly, G.R., 1999. Komatiites of the Mendon Formation: Late-stage ultramafic volcanism in the Barberton Greenstone Belt. *Special Paper-Geological Society of America*, (329), pp.189-211.

Byerly, G.R., Kröner, A., Lowe, D.R., Todt, W. and Walsh, M.M., 1996. Prolonged magmatism and time constraints for sediment deposition in the early Archean Barberton greenstone belt: evidence from the Upper Onverwacht and Fig Tree groups. *Precambrian Research*, *78*(1-3), pp.125-138.

Cavosie, A.J., Valley, J.W. and Wilde, S.A., 2007. The oldest terrestrial mineral record: a review of 4400 to 4000 Ma detrital zircons from Jack Hills, Western Australia. *Developments in Precambrian Geology*, *15*, pp.91-111.

Chauvel, C. and Blichert-Toft, J., 2001. A hafnium isotope and trace element perspective on melting of the depleted mantle. *Earth and Planetary Science Letters*, *190*(3-4), pp.137-151.

Chavagnac, V., 2004. A geochemical and Nd isotopic study of Barberton komatiites (South Africa): implication for the Archean mantle. *Lithos*, *75*(3-4), pp.253-281.

Chavagnac, V., Nägler, T.F. and Kramers, J.D., 1999. Migmatization by metamorphic segregation at subsolidus conditions: implications for Nd–Pb isotope exchange. *Lithos*, *46*(2), pp.275-298.

Cloete, M., 1991. An overview of metamorphism in the Barberton greenstone belt. In *Two Cratons and an Orogen—Excursion Guidebook and Review Articles for a Field Workshop through Selected Archean Terranes of Swaziland, South Africa and Zimbabwe* (pp. 84-98). Johannesburg, South Africa: Johannesburg, IGCP project 280, Dep. of Geol., Univ. of the Witwatersrand.

Compston, W. and Kröner, A., 1988. Multiple zircon growth within early Archaean tonalitic gneiss from the Ancient Gneiss Complex, Swaziland. *Earth and Planetary Science Letters*, *87*(1-2), pp.13-28.

Condie, K.C., 1981. Archean greenstone belts. *Elsevier.*

Dann, J.C., 2000. The 3.5 Ga Komati Formation, Barberton greenstone belt, South Africa, part I: new maps and magmatic architecture. *South African Journal of Geology*, *103*(1), pp.47-68.

Dann, J.C. and Grove, T.L., 2007. .4 Volcanology of the Barberton Greenstone Belt, South Africa: Inflation and Evolution of Flow Fields. *Developments in Precambrian geology*, *15*, pp.527-570.

de Ronde, C.E. and de Wit, M.J., 1994. Tectonic history of the Barberton greenstone belt, South Africa: 490 million years of Archean crustal evolution. *Tectonics*, *13*(4), pp.983-1005.

de Ronde, C.E. and Kamo, S.L., 2000. An Archł an arc-arc collisional event: a short-lived (ca 3 Myr) episode, Weltevreden area, Barberton greenstone belt, South Africa. *Journal of African Earth Sciences*, *30*(2), pp.219-248.

de Ronde, C.E.J., Kamo, S., Davis, D.W., De Wit, M.J. and Spooner, E.T.C., 1991. Field, geochemical and U-Pb isotopic constraints from hypabyssal felsic intrusions within the Barberton greenstone belt, South Africa: Implications for tectonics and the timing of gold mineralization. *Precambrian Research*, *49*(3-4), pp.261-280.

de Vries, S.T., 2004. *Early Archaean sedimentary basins: depositional environment and hydrothermal systems* (Doctoral dissertation, University Utrecht).

de Wit, M.J., 1982. Gliding and overthrust nappe tectonics in the Barberton greenstone belt. *Journal of Structural Geology*, *4*(2), pp.117-136.

de Wit, M.J., 1983. Notes on a preliminary 1: 25 000 geological map of the southern part of the Barberton greenstone belt.

de Wit, M.J., 1991. Archaean greenstone belt tectonism and basin development: some insights from the Barberton and Pietersburg greenstone belts, Kaapvaal Craton, South Africa. *Journal of African Earth Sciences (and the Middle East)*, *13*(1), pp.45-63.

de Wit, M.J., 1998. On Archean granites, greenstones, cratons and tectonics: does the evidence demand a verdict?. *Precambrian Research*, *91*(1-2), pp.181-226.

de Wit, M.J., 2004. Archean greenstone belts do contain fragments of ophiolites. *Developments in Precambrian Geology*, *13*, pp.599-614.

de Wit, M., Furnes, H., MacLennan, S., Doucouré, M., Schoene, B., Weckmann, U., Martinez, U. and Bowring, S., 2018. Paleoarchean bedrock lithologies across the Makhonjwa Mountains of South Africa and Swaziland linked to geochemical, magnetic and tectonic data reveal early plate tectonic genes flanking subduction margins. *Geoscience Frontiers*, *9*(3), pp.603-665.

de Wit, M.J., Furnes, H. and Robins, B., 2011. Geology and tectonostratigraphy of the Onverwacht Suite, Barberton greenstone belt, South Africa. *Precambrian Research*, *186*(1-4), pp.1-27.

de Wit, M.J., Hart, R.A. and Hart, R.J., 1987. The Jamestown Ophiolite Complex, Barberton mountain belt: a section through 3.5 Ga oceanic crust. *Journal of African Earth Sciences (1983)*, *6*(5), pp.681-730.

de Wit, M.J., Hart, R., Martin, A. and Abbott, P., 1982. Archean abiogenic and probable biogenic structures associated with mineralized hydrothermal vent systems and regional metasomatism, with implications for greenstone belt studies. *Economic Geology*, *77*(8), pp.1783-1802.

Diener, J.F., Stevens, G., Kisters, A.F. and Poujol, M., 2005. Metamorphism and exhumation of the basal parts of the Barberton greenstone belt, South Africa: Constraining the rates of Mesoarchaean tectonism. *Precambrian Research*, *143*(1-4), pp.87-112.

Droop, G.T.R., 1987. A general equation for estimating Fe 3+ concentrations in ferromagnesian silicates and oxides from microprobe analyses, using stoichiometric criteria. *Mineralogical magazine*, *51*(361), pp.431-435.

Dubacq, B., Vidal, O. and De Andrade, V., 2010. Dehydration of dioctahedral aluminous phyllosilicates: thermodynamic modelling and implications for thermobarometric estimates. *Contributions to Mineralogy and Petrology*, *159*(2), p.159.

Duchac, K.C. and Hanor, J.S., 1987. Origin and timing of the metasomatic silicification of an early Archean komatiite sequence, Barberton Mountain Land, South Africa. *Precambrian Research*, *37*(2), pp.125-146.

Dziggel, A., Stevens, G., Poujol, M., Anhaeusser, C.R. and Armstrong, R.A., 2002. Metamorphism of the granite–greenstone terrane south of the Barberton greenstone belt,

South Africa: an insight into the tectono-thermal evolution of the ‘lower’portions of the Onverwacht Group. *Precambrian Research*, *114*(3-4), pp.221-247.

Ferguson, J. and Currie, K.L., 1972. Silicate immiscibility in the ancient “basalts” of the Barberton Mountain Land, Transvaal. *Nature Physical Science*, *235*(57), pp.86-89.

Fripp, R.E.P., Van Nierop, D.A., Callow, M.J., Lilly, P.A. and Du Plessis, L.U., 1980. Deformation in part of the Archaean Kaapvaal craton, South Africa. *Precambrian Research*, *13*(2-3), pp.241-251.

Furnes, H., de Wit, M. and Dilek, Y., 2014. Precambrian greenstone belts host different ophiolite types. In *Evolution of Archean Crust and Early Life* (pp. 1-22). Springer, Dordrecht.

Furnes, H., de Wit, M.J., Robins, B. and Sandstå, N.R., 2011. Volcanic evolution of the upper Onverwacht Suite, Barberton greenstone belt, South Africa. *Precambrian Research*, *186*(1-4), pp.28-50.

Furnes, H., de Wit, M. and Robins, B., 2013. A review of new interpretations of the tectonostratigraphy, geochemistry and evolution of the Onverwacht Suite, Barberton Greenstone Belt, South Africa. *Gondwana Research*, *23*(2), pp.403-428.

Furnes, H., de Wit, M., Staudigel, H., Rosing, M. and Muehlenbachs, K., 2007. A vestige of Earth's oldest ophiolite. *science*, *315*(5819), pp.1704-1707.

Furnes, H., Robins, B. and De Wit, M.J., 2012. Geochemistry and petrology of lavas in the upper Onverwacht suite, Barberton Mountain Land, South Africa. *South African Journal of Geology*, *115*(2), pp.171-210.

Griffiths, R.W. and Fink, J.H., 1992. Solidification and morphology of submarine lavas: A dependence on extrusion rate. *Journal of Geophysical Research: Solid Earth*, *97*(B13), pp.19729-19737.

Grosch, E.G., 2019. Metamorphic processes preserved in early Archean supracrustal rocks of the Barberton Greenstone Belt, South Africa. *Geological Society, London, Special Publications*, *478*(1), pp.315-334.

Grosch, E.G., Kosler, J., McLoughlin, N., Drost, K., Slama, J. and Pedersen, R.B., 2011. Paleoarchean detrital zircon ages from the earliest tectonic basin in the Barberton Greenstone Belt, Kaapvaal craton, South Africa. *Precambrian Research*, *191*(1-2), pp.85-99.

Grosch, E.G. and McLoughlin, N., 2013. Paleoarchean sulfur cycle and biogeochemical surface conditions on the early Earth, Barberton, South Africa. *Earth and Planetary Science Letters*, *377*, pp.142-154.

Grosch, E.G. and Slama, J., 2017. Evidence for 3.3-billion-year-old oceanic crust in the Barberton greenstone belt, South Africa. *Geology*, *45*(8), pp.695-698.

Grosch, E.G., Vidal, O., Abu-Alam, T. and McLoughlin, N., 2012. P–T constraints on the metamorphic evolution of the Paleoarchean Kromberg type-section, Barberton Greenstone Belt, South Africa. *Journal of Petrology*, *53*(3), pp.513-545.

Grosch, E.G., Viola, G. and Ndlela, S. (2020) Geological record of Paleoarchean oceanic flake tectonics preserved in the c. 3.3 Ga Kromberg volcanic type-section, Barberton greenstone belt, South Africa. *Precambrian Research.* pp. 105815.

Grove, T.L. and Parman, S.W., 2004. Thermal evolution of the Earth as recorded by komatiites. *Earth and Planetary Science Letters*, *219*(3-4), pp.173-187.

Gruau, G., Chauvel, C. and Jahn, B.M., 1990. Anomalous Sm− Nd ages for the early Archean Onverwacht Group Volcanics. *Contributions to Mineralogy and Petrology*, *104*(1), pp.27-34.

Gruner, J.W., 1944. The hydrothermal alteration of feldspars in acid solutions between 300 degrees and 400 degrees C. *Economic Geology*, *39*(8), pp.578-589.

Hall, A.L., 1918. *The geology of the Barberton gold mining district, including adjoining portions of Northern Swaziland*. Government Print. and Stationery Office.

Hamilton, W.B., 1998. Archean magmatism and deformation were not products of plate tectonics. *Precambrian Research*, *91*(1-2), pp.143-179.

Hanor, J.S. and Duchač, K.C., 1990. Isovolumetric silicification of early Archean komatiites: geochemical mass balances and constraints on origin. *The Journal of Geology*, *98*(6), pp.863-877.

Hatton, C.J. and Sharpe, M.R., 1988. *Significance and origin of boninite-like rocks associated with the Bushveld Complex*. University of Pretoria Institute for Geological Research on the Bushveld Complex.

Herzberg, C., 1992. Depth and degree of melting of komatiites. *Journal of Geophysical Research: Solid Earth*, *97*(B4), pp.4521-4540.

Herzberg, C. and Rudnick, R., 2012. Formation of cratonic lithosphere: an integrated thermal and petrological model. *Lithos*, *149*, pp.4-15.

Heubeck, C. and Lowe, D.R., 1999. Sedimentary petrography and provenance of the Archean Moodies Group, Barberton greenstone belt. *Special paper-Geological Society of America*, (329), pp.259-286.

Hey, M.H., 1954. A new review of the chlorites. *Mineralogical Magazine and Journal of the Mineralogical Society*, *30*(224), pp.277-292.

Hofmann, A. and Harris, C., 2008. Silica alteration zones in the Barberton greenstone belt: a window into subseafloor processes 3.5–3.3 Ga ago. *Chemical Geology*, *257*(3-4), pp.221-239.

Hollocher, K., Robinson, P., Walsh, E. and Roberts, D., 2012. Geochemistry of amphibolite-facies volcanics and gabbros of the Støren Nappe in extensions west and southwest of Trondheim, Western Gneiss Region, Norway: a key to correlations and paleotectonic settings. *American Journal of Science*, *312*(4), pp.357-416.

Howie, R.A., Zussman, J. and Deer, W., 1992. *An introduction to the rock-forming minerals*. Longman.

Huppert, H.E. and Sparks, R.S.J., 1981. The fluid dynamics of a basaltic magma chamber replenished by influx of hot, dense ultrabasic magma. *Contributions to Mineralogy and Petrology*, *75*(3), pp.279-289.

Hurley, P.M., Pinson Jr, W.H., Nagy, B. and Teska, T.M., 1972. Ancient age of the middle marker horizon, Onverwacht group, Swaziland sequence, South Africa. *Earth and Planetary Science Letters*, *14*(3), pp.360-366.

Jahn, B.M., Gruau, G. and Glikson, A.Y., 1982. Komatiites of the Onverwacht Group, S. Africa: REE geochemistry, Sm/Nd age and mantle evolution. *Contributions to Mineralogy and Petrology*, *80*(1), pp.25-40.

Jensen, B.B., 1973. Patterns of trace element partitioning. *Geochimica et Cosmochimica Acta*, *37*(10), pp.2227-2242.

Johnson, J.E., Gerpheide, A., Lamb, M.P. and Fischer, W.W., 2014. O2 constraints from Paleoproterozoic detrital pyrite and uraninite. *Bulletin*, *126*(5-6), pp.813-830.

Johnson, K. and Barnes, C.G., 2006. Magma mixing and mingling in the Grayback pluton, Klamath Mountains, Oregon. *Special Paper-Geological Society of America. 410*, p.247.

Jweda, J., Bolge, L., Class, C. and Goldstein, S.L., 2016. High precision Sr-Nd-Hf-Pb isotopic compositions of USGS reference material BCR-2. *Geostandards and Geoanalytical Research*, *40*(1), pp.101-115.

Kamo, S.L. and Davis, D.W., 1994. Reassessment of Archean crustal development in the Barberton Mountain Land, South Africa, based on U-Pb dating. *Tectonics*, *13*(1), pp.167-192.

Kato, D., Aoki, K., Komiya, T., Yamamoto, S., Sawaki, Y., Asanuma, H., Sato, T., Tsuchiya, Y., Shozugawa, K., Matsuo, M. and Windley, B.F., 2018. Constraints on the P–T conditions of high-pressure metamorphic rocks from the Inyoni shear zone in the mid-Archean Barberton Greenstone Belt, South Africa. *Precambrian Research*, *315*, pp.1-18.

Kerr, A.C., Tarney, J., Marriner, G.F., Nivia, A., Klaver, G.T. and Saunders, A.D., 1996. The geochemistry and tectonic setting of late Cretaceous Caribbean and Colombian volcanism. *Journal of South American Earth Sciences*, *9*(1-2), pp.111-120.

Khanna, T.C., Sai, V.V., Jaffri, S.H., Krishna, A.K. and Korakoppa, M.M., 2018. Boninites in the~ 3.3 Ga Holenarsipur Greenstone Belt, Western Dharwar Craton, India. *Geosciences*, *8*(7), p.248.

Kleinhanns, I.C., Kramers, J.D. and Kamber, B.S., 2003. Importance of water for Archaean granitoid petrology: a comparative study of TTG and potassic granitoids from Barberton Mountain Land, South Africa. *Contributions to Mineralogy and Petrology*, *145*(3), pp.377-389.

Kroner, U. and Romer, R.L., 2013. Two plates—many subduction zones: the Variscan orogeny reconsidered. *Gondwana Research*, *24*(1), pp.298-329.

Johnson, T.E., Brown, M., Kaus, B., and VanTongeren, J.A., 2014. Delamination and recycling of Archaean crust caused by gravitational instabilities. *Nature Geoscience*, *7*, pp. 47–52.

Laflèche, M.R., Dupuy, C. and Bougault, H., 1992. Geochemistry and petrogenesis of Archean mafic volcanic rocks of the southern Abitibi Belt, Québec. *Precambrian Research*, *57*(3-4), pp.207-241.

Lafuente, B., Downs, R.T., Yang, H. and Stone, N., 2015. The power of databases: The RRUFF project. In: T. Armbruster and R.M. Danisi, eds. *Highlights in mineralogical crystallography.* Berlin: W. De Gruyter. pp. 1-30.

Lassiter, J.C. and DePaolo, D.J., 1997. Plume/lithosphere interaction in the generation of continental and oceanic flood basalts: chemical and isotopic constraints. *Geophysical Monograph-American Geophysical Union*, *100*, pp.335-356.

Leake, B.E., Woolley, A.R., Arps, C.E., Birch, W.D., Gilbert, M.C., Grice, J.D., Hawthorne, F.C., Kato, A., Kisch, H.J., Krivovichev, V.G. and Linthout, K., 1997. Nomenclature of amphiboles; report of the Subcommittee on Amphiboles of the International Mineralogical Association Commission on new minerals and mineral names. *Mineralogical magazine*, *61*(405), pp.295-310.

Lee, M.C., Klien, E.M.C., Burke, W.J., Zhang, A.X., Riddolls, R.J., Kuo, S.P., Sulzer, M.P. and Isham, B., 1999. Augmentation of natural ionospheric plasma turbulence by HF heater waves. *Geophysical research letters*, *26*(1), pp.37-40.

Le Maitre, R.W., Streckeisen, A., Zanettin, B., Le Bas, M.J., Bonin, B., Bateman, P., Bellieni, G., Dudek, A., Efremova, S., Keller, J. and Lamere, J., 2002. Igneous rocks: A classification and glossary of terms; Recommendations of the International Union of Geological Sciences. In *Subcommission on the Systematics of Igneous rocks*. Cambridge University Press.

López-Martínez, M., York, D. and Hanes, J.A., 1992. A 40Ar39Ar geochronological study of komatiites and komatiitic basalts from the Lower Onverwacht Volcanics: Barberton Mountain Land, South Africa. *Precambrian Research*, *57*(1-2), pp.91-119.

Lowe, D.R., 1991. Geology of the Barberton Greenstone Belt: an overview. In *Two Cratons and an Orogen—Excursion guidebook and review articles for a field workshop through selected Archaean terranes of Swaziland, South Africa and Zimbabwe. IGCP Project* (Vol. 280, pp. 47-58).

Lowe, D.R., 1994. Accretionary history of the Archean Barberton greenstone belt (3.55-3.22 Ga), southern Africa. *Geology*, *22*(12), pp.1099-1102.

Lowe, D.R., 1999a. Petrology and sedimentology of cherts and related silicified sedimentary rocks in the Swaziland Supergroup. *Geol. Soc. Am. Spec. Paper*, *329*, pp.83-114.

Lowe, D.R., 1999c. Geologic evolution of the Barberton Greenstone Belt and vicinity. *Special paper-Geological Society of America*, (329), pp.287-312.

Lowe, D.R. and Byerly, G.R. eds., 1999. *Geologic evolution of the Barberton greenstone belt, South Africa* (Vol. 329). Geological Society of America.

Lowe, D.R. and Byerly, G.R., 2007. .3 An Overview of the Geology of the Barberton Greenstone Belt and Vicinity: Implications for Early Crustal Development. *Developments in Precambrian geology*, *15*, pp.481-526.

Lowe, D.R. and Byerly, G.R., 2020. The non-glacial and non-cratonic origin of an early Archean felsic volcaniclastic unit, Barberton Greenstone Belt, South Africa. *Precambrian Research*, *341*, p.105647.

Lowe, D.R., Byerly, G.R., Ransom, B.L. and Nocita, B.W., 1985. Stratigraphic and sedimentological evidence bearing on structural repetition in early Archean rocks of the Barberton greenstone belt, South Africa. *Precambrian research*, *27*(1-3), pp.165-186.

McDonough, W.F. and Sun, S.S., 1995. The composition of the Earth. *Chemical geology*, *120*(3-4), pp.223-253.

Moore, J.G., 1965. Petrology of deep sea basalt near Hawaii. *American Journal of Science*, *263*(1), pp.40-52.

Moyen, J.F., Stevens, G. and Kisters, A., 2006. Record of mid-Archaean subduction from metamorphism in the Barberton terrain, South Africa. *Nature*, *442*(7102), pp.559-562.

Nédélec, A., Chevrel, M.O., Moyen, J.F., Ganne, J. and Fabre, S., 2012. TTGs in the making: Natural evidence from Inyoni shear zone (Barberton, South Africa). *Lithos*, *153*, pp.25-38.

Nesbitt, R.W. and Sun, S.S., 1976. Geochemistry of Archaean spinifex-textured peridotites and magnesian and low-magnesian tholeiites. *Earth and Planetary Science Letters*, *31*(3), pp.433-453.

Nijman, W. and De Vries, S.T., 2004. Early Archaean crustal collapse structures and sedimentary basin dynamics. *The Precambrian Earth: Tempos and Events. Developments in Precambrian Geology*, *12*, pp.139-155.

Nisbet, E.G., Cheadle, M.J., Arndt, N.T. and Bickle, M.J., 1993. Constraining the potential temperature of the Archaean mantle: a review of the evidence from komatiites. *Lithos*, *30*(3-4), pp.291-307.

Nutman, A.P., Friend, C.R., Horie, K. and Hidaka, H., 2007. The Itsaq Gneiss Complex of southern West Greenland and the construction of Eoarchaean crust at convergent plate boundaries. *Developments in Precambrian Geology*, *15*, pp.187-218.

Ohtani, E., Kawabe, I., Moriyama, J. and Nagata, Y., 1989. Partitioning of elements between majorite garnet and melt and implications for petrogenesis of komatiite. *Contributions to Mineralogy and Petrology*, *103*(3), pp.263-269.

Padrón-Navarta, J.A., Sánchez-Vizcaíno, V.L., Hermann, J., Connolly, J.A.D, Garrido, C.J., Gómez-Pugnaire, M.T. and Marchesi, C., 2013. Tschermak's substitution in antigorite and consequences for phase relations and water liberation in high-grade serpentinites. *Lithos, 178*, pp. 186-196.

Paris, I., Stanistreet, I.G. and Hughes, M.J., 1985. Cherts of the Barberton greenstone belt interpreted as products of submarine exhalative activity. *The Journal of Geology*, *93*(2), pp.111-129.

Parman, S.W., Dann, J.C., Grove, T.L. and De Wit, M.J., 1997. Emplacement conditions of komatiite magmas from the 3.49 Ga Komati Formation, Barberton greenstone belt, South Africa. *Earth and Planetary Science Letters*, *150*(3-4), pp.303-323.

Patchett, P.J. and Tatsumoto, M., 1980. Lu–Hf total-rock isochron for the eucrite meteorites. *Nature*, *288*(5791), pp.571-574.

Paton, C., Hellstrom, J., Paul, B., Woodhead, J. and Hergt, J., 2011. lolite: Freeware for visualisation and processing of mass spectrometric data. *Journal of Analytical Atomic Spectrometry, 26*(12), pp.2508-2518.

Pearce, J.A., 2008. Geochemical fingerprinting of oceanic basalts with applications to ophiolite classification and the search for Archean oceanic crust. *Lithos*, *100*(1-4), pp.14-48.

Pearce, J.A., Harris, N.B. and Tindle, A.G., 1984. Trace element discrimination diagrams for the tectonic interpretation of granitic rocks. *Journal of petrology*, *25*(4), pp.956-983.

Polat, A., Hofmann, A.W. and Rosing, M.T., 2002. Boninite-like volcanic rocks in the 3.7–3.8 Ga Isua greenstone belt, West Greenland: geochemical evidence for intra-oceanic subduction zone processes in the early Earth. *Chemical geology*, *184*(3-4), pp.231-254.

Polat, A., Kerrich, R. and Wyman, D.A., 1999. Geochemical diversity in oceanic komatiites and basalts from the late Archean Wawa greenstone belts, Superior Province, Canada: trace element and Nd isotope evidence for a heterogeneous mantle. *Precambrian Research*, *94*(3-4), pp.139-173.

Puchtel, I.S., Blichert-Toft, J., Touboul, M., Walker, R.J., Byerly, G.R., Nisbet, E.G. and Anhaeusser, C.R., 2013. Insights into early Earth from Barberton komatiites: evidence from lithophile isotope and trace element systematics. *Geochimica et Cosmochimica Acta*, *108*, pp.63-90.

Puchtel, I.S., Hofmann, A.W., Amelin, Y.V., Garbe-Schönberg, C.D., Samsonov, A.V. and Shchipansky, A.A., 1999. Combined mantle plume-island arc model for the formation of the 2.9 Ga Sumozero-Kenozero greenstone belt, SE Baltic Shield: Isotope and trace element constraints. *Geochimica et cosmochimica acta*, *63*(21), pp.3579-3595.

Ransom, B.L., 1987. *The paleoenvironmental, magmatic and geologic history of the 3, 500 myr old Kromberg Formation, west limb of the Onverwacht Anticline: Barberton Greenstone Belt, South Africa* (Doctoral dissertation, Louisiana State University, Baton Rouge).

Ransom, B., Byerly, G.R. and Lowe, D.R., 1999. Subaqueous to subaerial Archean ultramafic phreatomagmatic volcanism, Kromberg Formation, Barberton greenstone belt, South Africa. *Special paper-Geological Society of America*, (329), pp.151-166.

Reagan, M.K., Ishizuka, O., Stern, R.J., Kelley, K.A., Ohara, Y., Blichert-Toft, J., Bloomer, S.H., Cash, J., Fryer, P., Hanan, B.B. and Hickey-Vargas, R., 2010. Fore-arc basalts and subduction initiation in the Izu-Bonin-Mariana system. *Geochemistry, Geophysics, Geosystems*, *11*(3).

Robb, L.J., Anhaeusser, C.R. and Van Nierop, D.A., 1983. The recognition of the Nelspruit batholith north of the Barberton greenstone belt and its significance in terms of Archaean

crustal evolution. In: Anhaeusser, C. R. (ed.). *Contributions to the Geology of the Barberton Mountain Land*. South Africa: Special Publication Geological Society of South Africa*, 9,* pp.117-130.

Robin-Popieul, C.C., Arndt, N.T., Chauvel, C., Byerly, G.R., Sobolev, A.V. and Wilson, A., 2012. A new model for Barberton komatiites: deep critical melting with high melt retention. *Journal of Petrology*, *53*(11), pp.2191-2229.

Robins, B., Sandstå, N.R., Furnes, H. and de Wit, M., 2010. Flow banding in basaltic pillow lavas from the Early Archean Hooggenoeg Formation, Barberton Greenstone Belt, South Africa. *Bulletin of Volcanology*, *72*(5), pp.579-592.

Robins, B., Sandstå, N.R., Furnes, H. and De Wit, M., 2011. Evidence for refilling of previously emptied basaltic pillows in the Hooggenoeg Complex, Barberton Greenstone Belt. *Geological Magazine*, *148*(3), pp.435-441.

Rollinson, H.R., 1993. Using geochemical data: evaluation. *Presentation, Interpretation*, *352*.

Rudnick, R.L. and Gao, S., 2003. The crust. Treatise on geochemistry. *Elsevier Ltd. Oxford*, *3*, pp.1-64.

Rudnick, R.L. and Gao, S., 2004. Composition of the Continental Crust. University of Maryland, College Park, MD, USA.

Scherer, E., Münker, C. and Mezger, K., 2001. Calibration of the lutetium-hafnium clock. *Science*, *293*(5530), pp.683-687.

Schneider, K.P., Hoffmann, J.E., Münker, C., Patyniak, M., Sprung, P., Roerdink, D., Garbe-Schönberg, D. and Kröner, A., 2019. Petrogenetic evolution of metabasalts and metakomatiites of the lower Onverwacht Group, Barberton Greenstone Belt (South Africa). *Chemical Geology*, *511*, pp.152-177.

Schoene, B., de Wit, M.J. and Bowring, S.A., 2008. Mesoarchean assembly and stabilization of the eastern Kaapvaal craton: A structural-thermochronological perspective. *Tectonics, 27*(5).

Shirey, S.B. and Richardson, S.H., 2011. Start of the Wilson cycle at 3 Ga shown by diamonds from subcontinental mantle. *Science*, *333*(6041), pp.434-436.

Smith, JV. and Brown, WL., 1988. Feldspar minerals: Crystal structures, physical, chemical, and microtextural properties. *Springer-Verlag.*

Smith, H.S. and Erlank, A.J., 1982. Komatiites. *Geochemistry and Petrogeneis of Komatiites from the Barberton Greenstone Belt, South Africa. Allen & Unwin, London*, pp.347-397.

Stevens, G., Droop, G.T.R., Armstrong, R.A. and Anhaeusser, C.R., 2002. Amphibolite facies metamorphism in the Schapenburg schist belt: A record of the mid-crustal response to~ 3.23 Ga terrane accretion in the Barberton greenstone belt. *South African Journal of Geology*, *105*(3), pp.271-284.

Sun, S.S. and McDonough, W.F., 1989. Chemical and isotopic systematic of oceanic basalts: implication and processes/Magmatism in the Ocean Basins. *Geollogical Society of London. Special Publication*, (42), pp.313-345.

Taylor, S.R. and McLennan, S.M., 1985. The continental crust: its composition and evolution.

Thirlwall, M.F. and Anczkiewicz, R., 2004. Multidynamic isotope ratio analysis using MC–ICP–MS and the causes of secular drift in Hf, Nd and Pb isotope ratios. *International Journal of Mass Spectrometry*, *235*(1), pp.59-81.

Tice, M.M., Bostick, B.C. and Lowe, D.R., 2004. Thermal history of the 3.5–3.2 Ga Onverwacht and Fig Tree Groups, Barberton greenstone belt, South Africa, inferred by Raman microspectroscopy of carbonaceous material. *Geology*, *32*(1), pp.37-40.

Tomkinson, M.J. and King, V.J., 1991. The tectonics of the Barberton greenstone belt: an overview. In *Two Cratons and an Orogen* (pp. 69-83). Dep. Geol., Univ. Witwatersrand Johannesburg.

Trower, E.J. and Lowe, D.R., 2016. Sedimentology of the~ 3.3 Ga upper Mendon Formation, Barberton Greenstone Belt, South Africa. *Precambrian Research*, *281*, pp.473-494.

Tucker, M.E., 1988. *Techniques in sedimentology* (No. 552.5. 08 TEC). U.S. Geological Survey Certificate of Analysis, online source.

Turner, S., Rushmer, T., Reagan, M. and Moyen, J.F., 2014. Heading down early on? Start of subduction on Earth. *Geology*, *42*(2), pp.139-142.

van Hunen, J., and van den Berg, A.P., 2008. Plate tectonics on the early Earth: Limitations imposed by strength and buoyancy of subducted lithosphere. *Lithos*, *103*, pp. 217–235.

van Hunen, J., and Moyen, J.-F., 2012. Archean subduction: fact or fiction?. *Annual Review of Earth and Planetary Sciences*, *40*, pp. 195–219.

van Kranendonk, M.J., Kröner, A., Hegner, E. and Connelly, J., 2009. Age, lithology and structural evolution of the c. 3.53 Ga Theespruit Formation in the Tjakastad area, southwestern Barberton Greenstone Belt, South Africa, with implications for Archaean tectonics. *Chemical Geology*, *261*(1-2), pp.115-139.

Vennemann, T.W. and Smith, H.S., 1999. Geochemistry of mafic and ultramafic rocks in the Kromberg Formation in its type section, Barberton Greenstone Belt, South Africa. *Special Paper-Geological Society of America*, (329), pp.133-149.

Vervoort, J., 2015. Lu-Hf dating: the Lu-Hf isotope system. In: *Encyclopedia of Scientific Dating Methods*. Netherlands: Springer. pp. 379-390.

Vidal, O., De Andrade, V., Lewin, E., Munoz, M., Parra, T. and Pascarelli, S., 2006. P–T deformation Fe^{3+}/Fe^{2+} mapping at the thin section scale and comparison with XANES mapping: application to a garnet-bearing metapelite from the Sambagawa metamorphic belt (Japan). *Journal of Metamorphic Geology*, *24*(7), pp.669-683.

Viljoen, M.J., 1969. Evidence for the existence of a mobile extrusive peridotitic magma from the Komati Formation of the Onverwacht Group. In: Upper Mantle Project. *Geological Society of South Africa Special Publication*, *2*, pp.87-112.

Viljoen, M.J. and Viljoen, R., 1969. The geology and geochemistry of the lower ultramafic unit of the Onverwacht Group and a proposed new class of igneous rocks. *Geological Society of South Africa Special Publication*, *2*, pp.55-86.

Viljoen, M.J. and Viljoen, R.P., 1969. A reappraisal of the granite-greenstone terrains of shield areas based on the Barberton model. *Geol. Soc. S. Afr., Spec. Publ.*, *2*, pp.245-274.

Viljoen, M.J., Viljoen, R.P., Smith, H.S. and Erlank, A.J., 1983. Geological, textural and geochemical features of komatiitic flows from the Komati Formation.

Viljoen, R.P. and Viljoen, M.J., 1969. The geological and geochemical significance of the upper formations of the Onverwacht Group. *Geol. Soc. S. Afr., Spec. Publ.*, *2*, pp.113-151.

Visser, DJL. 1956. The geology of the Barberton area. Vol. 15. Union of South Africa, Department of Mines.

Williams, D.A.C. and Furnell, R.G., 1979. Reassessment of part of the Barberton type area, South Africa. *Precambrian Research*, *9*(3-4), pp.325-347.

Xie, W.H., Shiu, W.Y. and Mackay, D., 1997. A review of the effect of salts on the solubility of organic compounds in seawater. *Marine Environmental Research*, *44*(4), pp.429-444.

Zegers, T.E. and van Keken, P.E., 2001. Middle Archean continent formation by crustal delamination. *Geology,* 29(12), pp. 1083-1086.

Appendix

A1. Scanning Electron Microscope (SEM)

A1.1. Introduction

In addition to XRD, SEM (scanning electron microscope) analysis was conducted for the Kromberg type-section rocks. An X-ray analyser (Energy Dispersive Spectrometer – EDS) was performed on selected carbon coated thin sections at the Department of Physics, Rhodes University for element mapping and mineral identification. The instrument used is an Oxford INCAPenta microanalysis system with FETx3 detector attached to TESCAN VEGA LMU. The analyses were conducted with a high energy (20 kV) electron beam and calibrated using cobalt as a standard. An energy dispersive X-ray spectrometer was set to collect X-rays for 60 seconds at all energy levels. The data was converted into an X-ray spectrum of energy levels versus intensity (in counts), resulting into graphs of 'peaks' at energy levels corresponding to specific atoms. The maps produced were done and calculated at a spectrum range of 0-20 keV at 0.512 seconds per frame. The main aim of this chapter is to study the relationship between the optical image, backscattered electron image and the chemical composition of the minerals in the thin section. In the Kromberg type-section, 8 samples containing representative minerals of the type-section, were selected for SEM analysis. The selected samples for this chapter are KrO-45, KrO-46, KrT-50, KrK-21, KrDun-65, KrO-20, KrST-22 and KrK-44. For each sample analysed, an element map and graphs of 'peaks' at energy levels corresponding to specific atoms are provided. In this chapter, peak graphs with different atomic compositions for different minerals are provided as well as selected mineral maps for various microdomains in the samples.

A1.2. X-ray spectrum graphs

Rock compositions of the mid-lower Kromberg type-section record conditions ranging between greenschist to sub-greenschist facies (Grosch et al., 2018). Mineral phases analysed for SEM-EDS are thus pyroxene, actinolite, albite, quartz, calcite, chlorite, serpentine and magnetite. The backscattered image shows pyroxene crystals as grey-white minerals. The major elemental compositions in pyroxene crystals are O, Si, Ca, Mg and Fe. KrO-45 comprises 48.6 wt.% O, 25.8 wt.% Si, 13.6 wt.% Ca, 11.3 wt.% Mg and 3.8 wt.% Fe; and minor Cr and Al with 0.7 wt.% and 0.6 wt.%. KrST-22 comprises 56.8 wt.% O, 29.4 wt.% Si and 16.5 wt.% Ca. Mg, Fe and Al are estimated to be 11.5 wt.%, 6.6 wt.% and 1.5 wt.%. The major elemental composition in KrT-21 are O (66.0 wt.%), Si (34.6 wt.%), Ca (18.1 wt.%), Mg (13.9 wt. %), Fe (8.6 wt.%) and Al (1.7 wt.%). Minor elements (less than 0.5 wt.%) include Cr and Ti. Actinolite crystals replacing pyroxene in KrK-21 (**Figure A2.1b**) comprises 55.8 wt.% O, 28.6 wt.% Si, 12.5 wt.% Ca and 14.0 wt.% Fe. Other atomic concentrations include 8.8 wt.% Mg, 0.7 wt.% Al and 0.2 wt.% Mn. In KrSt-22 actinolite comprises 47.2 wt.% O, 22.8 wt.% Fe, 12.0 wt.% Si, 9.4 wt.% Al, 7.1 wt.% Mg and 0.3 wt.% Mn. Calcite is also found as a replacement mineral in KrT-50. Calcite comprises 42.0 wt.% O, 38.0 wt.% Ca, 0.2 wt.% Fe and 0.1 wt.% Si. Albite appears dark grey in a backscattered image. It has O, Si, Al and Fe as major elements. In KrT-50 (**Figure A2.1e**) O, Si and Fe makes up 51.8 wt.%, 27.0 wt.% and 13.7 wt.%. Other concentrations include 9.4 wt.% Ca, 7.2 wt.% Mg, 2.0 wt.% Al and minor elements like Mn, Na and K. KrK-44 was analysed for epidote. It (**Figure A2.1a**) comprises 54.4 wt.% O, 20.7 wt.% Si, 16.8 wt.% Al and 15.9 wt.% Ca. Fe and Na occur in minor concentrations of 1.5 wt.% and 0.9 wt.%.

Chlorite was analysed for in rock sample KrO-20 and KrT-50. Major elements making up chlorite are Si, O and Mg. In KrO-20 (**Figure A2.1d**) elemental compositions are estimated at 54.7 wt.% O, 16.1 wt.% Si, 15.8 wt.% Mg and 12.7 wt.% Fe. Other elements include Al at 8.5 wt.%, Cr at 0.7 wt.% and Mn at 0.2 wt.%. KrT-50 analysis for chlorite comprises 103.0 wt.% O, 29.3 wt.% Si, 28.2 wt.% Mg, 20.8 wt.% Fe and 13.4 wt.% Al. Serpentine appears dark-grey on a backscattered image. It has O, Si and Mg as major elements. In the Kromberg type-section, the selected samples that contain serpentine as an alteration product are KrDun-65, KrO-45 and KrO-20. In KrDun-65 (**Figure A2.1c**), the elemental composition for O, Mg and Si are 58.5, 24.3 and 20.4 wt.% respectively. Fe and Al

has been estimated to be 2.7 and 0.8 wt.% and trace elements like Ni and Cr. In KrO-45 serpentine elemental compositions for O, Si and Mg are estimated at 38.6, 14.6 and 13.6 wt.% and minor Al estimated at 0.4 wt.%. KrO-20 comprises 50.6, 27.3 and 11.1 wt.% for O, Si and Mg. Atoms in minor concentrations include Ca with 8.5 wt.%, Fe (7.9 wt.%), Al (0.5 wt.%), Mn (0.2 wt.%) and Yb with 0.1 wt.%. KrT-50 and KrST-22 were analysed for titanite. KrST-22 (**Figure A2.1f**) comprises 40.0 wt.% O, 32.2 wt.% Ti, 32.1 wt.% Fe and 4.4 wt.% Mn as major elements. Ca and Si occur in low concentrations with 1.1 wt.% and 0.3 wt.%. KrT-50 comprises 80.2 wt.% O, 32.6 wt.% Ti, 30.6 wt.% Ca, 26.0 wt.%, 2.3 wt.% Fe and 1.9 wt.% Mg. Al, Sc and I occur in low concentrations with 1.4 wt.%, 0.5 wt.% and 1.0 wt.%. Quartz occur as an interstitial phase with 39.4 wt.% Si and 47.9 wt.% O and traces of C. The sample analysed for magnetite is KrO-45. It is dominated by Fe, O and Cr. Fe, O and Cr which make up the major elements are estimated at 44.1 wt.%, 39.6 wt.% and 23.7 wt.%. Al, Ti and Mn have 4.6 wt.%, 3.9 wt.% and 2.2 wt.% respectively. Trace elements include Zn, V and Re.

Table A1. 1*: Table showing elemental compositions (in wt.%) for different minerals. These compositions correspond to the graphs in* ***Figure A2.1****.*

Mineral Sample	Serpentine KrDun-65	Epidote KrK-44	Chlorite KrO-20	Titanite KrST-22	Albite KrT-50	Actinolite KrT-21
O	83.47	61.49	78.46	40.10	66.58	69.61
Na	0.00	0.72	0.00	0.00	0.18	0.00
Mg	19.85	0.00	13.61	0.00	5.57	6.78
Al	0.50	13.94	6.84	0.00	1.58	0.51
Si	111.59	121.77	93.88	2.32	159.57	169.58
K	0.00	0.00	0.00	0.00	9.92	0.00
Ca	0.00	16.66	0.00	1.13	0.00	13.22
Fe	2.46	1.51	12.70	32.17	0.00	13.94
Mn	0.00	0.00	0.17	4.41	13.70	0.19
Cr	0.16	0.00	0.00	0.00	0.00	0.00
Ni	0.22	0.00	0.00	0.00	0.00	0.00
Ti	0.00	0.00	0.00	32.41	0.00	0.00
Cr	0.00	0.00	0.74	0.00	0.00	0.00
V	0.00	0.00	0.00	0.00	0.24	0.00
Re	0.00	0.00	0.00	0.00	257.50	0.00
S	0.00	0.00	0.00	0.00	0.16	0.00
Total	218.25	216.08	206.41	112.53	515.00	273.84

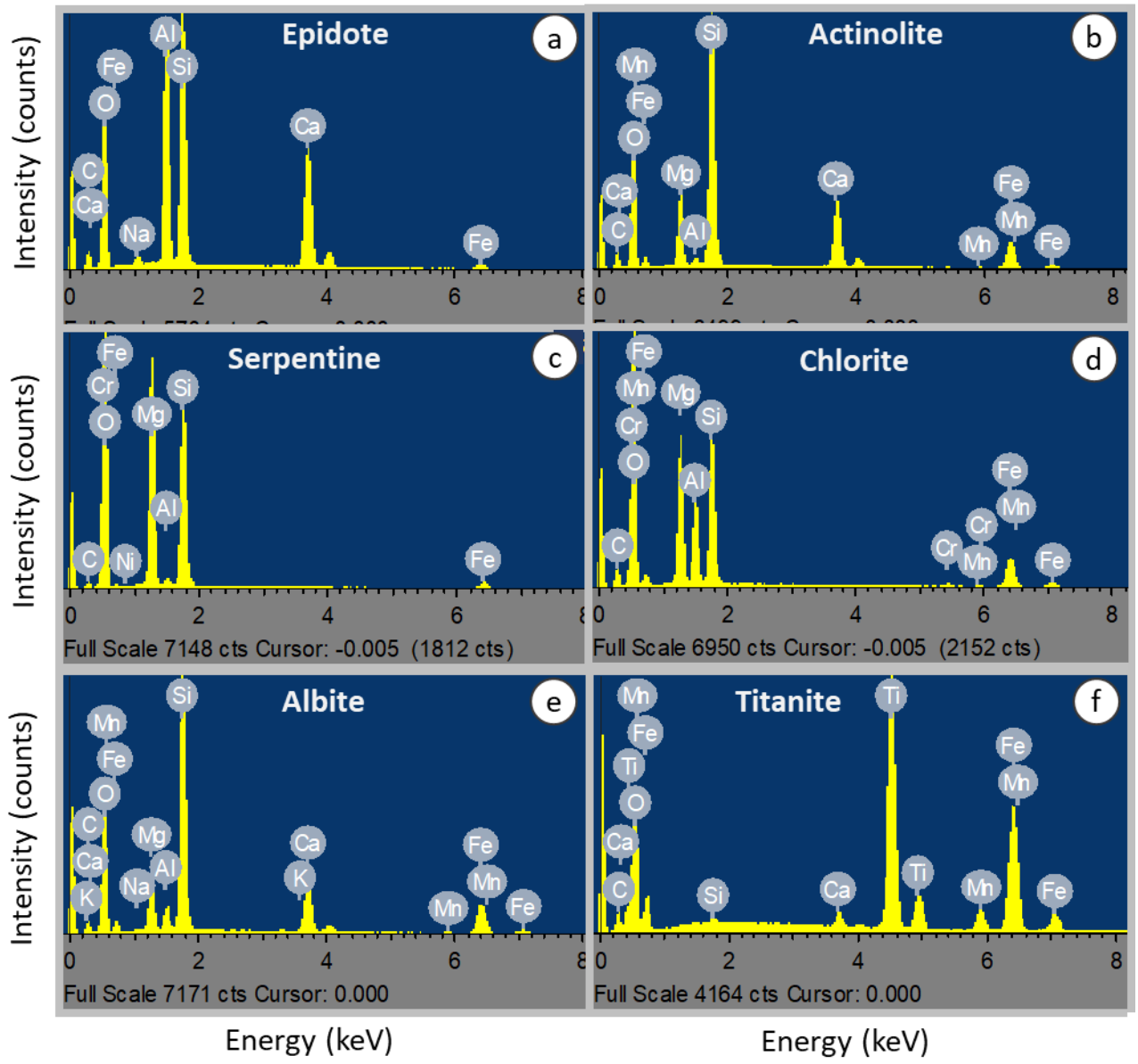

Figure A1. 1*: Graphs that show peaks at energy levels corresponding to different atoms for (a) epidote, (b) actinolite, (c) serpentine, (d) chlorite, (e) albite and (f) titanite.*

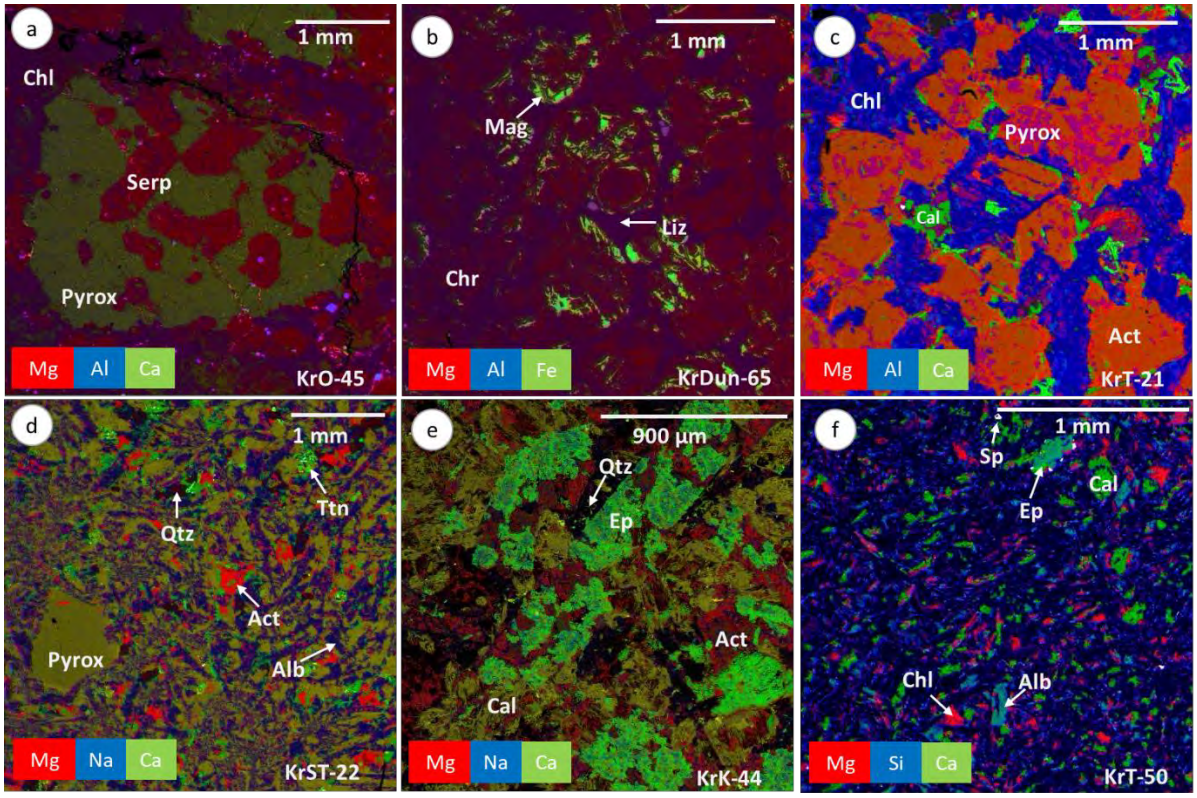

***Figure A1. 2**: Elemental maps for different samples in the Kromberg type-section. For each elemental map provided, three elements are chosen and given different colours. The resultant maps can either show a single elemental colour or a combination of two or three colours.*

A1.3 Elemental maps

Figure A1.2 show EDS maps of the analysed samples in the Kromberg type-section. In these maps, different colours have been assigned for selected atoms to show their distribution across the thin section. The colours used are red, blue and green. Different minerals may project different atomic concentrations thereby producing a combination of different colours. The atomic concentrations chosen are been included in each map and labels of minerals present included for each sample to ease readability. Out of eight samples analysed for EDS point analysis, only six samples are analysed for mineral mapping. These are KrO-45, KrDun-65, KrK-21, KrST-22, KrK-44 and KrT-50. KrT-21 (**Figure A1.2c**) shows pyroxene as Mg- and Al-rich and actinolite as Mg- and Ca-rich. Actinolite crystals forms

pseudomorphs of pyroxene where they grow from the rim inwards towards the core. As a result, relic pyroxene crystals are preserved at core. The sample also comprises Ca-rich calcite and Al-rich chlorite. Calcite is associated with the pyroxene crystals while chlorite forms the groundmass. **Figure A1.2d** shows KrST-22 to comprise Ca-rich pyroxene that is replaced by actinolite along its margins. Calcite is also evident with high Ca and albite show traces of Na. Titanite is also found in the sample with traces of Ca. KrK-44 (**Figure A1.2e**) comprises Ca-rich epidote, Mg-containing plagioclase, calcite and quartz forming the interstitial phase. From this sample, plagioclase is almost completely pseudomorphed by epidote and calcite. KrT-50 (**Figure A1.2f**) comprises Ca-rich epidote and calcite, chlorite and sphalerite. KrO-45 (**Figure A1.2a**) shows pyroxene crystals as Ca-rich, chlorite as Mg- and Al-rich and serpentine as Mg-rich with traces of Al. KrDun-65 (**Figure A1.2b**) comprises Fe-rich magnetite and serpentine replacing olivine crystals. In the preceding XRD chapter it was shown that the serpentine minerals in this rock is chrysotile and lizardite. From **Figure A1.2b** it is observed that two types of serpentine minerals occur, one replacing olivine along its cores and one occurring along olivine fractures. Chrysotile has been tested to contain relatively low concentrations of Al_2O_3 while lizardite is low in Fe^{2+} and the ratio of Fe^{2+} with Fe^{3+} (Page, 1968; Whittaker and Wicks, 1970). The atomic concentration in olivine crystals along fractures is more Al-rich compared to the core. Olivine crystals are thereby replaced by lizardite along its fractures and chrysotile at their core.

A2. Petrography

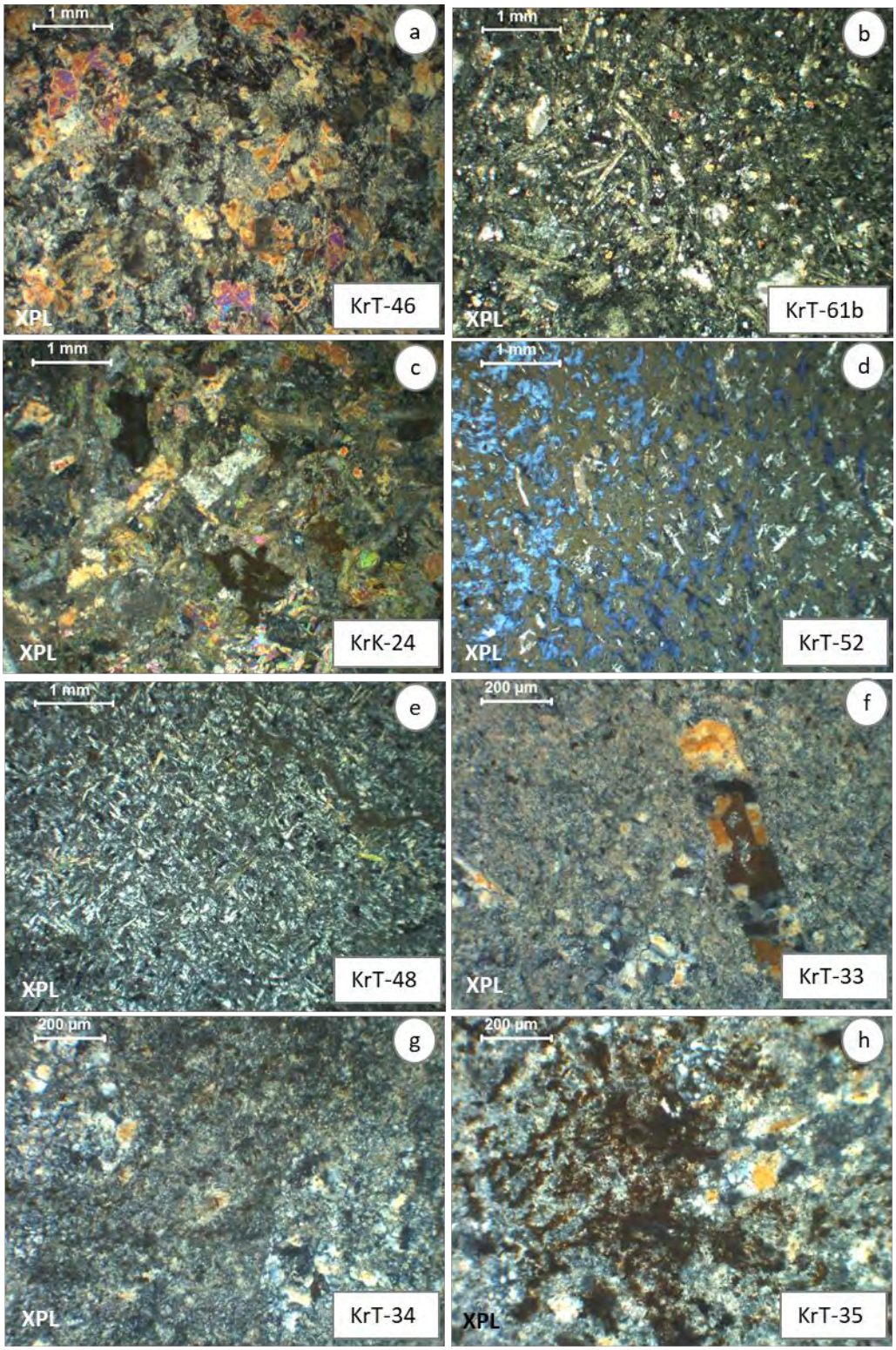

Figure A2. 1*: Photomicrographs of different rock samples in the Kromberg type-section. (a) is a komatiitic basalt, (b) a partially chloritized tholeiite, (c)-(e) highly chloritized tholeiites and (f)-(h) highly silicified tholeiites.*

The rock sample KrT-46 (**Figure A2.3a**) is a medium-grained and interstitial. It comprises pyroxene crystals making up ca. 70% of the rock, magnetite, ca. 20%, and quartz, ca. 10%. The pyroxene crystals are tabular, subhedral and moderately altered. They have lengths of ca. 0.25 mm to ca. 2.2 mm. They are colourless, have pale green pleochroism, have a moderate relief and have two cleavages intersecting at 90^{o}. They show up to second order blue interference colours and have a 90^{o} extinction angle. The pyroxene crystals are replaced by chlorite and actinolite with first order black and white interference colours. Magnetite is black and opaque and is found in between pyroxene crystals. Quartz crystals are colourless with a low relief. They have low first order grey-white interference colours and forms part of the matrix.

The rock, KrK-61 (**Figure A2.3b**), is amygdular, microcrystalline and medium-grained. It comprises ca. 40% green pyroxene, ca. 40% plagioclase and ca. 20% magnetite. Pyroxene is needle-shaped, has a moderate relief and has second order pink-yellow-blue interference colours. The green colour in pyroxene is an indication of its replacement by chlorite. Plagioclase is needle-shaped, colourless with some twins. It forms lengths of ca. 1.28 mm. It is replaced by sericite and clinozoisite. Sericite gives the mineral its pale brown to pinkish interference colours. Clinozoisite is a stubby, colourless and pleochroic. It has first order yellow interference colours. Chlorite is green with blue interference colours. Chlorite is observed within the amygdales. It is green with anomalous brown interference colours. The calcite amygdales are colourless with a rhombohedral cleavage. They have a twinkling relief and lamellae twins within the cleavages.

KrK-24 (**Figure A2.3c**) is similar to KrK-23 (**see Petrography Chapter 5**). It is medium-grained and has an intergranular texture. Pyroxene is replaced by actinolite and chlorite while colourless quartz and brown titanite is found in between the pyroxene interstices. The rock, KrT-52 (**Figure A2.3d**), is microcrystalline and fine-grained. It comprises ca. 40% pyroxene, ca. 20% plagioclase (albite), ca. 20% titanite and ca. 20% glassy matrix. The rock has an overall intersertal texture where the interstices between the feldspar crystals are filled with glass and secondary minerals like chlorite. The pyroxene crystals are tabular, colourless and pleochroic. They form lengths of ca. 0.564 mm. Their cleavages are not clearly formed as they have been heavily altered by chlorite. The pyroxene crystals are converted to actinolite. Their blue interference colours are a result of chloritization. The plagioclase crystals are needle shaped. They are colourless and pleochroic. They have first order grey-white interference colours and form lengths of ca. 0.6 mm.

Titanite is brown under plain- and crossed-polarized light. It forms dusty stains in the rock. The groundmass is glassy and chloritized. The thin section shows two regions of the pillow lavas. It shows the pillow rim and the pillow core. The pillow rim is more chloritized compared to the pillow core. This can be observed from the blue interference colours observed in the glassy matrix.

Rock sample KrT-48 (**Figure A2.3e**) is an aphanitic microcrystalline rock that comprise plagioclase crystals in a pyroxene matrix. It comprises ca. 60% plagioclase, ca. 20% titanite, ca. 20% pyroxene crystals. The length of the plagioclase crystals (ca. 0.571 mm) is larger than the pyroxene crystals (ca. 0.119 mm). The overall texture of the rock is therefore subophitic. The plagioclase crystals are fibrous due to alteration and form lengths of ca. 0.571 mm. They are green and pleochroic. Plagioclase pseudomorphs pyroxene crystals and appears green in plain-polarized light because of chloritization. It has a low relief and display low first order interference colours. Some simple twinning can be observed but some crystals displays endulose extinction. Pyroxene crystals are found in between the plagioclase crystals. They are tabular, colourless and pleochroic. They have a moderate relief, two cleavages intersecting at 90^{o}. They display second order interference colours. Titanite is found in between the plagioclase crystals and around the pyroxene crystals. It is brown and non-pleochroic. KrT-33 and KrT-34 (**Figure A2.3f-g**) comprises pyroxene crystals pseudomorphed by quartz resulting in first order interference colours. These rocks have an aphyric texture comprising of silicified groundmass. KrT-35 (**Figure A2.3g**) is aphanitic and comprises ca. 40 % glass, ca. 30% pyroxene and ca. 30% titanite. The pyroxene crystals have been heavily silicified. Titanite forms around the glassy matrix and pyroxene crystals and the glass is heavily silicified with first order interference colours.

A3: Mineral chemistry tables

Table A3. 1*: Microprobe analysis of pyroxene crystals*.

	Kr21-1	**Kr21-2**	**Kr21-3**	**Kr21-4**	**Kr21-5**	**Kr21-8**
SiO2	52.61	52.30	52.99	52.56	52.32	52.57
TiO2	0.19	0.32	0.30	0.31	0.32	0.29
Al2O3	1.76	1.71	1.70	1.71	1.75	1.75
Cr2O3	0.31	0.30	0.30	0.30	0.29	0.27
Fe2O3	0.00	0.00	0.00	0.00	0.00	0.00
FeO	8.10	7.50	8.16	8.15	8.46	8.08
MnO	0.20	0.19	0.23	0.15	0.20	0.21
MgO	16.94	16.49	17.06	16.97	16.71	17.05
CaO	17.82	18.87	18.19	18.29	18.41	17.63
Na2O	0.20	0.18	0.13	0.16	0.14	0.15
K2O	0.02	0.03	0.02	0.02	0.02	0.04
NiO	0.00	0.06	0.00	0.06	0.00	0.07
Total	98.15	97.94	99.06	98.67	98.62	98.11
Formula	No. of cations on the basis of 6 oxygen atoms					
Si	1.97	1.97	1.97	1.96	1.96	1.97
Ti	0.01	0.01	0.01	0.01	0.01	0.01
Al	0.08	0.08	0.07	0.08	0.08	0.08
Cr	0.01	0.01	0.01	0.01	0.01	0.01
Fe(iii)						
Fe(ii)	0.28	0.25	0.28	0.26	0.27	0.28
Mn	0.01	0.01	0.01	0.00	0.01	0.01
Mg	0.95	0.92	0.94	0.94	0.93	0.95
Ca	0.72	0.76	0.72	0.73	0.74	0.71
Na	0.01	0.01	0.01	0.01	0.01	0.01
K	0.00	0.00	0.00	0.00	0.00	0.00
Ni	0.00	0.00	0.00	0.00	0.00	0.00
tot.	4.02	4.02	4.03	4.01	4.00	4.03
End-member						
Fe*	13.53	12.55	13.51	13.38	13.97	13.53
Ca	37.23	39.47	37.52	37.81	38.02	36.86
Mg	49.24	47.98	48.97	48.81	48.01	49.61
Total	100.00	100.00	100.00	100.00	100.00	100.00

***Table A3.1**: (continued)*

	Kr22-3	Kr22-5	Kr22-6	Kr22-7	Kr22-8	Kr22-9
SiO2	47.99	49.42	49.41	49.86	49.08	49.95
TiO2	0.97	0.85	0.72	0.69	0.32	0.63
Al2O3	4.44	3.54	3.02	2.21	0.94	2.46
Cr2O3	0.14	0.15	0.11	0.00	0.00	0.08
Fe2O3	1.13	0.90	1.03	0.99	3.25	0.89
FeO	14.62	11.93	14.59	15.34	13.01	13.32
MnO	0.27	0.28	0.31	0.43	0.42	0.44
MgO	10.59	12.84	11.40	11.23	11.18	11.31
CaO	17.86	18.51	18.20	18.03	19.14	19.12
Na2O	0.32	0.22	0.24	0.25	0.22	0.39
K2O	0.04	0.02	0.02	0.04	0.04	0.02
NiO	0.00	0.00	0.00	0.08	0.00	0.00
Total	98.35	98.65	99.06	99.12	97.60	98.61
Formula	No. of cations on the basis of 6 oxygen atoms					
Si	1.86	1.89	1.90	1.93	1.93	1.93
Ti	0.03	0.02	0.02	0.02	0.01	0.02
Al	0.20	0.16	0.14	0.10	0.04	0.11
Cr	0.00	0.00	0.00	0.00	0.00	0.00
Fe(iii)	0.03	0.03	0.03	0.03	0.10	0.03
Fe(ii)	0.47	0.38	0.47	0.50	0.43	0.43
Mn	0.01	0.01	0.01	0.01	0.01	0.01
Mg	0.61	0.73	0.65	0.65	0.66	0.65
Ca	0.74	0.76	0.75	0.75	0.81	0.79
Na	0.02	0.02	0.02	0.02	0.02	0.03
K	0.00	0.00	0.00	0.00	0.00	0.00
Ni	0.00	0.00	0.00	0.00	0.00	0.00
tot.	4.00	4.00	4.00	4.00	4.00	4.00
End-member						
Fe*	27.58	21.84	26.63	27.87	26.90	24.61
Ca	39.67	39.78	39.19	38.64	40.32	41.36
Mg	32.74	38.38	34.18	33.49	32.78	34.03
Total	100.00	100.00	100.00	100.00	100.00	100.00

***Table A3.1**: (continued)*

	Kr46-2	Kr46-3	Kr46-4	Kr46-5	Kr46-11	Kr46-12
SiO2	53.276	52.589	52.543	52.439	52.604	52.624
TiO2	0.274	0.283	0.34	0.294	0.32	0.288
Al2O3	1.226	2.578	2.429	2.561	2.188	2.142
Cr2O3	0.539	0.69	0.794	0.957	0.769	0.599
Fe2O3	0.00	0.00	0.00	0.00	0.00	0.00
FeO	5.333	5.304	5.394	5.559	5.731	5.409
MnO	0.168	0.172	0.139	0.145	0.184	0.134
MgO	18.461	17.342	17.572	17.364	17.599	16.939
CaO	19.505	19.863	19.519	19.19	18.996	19.757
Na2O	0.163	0.141	0.205	0.216	0.173	0.168
K2O	0.022	0.029	0.016	0.038	0.04	0.023
NiO	0.131	0.082	0.047	0.073	0.102	0.053
Total	99.098	99.073	98.998	98.836	98.706	98.136
Formula	No. of cations on the basis of 6 oxygen atoms					
Si	1.96	1.94	1.94	1.94	1.95	1.96
Ti	0.01	0.01	0.01	0.01	0.01	0.01
Al	0.05	0.11	0.11	0.11	0.10	0.09
Cr	0.02	0.02	0.02	0.03	0.02	0.02
Fe(iii)	0.01					
Fe(ii)	0.15	0.18	0.17	0.19	0.19	0.21
Mn	0.01	0.01	0.00	0.00	0.01	0.00
Mg	1.01	0.95	0.97	0.96	0.97	0.94
Ca	0.77	0.78	0.77	0.76	0.75	0.79
Na	0.01	0.01	0.01	0.02	0.01	0.01
K	0.00	0.00	0.00	0.00	0.00	0.00
Ni	0.00	0.00	0.00	0.00	0.00	0.00
tot.	4.00	4.01	4.01	4.02	4.00	4.00
End-member						
Fe*	8.68	8.86	8.95	9.32	9.60	9.08
Ca	39.41	41.15	40.42	40.14	39.49	41.46
Mg	51.91	49.99	50.64	50.54	50.91	49.46
Total	100.00	100.00	100.00	100.00	100.00	100.00

***Table A3.1**: (continued)*

	Kr45-1	Kr45-2	Kr45-3	Kr45-4	Kr45-7	Kr45-8
SiO2	53.305	53.831	53.543	53.089	53.739	53.363
TiO2	0.291	0.205	0.224	0.213	0.22	0.231
Al2O3	2.12	1.839	1.535	1.687	1.562	1.334
Cr2O3	0.926	1.064	1.083	1.047	1.081	0.895
Fe2O3	0.00	0.00	0.00	0.00	0.00	0.00
FeO	5.766	5.371	5.19	5.182	5.178	5.026
MnO	0.145	0.094	0.119	0.187	0.141	0.134
MgO	17.62	18.011	17.943	17.942	18.162	18.313
CaO	19.18	19.186	19.184	18.874	18.952	18.877
Na2O	0.199	0.194	0.187	0.197	0.211	0.172
K2O	0.029	0.024	0	0.018	0	0.027
NiO	0.058	0	0	0.044	0.048	0.074
Total	99.639	99.819	99.008	98.48	99.294	98.446
Formula	No. of cations on the basis of 6 oxygen atoms					
Si	1.96	1.97	1.97	1.97	1.97	1.97
Ti	0.01	0.01	0.01	0.01	0.01	0.01
Al	0.09	0.08	0.07	0.07	0.07	0.06
Cr	0.03	0.03	0.03	0.03	0.03	0.03
Fe(iii)						
Fe(ii)	0.21	0.21	0.21	0.20	0.20	0.19
Mn	0.00	0.00	0.00	0.01	0.00	0.00
Mg	0.96	0.98	0.99	0.99	0.99	1.01
Ca	0.75	0.75	0.76	0.75	0.75	0.75
Na	0.01	0.01	0.01	0.01	0.02	0.01
K	0.00	0.00	0.00	0.00	0.00	0.00
Ni	0.00	0.00	0.00	0.00	0.00	0.00
tot.	4.03	4.04	4.05	4.03	4.04	4.03
End-member						
Fe*	9.55	8.79	8.58	8.73	8.58	8.33
Ca	39.70	39.55	39.72	39.29	39.17	39.01
Mg	50.75	51.66	51.70	51.98	52.24	52.66
Total	100.00	100.00	100.00	100.00	100.00	100.00

***Table A3. 2**: Microprobe analyses of plagioclase crystals*.

	Kr50-16	**Kr50-17**	**Kr50-19**	**Kr50-20**	**Kr22-10**	**Kr22-12**	**Kr22-13**	**Kr22-14**
SiO2	66.70	68.58	68.54	69.04	64.66	69.14	64.85	64.56
TiO2	0.00	0.00	0.00	0.04	0.00	0.00	0.00	0.04
Al2O3	19.12	19.23	19.97	19.91	22.99	20.58	23.17	22.35
FeO	1.93	0.42	1.08	0.48	1.12	0.42	0.85	0.87
CaO	0.37	0.45	0.38	0.40	1.22	0.61	1.03	1.03
Na2O	11.02	11.44	11.15	11.45	9.15	11.46	8.85	9.00
K2O	0.19	0.19	0.37	0.14	2.20	0.12	2.38	2.42
MgO	0.66	0.17	0.37	0.13	0.33	0.05	0.25	0.24
BaO	0.04	0.00	0.04	0.00	0.04	0.05	0.02	0.00
F	0.00	0.07	0.00	0.00	0.00	0.00	0.00	0.00
SrO	0.35	0.38	0.31	0.32	0.40	0.41	0.41	0.38
Total	100.37	100.93	102.21	101.90	102.11	102.83	101.79	100.88
Formula			No. of cations on the basis of 32 oxygen atoms					
Si	11.78	11.94	11.83	11.90	11.29	11.82	11.33	11.39
Ti	0.00	0.00	0.00	0.01	0.00	0.00	0.00	0.01
Al	3.98	3.95	4.06	4.04	4.73	4.15	4.77	4.65
Fe(ii)	0.28	0.06	0.16	0.07	0.16	0.06	0.12	0.13
Ca	0.07	0.08	0.07	0.07	0.23	0.11	0.19	0.19
Na	3.77	3.86	3.73	3.82	3.10	3.80	3.00	3.08
K	0.04	0.04	0.08	0.03	0.49	0.03	0.53	0.54
Mg	0.17	0.05	0.10	0.03	0.08	0.01	0.06	0.06
Ba	0.00	0.00	0.00	0.00	0.00	0.00	0.00	0.00
F	0.00	0.04	0.00	0.00	0.00	0.00	0.00	0.00
Sr	0.04	0.04	0.03	0.03	0.04	0.04	0.04	0.04
TOTAL	20.14	20.06	20.05	20.01	20.13	20.02	20.05	20.09
An	1.78	2.09	1.82	1.87	5.99	2.81	5.17	5.08
Or	1.10	1.08	2.08	0.79	12.85	0.69	14.25	14.26
Ab	97.13	96.83	96.10	97.34	81.16	96.50	80.59	80.66

***Table A3. 3**: Microprobe analysis of chlorite*

Comment	Kr45	Kr45-9	Kr45-17	Kr45-22
SiO2	43.143	40.521	37.743	35.747
TiO2	0.066	0.231	0	0
Al2O3	7.742	10.015	9.38	11.54
Fe2O3	0.00	0.00	0.00	0.00
FeO	8.113	7.862	11.107	11.456
MnO	0.042	0.108	0.111	0.106
MgO	30.966	30.64	28.067	29.236
CaO	0.121	0.109	1.227	0.111
Na2O	0	0.043	0.058	0.08
K2O	0.021	0.034	0.112	0.19
Cr2O3	0.687	0.243	0	0.049
Total	90.901	89.806	87.805	88.515
Formula	No. of cations on the basis of 14O atoms			
Si	3.92	3.73	3.65	3.44
Al(iv)	0.08	0.27	0.35	0.56
T site	4.00	4.00	4.00	4.00
Al(vi)	0.75	0.82	0.72	0.75
Fe(iii)	0.00	0.00	0.00	0.00
Ti	0.00	0.02	0.00	0.00
Mg	4.20	4.21	4.05	4.19
Fe(ii)	0.62	0.61	0.90	0.92
Mn	0.00	0.01	0.01	0.01
Ca	0.01	0.01	0.13	0.01
Na	0.00	0.01	0.01	0.01
K	0.00	0.00	0.01	0.02
Cr(3+)	0.05	0.02	0.00	0.00
O site	5.64	5.70	5.83	5.92
[R3+]OctTriv	0.75	0.82	0.72	0.75
XMg	0.87	0.87	0.82	0.82
X Fe	0.13	0.13	0.18	0.18
non-interlayer	9.57	9.66	9.68	9.87
Al (tot)	0.83	1.09	1.07	1.31
Al(iv)	0.08	0.27	0.35	0.56
x (Chl)	0.61	0.69	0.70	0.88

***Table A3. 4**: Microprobe analysis of amphiboles*

	Kr39-5	Kr39-6	Kr39-7	Kr39-8	Kr39-9	Kr21-7
SiO2	52.67	54.22	54.94	55.20	53.62	50.70
TiO2	0.00	0.11	0.23	0.05	0.25	0.00
Al2O3	1.56	1.16	3.02	0.87	1.99	2.61
FeO	13.69	12.44	14.03	11.76	12.83	16.41
MnO	0.47	0.28	0.27	0.36	0.28	0.22
MgO	14.46	16.14	14.32	16.27	15.01	11.87
CaO	12.69	12.60	11.93	13.26	12.53	11.80
Na2O	0.14	0.19	0.80	0.13	0.35	0.22
K2O	0.05	0.08	0.07	0.04	0.10	0.15
Cr2O3	0.00	0.00	0.00	0.00	0.00	0.11
NiO	0.00	0.00	0.00	0.00	0.00	0.00
Total	95.73	97.22	99.61	97.94	96.96	94.08
Formula	No. of cations on the basis of 23 oxygen atoms					
Si	7.80	7.84	7.78	7.90	7.79	7.74
Al(iv)	0.20	0.16	0.22	0.10	0.21	0.26
T site	**8.00**	**8.00**	**8.00**	**8.00**	**8.00**	**8.00**
Al(vi)	0.07	0.04	0.28	0.04	0.13	0.21
Fe(3+)	0.00	0.00	0.00	0.00	0.00	0.00
Ti	0.00	0.01	0.02	0.01	0.03	0.00
Mg	3.19	3.48	3.02	3.47	3.25	2.70
Fe(2+)	1.70	1.47	1.66	1.41	1.56	2.09
Mn	0.00	0.00	0.00	0.00	0.00	0.00
Cr	0.00	0.00	0.00	0.00	0.00	0.01
Ni	0.00	0.00	0.00	0.00	0.00	0.00
C site	**4.96**	**5.00**	**4.99**	**4.93**	**4.97**	**5.01**
Fe(2+)	0.00	0.03	0.00	0.00	0.00	0.00
Mn	0.06	0.03	0.03	0.04	0.03	0.03
Ca	2.01	1.95	1.81	2.03	1.95	1.93
Na	0.00	0.00	0.00	0.00	0.00	0.00
B site	**2.07**	**2.02**	**1.84**	**2.08**	**1.98**	**1.96**
Ca	0.00	0.00	0.00	0.00	0.00	0.00
Na	0.04	0.05	0.22	0.04	0.10	0.06
K	0.01	0.02	0.01	0.01	0.02	0.03
A site	**0.05**	**0.07**	**0.23**	**0.04**	**0.12**	**0.09**
Total	15.09	15.09	15.06	15.05	15.07	15.07
Mg/Mg+Fe	0.65	0.70	0.65	0.71	0.68	0.56

***Table A3. 5**: Microprobe analysis of serpentine.*

	Kr45-5	Kr45-21	Kr45-23	Kr65-7	Kr65-10	Kr65-16	Kr65-17
SiO2	40.55	40.11	41.69	43.06	42.35	43.64	44.41
Al2O3	2.25	2.36	2.85	1.71	1.68	1.90	1.51
TiO2	0.00	0.11	0.00	0.00	0.00	0.00	0.12
MgO	32.56	29.68	30.17	39.47	39.43	41.08	40.97
FeO	10.88	8.66	11.77	3.12	3.48	3.02	2.71
MnO	0.14	0.19	0.10	0.00	0.00	0.00	0.10
CaO	0.11	0.09	0.36	0.08	0.00	0.06	0.00
Na2O	0.00	0.35	0.11	0.00	0.00	0.07	0.00
K2O	0.00	0.16	0.00	0.00	0.00	0.00	0.06
Cr2O3	0.14	0.00	0.17	0.39	0.15	0.00	0.00
NiO	0.46	0.29	0.49	0.00	0.25	0.27	0.21
Total	87.08	81.98	87.71	87.83	87.35	90.04	90.08
T site							
Si	32.78	33.97	33.49	33.05	32.81	32.71	33.17
Al	1.22	0.03	0.51	0.95	1.19	1.29	0.83
Total T	34.00	34.00	34.00	34.00	34.00	34.00	34.00
M site							
Al	0.93	2.33	2.19	0.59	0.34	0.39	0.50
Ti	0.00	0.07	0.00	0.00	0.00	0.00	0.07
Mg	39.25	37.47	36.13	45.16	45.53	45.91	45.63
Fe	7.35	6.13	7.90	2.00	2.25	1.89	1.69
Mn	0.10	0.13	0.07	0.00	0.00	0.00	0.06
Ca	0.09	0.08	0.31	0.07	0.00	0.05	0.00
Na	0.00	0.57	0.17	0.00	0.00	0.11	0.00
K	0.00	0.17	0.00	0.00	0.00	0.00	0.05
Cr	0.09	0.00	0.11	0.24	0.09	0.00	0.00
Ni	0.30	0.20	0.31	0.00	0.16	0.16	0.12
Total M	48.10	47.15	47.19	48.06	48.38	48.50	48.13

***Table A3.5**: (continued).*

	Kr65-19	Kr65-20	Kr38-8	Kr38-10	Kr38-11	Kr38-13	Kr38-14	Kr38-15
SiO2	43.35	43.79	41.96	42.47	43.87	43.18	42.73	42.33
Al2O3	1.60	1.96	2.14	1.79	0.45	0.81	0.60	1.65
TiO2	0.00	0.16	0.13	0.00	0.00	0.00	0.00	0.17
MgO	40.94	41.65	35.13	36.33	36.63	36.48	36.71	36.18
FeO	2.70	2.80	8.87	7.75	7.30	8.00	7.20	8.31
MnO	0.00	0.00	0.00	0.17	0.23	0.00	0.13	0.00
CaO	0.05	0.04	0.00	0.15	0.00	0.12	0.00	0.14
Na2O	0.08	0.00	0.00	0.00	0.00	0.10	0.07	0.00
K2O	0.00	0.00	0.00	0.07	0.04	0.00	0.08	0.00
Cr2O3	0.16	0.16	0.33	0.11	0.18	0.30	0.00	0.00
NiO	0.26	0.00	0.20	0.20	0.20	0.33	0.19	0.37
Total	89.14	90.56	88.76	89.04	88.89	89.31	87.71	89.14
T site								
Si	32.79	32.57	32.83	32.98	33.96	33.46	33.57	32.92
Al	1.21	1.43	1.17	1.02	0.04	0.54	0.43	1.08
Total T	34.00	34.00	34.00	34.00	34.00	34.00	34.00	34.00
M site								
Al	0.22	0.29	0.81	0.61	0.38	0.19	0.13	0.43
Ti	0.00	0.09	0.08	0.00	0.00	0.00	0.00	0.10
Mg	46.17	46.19	40.98	42.06	42.27	42.14	42.99	41.94
Fe	1.71	1.74	5.80	5.03	4.72	5.19	4.73	5.40
Mn	0.00	0.00	0.00	0.11	0.15	0.00	0.09	0.00
Ca	0.04	0.04	0.00	0.13	0.00	0.10	0.00	0.11
Na	0.12	0.00	0.00	0.00	0.00	0.15	0.11	0.00
K	0.00	0.00	0.00	0.07	0.04	0.00	0.08	0.00
Cr	0.10	0.09	0.20	0.07	0.11	0.19	0.00	0.00
Ni	0.16	0.00	0.12	0.12	0.12	0.20	0.12	0.23
Total M	48.51	48.43	48.00	48.21	47.79	48.16	48.24	48.22

A4. Precambrian Research paper abstract

Geological record of Paleoarchean oceanic flake tectonics preserved in the c. 3.3 Ga Kromberg volcanic type-section, Barberton greenstone belt, South Africa

Eugene G. Grosch[1*], Giulio Viola[2], Sibusisiwe Ndlela[1]

1: Geology Department, Rhodes University, P.O. Box 94, Grahamstown 6140, South Africa

2: Department of Biological, Geological & Environmental Sciences (BiGeA), University of Bologna, Bologna, Italy

*Corresponding author: geogene@gmail.com

Abstract

The geology and existing geodynamic models for the c. 3.3 Kromberg mafic-ultramafic sequence of rocks in the Barberton greenstone belt (South Africa) have been the subject of intense debate as, in addition to their regional significance, they have bearing also upon possible Paleoarchean tectonic processes on the early Earth. Models for the origin of the Kromberg sequence of rocks range from formation in an autochthonous, plume-type setting to that of an allochthonous, ophiolite thrust sheet emplaced in a modern-style plate-tectonic regime. This study reports new high-resolution field mapping results, drill core observations and secondary ion microprobe U-Pb detrital zircon age constraints across the Kromberg type-section on both the eastern and western sides of the Komati River. The new observations indicate that the Kromberg type-section represents a ca. 1.65 km thick dismembered and variably silicified mélange of oceanic supracrustal rocks with minor metadunites, which are structurally bound by chlorite-carbonate-quartz shear zones. Field observations and microstructural analysis allow for the rheological behaviour of the Mesoarchean oceanic lithosphere to be explored. It is proposed herein that the observed structural and volcanic geology is compatible with a mid-Archean oceanic flake tectonic process, involving detachment along a brittle-ductile transition zone and horizontal accretion of thin, rigid, silicified slivers of upper Archean oceanic crust. These accreted allochthonous oceanic

fragments would have delaminated from thick, weaker, lower oceanic crust that was recycled into the hot Paleoarchean mantle, and thus removed from the geological record. The model invoked here suggests that, although the well-preserved mafic-ultramafic Kromberg volcanic sequence may share some significant similarities with modern Phanerozoic ophiolites in the field, it most likely did not form by modern-style plate-tectonic processes. The new field observations herein support highly elevated oceanic geothermal gradients at the time due to a hotter, more vigorously convecting, mid-Archean mantle and crustal geodynamic processes unique to the Paleoarchean era of Earth history in the absence of a global-scale, fully developed plate-tectonic regime.